

ATMOSPHERES OF THE COMPONENTS OF  
CLOSE BINARY STARS

*A Thesis*  
*Submitted For The Degree of*  
*Doctor of Philosophy In The Faculty of Science*

BANGALORE UNIVERSITY

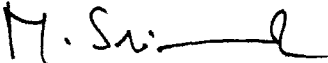
BY  
M. SRINIVASA RAO

INDIAN INSTITUTE OF ASTROPHYSICS  
BANGALORE  
INDIA

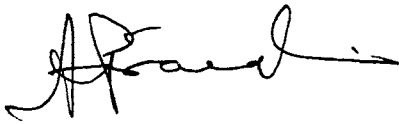
MARCH 2001

## DECLARATION

I here by declare that the matter embodied in this thesis is the result of the investigations carried out by me in the Indian Institute of Astrophysics, Koramangala, Bangalore, under the supervision of Prof. A. Peraiah and has not been submitted for award of any degree, diploma, associateship, fellowship etc., of any university or Institute.

  
(M. Srinivasa Rao)

Candidate



Prof. A. Peraiah

Supervisor

Bangalore

Date 15/3/2011

## DEDICATION

*This thesis is dedicated to the memory  
of my parents who constantly encouraged me to  
continue my studies even in the most difficult times*

## *Acknowledgments*

I am greatly indebted to my supervisor Prof. A. Peraiah who suggested this research problem, and took keen interest in all aspects of the work presented in this thesis. Many discussions which I had with him have helped me widen my understanding of the problem. This thesis would not have been possible without his constant encouragement and invaluable guidance.

I am extremely grateful to Prof. M. N. Anandaram for his help in the university formalities related to the Ph.D programme. I wish to thank Prof. Ramnath Cowsik, Director, Indian Institute of Astrophysics for providing the excellent research facilities. I am grateful to Prof. N. Kameswara Rao, Dean of academic division, Indian Institute of Astrophysics, for his cheerful and continued encouragement. I thank Prof. R. Srinivasan Dean of electronics division of Indian Institute of Astrophysics for his support and encouragement in the completion of this work.

I am especially thankful to Dr. D. Mohan Rao, who always drew my attention to the mathematical **aspects** of the problem. The innumerable suggestions and critical comments which I have received from him have helped me a great deal. I am equally thankful to Mr. Baba Anthony Varghese who always helped me in programming, and is indeed a friend in need. I am grateful to my colleagues Dr. K. N. Nagendra, Dr. K. E. Rangarajan for their constant encouragement. It is a pleasure to thank Dr. K. B. Ramesh who very patiently corrected the typographical errors and for his active help in timely completion of this thesis. I am also

thankful to Dr. M. F. Ingalgi for his help and moral support.

I am thankful to the staff of our computer centre Mr. A. V. Ananth and Mr. J. S. Nathan for providing the full time computing facility. Dr. A. Vagiswari, Mrs. Christina Louis have kindly provided me all the required library facilities through the course of this work and I am thankful to them for this gesture. Mr. P. N. Prabhakara has carefully reproduced several copies of the thesis. Mr. D. Kanakaraj has got the copies of the thesis attractively bound. I thankfully acknowledge them for their efforts and help.

My acknowledgment, beyond words are due to all my brothers, sisters, brothers-in-law, sisters-in-law, nephews, niece, uncles and aunts who gave me love, affection, appreciation, criticism and everything during my studies. I am grateful to my parents-in-law who always helped in every aspect of my family matters. I also thank my school teachers, school mates, college lecturers, college mates, room mates and close friends for their support and help during my school and college days.

I always remember our family friend, Sri. Neelamraju Narasimha Rao, and all his family members who have encouraged and supported me althrough. I sincerely thank all of them.

Finally and most importantly, I thank my wife Mrs. M. Seetha not only for her love, friendship and cooperation, but also for providing more time to work on the thesis. I cheerfully acknowledge the love and understanding of my sons M. V. Bharadwaj, and M. S. Tejaswi.

## *List of publications*

1. A series of theoretical line profiles formed in the irradiated expanding atmospheres of close binary components,  
A. Peraiah and **M. Srinivasa Rao**,  
*Astronomy and Astrophysics Suppl.* **132**, 45-54, 1998
2. Radiative transfer in the dusty, irradiated expanding atmospheres of close binary components,  
**M. Srinivasa Rao** and A. Peraiah,  
*Astronomy and Astrophysics Suppl.* **145**, 525-532, 2000
3. Radiative transfer in the distorted and irradiated atmospheres of close binary components,  
A. Peraiah and **M. Srinivasa Rao**  
(Submitted)

# Contents

	Page No
<b>Acknowledgements</b> ...	iv
<b>List of Publications</b> ...	vi
<b>ABSTRACT</b> ...	1
<b>Introduction</b> ...	5
<i>Chapter 1</i> <b>Discrete space theory of radiative transfer</b> ...	10
1.1 Introduction	10
1.1.1 Interaction Principle ...	11
1.1.2 Star Product ...	14
1.1.3 Calculation of radiation field at internal points ...	16
1.2 Applications of discrete Space theory ...	18
1.2.1 Solution of monochromatic equation of radiative transfer in spherical symmetry ...	19
1.2.2 Flux conservation in the monochromatic case ...	26
1.2.3 Line formation in expanding media ...	27
1.2.4 The equation of transfer in comoving frame ...	28
1.2.5 Calculation of line fluxes for an observer at infinity ...	37

<i>Chapter 2</i>	<b>Reflection effect in close binaries</b>	... 43
2.1	Introduction	... 43
2.2	Distribution of radiation incident from a point source	... 45
2.2.1	Description of rod model	... 46
2.2.2	Calculation of self radiation of the primary component	... 49
2.2.3	Brief description of computational procedure	... 51
2.2.4	Result and discussions	... 52
2.3	Distribution of emergent radiation along the line of sight when incident radiation is from a point source	... 58
2.3.1	Method to calculate radiation field from center to limb	... 58
2.3.2	Result and discussions	... 61
2.4	Temperature changes due to reflection	... 66
2.4.1	Result and discussions	... 66
<i>Chapter 3</i>	<b>Incident radiation from an extended source</b>	... 69
3.1	Introduction	... 69
3.2	Distribution of radiation incident from an extended source	... 70
3.2.1	Brief description of the method	... 75
3.2.2	Result and discussion	... 75
3.3	Distribution of emergent radiation along the line of sight when radiation is incident from an extended source	... 80
3.3.1	Method to calculate radiation field from center to limb	... 81
3.3.2	Result and discussions	... 84

<i>Chapter 4</i>	<b>Effects of reflection on spectral lines</b>	...	91
4.1	Introduction	...	91
4.1.1	Brief description of the method	...	92
4.2	Calculation of line profiles in a static medium	...	97
4.2.1	Result and discussion	...	98
4.3	Theoretical line profiles formed in the irradiated expanding atmosphere of close binary components	...	104
4.3.1	Result and discussion	...	109
4.4	Radiative transfer in the dusty irradiated expanding atmospheres of close binary components	...	117
4.5	The equation of transfer in comoving frame in a dusty atmosphere	...	118
4.5.1	Boundary conditions	...	120
4.5.2	Result and discussions	...	122
<i>Chapter 5</i>	<b>Distortion due to rotation and tidal forces</b>	...	133
5.1	Introduction	...	133
5.2	Formulation of equations for the distorted surface of the component due to rotation and tidal force	...	135
5.3	Results and discussion	...	140
5.3.1	Effects on luminosity	...	140
5.3.2	Limb darkening	...	142
5.3.3	Luminosities with limb darkening	...	144
5.4	Rotational effects on line source function	...	146
5.4.1	Brief description of the method and computational procedure	...	146

<i>Chapter 6</i>	<b>Effects of gravity darkening on spectral lines</b>	... 153
6.1	Introduction	... 153
6.2	Calculation of source functions in the distorted atmosphere	... 154
6.3	Result and discussion	... 159
<i>Chapter 7</i>	<b>Conclusions</b>	... 170
7.1	Discrete space theory of radiative transfer	... 170
7.2	Incident radiation from a point source	... 170
7.3	Incident radiation from an extended source	... 171
7.4	Effects of reflection on spectral lines	... 172
7.5	Distortion due to rotation and tidal forces	... 172
7.6	Effects of gravity darkening on spectral lines	... 173
	<b>References</b>	... 175

# *Abstract*

For theoretical modeling of binary systems one has to consider realistic models which takes into account the radiative transfer, hydrodynamics, reflection effect etc. Since the problem is complex, we study in the thesis some of idealized models which will help us in understanding the important physical processes in close binaries. Initially we have computed the theoretical lines in the expanding and extended distorted atmospheres of the components of close binary system. I have considered the necessary geometrical formalism for illumination of a stellar atmospheres from a source. We describe the method to calculate the radiation field from the irradiated surface of the component in a binary system.

## *Chapter 1*

**Discrete Space theory of Radiative transfer :** In this chapter a concise description of the method of obtaining the solution of radiative transfer equation which can be applied to different geometrical and physical systems is given. This method was developed by Grant and Peraiah (1972), and Peraiah and Grant(1973). This chapter deals with (1) interaction principle (2) star product (3) calculation of radiation field at internal points (4) integration of monochromatic radiative transfer equation and derivation of  $r$  and  $t$  operators of the "cell". (5) flux conservation and (6) line formation in expanding media.

The radiative transfer equation in spherical symmetry is used for calculating the self radiation of the primary star in a binary system.

## *Chapter 2*

**Reflection effect in close binaries :** The aim of this section is to estimate the radiation field along the spherical surface of a primary component irradiated by an external point source of radiation. This can be applied to very widely separated systems. The transfer of radiation incident on the atmosphere of the component from the companion cannot be studied by using any symmetric solution of the equation of transfer. This needs a special treatment. We adopt angle-free one dimensional model (see Sobolev 1963).

## *Chapter 3*

**Incident radiation from an extended source :** The effects of irradiation from an extended source of the secondary component on the atmospheres of the primary are studied.

## *Chapter 4*

(1) **Effects of reflection on spectral line formation:** Effects of reflection on formation of spectral lines in a purely scattering atmosphere and studied how the equivalent widths change when irradiation from the secondary is taken into account. However, these calculations were done in static atmospheres. So in the next step we have included the expanding atmospheres.

(2) **Effects of irradiation on the line formation in the expanding atmospheres of the components of a close binary system :** We studied the formation of lines in the irradiated expanding atmospheres of the component of close binary system. We considered two-level atom approximation in non-LTE situation with complete redistribution. We

assumed that the dust scatters isotropically in the atmosphere. The line profiles of the dusty atmosphere are compared with those formed in dust free atmosphere. The profiles are presented for different velocities of expansion, proximity of secondary component to the primary, and dust optical depths.

The line profiles for a dust free atmosphere with and without reflection effects are computed and compared.

### *Chapter 5*

**Distorted surface due to self rotation and tidal forces :** In this chapter a general expression for gravity darkening of the tidally uniformly rotating roche components of close binary system is derived. This theory is used to calculate the line profiles taking into account rotation and expansion velocities.

### *Chapter 6*

**Effect of gravity darkening on spectral line formation :** We studied the transfer of line radiation in the atmospheres of close binary components whose atmospheres are distorted by the self radiation and tidal forces due to the presence of the secondary component. The distortion is measured in terms of the ratio of angular velocities at the equator and pole, mass ratio of the two components, the ratio of centrifugal force to that of gravity at the equator and the ratio of the equatorial radius to the distance between the centers of gravity. We obtain the equation of the distorted surface by solving a seventh degree equation which contains the above parameters. Transfer of line radiation is studied in such asymmetric atmosphere assuming complete redistribution and a two-level atom approximation. The atmosphere is assumed to be expanding radially.

Various black body temperatures are being used to describe the total luminosity of the components for the purpose of irradiation.

### *Chapter 7*

**Conclusions :** We present important results obtained from this study of research from each chapter.

## *Introduction*

Binary stars occupy an important place in the study of structure and evolution of the stars. They provide some of the basic parameters such as masses and radii. An analysis of the observational data is required to derive these parameters. One of the observational data involves the changes in the total light during the eclipses in close pairs and these changes contain a wealth of information about the components of the close binary systems. The total light received is the sum of the light from the individual components and the mutually reflected light in the observers direction. If the components are very close, the reflected light forms a considerable fraction of the total light and therefore has to be estimated accurately. It is known that the radiation, that is received at infinity from the portion of the primary star atmosphere exposed to the secondary, consists of radiation fields from both the components. The incident radiation is modified by the atmosphere of the primary star and its radiation field. We realize that there are two important aspects to the problem. (1) The physical processes that take place in the medium, and (2) the geometrical shape of the illuminated surface which reflects the radiation. It is a standard practice to assume a simplified law of limb darkening and estimate the reflected radiation. This does not explicitly take into account the above mentioned two characteristics. The geometrical shape of the primary star's reflecting surface can change due to (1) the self rotation and (2) the tidal effects caused by the secondary component. Therefore, the standard law of limb darkening fails and we have to perform detailed calculations to compute the radiation field. The

process of calculating radiation field from such distorted surfaces become complicated when various competing physical processes are taken into account. Geometrical considerations alone would complicate the calculations considerably. The solution of radiative transfer equation in simplified symmetric geometries cannot accurately describe the radiation field emanating from such surfaces. Those geometrical configurations (plane parallel, spherical or cylindrical) assume symmetric boundary conditions, and whenever, we have asymmetric incident radiation, the solutions developed even in the context of symmetrical geometries will have to be modified.

Several works attempted the calculation of radiation received from the irradiated component of a close binary system. Chandrashekar(1958) has calculated the diffuse scattering function in a plane parallel medium when a pencil of beam of radiation from a point source is incident on it (searchlight problem). Subsequently, there were several attempts to calculate the diffuse radiation field in such simple geometries but the problem remained unsolved because of its complexity. Buerger (1969) employed plane parallel approximation in computing the continuum and the line radiation emitted by a rotationally and tidally distorted surface of the component which is irradiated by the radiation from the secondary component. This approach is adopted in order to avoid the complexities in estimating the radiation field in distorted atmospheres.

Regarding the observational studies of the problem, Yu. Skulskij (1993) considered the variability of equivalent widths with phases and other characteristics of absorption and emission components of Si II 6347 Å, 6371 Å lines in a study of  $\beta$  Lyre with CCD spectra. He showed that the variation of the absorption line equivalent widths depends on the or-

bital modulation and on the structure of the circumstellar gas in the close binary system. Fergusson and James (1994) studied the eclipsing binary BE UMa for the well known role of the reflection effect as well as the characteristics of cataclysmic variable progenitors. In this system, the reflection effect is important due to the relative proximity (about  $8R_{\odot}$ ) of a late type secondary to a very hot  $T \sim 10^5$  K primary  $S_dO$  star. Parthasarathy et.al. (1990) analyzed the ultraviolet spectrum (1175 Å to 3200 Å) of the hydrogen-poor binary star HD 30353. The high resolution spectra of the star show stellar wind profiles of NV, CIV, SiIV, CII, SiII, AlII, AlIII, MgII and FeII resonance lines. These line profiles appear to shift towards the shorter wavelengths side of the spectrum. They concluded that extended and multiple shells exist around the primary central star with a source at temperature of 30,000 K, which could be a O-type or an early B-type star as suggested by the far UV flux distribution.

To explain these observations, one has to consider realistic models which take into account the reflection effect in the solution of radiative transfer equation. Dugan (1908) and Stebbins (1911) were the first to observe this effect, since then referred to under the generic name reflection effect. Initial theoretical investigations were carried out by Eddington (1926) and Milne (1927). Eddington showed that, for stars in radiative equilibrium, the bolometric albedo is 1.0 and Milne studied the distribution of the temperature as a function of the optical depth leading to a reasonable agreement with the observations available at that time. Chandrasekhar (1947, 1950) studied the problem and presented an exact solution for grey atmosphere. However, all these results were obtained under the assumption that irradiation takes place as plane-parallel beams. Some later investigations have taken into account the finite size

of the components ( Russel 1949; Matukuma 1950; Kopal 1954).

In this thesis we study some of the idealized models which will help us in understanding the important physical processes in close binary systems. In the following chapters we describe how the radiation field from the irradiated surface of the component in a binary system is calculated.

In *Chapter 1* a concise description of the numerical method based on "discrete space theory " in solving the radiative transfer is described. The method is developed by Grant and Peraiah (1972), and Peraiah and Grant (1973). The solution of transfer equation is used to calculate the self radiation of the primary component in a close binary system.

In *Chapter 2* a method to calculate the radiation field emitted by a spherical surface irradiated by an external point source of radiation is studied ( see Peraiah 1982). This method can be applied to widely separated systems also. The transfer of radiation incident on the atmosphere of the primary star cannot be studied by using solution of the transfer equation in symmetric geometries. This needs a special treatment. We adopt an angle-free one dimensional model (see Sobolev 1963). This procedure gives a fairly accurate solution, provided we take large number of incident rays.

In *Chapter 3* the method developed in *chapter 2* is used to handle the reflection effect when the secondary component is an extended source (see Peraiah 1983 a).

In *Chapter 4* effects of reflection on the formation of spectral lines in a purely scattering atmosphere is studied (see Peraiah & Srinivasa Rao 1983b). These calculations were done in static atmospheres. As a next step we studied the effects of irradiation on the line formation

in expanding atmospheres of the primary (see Peraiah & Srinivasa Rao 1998). In subsequent paper (see Srinivasa Rao & Peraiah 2000), we included the presence of dust in the primary star atmosphere. In both of these studies, the expansion of the primary star atmosphere is taken into account.

A general expression for the gravity darkening of the tidally and non-uniformly rotating Roche components of close binary systems is derived in Peraiah (1970). In *Chapter 5* these expressions are employed to calculate the line profiles, taking into account the rotation and expansion of the primary atmosphere. However, we have restricted ourselves to the rotational distortion of a single star (primary).

In *Chapter 6* the method of solution presented in *chapter 5* is further used to include tidal distortion caused by the presence of secondary component.

In *Chapter 7* we present the conclusions on reflection effect in close binaries stars.

# Chapter 1

## Discrete space theory of radiative transfer

### 1.1 Introduction

The study of transfer of radiation is an essential part in the stellar astrophysics research. The complex physical processes that occur in stellar atmospheres do not permit us to obtain the solution of radiative transfer equation easily. Various people working with the problems of stellar atmospheres have developed different techniques depending upon their needs and tastes. Among the most notable methods of solving the equation of radiative transfer is the one based on the principles of invariant embedding due to Ambarzumian (1943) and Chandrasekhar (1950). These principles are a special case of interaction principle and the star product Redheffer (1962) and Preisendorfer (1965) is applicable to any inhomogeneous media in curved geometries. In general we follow the following procedure.

- We divide the medium into a number of 'cells' whose thickness is defined by  $\tau$  which is less than or equal to the critical thickness ( $\tau_{\text{crit}}$ ). The critical thickness is determined on the basis of the physical characteristics of the medium.  $\tau_{\text{crit}}$  ensures stability and uniqueness of the solution.
- The integration of the transfer equation is performed on the 'cell' which is a two-dimensional grid of radius - angle bounded by

$$[r_n, r_{n+1}] \times [\mu_{j-\frac{1}{2}}, \mu_{j+\frac{1}{2}}],$$

where

$$\mu_{j+\frac{1}{2}} = \sum_{k=1}^j C_k, \quad j = 1, 2, \dots, J$$

where  $C^s$  being the corresponding weights for the zeros  $\mu_j$  of a suitable quadrature and  $\mu_{j+\frac{1}{2}} \leq \mu_j \leq \mu_{j+\frac{1}{2}}$ . We shall select the roots and weights Gauss Legendre quadrature formula of the order  $J$  over  $(0,1)$ .

- We compare these discrete equations with the canonical equations of the interaction principle and obtain the transmission and reflection operators of the 'cell'.
- Lastly, we combine all the cells by star algorithm and obtain the radiation field.

(we can divide the medium into shells whose thicknesses are larger than  $\tau_{\text{crit}}$  but integration is done only on 'cell' and star algorithm is used to obtain the transmission and reflection operators of the shells by 'adding' the cells.)

We describe the method in the following sections.

### 1.1.1 Interaction principle

The interaction principle relates the incident and emergent radiation field from a medium of given optical thickness. In figure 1.1, we have shown a shell of optical thickness with incident and emergent intensities. We assume that specific intensities  $U_n^+$  and  $U_{n+1}^-$  are incident at the boundaries  $n$  and  $n+1$  respectively of the shell with optical thickness  $\tau$ . The symbols with signs  $+$  and  $-$  represent specific intensities of the rays traveling in opposite directions.

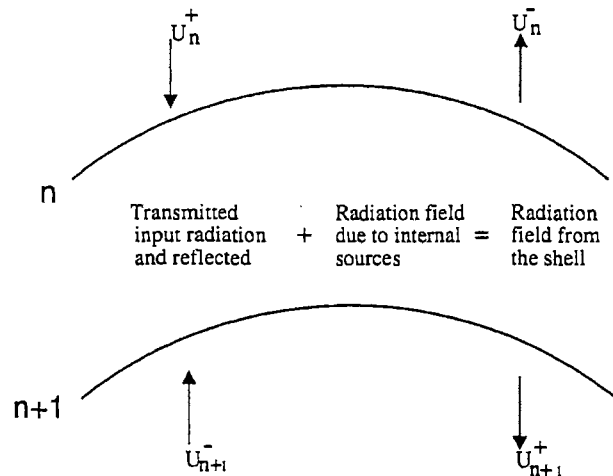


Figure 1.1: Schematic diagram showing the interaction principle.

If  $\mu$  represents the cosine of the angle made by a ray relative to the common normal (in the spherical case,  $\mu$  is the angle made by the ray direction with the radius vector) to the stratification in the direction in which  $n$  increases. That is,

$$\mathbf{U}_n^+ \{U_n(\mu) \quad : 0 < \mu \leq 1\},$$

and

$$\mathbf{U}_n^- \{U_n(-\mu) \quad : 0 < \mu \leq 1\},$$

where

$$\mathbf{U}_n^\pm = 4\pi r_n^2 \mathbf{I}_n^\pm,$$

$\mathbf{I}_n^+$  represents the specific intensity of the ray traveling in the direction  $\mu$  and  $\mathbf{I}_n^-$  represents the specific intensity of the ray traveling in the opposite direction. In the case of plane parallel geometry  $\mathbf{U}_n^\pm = \mathbf{I}_n^\pm$ . We select a finite set of values of  $\mu$  ( $\mu_j : 1 \leq j \leq m; 0 < \mu_1 < \mu_2 < \mu_3 \dots \mu_m < 1$ ).

Then

$$\mathbf{U}_n^+ = \begin{pmatrix} U_n(\mu_1) \\ U_n(\mu_2) \\ \vdots \\ U_n(\mu_m) \end{pmatrix},$$

and

$$\mathbf{U}_n^- = \begin{pmatrix} U_n(-\mu_1) \\ U_n(-\mu_2) \\ \vdots \\ U_n(-\mu_m) \end{pmatrix}$$

are  $m$  - dimensional vectors.

The incident intensity vectors are  $\mathbf{U}_n^+$  and  $\mathbf{U}_{n+1}^-$ .

The emergent intensity vectors are  $\mathbf{U}_n^-$  and  $\mathbf{U}_{n+1}^+$ .

The emergent radiation field will have the contributions from the internal sources say,  $\Sigma^+(n+1, n)$  and  $\Sigma^-(n, n+1)$  corresponding to the output intensity vectors  $\mathbf{U}_{n+1}^+$  and  $\mathbf{U}_n^-$  respectively.

We assume certain linear operators which reflect and transmit the incident radiation namely,  $\mathbf{t}(n+1, n)$ ,  $\mathbf{r}(n, n+1)$ ,  $\mathbf{t}(n, n+1)$  and  $\mathbf{r}(n+1, n)$ . Then we can write the output intensities in terms of the transmitted and reflected input intensities together with the internal sources as

$$\begin{aligned} \mathbf{U}_{n+1}^+ &= \mathbf{t}(n+1, n)\mathbf{U}_n^+ + \mathbf{r}(n, n+1)\mathbf{U}_{n+1}^- + \Sigma^+(n+1, n), \\ \mathbf{U}_n^- &= \mathbf{r}(n+1, n)\mathbf{U}_n^+ + \mathbf{t}(n, n+1)\mathbf{U}_{n+1}^- + \Sigma^-(n, n+1). \end{aligned} \quad (1.1)$$

The introduction of the internal source terms namely,  $\Sigma^+(n+1, n)$  and  $\Sigma^-(n, n+1)$  was due to Grant and Hunt (1969a). The relationship given by equation (1.1) is called the "Interaction Principle". Equation (1.1) can also be written concisely as

$$\begin{pmatrix} \mathbf{U}_{n+1}^+ \\ \mathbf{U}_n^- \end{pmatrix} = \mathbf{S}(n, n+1) \begin{pmatrix} \mathbf{U}_n^+ \\ \mathbf{U}_{n+1}^- \end{pmatrix} + \Sigma(n, n+1), \quad (1.2)$$

where

$$\mathbf{S}(n, n+1) = \begin{pmatrix} \mathbf{t}(n+1, n) & \mathbf{r}(n, n+1) \\ \mathbf{r}(n+1, n) & \mathbf{t}(n, n+1) \end{pmatrix}. \quad (1.3)$$

### 1.1.2 Star product

If there is another shell with boundaries  $(n+1, n+2)$  adjacent to  $(n, n+1)$ . interaction principle for this shell can be written as

$$\begin{pmatrix} \mathbf{U}_{n+2}^+ \\ \mathbf{U}_{n+1}^- \end{pmatrix} = \mathbf{S}(n+1, n+2) \begin{pmatrix} \mathbf{U}_{n+1}^+ \\ \mathbf{U}_{n+2}^- \end{pmatrix} + \Sigma(n+1, n+2), \quad (1.4)$$

where  $\mathbf{S}(n+1, n+2)$  is similarly defined as in equation (1.3). If we combine the two shells  $(n, n+1)$  and  $(n+1, n+2)$ , then the interaction principle for the combined shell is written as, (thickness is arbitrarily defined)

$$\begin{pmatrix} \mathbf{U}_{n+2}^+ \\ \mathbf{U}_n^- \end{pmatrix} = \mathbf{S}(n, n+2) \begin{pmatrix} \mathbf{U}_n^+ \\ \mathbf{U}_{n+2}^- \end{pmatrix} + \Sigma(n, n+2). \quad (1.5)$$

Redheffer (1962) calls  $\mathbf{S}(n, n+2)$  the *star product* of the two S-matrices  $\mathbf{S}(n, n+1)$  and  $\mathbf{S}(n+1, n+2)$ . It is written as

$$\mathbf{S}(n, n+2) = \mathbf{S}(n, n+1) \star \mathbf{S}(n+1, n+2). \quad (1.6)$$

Equation (1.5) is obtained by elimination  $\mathbf{U}_{n+1}^+$  and  $\mathbf{U}_{n+1}^-$  from equations (1.2) and (1.4). We can write  $\mathbf{r}$  and  $\mathbf{t}$  operators for the composite cell as

$$\mathbf{t}(n+2, n) = \mathbf{t}(n+2, n+1)[\mathbf{I} - \mathbf{r}(n, n+1)\mathbf{r}(n+2, n+1)]^{-1}\mathbf{t}(n+1, n),$$

$$\mathbf{t}(n, n+2) = \mathbf{t}(n, n+1)[\mathbf{I} - \mathbf{r}(n+2, n+1)\mathbf{r}(n, n+1)]^{-1}\mathbf{t}(n+1, n+2),$$

$$\begin{aligned} \mathbf{r}(n+2, n) &= \mathbf{r}(n+1, n) + \mathbf{t}(n, n+1)\mathbf{r}(n+2, n+1) \times \\ &\quad [\mathbf{I} - \mathbf{r}(n, n+1)\mathbf{r}(n+2, n+1)]^{-1} \times \mathbf{t}(n+1, n), \end{aligned}$$

$$\begin{aligned} \mathbf{r}(n, n+2) &= \mathbf{r}(n+1, n+2) + \mathbf{t}(n+2, n+1)\mathbf{r}(n, n+1) \times \\ &\quad [\mathbf{I} - \mathbf{r}(n+2, n+1)\mathbf{r}(n, n+1)]^{-1} \times \mathbf{t}(n+1, n+2), \end{aligned} \quad (1.7)$$

and

$$\begin{aligned} \Sigma(n, n+2) &= \Lambda(n, n+1; n+2)\Sigma(n, n+1) + \\ &\quad \Lambda'(n; n+1, n+2)\Sigma(n+1, n+2), \end{aligned} \quad (1.8)$$

where  $\mathbf{I}$  the identity matrix and

$$\begin{aligned} \Lambda(n, n+1; n+2) &= \\ &\begin{pmatrix} \mathbf{t}(n+2, n+1)[\mathbf{I} - r(n, n+1)\mathbf{r}(n+2, n+1)]^{-1} & \mathbf{0} \\ \mathbf{t}(n, n+1)\mathbf{r}(n+2, n+1)[\mathbf{I} - \mathbf{r}(n, n+1)\mathbf{r}(n+2, n+1)]^{-1} & \mathbf{I} \end{pmatrix}. \\ \Lambda'(n; n+1, n+2) &= \\ &\begin{pmatrix} \mathbf{I} & \mathbf{t}(n+2, n+1)\mathbf{r}(n, n+1)[\mathbf{I} - \mathbf{r}(n+2, n+1)\mathbf{r}(n, n+1)]^{-1} \\ \mathbf{0} & \mathbf{t}(n, n+1)[\mathbf{I} - \mathbf{r}(n+2, n+1)\mathbf{r}(n, n+1)]^{-1} \end{pmatrix}. \end{aligned} \quad (1.9)$$

and

$$\Sigma(n, n+1) = \begin{pmatrix} \Sigma^+(n+1, n+2) \\ \Sigma^-(n, n+1) \end{pmatrix}. \quad (1.10)$$

Similarly  $\Sigma(n+1, n+2)$  is defined. If we write  $\mathbf{S}(\alpha)$  to designate the shell  $\alpha$  then

$$\mathbf{S}(\alpha \star \beta) = \mathbf{S}(\alpha) \star \mathbf{S}(\beta), \quad (1.11)$$

where  $\alpha \star \beta$  denotes the region obtained by putting the two shells  $\alpha$  and  $\beta$  together. If the shells are homogeneous and plane parallel then

$$\alpha \star \beta = \beta \star \alpha. \quad (1.12)$$

In general star multiplication is non-commutative. However, star multiplication is associative. If we have to add several layers  $\alpha, \beta, \gamma \dots$  then

$$\mathbf{S}[(\alpha \star (\beta \star \gamma) \star \dots)] = \mathbf{S}[(\alpha \star \beta) \star \gamma \star \dots] \text{ etc.} \quad (1.13)$$

If the medium is homogeneous and very thick then we can use what is known as ‘doubling method’ (see van de Hulst 1965). For example,

$$\mathbf{S}(2^P d) = \mathbf{S}(2^{P-1} d) \star \mathbf{S}(2^{P-1} d), (P = 1, 2, 3, \dots), \quad (1.14)$$

which means that we can generate the  $\mathbf{S}$ -matrix for a layer of thickness  $2^p d$  in  $P$  cycles starting with  $\mathbf{S}(d)$  rather than in  $2^p$  cycles of adding the  $\mathbf{S}(d)$ ’s one by one. If  $p = 10$ , then only a fraction  $10/2^{10} \simeq 10^{-2}$  of the computational work is needed to add  $2^{10}$  layers of thickness  $d$ .

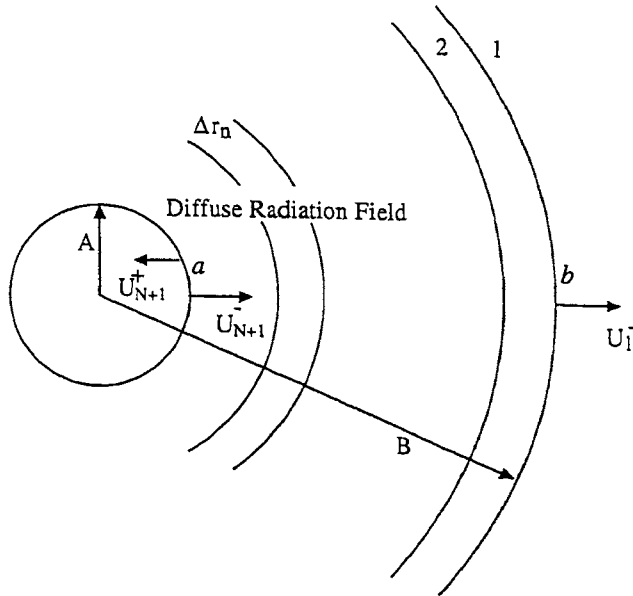


Figure 1.2: Schematic diagram showing the diffuse radiation.

### 1.1.3 Calculation of radiation field at internal points

We expect the reflection and transmission operators to be non-negative on the physical grounds that intensities are always non-negative. This condition will be satisfied only when the optical thickness of the shell is less than certain value called the 'critical size'  $\tau_{\text{crit}}$ . If the optical thickness  $\tau$  of the shell in question is larger than the  $\tau_{\text{crit}}$  then we can divide the shell into several subshells whose  $\tau$  is less than the  $\tau_{\text{crit}}$  and then use star algorithm to calculate combined response from the subshells whose total thickness is  $T$ . If, for example we need the radiation field at internal points in the atmosphere, we shall have to divide the entire medium into as many shells as we need and calculate the radiation field at the  $N$  points in the medium. One can write down the interaction principle for each shell and solve the whole system of equations (see Grant and Hunt 1968).

In figure 1.2, we show the atmosphere in which we calculate the internal radiation field. The atmosphere is divided into  $N$  shells (homogeneous or

inhomogeneous) with A and B as the inner and outer radii. The solution  $\mathbf{U}_{n+1}^+$  and  $\mathbf{U}_n^-$  (for any shell between shell 1 (at  $b$ ) and shell N (at  $a$ ) are obtained from the relations

$$\begin{aligned}\mathbf{U}_{n+1}^+ &= \mathbf{r}(1, n+1)\mathbf{U}_{n+1}^- + \mathbf{V}_{n+\frac{1}{2}}^+, \\ \mathbf{U}_n^- &= \mathbf{t}(n, n+1)\mathbf{U}_{n+1}^- + \mathbf{V}_{n+\frac{1}{2}}^-, \end{aligned} \quad (1.15)$$

with the boundary conditions  $\mathbf{U}_{N+1}^- = \mathbf{U}^-(a)$ . The quantities  $\mathbf{r}(1, n+1)$ ,  $\mathbf{V}_{n+\frac{1}{2}}^+$  and  $\mathbf{V}_{n+\frac{1}{2}}^-$  are calculated by employing the initial conditions  $\mathbf{r}(1, 1) = 0$  and  $\mathbf{V}_{\frac{1}{2}}^+ = \mathbf{U}^+(b)$ . The computation is done by the following recursive relation.

$$\mathbf{r}(1, n+1) = \mathbf{r}(n, n+1) + \mathbf{t}(n+1, n)\mathbf{r}(1, n)[\mathbf{I} - \mathbf{r}(n+1, n)\mathbf{r}(1, n)]^{-1}\mathbf{t}(n, n+1),$$

$$\begin{aligned}\mathbf{V}_{n+\frac{1}{2}}^+ &= \mathbf{t}(n+1, n)\mathbf{V}_{n-\frac{1}{2}}^+ + \mathbf{\Sigma}^+(n+1, n) + \mathbf{R}_{n+\frac{1}{2}}\mathbf{\Sigma}^-(n, n+1), \\ \mathbf{V}_{n+\frac{1}{2}}^- &= \mathbf{r}(n+1, n)\mathbf{V}_{n-\frac{1}{2}}^+ + \mathbf{T}_{n+\frac{1}{2}}\mathbf{\Sigma}^-(n, n+1), \end{aligned} \quad (1.16)$$

where

$$\begin{aligned}\mathbf{t}(n+1, n) &= \mathbf{t}(n+1, n)[\mathbf{I} - \mathbf{r}(1, n)\mathbf{r}(n+1, n)]^{-1}, \\ \mathbf{r}(n+1, n) &= \mathbf{r}(n+1, n)[\mathbf{I} - \mathbf{r}(1, n)\mathbf{r}(n+1, n)]^{-1}, \\ \mathbf{R}_{n+\frac{1}{2}} &= \mathbf{t}(n+1, n)\mathbf{r}(1, n), \\ \mathbf{T}_{n+\frac{1}{2}} &= [\mathbf{I} - \mathbf{r}(n+1, n)\mathbf{r}(1, n)]^{-1}, \end{aligned} \quad (1.17)$$

and

$$\mathbf{t}(n, n+1) = \mathbf{T}_{n+\frac{1}{2}}\mathbf{t}(n, n+1). \quad (1.18)$$

To calculate the radiation field at the internal points we proceed as follows:

- Divide the medium into a number of shells (say N) with N+1 boundaries as mentioned earlier.

- Start calculating the two pairs of reflection and transmission operators  $\mathbf{r}(n+1, n), \mathbf{r}(n, n+1), \mathbf{t}(n+1, n)$  and  $\mathbf{t}(n, n+1)$  in each shell (if the optical thickness in each shell is larger than  $\tau_{\text{crit}}$ , then apply star algorithm or use doubling procedure if the medium is homogeneous).
- With the boundary condition that  $\mathbf{r}(1, 1)=0$  and  $\mathbf{V}_{\frac{1}{2}}^+ = \mathbf{U}^+(a)$  and the  $\mathbf{r}$  and  $\mathbf{t}$  operators mentioned above compute recursively  $\mathbf{r}(1, n+1), \mathbf{V}_{\frac{1}{2}}^\pm$  and  $\mathbf{t}(n, n+1)$  given in equations (1.16) to (1.18) from shell 1 to shell N (i.e. from  $b$  to  $a$  in figure 1.2).
- Next we shall sweep back from  $a$  to  $b$  (see figure 1.2) calculating the radiation field given in equation (1.15) with the boundary condition  $\mathbf{U}_{n+1}^- = \mathbf{U}^-(a)$ . If the surface at  $a$  is reflecting, we can write

$$\mathbf{U}_{N+1}^- = \mathbf{r}_G \mathbf{U}_{N+1}^+, \quad (1.19)$$

where  $\mathbf{r}_G$  is the reflection operator. For a totally reflecting surface  $\mathbf{r}_G = \mathbf{I}$ . Therefore, we have

$$\mathbf{U}_{N=1}^+ = [\mathbf{I} - \mathbf{r}(1, N+1)\mathbf{r}_G]^{-1} \mathbf{V}_{N+\frac{1}{2}}^+, \quad (1.20)$$

from which one can calculate  $\mathbf{U}_{N+1}^-$  from equation (1.19). Rest of the calculations follow equation (1.15).

## 1.2 Applications of discrete space theory

The discrete space theory of radiative transfer which was described in the previous section will be applied to few simple physical situations. The two important situations will be (1) monochromatic and (2) spectral line transfer. In monochromatic situation we have to consider the discretization of radius and angle while in the line transfer case we have

to treat discretization of radius, angle and frequency. We shall apply first to the monochromatic case and study how the discrete space theory can be applied very efficiently and in particular to the scattering problems.

### 1.2.1 Solution of monochromatic equation of radiative transfer in spherical symmetry

In this section we shall consider equation of transfer with monochromatic radiation field scattering isotropically (see Peraiah and Grant 1973).

The equation of transfer is given in the form

$$\begin{aligned} & \frac{\mu}{r^2} \frac{\partial}{\partial r} [r^2 I(r, \mu)] + \frac{1}{r} \frac{\partial}{\partial \mu} [(1 - \mu^2) I(r, \mu)] + \sigma(r) I(r, \mu) \\ & = \sigma(r) \left[ [1 - \omega(r)] b(r) + \frac{1}{2} \omega(r) \int_{-1}^1 p(r, \mu, \mu') I(r, \mu') d\mu' \right], \end{aligned} \quad (1.21)$$

where  $\omega(r)$  is the albedo for single scattering,  $I(r, \mu)$  is the specific intensity of the ray,  $r$  is the radius,  $\mu = \cos \theta$  (is the cosine of the angle made by the ray with radius vector),  $\sigma(r)$  is the absorption coefficient,  $b(r)$  represents the sources inside the cell and  $p(r, \mu, \mu')$  is the phase function.

$$b(r) \geq 0, \quad \sigma(r) \geq 0, \quad 0 \leq \omega(r) \leq 1,$$

and

$$\frac{1}{2} \int_{-1}^{+1} p(r, \mu, \mu') d\mu' = 1, \quad p(r, \mu, \mu') \geq 0,$$

and

$$-1 \leq \mu, \mu' \leq 1. \quad (1.22)$$

If we write  $A(r) = 4\pi r^2$ ,

$$\mathbf{U}(r, \mu) = A(r) I(r, \mu),$$

$$\mathbf{B}(r) = A(r) b(r).$$

We can rewrite the equation (1.21) of transfer in the form

$$\begin{aligned} & \mu \frac{\partial \mathbf{U}(r, \mu)}{\partial r} + \frac{1}{r} \frac{\partial}{\partial \mu} [(1 - \mu^2) \mathbf{U}(r, \mu)] + \sigma(r) \mathbf{U}(r, \mu) \\ & = \sigma(r) \left[ [1 - \omega(r)] \mathbf{B}(r) + \frac{1}{2} \omega(r) \int_{-1}^{+1} p(r, \mu, \mu') \mathbf{U}(r, \mu') d\mu' \right], \end{aligned} \quad (1.23)$$

for outward going rays, and

$$\begin{aligned} & -\mu \frac{\partial \mathbf{U}(r, -\mu)}{\partial r} - \frac{1}{r} \frac{\partial}{\partial \mu} [(1 - \mu^2) \mathbf{U}(r, -\mu)] + \sigma(r) \mathbf{U}(r, -\mu) \\ & = \sigma(r) \left[ [1 - \omega(r)] \mathbf{B}(r) + \frac{1}{2} \omega(r) \int_{-1}^{+1} p(r, -\mu, \mu') \mathbf{U}(r, \mu') d\mu' \right] \end{aligned} \quad (1.24)$$

for inward going rays, where we have restricted  $\mu$  to lie in the interval  $[0, 1]$ . We represent derivatives by differences and integrals by sums. In the 'cell' method of deriving difference equations one formally integrates (1.23) and (1.24) over an interval  $[r_n, r_{n+1}] \times [\mu_{j-\frac{1}{2}}, \mu_{j+\frac{1}{2}}]$  defined on a two dimensional grid (Lathrop and Carlson, 1967 and 1971). The choice of the set  $\{r_n\}$  will be discussed when radial integration is performed. The choice of  $\{\mu_{j+\frac{1}{2}}\}$  is dictated by convenience. We shall employ the roots  $\mu_j$  and weights  $c_j$  of the Gauss-Legendre quadrature formula of order  $J$  over  $[0, 1]$  and define the cell boundaries by writing  $\mu_{\frac{1}{2}} = 0$  and taking

$$\mu_{j+\frac{1}{2}} = \sum_{k=1}^j C_k, \quad j = 1, 2, \dots, J. \quad (1.25)$$

Here we have to do the integration on angle grid and radial grid. We will perform the angle integration for the equation (1.23). This gives us

$$\begin{aligned} & C_j \mu_j \frac{\partial U_j^+(r)}{\partial r} + \frac{1}{r} \left[ (1 - \mu_{j+\frac{1}{2}}^2) U_{j+\frac{1}{2}}^+(r) - (1 - \mu_{j-\frac{1}{2}}^2) U_{j-\frac{1}{2}}^+(r) \right] \\ & + C_j \sigma(r) U_j^+(r) = \sigma(r) C_j \left[ (1 - \omega(r)) B(r) + \frac{1}{2} \omega(r) \right. \\ & \left. \sum_{j'=1}^J \left( P^{++}(r)_{jj'} C_j U_{j'}^+(r) + P^{+-}(r)_{jj'} C_{j'} U_{j'}^-(r) \right) \right], \end{aligned} \quad (1.26)$$

where

$$U_j^+(r) = U(r, \mu_j),$$

$$\begin{aligned}
U_j^-(r) &= U(r, -\mu_j), \\
P^{++}(r)_{jj'} &= p(r, \mu_j, \mu_{j'}), \\
P^{-+}(r)_{jj'} &= p(r, -\mu_j, \mu_{j'}), \text{ etc.}
\end{aligned}$$

We get a similar equation from (1.24). The reason for the choice (1.25) should now be obvious; it permits us to evaluate the scattering integral term with the maximum accuracy assuming that the solutions  $U_j^+$ ,  $U_j^-$  are sufficiently smooth. Provided we consider the diffuse field we can be sure that this is the case. However, we have not yet defined  $U_{j+\frac{1}{2}}^\pm$  and we do this, with some loss of accuracy, by writing

$$U_{j+\frac{1}{2}}^+ = \frac{(\mu_{j+1} - \mu_{j+\frac{1}{2}})U_j^\pm + (\mu_{j+\frac{1}{2}} - \mu_j)U_{j+1}^\pm}{\mu_{j+1} - \mu_j}, \quad j = 1, 2, \dots, J-1, \quad (1.27)$$

and for convenience, define  $U_{\frac{1}{2}}^+ = U_{\frac{1}{2}}^-$  by interpolation

$$\begin{aligned}
U_{\frac{1}{2}}^+ &= U_{\frac{1}{2}}^- = \frac{1}{2}(U_1^+ + U_1^-), \\
\mathbf{U}^\pm(r) &= [U_1^\pm(r), \dots, U_J^\pm(r)]^T, \quad (1.28)
\end{aligned}$$

by writing

$$\mathbf{U}^\pm(r) = \begin{pmatrix} U_1^\pm(r) \\ U_2^\pm(r) \\ \vdots \\ U_J^\pm(r) \end{pmatrix}, \quad (1.29)$$

and making use of equations (1.27), (1.28) and (1.29) the equation (1.26) can be rewritten for all the angles in matrix form. This is given by

$$\begin{aligned}
&\mathbf{M} \frac{\partial \mathbf{U}^+(r)}{\partial r} + \frac{1}{r} [\mathbf{\Lambda}^+ \mathbf{U}^+(r) + \mathbf{\Lambda}^- \mathbf{U}^-(r)] + \sigma(r) \mathbf{U}^+(r) \\
&= \sigma(r) \left[ (1 - \omega(r)) \mathbf{B}^+(r) + \frac{1}{2} \omega(r) (\mathbf{P}^{++}(r) \right. \\
&\quad \left. \mathbf{C} \mathbf{U}^+(r) + \mathbf{P}^{+-}(r) \mathbf{C} \mathbf{U}^-(r)) \right], \quad (1.30)
\end{aligned}$$

and similarly equation (1.24) can be rewritten

$$\begin{aligned}
& -\mathbf{M} \frac{\partial \mathbf{U}^-(r)}{\partial r} + \frac{1}{r} [\mathbf{\Lambda}^+ \mathbf{U}^-(r) + \mathbf{\Lambda}^- \mathbf{U}^+(r)] + \sigma(r) \mathbf{U}^-(r) \\
& = \sigma(r) \left[ (1 - \omega(r)) \mathbf{B}^-(r) + \frac{1}{2} \omega(r) (\mathbf{P}^{-+}(r) \right. \\
& \quad \left. \mathbf{C} \mathbf{U}^+(r) + \mathbf{P}^{--}(r) \mathbf{C} \mathbf{U}^-(r)) \right], \tag{1.31}
\end{aligned}$$

here  $\mathbf{C}$  and  $\mathbf{M}$  are diagonal matrices with elements  $[C_j \delta_{jj'}]$ ,  $[\mu_j \delta_{jj'}]$  respectively,  $\mathbf{B}^+$  and  $\mathbf{B}^-$  are vectors with a similar structure to (1.28) and  $\mathbf{\Lambda}^+$  and  $\mathbf{\Lambda}^-$  are square  $\mathbf{J} \times \mathbf{J}$  matrices defined by the equations

$$\begin{aligned}
C_j \Lambda_{jk}^+ & = \frac{(1 - \mu_{j+\frac{1}{2}}^2)(\mu_{j+\frac{1}{2}} - \mu_j)}{(\mu_{j+1} - \mu_j)}, \quad k = j + 1, j = 1, 2 \dots J - 1 \\
& = \frac{(1 - \mu_{j+\frac{1}{2}}^2)(\mu_{j+1} - \mu_{j+\frac{1}{2}})}{(\mu_{j+1} - \mu_j)} - \frac{(1 - \mu_{j-\frac{1}{2}}^2)(\mu_{j-\frac{1}{2}} - \mu_{j-1})}{(\mu_j - \mu_{j-1})} \\
& \quad k = j, j = 1, 2 \dots J. \\
& = -\frac{(1 - \mu_{j-\frac{1}{2}}^2)(\mu_j - \mu_{j-\frac{1}{2}})}{(\mu_j - \mu_{j-1})}, \quad k = j - 1, j = 2, 3, \dots J,
\end{aligned}$$

and

$$C_j \Lambda_{jk}^- = -\frac{1}{2} \delta_{j,1} \delta_{k,1}.$$

The quantities  $\mathbf{\Lambda}^+$  and  $\mathbf{\Lambda}^-$  are called the curvature matrices. These matrices are the representation of curvature term given by

$$\frac{1}{r} \frac{\partial}{\partial \mu} (1 - \mu^2) I(r, \mu).$$

We will give  $\mathbf{\Lambda}^+$  and  $\mathbf{\Lambda}^-$  matrices for  $J = 2$

$$\mu_1=0.21132, \quad \mu_2=0.78868; \quad \text{and } c_1=c_2=0.5$$

where  $\mu$ 's and  $c$ 's are the roots and weights of Gauss-Legendre quadrature on  $\mu \in (0, 1)$  (see Abramowitz and Stegun 1970, Page 921) we have

$$\begin{aligned}
\mathbf{\Lambda}^+ & = \begin{pmatrix} -0.25 & 0.75 \\ -0.75 & -0.75 \end{pmatrix}, \\
\mathbf{\Lambda}^- & = \begin{pmatrix} -1 & 0 \\ 0 & 0 \end{pmatrix}.
\end{aligned}$$

For  $J = 4$ ,  $\mu_1=0.06943$ ,  $\mu_2= 0.33001$ ,  $\mu_3=0.66999$ ,  $\mu_4= 0.93057$ ; and  
 $c1= 0.17393$ ,  $c2 = 0.32607$ ,  $c3=32607$ ,  $c4=0.17393$

$$\Lambda^+ = \begin{pmatrix} 0.46494 & 2.23590 & 0 & 0 \\ -1.78139 & -0.04258 & 1.15005 & 0 \\ 0 & -0.15005 & -0.75945 & 0.58343 \\ 0 & 0 & -0.73228 & -0.09379 \end{pmatrix},$$

$$\Lambda^- = -2.87476\delta_{j,1}\delta_{k,1}.$$

Moreover, the curvature matrices should satisfy the relationship

$$\sum_{j=1}^J C_j [\Lambda_{jk}^+ - \Lambda_{jk}^-] = 0, \quad (1.32)$$

which is a necessary and sufficient condition for flux conservation in the spherically symmetric case. Now we will integrate (1.30) and (1.31) over the radial coordinate from  $r_n$  to  $r_{n+1}$ . This gives us

$$\begin{aligned} \mathbf{M}[\mathbf{U}_{n+1}^+ - \mathbf{U}_n^+] + \tau_{n+\frac{1}{2}}\mathbf{U}_{n+\frac{1}{2}}^+ &= \tau_{n+\frac{1}{2}} \left[ (1 - \omega_{n+\frac{1}{2}}) \mathbf{B}_{n+\frac{1}{2}}^+ \right. \\ &\left. \left( \frac{1}{2} \omega_{n+\frac{1}{2}} \mathbf{P}_{n+\frac{1}{2}}^{++} \mathbf{C} - \frac{\rho \Lambda^+}{\tau_{n+\frac{1}{2}}} \right) \mathbf{U}_{n+\frac{1}{2}}^+ + \left( \frac{1}{2} \omega_{n+\frac{1}{2}} \mathbf{P}_{n+\frac{1}{2}}^{+-} \mathbf{C} - \frac{\rho \Lambda^-}{\tau_{n+\frac{1}{2}}} \right) \mathbf{U}_{n+\frac{1}{2}}^- \right], \end{aligned} \quad (1.33)$$

similarly

$$\begin{aligned} \mathbf{M}[\mathbf{U}_n^- - \mathbf{U}_{n+1}^-] + \tau_{n+\frac{1}{2}}\mathbf{U}_{n+\frac{1}{2}}^- &= \tau_{n+\frac{1}{2}} \left[ (1 - \tau_{n+\frac{1}{2}}) \mathbf{B}_{n+\frac{1}{2}}^- + \right. \\ &\left. \left( \frac{1}{2} \tau_{n+\frac{1}{2}} \mathbf{P}_{n+\frac{1}{2}}^{-+} \mathbf{C} + \frac{\rho \Lambda^-}{\tau_{n+\frac{1}{2}}} \right) \mathbf{U}_{n+\frac{1}{2}}^+ + \left( \frac{1}{2} \omega_{n+\frac{1}{2}} \mathbf{P}_{n+\frac{1}{2}}^{--} \mathbf{C} + \frac{\rho \Lambda^+}{\tau_{n+\frac{1}{2}}} \right) \mathbf{U}_{n+\frac{1}{2}}^- \right], \end{aligned} \quad (1.34)$$

where

$$\mathbf{U}_n^+ = \mathbf{U}^+(r_n),$$

and variable subscribed with  $n+\frac{1}{2}$ , for example  $\mathbf{U}_{n+\frac{1}{2}}^+$ ,  $\tau_{n+\frac{1}{2}}$ ,  $\omega_{n+\frac{1}{2}}$  must be associated with some suitable average over the cell whose radial boundaries are  $r_n$  and  $r_{n+1}$ .

$$\Delta r_{n+\frac{1}{2}} = r_{n+1} - r_n,$$

$$\tau_{n+\frac{1}{2}} = \sigma_{n+\frac{1}{2}} \Delta r_{n+\frac{1}{2}},$$

and

$$\rho = \Delta r_{n+\frac{1}{2}} / r_{n+\frac{1}{2}},$$

where  $r_{n+\frac{1}{2}}$  is a suitable mean radius, for example  $\frac{1}{2}(r_{n+1} + r_n)$ . The quantities of  $\mathbf{U}_{n+\frac{1}{2}}^+, \mathbf{U}_{n+\frac{1}{2}}^-$  is

$$\mathbf{U}_{n+\frac{1}{2}}^+ = \frac{1}{2} \left( \mathbf{U}_{n+1}^+ + \mathbf{U}_n^+ \right) \quad ; \quad \mathbf{U}_{n+\frac{1}{2}}^- = \frac{1}{2} \left( \mathbf{U}_{n+1}^- + \mathbf{U}_n^- \right), \quad (1.35)$$

which is nothing but the 'diamond' difference scheme. We substitute equation (1.35) into equation equations (1.33) and (1.34) and rearrange the input and output intensities in the form of interaction principle. Comparing these equations with those given (1.1) we obtain the transmission and reflection operators.

$$\begin{pmatrix} \mathbf{U}_{n+1}^+ \\ \mathbf{U}_n^- \end{pmatrix} = \begin{pmatrix} \mathbf{t}(n+1, n) & \mathbf{r}(n, n+1) \\ \mathbf{r}(n+1, n) & \mathbf{t}(n, n+1) \end{pmatrix} \begin{pmatrix} \mathbf{U}_n^+ \\ \mathbf{U}_{n+1}^- \end{pmatrix} + \begin{pmatrix} \Sigma_{n+\frac{1}{2}}^+ \\ \Sigma_{n+\frac{1}{2}}^- \end{pmatrix}. \quad (1.36)$$

The  $\mathbf{r}$  and  $\mathbf{t}$  matrices and the vectors  $\Sigma^\pm$  can be expressed in terms of the matrices and vectors appearing in (1.33) and (1.34). We obtain the transmission and reflection operators as follows: Define first

$$\begin{aligned} \mathbf{Q}_{n+\frac{1}{2}}^{++} &= \frac{1}{2} \omega_{n+\frac{1}{2}} \mathbf{P}_{n+\frac{1}{2}}^{++} \mathbf{C} - \frac{\rho \Lambda^+}{\tau_{n+\frac{1}{2}}}, \\ \mathbf{Q}_{n+\frac{1}{2}}^{--} &= \frac{1}{2} \omega_{n+\frac{1}{2}} \mathbf{P}_{n+\frac{1}{2}}^{--} \mathbf{C} + \frac{\rho \Lambda^+}{\tau_{n+\frac{1}{2}}}, \\ \mathbf{Q}_{n+\frac{1}{2}}^{-+} &= \frac{1}{2} \omega_{n+\frac{1}{2}} \mathbf{P}_{n+\frac{1}{2}}^{-+} \mathbf{C} + \frac{\rho \Lambda^-}{\tau_{n+\frac{1}{2}}}, \\ \mathbf{Q}_{n+\frac{1}{2}}^{+-} &= \frac{1}{2} \omega_{n+\frac{1}{2}} \mathbf{P}_{n+\frac{1}{2}}^{+-} \mathbf{C} - \frac{\rho \Lambda^-}{\tau_{n+\frac{1}{2}}}, \end{aligned} \quad (1.37)$$

and then

$$\mathbf{S}^{++} = \mathbf{M} - \frac{1}{2} \tau_{n+\frac{1}{2}} (\mathbf{I} - \mathbf{Q}_{n+\frac{1}{2}}^{++}),$$

$$\begin{aligned}
\mathbf{S}^{--} &= \mathbf{M} - \frac{1}{2}\tau_{n+\frac{1}{2}}(\mathbf{I} - \mathbf{Q}_{n+\frac{1}{2}}^{--}), \\
\mathbf{S}^{-+} &= \frac{1}{2}\tau_{n+\frac{1}{2}}\mathbf{Q}_{n+\frac{1}{2}}^{-+}, \\
\mathbf{S}^{+-} &= \frac{1}{2}\tau_{n+\frac{1}{2}}\mathbf{Q}_{n+\frac{1}{2}}^{+-},
\end{aligned} \tag{1.38}$$

and

$$\begin{aligned}
\Delta^+ &= \left[ \mathbf{M} + \frac{1}{2}\tau_{n+\frac{1}{2}}(\mathbf{I} - \mathbf{Q}_{n+\frac{1}{2}}^{++}) \right]^{-1}, \\
\Delta^- &= \left[ \mathbf{M} + \frac{1}{2}\tau_{n+\frac{1}{2}}(\mathbf{I} - \mathbf{Q}_{n+\frac{1}{2}}^{--}) \right]^{-1}.
\end{aligned} \tag{1.39}$$

Write

$$\mathbf{r}^{+-} = \Delta^+\mathbf{S}^{+-}, \quad \mathbf{r}^{-+} = \Delta^-\mathbf{S}^{-+}, \tag{1.40}$$

and

$$\begin{aligned}
\mathbf{t}^+ &= [\mathbf{I} - \mathbf{r}^{+-}\mathbf{r}^{-+}]^{-1}, \\
\mathbf{t}^- &= [\mathbf{I} - \mathbf{r}^{-+}\mathbf{r}^{+-}]^{-1}.
\end{aligned} \tag{1.41}$$

Then

$$\begin{aligned}
\mathbf{t}(n+1, n) &= \mathbf{t}^+[\Delta^+\mathbf{S}^{++} + \mathbf{r}^{+-}\mathbf{r}^{-+}], \\
\mathbf{t}(n, n+1) &= \mathbf{t}^-[\Delta^-\mathbf{S}^{--} + \mathbf{r}^{-+}\mathbf{r}^{+-}], \\
\mathbf{r}(n+1, n) &= 2\mathbf{t}^-\mathbf{r}^{-+}\Delta^+\mathbf{M}, \\
\mathbf{r}(n, n+1) &= 2\mathbf{t}^+\mathbf{r}^{+-}\Delta^-\mathbf{M},
\end{aligned} \tag{1.42}$$

and

$$\begin{aligned}
\Sigma_{n+\frac{1}{2}}^+ &= \tau_{n+\frac{1}{2}}(1 - \omega_{n+\frac{1}{2}})\mathbf{t}^+[\Delta^+\mathbf{B}^+ + \mathbf{r}^{+-}\Delta^-\mathbf{B}^-], \\
\Sigma_{n+\frac{1}{2}}^- &= \tau_{n+\frac{1}{2}}(1 - \omega_{n+\frac{1}{2}})\mathbf{t}^-[\Delta^-\mathbf{B}^- + \mathbf{r}^{-+}\Delta^+\mathbf{B}^+].
\end{aligned} \tag{1.43}$$

This can be achieved only if

$$\tau_{n+\frac{1}{2}} \leq \tau_{\text{crit}} = \min_j \left| \frac{\mu_j^\pm + \frac{1}{2}\rho\Lambda_{jj}^+}{\frac{1}{2}(1 - \omega_{n+\frac{1}{2}}p_{jj}^{++}c_j)} \right|. \tag{1.44}$$

Generally, we take the critical step size to be approximately equal to

$$\tau_{\text{crit}} = 2\mu_1. \quad (1.45)$$

For four angle quadrature  $\tau_{\text{crit}}=0.14$ . Once we calculate the  $r$  and  $t$  operators corresponding to this optical depth, we can use the star algorithm for for obtaining the radiation field for a shell of larger optical thickness.

### 1.2.2 Flux conservation in the monochromatic case

We must have the solution checked for flux conservation. The system should neither create nor destroy energy and we must show that the solution obtained in the frame work of discrete space theory does conserve flux (see Grant and Hunt 1969b and Peraiah and Grant 1973). The simplest case is that when we have purely scattering media. In this case we have  $\omega=1$ . We solve the transfer equation equation as described in the previous section and obtain the operators  $\mathbf{r}(n, n+1), \mathbf{r}(n+1, n), \mathbf{t}(n, n+1), \mathbf{t}(n+1, n)$ . Then we should show that

$$\|\mathbf{t}(n+1, n) + \mathbf{r}(n+1, n)\| = 1 + 0(\Delta\tau), \quad (1.46)$$

where  $\|\cdot\|$  means we take the norm defined by

$$\|A\| = \sum_{j=1}^m |(DAD^{-1})_{jk}|, \quad k = 1, 2, 3, \dots, J, \quad (1.47)$$

and

$$D = 2\pi\mathbf{MC}. \quad (1.48)$$

As a consequence of condition(1.46)

$$(1) \quad \frac{1}{2} \sum_{j=1}^J C_j \left[ \mathbf{P}_{jk}^{++}(n) + \mathbf{P}_{jk}^{-+}(n) \right] = 1 \quad k = 1, 2, \dots, J, \quad (1.49)$$

this is due to scattering, and

$$(2) \quad \sum_{j=1}^J C_j \left[ \mathbf{\Lambda}_{jk}^+ - \mathbf{\Lambda}_{jk}^- \right] = 0 \quad k = 1, 2, \dots, J, \quad (1.50)$$

this is due to the nature of the curvature terms. A more practical way of testing the system for flux conservation is as follows; We introduce some flux at the point  $a$  and calculate the fluxes that emerge out at  $a$  and  $b$  (see figure 1.2). Thus  $F$  denotes the flux, we must have

$$F^-(a) = F^-(b) + F^+(a). \quad (1.51)$$

We notice that we did not give any flux at  $b$  (i.e),  $U_1^+ = 0$ , where  $F^-(b)$  is the flux emerging at  $r = b$  and  $F^+(a)$  is the flux back scattered into the inner region.

### 1.2.3 Line formation in expanding media

The spectral lines formed in stellar atmospheres contain information regarding temperature, pressure, composition, dynamical state of the gas etc. Therefore, it is necessary to study the formation of lines in stellar atmospheres. There are several important steps that one has to consider while calculating the lines. These are as follows:

- The effects of curvature on the radiation field,
- The geometrical extension of the atmospheres,
- Consideration whether the lines is formed in LTE or in non-LTE,
- Consideration of the photon redistribution regarding whether the line is formed with complete redistribution or with partial redistribution,
- The hydrodynamic status of the medium whether medium is expanding or contracting or static,
- The distribution of temperature in the atmosphere,
- The effect of radiation field on the ionization structure of the gas and dust,

- The abundance of the line forming ions and this ratio with respect to the abundance of other elements,
- The statistical equilibrium equation representing several levels of the atom,
- The equation of state of the gas of the atmosphere in which we study the pressure, temperature, composition of the medium.

All the above characteristics shall have to be taken into account simultaneously to study the spectral line. It is however, very difficult to include all these effects into the calculations of the lines simultaneously. In the following we will add one by one and make the calculations as complicated as permitted by the available computing facilities. Now we shall discuss the effects of extendedness, curvature of the medium and non-LTE.

#### 1.2.4 The equation of transfer in comoving frame

In spherical geometry the terms that should be included in the transfer equation when it is transformed into the comoving frame are given by (see Chandrasekhar, 1945; Mihalas et al., 1975, Mihalas, 1978);

$$\left[ (1 - \mu^2) \frac{V(r)}{r} + \mu^2 \frac{dV(r)}{dr} \right] \frac{\partial I(x, \mu, r)}{\partial x}, \quad (1.52)$$

where  $I(x, \pm\mu, r)$  is the specific intensity of the ray at an angle  $\cos^{-1} \mu$  [ $\mu \in (0, 1)$ ] with the radius vector at the radial point  $r$  with frequency  $x (= (\nu - \nu_o) / \Delta\nu_D$  where  $\nu_o$  and  $\nu$  are the frequency points at the line centre and at any point in the line and  $\Delta\nu_D$  is the standard frequency interval such as Doppler width),  $V(r)$  is the velocity of the gas at  $r$  in units of mean thermal units (mtu).

Equation of line transfer in the in the comoving frame with absorption and emission due to dust and gas (see Peraiah and Wehrse, 1978; Peraiah 1984, Wehrse and Kalkofen, 1985; Peraiah, A., Varghese, B. A., Rao, M. S., 1987) is given by,

$$\begin{aligned} \mu \frac{\partial I(x, \mu, r)}{\partial r} + \frac{(1 - \mu^2)}{r} \frac{\partial I(x, \mu, r)}{\partial \mu} &= K_L(r) [(\phi(x) + \beta)] [S(r, \mu, x) - I(r, \mu, x)] \\ &+ \left[ (1 - \mu^2) \frac{V(r)}{r} + \mu^2 \frac{dV(r)}{dr} \right] \frac{\partial I(r, \mu, x)}{\partial x} \\ &+ K_{dust} [S_{dust}(r, \mu, x) - I(r, \mu, x)], \end{aligned} \quad (1.53)$$

and

$$\begin{aligned} -\mu \frac{\partial I(x, -\mu, r)}{\partial r} - \frac{(1 - \mu^2)}{r} \frac{\partial I(x, -\mu, r)}{\partial \mu} &= K_L(r) [(\phi(x) + \beta)] [S(r, -\mu, x) - I(r, -\mu, x)] \\ &+ \left[ (1 - \mu^2) \frac{V(r)}{r} + \mu^2 \frac{dV(r)}{dr} \right] \frac{\partial I(r, -\mu, x)}{\partial x} \\ &+ K_{dust} [S_{dust}(r, -\mu, x) - I(r, -\mu, x)], \end{aligned} \quad (1.54)$$

Here  $K_L(r)$  is the line-centre absorption coefficient,  $\beta$  is the ratio of continuum to the line opacities.  $\phi(x)$  is the profile function subjected to normalization such that

$$\phi(x) = \frac{1}{\delta \sqrt{\pi}} e^{-\left(\frac{x}{\delta}\right)^2}, \quad (1.55)$$

where  $\delta$  is the Doppler width. The quantity  $S(r, \pm\mu, x)$  is the source function given by;

$$S(r, \pm\mu, x) = \frac{\phi(x)}{\beta + \phi(x)} S_L(r) + \frac{\beta}{\beta + \phi(x)} S_c(r, x), \quad (1.56)$$

and

$$S_L(r) = \frac{(1 - \epsilon)}{2} \int_{-\infty}^{+\infty} \phi(x) dx \int_{-\infty}^{+\infty} I(r, \mu', x) dx d\mu' + \epsilon B(x, T(r)), \quad (1.57)$$

is the line source function. The quantity  $S_c(r)$  is the continuum source function given by;

$$S_c(r) = \rho(r)B(x, T(r)). \quad (1.58)$$

Here  $\epsilon$  is the probability per each scattering that a photon will be destroyed by collisional de-excitation.  $\rho(r)$  is an arbitrary factor less than one and  $B(x, T(r))$  is the Planck function with frequency  $x$ , and temperature  $T$  at the radial point  $r$ .  $K_{dust}(r)$  is the absorption coefficient of the dust and the dust source function  $S_{dust}(r, \pm\mu, x)$  is given by,

$$S_{dust}(r, \pm\mu, x) = (1 - \omega)B_{dust} + \frac{\omega}{2} \int_{-\infty}^{+\infty} P(\mu, \mu', r)I(r, \mu', x)d\mu', \quad (1.59)$$

where  $B_{dust}$  is the Planck function for the dust emission,  $\omega$  the albedo of the dust and  $P$  the isotropic and coherent scattering phase function. The quantity  $B_{dust}$  is normally neglected because the re-emission will be far away from the line centre and therefore may not contribute to the line radiation. Although we need not consider the term containing  $B_{dust}$ , we have included it for the sake of completeness.

We have adopted the "CELL" method described by Peraiah (1984) to solve the equation (1.53) and (1.54); This is done by suitable discretization in frequency, angle as radius. For frequency discretization we choose the discrete points  $x_i$  and weights  $a_i$  such that

$$\int_{-\infty}^{+\infty} \phi(x)f(x)dx \simeq \sum_{i=-I}^I a_i f(x), \quad \sum_{i=-I}^I a_i = 1. \quad (1.60)$$

The angle discretization is done with abscissae  $\{\mu_j\}$  and weights  $\{C_j\}$  such that

$$\int_0^1 f(x)d\mu \simeq \sum_{j=1}^m C_j f(\mu_j), \quad \sum_{j=1}^m C_j = 1. \quad (1.61)$$

We choose the radial point  $r_n$  and  $r_{n+1}$  as discrete points for radial discretization. The integration of equation (1.53) and (1.54) is done on the 'Cell' bounded by:

$$\left[ r_n, r_{n+1} \right] \left[ \mu_{j-\frac{1}{2}}, \mu_{j+\frac{1}{2}} \right] \left[ x_i, x_{i+1} \right]. \quad (1.62)$$

The quantities  $\mu_{j+\frac{1}{2}}$  are chosen according to convenience. In this problem we choose  $\mu_{j+\frac{1}{2}}$  by the relation

$$\mu_{j+\frac{1}{2}} = \sum_{k=1}^j C_k \quad j = 1, 2, 3, \dots, m. \quad (1.63)$$

We have chosen  $\mu$ 's and  $C$ 's to be roots and weights of Gauss-Legendre quadrature. We shall write the following  $m$  vectors

$$\mathbf{h} = [1, 1, 1, \dots, 1]^T, \quad (1.64)$$

where T indicates transpose. Let us introduce

$$\mathbf{U}_{i,n}^+ = 4\pi r_n^2 \begin{pmatrix} I(\tau_n, \mu_1, x_i) \\ I(\tau_n, \mu_2, x_i) \\ I(\tau_n, \mu_3, x_i) \\ \dots \\ I(\tau_n, \mu_m, x_i) \end{pmatrix}, \quad (1.65)$$

$$\mathbf{U}_{i,n}^- = 4\pi r_n^2 \begin{pmatrix} I(\tau_n, -\mu_1, x_i) \\ I(\tau_n, -\mu_2, x_i) \\ I(\tau_n, -\mu_3, x_i) \\ \dots \\ I(\tau_n, -\mu_m, x_i) \end{pmatrix}, \quad (1.66)$$

and

$$\mathbf{B}'(\nu_0, T_e(r)) = 4\pi r_n^2 \mathbf{B}(\nu_0, T_e(r)). \quad (1.67)$$

After integration (1.53) and (1.54) reduces to;

$$\mathbf{M}_{\text{in}} \left( \mathbf{U}_{i,n+1}^+ - \mathbf{U}_{i,n}^+ \right) + \rho_c \left( \mathbf{\Lambda}_m^+ \mathbf{U}_{i,n+\frac{1}{2}}^+ + \mathbf{\Lambda}_m^- \mathbf{U}_{i,n+\frac{1}{2}}^- \right) + \tau_{g,n+\frac{1}{2}} \left( \beta + \phi_i \right)_{n+\frac{1}{2}} \mathbf{U}_{i,n+\frac{1}{2}}^+ + \tau_{d,n+\frac{1}{2}} \mathbf{U}_{i,n+\frac{1}{2}}^+$$

$$\begin{aligned}
&= \tau_{g,n+\frac{1}{2}} \left( \rho\beta + \epsilon\phi_i \right)_{n+\frac{1}{2}} \mathbf{B}'_{g,n+\frac{1}{2}} \mathbf{h} \\
&+ \frac{1}{2} \tau_{g,n+\frac{1}{2}} \sigma_{n+\frac{1}{2}} \phi_{i,n+\frac{1}{2}} \sum_{i'=-I}^I a_{i',n+\frac{1}{2}} (\mathbf{h}\mathbf{h}^T) \mathbf{C}_m (\mathbf{U}^+ + \mathbf{U}^-)_{i',n+\frac{1}{2}} \\
&+ \frac{1}{2} \tau_{d,n+\frac{1}{2}} \omega_{n+\frac{1}{2}} \left( \mathbf{P}_{m,n+\frac{1}{2}}^{++} \mathbf{C}_m \mathbf{U}_{i,n+\frac{1}{2}}^+ + \mathbf{P}_{m,n+\frac{1}{2}}^{+-} \mathbf{C}_m \mathbf{U}_{i,n+\frac{1}{2}}^- \right) \\
&+ \mathbf{M}_{1,i+\frac{1}{2}} \mathbf{d}_{i+\frac{1}{2}} \mathbf{U}_{i+\frac{1}{2},n+\frac{1}{2}}^+ + \tau_{d,n+\frac{1}{2}} (1-\omega)_{n+\frac{1}{2}} \mathbf{B}'_{d,n+\frac{1}{2}} \mathbf{h}, \quad (1.68)
\end{aligned}$$

$$\begin{aligned}
&\mathbf{M}_m (\mathbf{U}_{i,n}^- - \mathbf{U}_{i,n+1}^-) - \rho_c \left( \Lambda_m^+ \mathbf{U}_{i,n+\frac{1}{2}}^- + \Lambda_m^- \mathbf{U}_{i,n+\frac{1}{2}}^+ \right) + \\
&\tau_{g,n+\frac{1}{2}} \left( \beta + \phi_i \right)_{n+\frac{1}{2}} \mathbf{U}_{i,n+\frac{1}{2}}^- + \tau_{d,n+\frac{1}{2}} \mathbf{U}_{i,n+\frac{1}{2}}^- \\
&= \tau_{g,n+\frac{1}{2}} \left( \rho\beta + \epsilon\phi_i \right)_{n+\frac{1}{2}} \mathbf{B}'_{g,n+\frac{1}{2}} \mathbf{h} \\
&+ \frac{1}{2} \tau_{g,n+\frac{1}{2}} \sigma_{n+\frac{1}{2}} \phi_{i,n+\frac{1}{2}} \sum_{i'=-I}^I a_{i',n+\frac{1}{2}} (\mathbf{h}\mathbf{h}^T) \mathbf{C}_m (\mathbf{U}^+ + \mathbf{U}^-)_{i',n+\frac{1}{2}} \\
&+ \frac{1}{2} \tau_{d,n+\frac{1}{2}} \omega_{n+\frac{1}{2}} \left( \mathbf{P}_{m,n+\frac{1}{2}}^{-+} \mathbf{C}_m \mathbf{U}_{i,n+\frac{1}{2}}^+ + \mathbf{P}_{m,n+\frac{1}{2}}^{--} \mathbf{C}_m \mathbf{U}_{i,n+\frac{1}{2}}^- \right) \\
&+ \mathbf{M}_{1,i+\frac{1}{2}} \mathbf{d}_{i+\frac{1}{2}} \mathbf{U}_{i+\frac{1}{2},n+\frac{1}{2}}^- + \tau_{d,n+\frac{1}{2}} (1-\omega)_{n+\frac{1}{2}} \mathbf{B}'_{d,n+\frac{1}{2}} \mathbf{h}, \quad (1.69)
\end{aligned}$$

$$\mathbf{M}_m = [\mu_j \delta_{jk}], \quad \mathbf{C}_m = [C_j \delta_{jk}], \quad (1.70)$$

$$d_{i+\frac{1}{2}} = (x_{i+1} - x_i)^{-1}, \quad \mathbf{U}_{i+\frac{1}{2}}^\pm = \frac{1}{2} (\mathbf{U}_i^\pm + \mathbf{U}_{i+1}^\pm), \quad (1.71)$$

the subscript  $n + \frac{1}{2}$  correspondence to the average of the quantity over the  $\langle\langle \text{Cell} \rangle\rangle$  bounded by  $r_n$  and  $r_{n+1}$ . The quantities  $\Lambda_m^+$  and  $\Lambda_m^-$  are the curvature matrices and

$$\mathbf{M}_{1,i+\frac{1}{2}} = \mathbf{M}_{i+\frac{1}{2}} \Delta \mathbf{V}_{n+\frac{1}{2}} + \mathbf{M}_{i+\frac{1}{2}} \rho_c \mathbf{V}_{n+\frac{1}{2}}, \quad (1.72)$$

$$\mathbf{M}_{1,i+\frac{1}{2}}^1 = [\mu_j^2 \delta_{jk}]; \quad \mathbf{M}_{i+\frac{1}{2}}^2 = [(1 - \mu_j^2) \delta_{jk}], \quad (1.73)$$

with

$$\Delta \mathbf{V}_{n+\frac{1}{2}} = \mathbf{V}_{n+1} - \mathbf{V}_n. \quad (1.74)$$

Further more, we have ,

$$\tau_{g,n+\frac{1}{2}} = \mathbf{K}_{gas} \Delta r, \quad \tau_{d,n+\frac{1}{2}} = \mathbf{K}_{dust} \Delta r, \quad (1.75)$$

$$\sigma_{n+\frac{1}{2}} = 1 - \epsilon_{n+\frac{1}{2}}. \quad (1.76)$$

The quantity  $\rho_c$  is called the curvature factor given by:

$$\rho_c = \frac{\Delta r}{r_{n+\frac{1}{2}}}. \quad (1.77)$$

The matrices  $\mathbf{P}^{++}$ ,  $\mathbf{P}^{+-}$ ,  $\mathbf{P}^{-+}$ ,  $\mathbf{P}^{--}$  are the phase matrices of dimension  $m$  and for isotropic scattering, all the elements of these matrices are equal to unity. Equations (1.68) and (1.69) are rewritten for  $I$  frequency points as follows:

$$\begin{aligned} & \mathbf{M}(\mathbf{U}_{n+1}^+ - \mathbf{U}_n^+) + \rho_c(\mathbf{\Lambda}^+\mathbf{U}_{n+\frac{1}{2}}^+ + \mathbf{\Lambda}^-\mathbf{U}_{n+\frac{1}{2}}^-) + \tau_{g,n+\frac{1}{2}}\phi_{n+\frac{1}{2}}\mathbf{U}_{n+\frac{1}{2}}^+ + \\ & + \tau_{d,n+\frac{1}{2}}\mathbf{E}\mathbf{U}_{n+\frac{1}{2}}^+ = \tau_{g,n+\frac{1}{2}}\mathbf{S}_{n+\frac{1}{2}}^+ + \frac{1}{2}\tau_{g,n+\frac{1}{2}}\sigma_{n+\frac{1}{2}}(\phi\phi^T\mathbf{W})(\mathbf{U}^+ + \mathbf{U}^-)_{n+\frac{1}{2}} \\ & + \frac{1}{2}\tau_{d,n+\frac{1}{2}}\omega_{n+\frac{1}{2}}(\mathbf{P}^{++}\mathbf{C}\mathbf{U}^+ + \mathbf{P}^{+-}\mathbf{C}\mathbf{U}^-)_{n+\frac{1}{2}} + \tau_{d,n+\frac{1}{2}}(1 - \omega_{n+\frac{1}{2}})\mathbf{B}_{d,n+\frac{1}{2}}^{\prime,+} \\ & + \mathbf{M}_1\mathbf{d}\mathbf{U}_{n+\frac{1}{2}}^+, \end{aligned} \quad (1.78)$$

$$\begin{aligned} & \mathbf{M}(\mathbf{U}_n^- - \mathbf{U}_{n+1}^-) - \rho_c(\mathbf{\Lambda}^+\mathbf{U}_{n+\frac{1}{2}}^- + \mathbf{\Lambda}^-\mathbf{U}_{n+\frac{1}{2}}^+) + \tau_{g,n+\frac{1}{2}}\phi_{n+\frac{1}{2}}\mathbf{U}_{n+\frac{1}{2}}^- + \\ & + \tau_{d,n+\frac{1}{2}}\mathbf{E}\mathbf{U}_{n+\frac{1}{2}}^- = \tau_{g,n+\frac{1}{2}}\mathbf{S}_{n+\frac{1}{2}}^- + \frac{1}{2}\tau_{g,n+\frac{1}{2}}\sigma_{n+\frac{1}{2}}(\phi\phi^T\mathbf{W})(\mathbf{U}^+ + \mathbf{U}^-)_{n+\frac{1}{2}} \\ & + \frac{1}{2}\tau_{d,n+\frac{1}{2}}\omega_{n+\frac{1}{2}}(\mathbf{P}^{-+}\mathbf{C}\mathbf{U}^+ + \mathbf{P}^{--}\mathbf{C}\mathbf{U}^-)_{n+\frac{1}{2}} + \tau_{d,n+\frac{1}{2}}(1 - \omega_{n+\frac{1}{2}})\mathbf{B}_{d,n+\frac{1}{2}}^{\prime,-} \\ & + \mathbf{M}_1\mathbf{d}\mathbf{U}_{n+\frac{1}{2}}^-, \end{aligned} \quad (1.79)$$

where

$$\mathbf{U}_N^\pm = [\mathbf{U}_{1,n}^\pm, \mathbf{U}_{2,n}^\pm, \mathbf{U}_{3,n}^\pm, \dots, \mathbf{U}_{i,n}^\pm, \dots, \mathbf{U}_{I,n}^\pm]^T, \quad (1.80)$$

T indicates the transpose of the vector.

$$\mathbf{M} = \begin{pmatrix} \mathbf{M}_m & & & \\ & \mathbf{M}_m & & \\ & & \dots & \\ & & & \mathbf{M}_m \end{pmatrix}, \mathbf{C} = \begin{pmatrix} \mathbf{C}_m^+ & & & \\ & \mathbf{C}_m^+ & & \\ & & \dots & \\ & & & \mathbf{C}_m^+ \end{pmatrix}, \quad (1.81)$$

$$\phi_{n+\frac{1}{2}} = [\phi_{kk'}]_{n+\frac{1}{2}} = (\beta + \phi_k)_{n+\frac{1}{2}}\delta_{kk'}, \quad (1.82)$$

$$k = j + (i - 1)m, \quad 1 \leq k \leq K = mI,$$

$i, j$  being running indices of frequency and angle discretization, and:

$$S_{n+\frac{1}{2}} = (\rho\beta + \epsilon\phi_k)\mathbf{B}'_{n+\frac{1}{2}}\delta_{kk'},$$

$$\phi_i W_k = A_i C_j,$$

where

$$A_i = \frac{a_i \phi_i}{\sum_{i'=1}^I A_{i'} \phi(x_{i'})}, \quad (1.83)$$

$\mathbf{E}$  is the unit matrix of  $(K \times K)$  dimensions. The quantities  $\mathbf{P}^{++}$  etc., are given by;

$$\mathbf{P}^{++} = \begin{pmatrix} \mathbf{P}_m^{++} & & & \\ & \mathbf{P}_m^{++} & & \\ & & \dots & \\ & & & \mathbf{P}_m^{++} \end{pmatrix}. \quad (1.84)$$

For isotropic scattering  $\mathbf{P}^{++}$ ,  $\mathbf{P}^{--}$  etc., are equal. Further more,

$$\mathbf{B}'_{d,n+\frac{1}{2}} = \mathbf{B}'_{d,n+\frac{1}{2}} \mathbf{h},$$

$$\mathbf{M}_1 = [\mathbf{M}^1 \Delta \mathbf{V}_{n+\frac{1}{2}} + \mathbf{M}^2 \rho_c \mathbf{V}_{n+\frac{1}{2}}], \quad (1.85)$$

$$\mathbf{M}^1 = \begin{pmatrix} \mathbf{M}_m^1 & & & \\ & \mathbf{M}_m^1 & & \\ & & \dots & \\ & & & \mathbf{M}_m^1 \end{pmatrix}, \mathbf{M}_m^1 = [\mu_j^2 \delta_{jl}], \quad (1.86)$$

$$\mathbf{M}^2 = \begin{pmatrix} \mathbf{M}_m^2 & & & \\ & \mathbf{M}_m^2 & & \\ & & \dots & \\ & & & \mathbf{M}_m^2 \end{pmatrix}, \mathbf{M}_m^2 = [(1 - \mu_j^2) \delta_{jl}], \quad (1.87)$$

$j, l = 1, 2, \dots, m$ , and;

$$\mathbf{d} = \begin{pmatrix} -d_1 & d_1 & \dots & & \\ -d_2 & 0 & d_2 & \dots & \\ & -d_3 & 0 & & \\ & & -d_4 & & \\ & & & & d_{I-1} \\ & & & -d_I & d_I \end{pmatrix}, \quad (1.88)$$

$$d_i = (x_{i+1} - x_{i-1})^{-1} \quad i = 2, 3, \dots, I - 1. \quad (1.89)$$

We replace  $\mathbf{U}_{n+\frac{1}{2}}^+$ ,  $\mathbf{U}_{n+\frac{1}{2}}^-$  by the diamond scheme given by,

$$\begin{aligned} \frac{1}{2}(\mathbf{U}_n^+ + \mathbf{U}_{n+1}^+) &= \mathbf{U}_{n+\frac{1}{2}}^+, \\ \frac{1}{2}(\mathbf{U}_n^- + \mathbf{U}_{n+1}^-) &= \mathbf{U}_{n+\frac{1}{2}}^-. \end{aligned} \quad (1.90)$$

Substitution of equations (1.90) into equations (1.78) and (1.79) will give us:

$$\begin{aligned} \begin{pmatrix} t_{11} & t_{12} \\ t_{21} & t_{22} \end{pmatrix} \begin{pmatrix} \mathbf{U}_{n+1}^+ \\ \mathbf{U}_n^- \end{pmatrix} &= \begin{pmatrix} r_{11} & r_{12} \\ r_{21} & r_{22} \end{pmatrix} \begin{pmatrix} \mathbf{U}_n^+ \\ \mathbf{U}_{n+1}^- \end{pmatrix} \\ &+ \tau_g \begin{pmatrix} \mathbf{S}^+ \\ \mathbf{S}^- \end{pmatrix} + \tau_d(1 - \omega) \begin{pmatrix} \mathbf{B}',+ \\ \mathbf{B}',- \end{pmatrix}, \end{aligned} \quad (1.91)$$

where

$$\begin{aligned} t_{11} &= \mathbf{M} + \frac{1}{2}\rho_c\Lambda^+ + \frac{1}{2}\tau_g\left(\phi - \frac{1}{2}\sigma\phi\phi^T\mathbf{W}\right) + \frac{1}{2}\tau_d\left(\mathbf{E} - \frac{1}{2}\omega\mathbf{P}^{++}\mathbf{C}\right) \\ &\quad - \frac{1}{2}\mathbf{M}_1\mathbf{d}, \\ t_{12} &= \frac{1}{2}\rho_c\Lambda^- - \frac{1}{4}\tau_g\sigma\left(\phi\phi^T\mathbf{W}\right) - \frac{1}{4}\tau_d\mathbf{P}^{+-}\mathbf{C}, \\ t_{21} &= -\frac{1}{2}\rho_c\Lambda^- - \frac{1}{4}\tau_g\sigma\left(\phi\phi^T\mathbf{W}\right) - \frac{1}{4}\tau_d\mathbf{P}^{-+}\mathbf{C}, \\ t_{22} &= \mathbf{M} - \frac{1}{2}\rho_c\Lambda^+ + \frac{1}{2}\tau_g\left(\phi - \frac{1}{2}\sigma\phi\phi^T\mathbf{W}\right) + \frac{1}{2}\tau_d\left(\mathbf{E} - \frac{1}{2}\omega\mathbf{P}^{--}\mathbf{C}\right) \\ &\quad - \frac{1}{2}\mathbf{M}_1\mathbf{d}, \\ r_{11} &= \mathbf{M} - \frac{1}{2}\rho_c\Lambda^+ - \frac{1}{2}\tau_g\left(\phi - \frac{1}{2}\sigma\phi\phi^T\mathbf{W}\right) - \frac{1}{2}\tau_d\left(\mathbf{E} - \frac{1}{2}\omega\mathbf{P}^{++}\mathbf{C}\right) \\ &\quad + \frac{1}{2}\mathbf{M}_1\mathbf{d}, \\ r_{12} &= -\frac{1}{2}\rho_c\Lambda^- + \frac{1}{4}\tau_g\sigma\left(\phi\phi^T\mathbf{W}\right) + \frac{1}{4}\tau_d\mathbf{P}^{+-}\mathbf{C}, \\ r_{21} &= \frac{1}{2}\rho_c\Lambda^- + \frac{1}{4}\tau_g\sigma\left(\phi\phi^T\mathbf{W}\right) + \frac{1}{4}\tau_d\mathbf{P}^{-+}\mathbf{C}, \\ r_{22} &= \mathbf{M} + \frac{1}{2}\rho_c\Lambda^+ - \frac{1}{2}\tau_g\left(\phi - \frac{1}{2}\sigma\phi\phi^T\mathbf{W}\right) - \frac{1}{2}\tau_d\left(\mathbf{E} - \frac{1}{2}\omega\mathbf{P}^{--}\mathbf{C}\right) \\ &\quad + \frac{1}{2}\mathbf{M}_1\mathbf{d}, \end{aligned}$$

where  $\mathbf{E}$  is the unit matrix. Let us define the following matrices,

$$\mathbf{Z}^{++} = \left( \phi - \frac{1}{2} \sigma \phi \phi^T \mathbf{W} \right) + \frac{\tau_d}{\tau_g} \left( \mathbf{E} - \frac{1}{2} \omega \mathbf{P}^{++} \mathbf{C} \right) - \frac{\mathbf{M}_1 \mathbf{d}}{\tau_g} + \frac{\rho_c \Lambda^+}{\tau_g}, \quad (1.92)$$

$$\mathbf{Z}^{--} = \left( \phi - \frac{1}{2} \sigma \phi \phi^T \mathbf{W} \right) + \frac{\tau_d}{\tau_g} \left( \mathbf{E} - \frac{1}{2} \omega \mathbf{P}^{--} \mathbf{C} \right) - \frac{\mathbf{M}_1 \mathbf{d}}{\tau_g} - \frac{\rho_c \Lambda^+}{\tau_g}, \quad (1.93)$$

$$\Delta^+ = \left( \mathbf{M} + \frac{1}{2} \tau_g \mathbf{Z}^{++} \right)^{-1}; \quad \Delta^- = \left( \mathbf{M} + \frac{1}{2} \tau_g \mathbf{Z}^{--} \right)^{-1}, \quad (1.94)$$

$$\mathbf{Y}^{+-} = \frac{1}{2} \sigma \phi \phi^T \mathbf{W} + \frac{1}{2} \frac{\tau_d}{\tau_g} \omega \mathbf{P}^{+-} \mathbf{C} - \frac{\rho_c \Lambda^-}{\tau_g}, \quad (1.95)$$

$$\mathbf{Y}^{-+} = \frac{1}{2} \sigma \phi \phi^T \mathbf{W} + \frac{1}{2} \frac{\tau_d}{\tau_g} \omega \mathbf{P}^{-+} \mathbf{C} + \frac{\rho_c \Lambda^-}{\tau_g}, \quad (1.96)$$

$$\mathbf{A} = \mathbf{M} - \frac{1}{2} \tau_g \mathbf{Z}^{++}; \quad \mathbf{D} = \mathbf{M} - \frac{1}{2} \tau_g \mathbf{Z}^{--}, \quad (1.97)$$

$$\mathbf{g}^{+-} = \frac{1}{2} \tau_g \Delta^+ \mathbf{Y}^{+-} \quad \mathbf{g}^{-+} = \frac{1}{2} \tau_g \Delta^- \mathbf{Y}^{-+}, \quad (1.98)$$

$$\mathbf{G}^{+-} = \left[ \mathbf{E} - \mathbf{g}^{+-} \mathbf{g}^{-+} \right]^{-1}, \quad \mathbf{G}^{-+} = \left[ \mathbf{E} - \mathbf{g}^{-+} \mathbf{g}^{+-} \right]^{-1}, \quad (1.99)$$

$$\mathbf{S}_1^+ = \mathbf{S}^+ + \frac{\tau_d}{\tau_g} (1 - \omega) \mathbf{B}_d'^+, \quad (1.100)$$

$$\mathbf{S}_1^- = \mathbf{S}^- + \frac{\tau_d}{\tau_g} (1 - \omega) \mathbf{B}_d'^-. \quad (1.101)$$

Using equations (1.92) to (1.101) we can write the reflection and transmission matrices. These are given by

$$\mathbf{t}(n+1, n) = \mathbf{G}^{+-} [\Delta^+ \mathbf{A} + \mathbf{g}^{+-}, \mathbf{g}^{-+}] \quad (1.102)$$

$$\mathbf{t}(n, n+1) = \mathbf{G}^{-+} [\Delta^- \mathbf{D} + \mathbf{g}^{-+} \mathbf{g}^{+-}], \quad (1.103)$$

$$\mathbf{r}(n+1, n) = \mathbf{G}^{-+} \mathbf{g}^{-+} [\mathbf{E} + \Delta^+ \mathbf{A}], \quad (1.104)$$

$$\mathbf{r}(n, n + 1) = \mathbf{G}^{+-} \mathbf{g}^{+-} [\mathbf{E} + \Delta^- \mathbf{D}], \quad (1.105)$$

and

$$\Sigma^+ = \tau_g \mathbf{G}^{+-} [\Delta^+ \mathbf{S}_1^+ + \mathbf{g}^{+-} \Delta^- \mathbf{S}_1^-], \quad (1.106)$$

$$\Sigma^- = \tau_g \mathbf{G}^{-+} [\Delta^- \mathbf{S}_1^- + \mathbf{g}^{-+} \Delta^+ \mathbf{S}_1^+], \quad (1.107)$$

The transmission and reflection operators and the source vectors which are represented in equations (1.102) to (1.107) are estimated in each shell whose thickness is  $\tau_{\text{crit}}$ . Note that  $\tau_{\text{crit}}$  is determined by the physical character of the medium. Using these operators we calculate the internal radiation field with the help of the above procedure. The frequency-dependent radiation field thus calculated is transformed on to the observer's frame at infinity.

### 1.2.5 Calculation of line fluxes for an observer at infinity

Once we obtain the source function  $S(r, x)$  in the comoving frame, we need to compute line fluxes in the frame of the observer at infinity.

In figure 1.3a, we give a spherically symmetric radially expanding atmosphere surrounding a star. One can explain qualitatively the absorption and emission features of a spectral line formed in these objects. Formation of lines in these atmospheres depend on several factors: density distribution, geometrical extension, expansion velocities etc. Let us consider a transparent envelope so that all photons reach the observer. For the sake of simplicity, we consider line centre frequency for either emission or absorption to occur so that the external observer will receive the line centre frequency from any part of the medium Doppler shifted by an amount corresponding to the velocity of expansion along the line of sight.

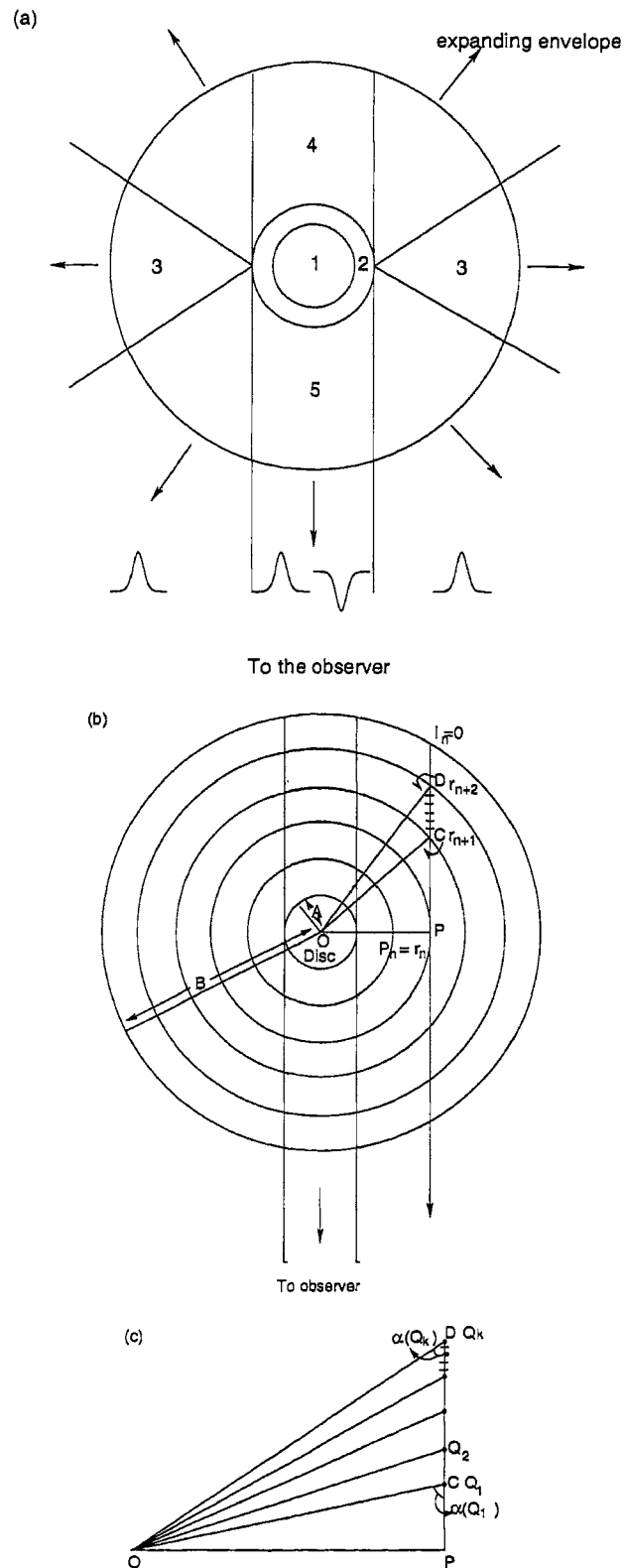


Figure 1.3: Schematic diagram of an expanding stellar envelope (1) central star (2) photospheric surface (3) emission lobe (4) occulted region from the observer (5) absorption feature region (sometimes even emission).

The region 4 in figure 1.3a is the occulted region from the observer by the stellar disc and therefore cannot be seen by the observer. The region 5, the region projected on the stellar disc can either emit radiation without any major reabsorption (similar to the formation of a forbidden line in a nebula) or when the electron temperature is much greater than the colour temperature of the radiation from the background photosphere. In this case, one would obtain a violet shifted emission feature. The second possibility that can occur in this region is that the incident photospheric radiation is absorbed or scattered out of the line of sight resulting in the formation of a violet shifted absorption feature. The region 3 (the emission lobes of the sides of the disc) generates photons which are emitted thermally or scattered from both stellar and diffuse radiation field from the envelope. In these emission lobes, the line of sight velocities lie between positive and negative values producing a symmetric emission feature covering from violet to red side of the central frequency of the line. As the region 4 is occulted from the observer by the stellar disc, we cannot observe the maximum red shift, therefore we can obtain information about the velocities only from the blue shift of the absorption or emission feature.

We shall describe a method to obtain the flux profiles once the source functions is known as a function of frequency and radius. The envelope is divided into  $N$  shells (strictly speaking sectors) with radii  $r_n$ ,  $r_1 = A$  (the inner radius and  $r_N = B$ , the outer radius. We know in advance the values of the absorption coefficient  $\kappa(r)$ ,  $S(r)$ ,  $V(r)$ . We select a set of  $N$  parallel rays parallel to the direction of the observer at infinity. First we consider the side lobes (regions 3). Each ray is defined by an impact parameter  $p_n$  corresponding to the ray  $n$  tangential to the sector

with radius  $r_n$ . This ray will intersect  $2(N - n) + 1$  sectors, the number 1 represents the sector with which the ray is a tangent. We need to evaluate the transfer in each segment such as CD (see figure 1.3b). We shall apply the formal solution

$$I^n(C) = I^{n+1}(B)e^{-\tau} + \int_0^\tau S_{n+\frac{1}{2}}(t)e^{-[\tau-t]}dt, \quad (1.108)$$

where  $\tau$  is the optical depth of the segment such as CD. In the observers frame, the line frequencies will have Doppler shifts from  $(-x$  to  $+x)$  to  $(x \pm \mu V)$  due to velocities. Therefore the source functions calculated for the lines with frequencies  $-x$  to  $x$  in the comoving frame cannot cover the red and blue shifts corresponding to velocities  $\pm V$  in the line frequencies in the rest frame. Therefore we integrate the source function over the line with respect to frequency so that it can be used over whole range of line frequencies in the observer frame. This is given as

$$S_n = \sum_{i=-I}^{+I} A_i S_n(x_i, \tau_n), \quad (1.109)$$

$$S_{n+\frac{1}{2}} = \frac{1}{2} (S_n + S_{n+1}). \quad (1.110)$$

We need to estimate the optical depth  $\tau_{CD}$  accurately to compute  $I^n(C)$ . We divided this segment  $CD$  into say,  $K$  smaller segments. Let  $OD = r_{n+2}$ ;  $OC = r_{n+1}$ . Divide the segment  $CD$  into  $k$  smaller segments each of equal length at point  $Q_1$  (this is at  $C$ ),  $Q_2 \dots Q_k$  (see figure 1.3c). Let each segment is equal to  $\Delta Q = CD/k$ . we need to find cosines of the angles  $\alpha(Q_k)$  made by the lines such as  $OQ_1, OQ_2, \dots OQ_k$  with the ray at  $Q_1, Q_2, \dots Q_k$ . We now obtain  $\mu(Q_k)$  as

$$\mu(Q_k) = \cos(\alpha(Q_k)) = \frac{PQ_k}{OQ_k}, \quad (1.111)$$

where

$$OQ_k^2 = OP^2 + PQ_k^2, \quad OP = r_n,$$

$$\begin{aligned}
PQ_k &= PC + k \cdot \Delta Q, \quad k = 0, 1, \dots, k \\
PC &= (r_{n+1}^2 - r_n^2)^{\frac{1}{2}}, \\
\Delta Q &= CD/k, \\
CD &= (r_{n+2}^2 - r_n^2)^{\frac{1}{2}} - (r_{n+1}^2 - r_n^2)^{\frac{1}{2}}.
\end{aligned} \tag{1.112}$$

Now we can compute the frequencies in the observers frame using the relation

$$x_0 = x \pm \mu(Q_k) \cdot V(Q_k), \tag{1.113}$$

where  $V(Q_k)$  is the radial velocity along the radius vector  $OQ_k$  at the point  $Q_k$ . The source functions at the points  $Q_1, Q_2, \dots$  are obtained by a simple linear interpolation of the values at  $r_{n+1}$  and  $r_{n+2}$ . For this purpose, one should take as many shells as possible which is equal to the number of rays. One can use a large number of rays. The boundary condition where the ray crosses the  $N$ th shell is given as  $I^N = 0$ . Then  $I^{(N-1)}$  is estimated using the equation (1.108) repeatedly along the segment such as  $CD$ . The profile function is computed using the relation (1.113). For redistribution functions one can use the profile function. We have computed the intensities for each ray corresponding to each frequency in the range  $x_0 \rightarrow x \pm \mu(Q_k)V(Q_k)$ .

The optical depth in each segment such as  $(Q_k Q_{k-1})$  along the line of sight is computed using the relation

$$\tau(x, Q_k, Q_{k-1}) = \kappa(Q_k, Q_{k-1})\phi(x_0), \tag{1.114}$$

where  $\phi(x_0)$  is the profile function.  $\kappa(Q_k, Q_{k-1})$  is the absorption coefficient between the points  $Q_k$  and  $Q_{k-1}$ . Thus, the monochromatic flux is computed by using the formula

$$F_x = 2\pi \int_{r_1}^{r_N} I(p)pdp. \tag{1.115}$$

A similar calculation of the intensities in the region 5 (of figure 1.3a) is also performed.

## Chapter 2

### Reflection effect in close binaries

#### 2.1 Introduction

Most stars are found in groups that are gravitationally bound to each other. The majority of these stars are found in binary systems which are systems of two stars in orbit around a common center of mass. Binaries are useful systems for astronomers because two stars in orbit obey well understood laws of motion. From their orbital velocities and periods, it's possible to calculate the combined and individual masses of the stars in a system. When the stars are plotted by their brightness and their spectral type on Hertzsprung-Russell diagram, most stars falls on to a narrow band called main sequence. But the stars that compose close binary systems are not the same luminosity as star of similar type, so they fall slightly off the main sequence-the primary stars tend to appear below it, while the secondary above it.

Kopal (1959) first classified all close binaries into three groups - detached, semi-detached, and contact systems. In detached systems both star remain well within their respective Roche lobes ( $\beta$ -Aurigae). In semi-detached systems however, one component fills its Roche lobes (Algol,  $\beta$  Persi). Contact binaries are still exotic -both components fill their Roche lobes and continually interact (44-Bootis B).

One can think of a quite a number of binary star configurations in which relatively simple numerical treatment of reflection will be adequate. Most obvious is that of slowly rotating stars, which are well detached from their limiting lobes and are therefore, not far from spherical. Systems of main sequence stars with radii of the order of 10%-15% of their separation fall into this category and are reasonably common (for stars which are smaller than this there is, in most cases, hardly any reflection effect).

In a close binary system each component will receive the radiation from its companion. If a star is to remain in radiative equilibrium, all the energy received from outside must be re-emitted, without altering the rate of escape of radiation from the deep interior. This phenomenon, known as the "reflection effect" is inevitable in close binaries. To explain this effect properly further study of the problem is necessary to answer - or at least to give some clues to - several fundamental parameters such as mass and radii. In radiative transfer theory, we solve the equation of radiative transfer by assuming certain geometrical configuration such as plane parallel or spherical symmetric stratification of the media. These geometrical configurations assume symmetric boundary conditions and whenever we have asymmetric incident radiation, the solutions developed in the context of symmetrical geometries as mentioned above, will have to be modified. Such problems are encountered in the evaluation of radiation from the irradiated component of the binary system. If we treat one of the component as a point source in a binary system then the problem of incident radiation from such source is equivalent to the searchlight problem. Chandrasekhar (1958) has calculated the diffuse scattering function in a plane parallel medium when a pencil of beam of radiation from a point source is incident. There have been several

attempts for calculating the diffuse radiation field in such simple geometries. However, the calculation of the radiation field during the eclipses in close binaries is of different complexity. There are two important aspects one should take into account: (1) the physical processes that takes place inside the atmosphere and (2) the geometrical shape of the illuminated surface which reflects the light. Generally, if the atmosphere of the component under consideration is extended or fills its Roche lobe, then the problem of determining the emergent radiation from such surfaces become very difficult. The process of estimating the radiation field from such surfaces become complicated when the various competing physical processes are taken into account. Geometrical considerations alone would complicate the calculations because of the deformed shape due to tidal effects from the neighbour and due to self radiation. The resultant shape would be an ellipsoid and the problem requires special treatment. The solution of radiative transfer equation either in plane parallel symmetry or in spherical symmetry or in cylindrical symmetry cannot accurately describe the radiation field emanating from such surfaces.

Now in this chapter we will describe a method for estimating the reflected radiation from a primary component in a binary system.

## **2.2 Distribution of radiation incident from a point source**

We shall assume that the components are spherical (the method can be extended for non spherical shapes). We have assumed the albedo of single scattering to be unity, i.e. purely scattering medium. In figure 2.1, let O is the centre of the primary component whose atmosphere is divided in spherical shells. Let S be a point source outside the star (secondary

component) on axis OX and the OY is perpendicular to OX. We shall assume that the radiation is coming from point source S is incident on primary component at points such as  $P_1, P_2, \dots$  etc. These rays travel through the medium intersecting the shells at given radial points. We choose a radius vector corresponding to a given  $\theta$  (the colatitude) and calculate the source functions where this radius vector meets the shell boundaries at points such as  $Q_1, Q_2, Q_3, \dots$ , etc. The calculation of source function is done by employing the 'Rod' model of one-dimensional radiative transfer (Sobolev 1963, Wing 1962) along the ray path inside the medium. This means we calculate the source functions at points  $Q_1, Q_2, Q_3, \dots$ , etc.

### 2.2.1 Description of rod model

We shall assume a steady state, monochromatic ray with or without internal sources (see figure 2.2). The optical depth is calculated using the relation

$$\tau = \tau(\xi) = \int_0^l \sigma(\xi') d\xi', \quad \tau(l) = T. \quad (2.1)$$

The transfer of radiation is assumed to take place along the ray paths  $P_1Q_1, P_2Q_2, P_3Q_3, \dots$ , etc. (in figure 2.1) or along  $ol$  (in figure 2.2) with isotropic scattering ( $\mu = \pm 1$  and  $p(\tau) =$  phase matrix elements). The source function that includes diffuse radiation can be written as (see Peraiah 1982),

$$S_d^+(\tau) = S^+(\tau) + \omega(\tau) \left[ p(\tau) I_1 e^{-\tau} + (1 - p(\tau)) I_2 e^{-(T-\tau)} \right], \quad (2.2)$$

and

$$S_d^-(\tau) = S^-(\tau) + \omega(\tau) \left[ (1 - p(\tau)) I_1 e^{-\tau} + p(\tau) I_2 e^{-(T-\tau)} \right], \quad (2.3)$$



where

$$S^+(\tau) = \omega(\tau) \left[ p(\tau) I^+(\tau) + (1 - p(\tau)) I^-(\tau) \right], \quad (2.4)$$

$$S^-(\tau) = \omega(\tau) \left[ (1 - p(\tau)) I^+(\tau) + p(\tau) I^-(\tau) \right], \quad (2.5)$$

where  $\omega(\tau)$  is the albedo for single scattering which is equal to unity in a pure scattering medium,  $p(\tau)$  is the phase matrix (here it is equal to  $\frac{1}{2}$ ) and the specific intensities (see figure 2.2)  $I^+(\tau)$  and  $I^-(\tau)$  are given by the differential equations.

$$\frac{dI^+}{d\tau} + I^+ = S^+, \quad (2.6)$$

$$\frac{dI^-}{d\tau} + I^- = S^-. \quad (2.7)$$

The boundary condition at  $\tau = 0$  and  $\tau = T$  are given by

$$I^+(0) = I_1, \quad (2.8)$$

and

$$I^-(T) = I_2. \quad (2.9)$$

We shall specify  $I_1$  later and set  $I_2 = 0$ . From equations (2.6) and (2.7) the solution can be obtained and is given by,

$$I^+(\tau) = I_1 \frac{1 + (T - \tau)(1 - p)}{1 + T(1 - p)}, \quad (2.10)$$

and

$$I^-(\tau) = I_1 \frac{(T - \tau)(1 - p)}{1 + T(1 - p)}. \quad (2.11)$$

From equations (2.10) and (2.11) we obtain,

$$I^+(\tau = T) = I_1 \frac{1}{1 + T(1 - p)}, \quad (2.12)$$

$$I^-(\tau = 0) = I_1 \frac{T(1 - p)}{1 + T(1 - p)}. \quad (2.13)$$

Moreover,

$$r(T) = \frac{T(1 - p)}{1 + T(1 - p)} \rightarrow 1 \quad \text{as} \quad T \rightarrow \infty, \quad (2.14)$$

and

$$t(T) = \frac{1}{1 + T(1 - p)} \rightarrow 0, \quad \text{as } T \rightarrow \infty \quad (2.15)$$

where  $r(T)$  and  $t(T)$  are the reflection and transmission coefficients respectively. From (2.14) and (2.15) we find

$$r(T) + t(T) = 1, \quad (2.16)$$

which is the expression for conservation of energy.

Using the results of above analysis we can calculate the source functions according to one-dimensional rod model at points where the radii corresponding to each  $\theta$  meet the shell boundaries. Our aim is to obtain the source functions described in equations (2.2) and (2.3). Here we calculate the optical depth along the ray path eg.,  $P_1Q_1$ ,  $P_2Q_2$ ,  $P_3Q_3$ , ...etc. and employ this optical depth to estimate the specific intensities and source functions at these points.

### 2.2.2 Calculation of self radiation of the primary component

In addition to the incident radiation from the secondary component, we have the radiation of the primary component itself. This self radiation of the primary component can be calculated easily by employing the radiative transfer equation in a spherically-symmetric approximation.

The equation of transfer is given in the form

$$\begin{aligned} & \frac{\mu}{r^2} \frac{\partial}{\partial r} [r^2 I(r, \mu)] + \frac{1}{r} \frac{\partial}{\partial \mu} [(1 - \mu^2) I(r, \mu)] + \sigma(r) I(r, \mu) \\ & = \sigma(r) \left[ [1 - \omega(r)] b(r) + \frac{1}{2} \omega(r) \int_{-1}^1 p(r, \mu, \mu') I(r, \mu') d\mu \right], \end{aligned} \quad (2.17)$$

where  $\omega(r)$  is the albedo for single scattering,  $I(r, \mu)$  is the subject to the conditions in discrete space theory as described in *Chapter 1* section (1.2.1).

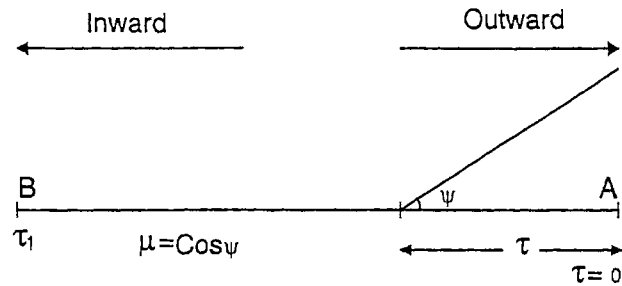


Figure 2.3: Plane parallel model

Therefore, if  $S(r, \theta)$  is the total radiation,  $S_I(r, \theta)$  is the source function due to irradiation from external source and  $S_S(r)$  is that due to self-radiation of the star itself, then

$$S(r, \theta) = S_I(r, \theta) + S_S(r). \quad (2.18)$$

Next step is to calculate the distribution of intensities at the internal points like  $Q_1, Q_2 \dots$  etc., along the radius and find out the distribution of the emergent radiation field at points like  $P_1, P_2, \dots$  etc. . The radiation field is given by the formal solution of radiative transfer equation in plane parallel approximation (Chandrasekhar 1960, equations 64 and 65 on p.12., and figure 2.3 here).

$$I(\tau, +\mu) = I(\tau_1, \mu) \exp[-(\tau_1 - \tau)/\mu] + \int_{\tau}^{\tau_1} S(t) \exp[-(t - \tau)] \frac{dt}{\mu}, \quad (2.19)$$

for outward intensities and

$$I(\tau, -\mu) = I(0, -\mu) \exp[-(\tau/\mu)] + \int_0^{\tau} S(t) \exp[-(\tau - t)/\mu] \frac{dt}{\mu}, \quad (2.20)$$

for inward intensities. For the explanation of various terms see figure 2.3. The optical depths are always measured from A to B, and  $1 > \mu > 0$  where  $\cos^{-1} \mu$  is the angle made by the ray with AB. The equations (2.19) and (2.20) describe the radiation field emerging from the irradiated surface which receives the incident radiation coming from the point source S.

### 2.2.3 Brief description of the computational procedure

We have considered a component whose outer radius is  $R_{\text{out}} (= 10^{12} \text{cm})$  and atmosphere thickness is  $\simeq 0.5 R_{\text{out}}$ . Let us assume that incident radiation is coming from a point S at a distance of  $4.5 \times R_{\text{out}}$  cm away from the centre of the primary component with its centre at O. We divided the atmosphere of primary component into 25 spherical shells (interms of shell number where shell numbers are counted outside to inside ie,  $n=1$  at  $R_{\text{out}}$  and  $n=25$  at  $R_{\text{in}}$ ). We calculate the source functions at points  $Q_1, Q_2, Q_3, \dots$ , etc., on radius vector co-latitude  $\theta$ . This is done by employing the rod model described in equations (2.2), (2.3), (2.4) and (2.5). We calculate the segments  $P_1Q_1, P_2Q_2, \dots$ , etc., and estimate the optical depths according to the law that the density varies as  $\frac{1}{r}$ . The electron scattering has been assumed in the medium with  $N_0$  (at  $R_{\text{out}} = 10^{12} \text{cm}) = 10^{12} \text{cm}^{-3}$  to  $10^{15} \text{cm}^{-3}$ . We have presented the results for  $N_0 = 10^{14} \text{cm}^{-3}$  and with this density (which is varying as  $\frac{1}{r}$ ), the radial optical depth becomes 1.1. Here while calculating the source functions due to self radiation, we have used the spherically symmetric approximations and calculated the source functions.

The results are given in the form of distribution of radiation at different points along the radii such as  $Q_1, Q_2, Q_3, \dots$ , etc., by solving the equations (2.19) and (2.20). Let  $I_Q$  be the intensity of radiation incident spherically symmetrically on the inner boundary of the atmosphere of the star and the intensity coming from point S be  $I_S$ . The incident radiation at the point P will be  $I_S \mu \cos \gamma$ . We have considered the following cases.

Case 1:  $I_Q/I_S = 0.1$

Case 2:  $I_Q/I_S = 1$

Case 3:  $I_Q/I_S = 10$

The figures 2.4, to 2.9 shows the radiation field  $I(r, \mu, \theta)$  are plotted against  $\mu$  for a specified  $\theta$  and  $r$  representing cases 1, 2 and 3 respectively. In these figures the continuous ( $I$ ) curves denote the distribution of radiation due to the incident radiation from the point source and the dotted curves ( $I_S$ ) denote the resultant radiation field due to external and self radiation fields.

#### 2.2.4 Results and discussion

These results represent the radiation on the outermost layers of the reflected surface. In the figures 2.4, 2.5, 2.6, we have plotted  $I(n = 1, \mu)$  for case 1, 2 and 3 respectively. From figure 2.4, one can see that the intensities at  $\theta = 0^\circ$  are quite small and increase considerably at  $\theta = 90^\circ$ . In case 2, we have again the same phenomenon (figure 2.5) although at  $\theta = 90^\circ$  (along OS see figure 2.1) more radiation goes into the star than the outcoming radiation.  $I(n = 1, \mu)$  for case 3 figure 2.6 shows again the same features of figure 2.5, with much less radiation going into the star both at  $\theta = 0^\circ$  and  $\theta = 90^\circ$ .

In the figures 2.7, 2.8, 2.9 we have plotted  $I(r, \mu)$  at  $\theta = 0^\circ$  for case 1, case 2, and case 3. The continuous curves denote the external radiation and the dotted curve indicate the resultant radiation field due to both external and self radiation. Here the co-latitude  $\theta = 0^\circ$ , corresponds to the radiation along OY (see figure 2.1). At the bottom of the atmosphere  $n = 25$  or  $r=R_{iN}$ ) the effect of external radiation is not much in figure 2.7 (ie case 1) but increases when the self radiation is added to it. At the shell  $n = 15$ , we see that the combined radiation field is maximum while at the outermost layer ( $n = 1$ ) it is not as large as that ( $n = 15$ ). This is not difficult to understand on physical grounds. We have diluted

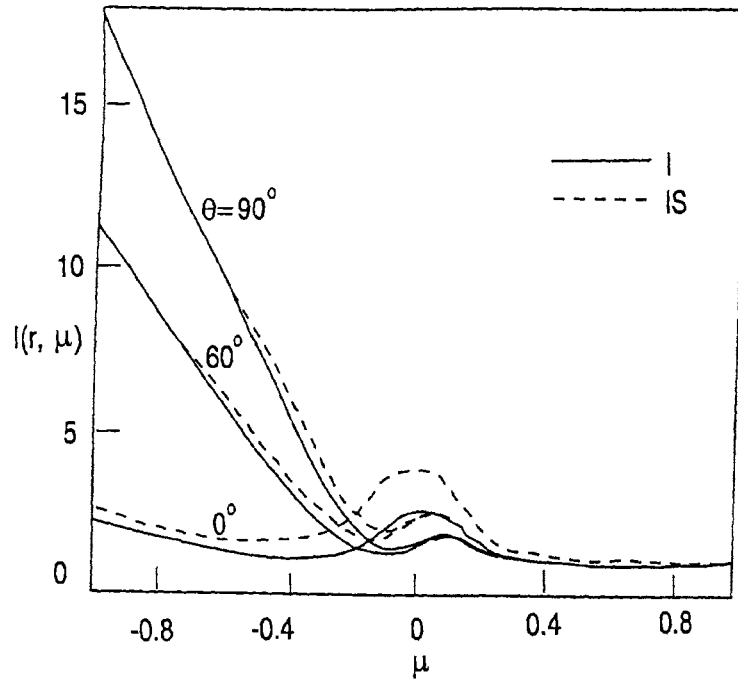


Figure 2.4: Distribution of the emergent radiation field at  $\theta = 0^\circ, 60^\circ, 90^\circ$  for case 1

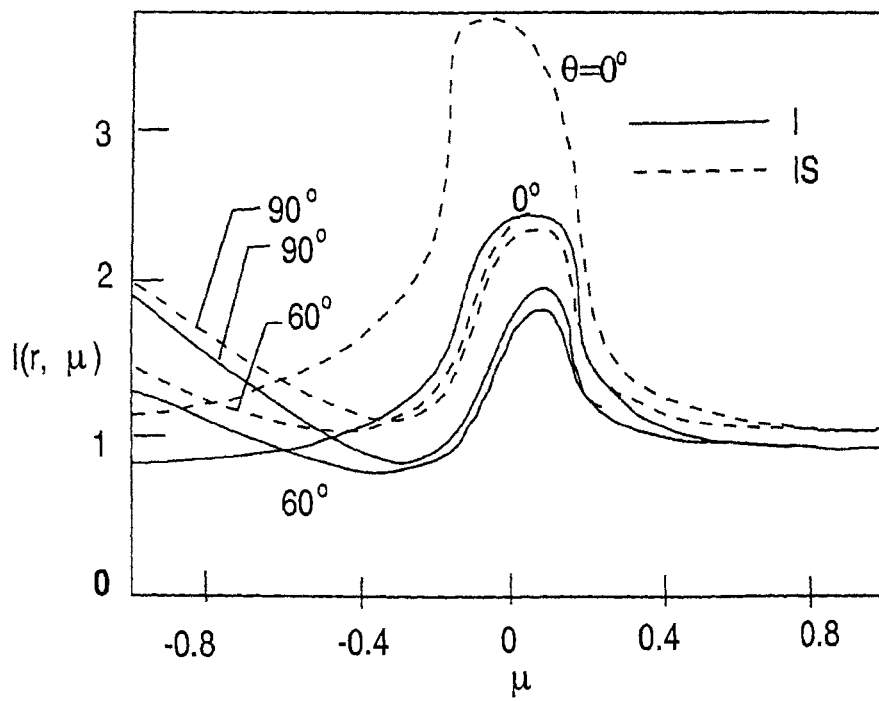


Figure 2.5: Distribution of the emergent radiation field at  $\theta = 0^\circ, 60^\circ, 90^\circ$  for case 2

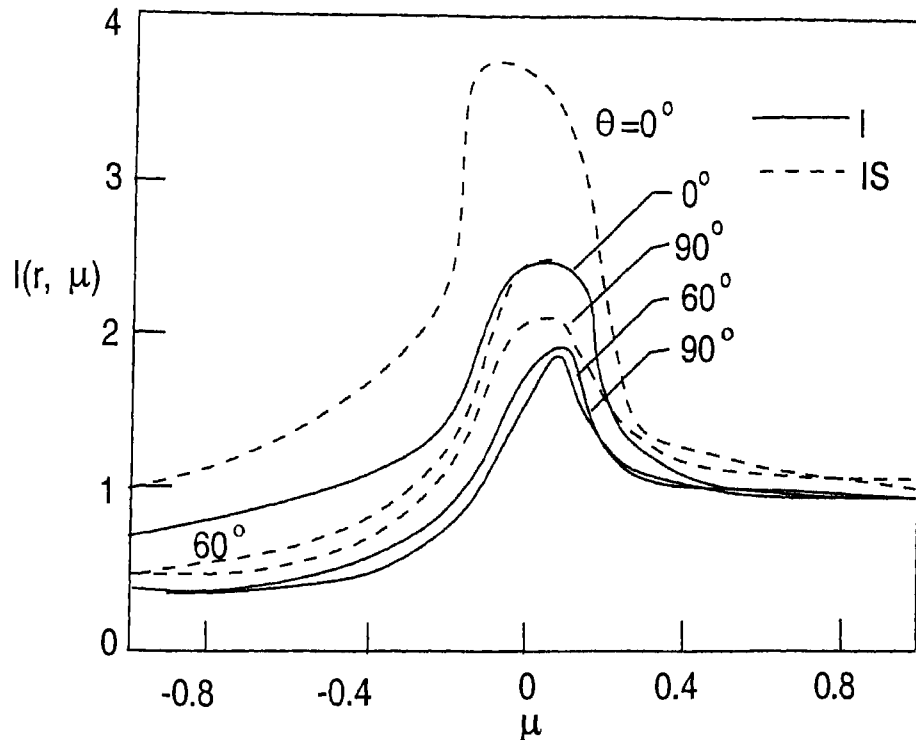


Figure 2.6: Distribution of the emergent radiation field at  $\theta = 0^\circ, 60^\circ, 90^\circ$  for case 3

self radiation and at  $n = 25$  the external radiation becomes weak. In the middle we have the combined radiation field of both, although partly diluted. The similar kind of trend can be seen in figures 2.8, and 2.9.

In the figures 2.10, 2.11, 2.12 we have plotted  $I(r, \mu)$  at  $\theta = 60^\circ$  for case 1, case 2, and case 3. We also observe similar kind of features as in figures 2.7, 2.8, and 2.9. The main difference between these set of figures is more radiation comes out in all cases when  $\theta = 60^\circ$  when compared to that at  $\theta = 0^\circ$ .

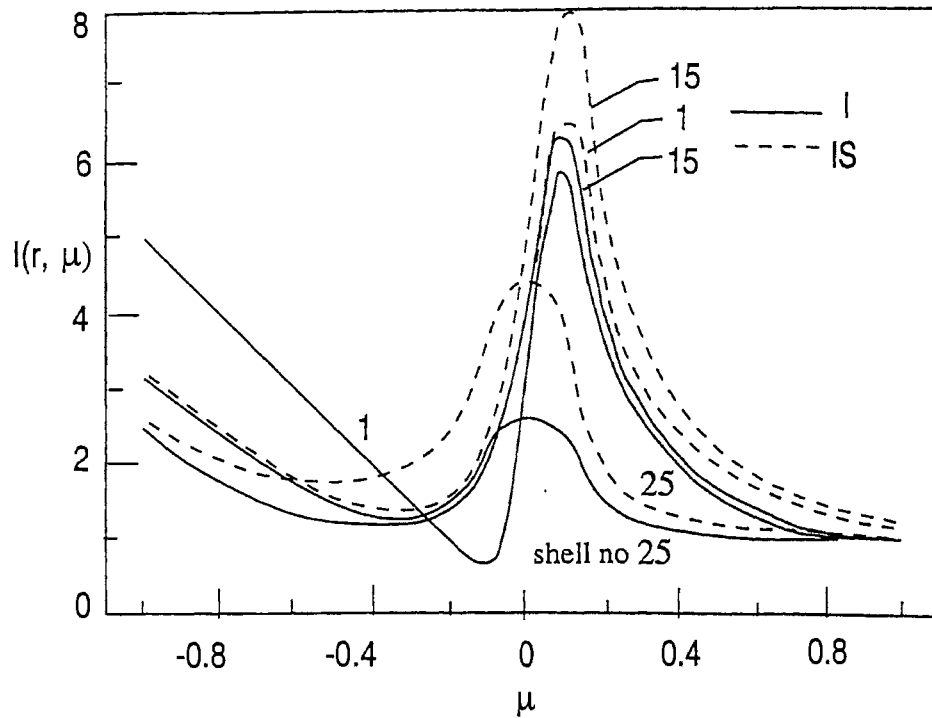


Figure 2.7: Distribution of the emergent radiation field at  $\theta = 0^\circ$  for case 1, for the shell numbers shown in the figure. I stands for irradiation, and IS stands for irradiation plus self radiation.

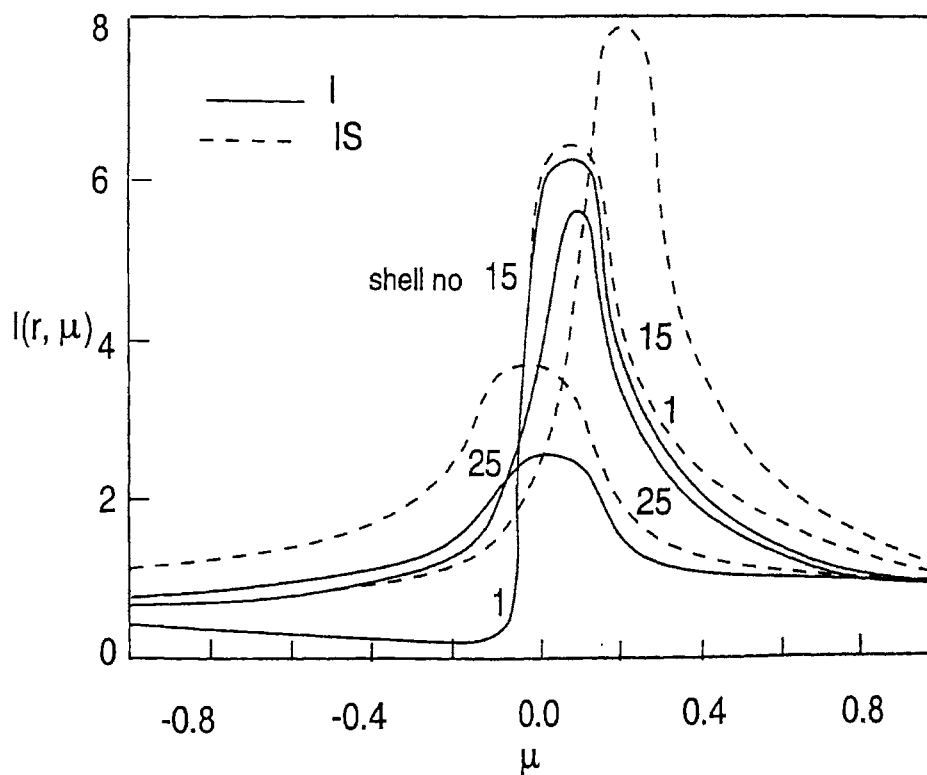


Figure 2.8: Distribution of the emergent radiation field at  $\theta = 0^\circ$  for case 2

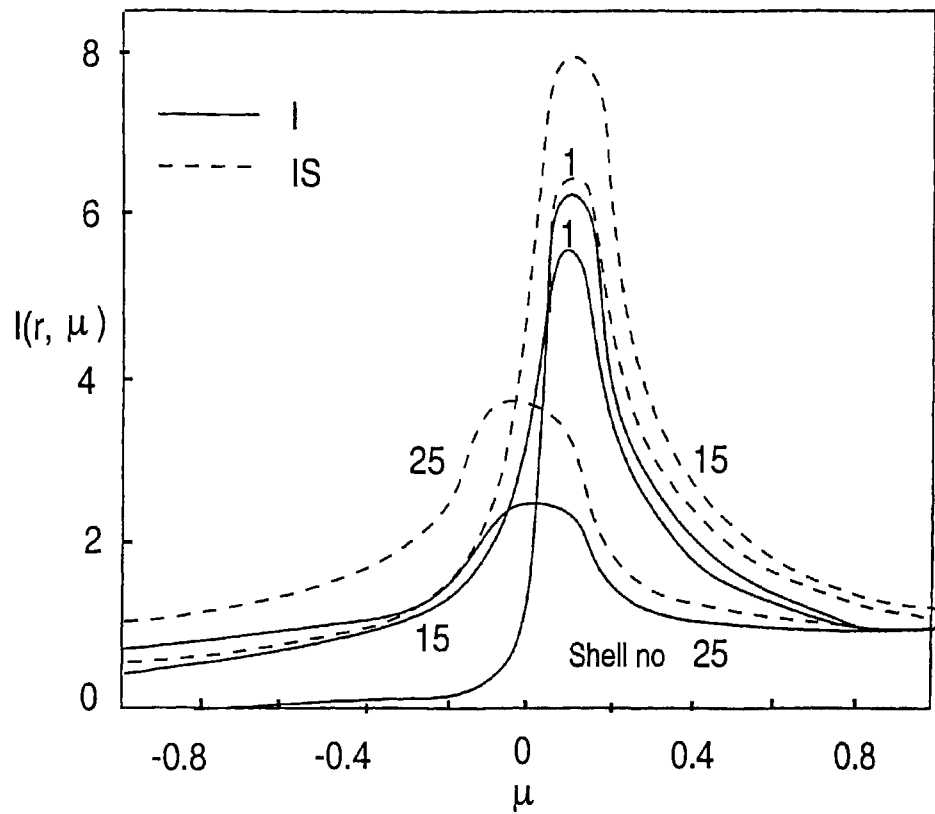


Figure 2.9: Distribution of the emergent radiation field at  $\theta = 0^\circ$  for case 3

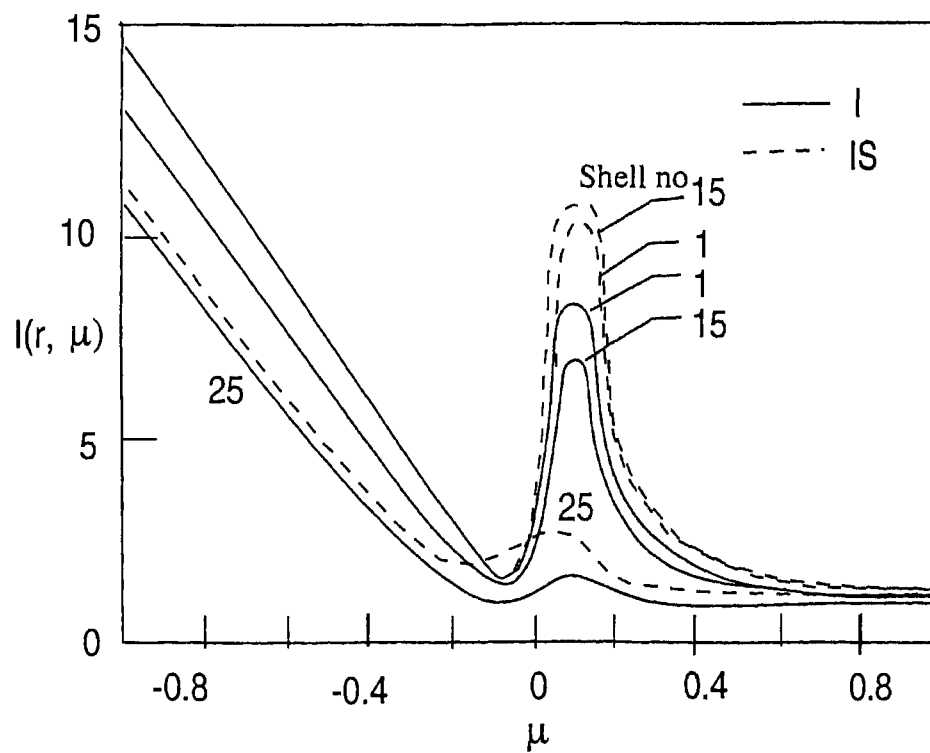


Figure 2.10: Distribution of the emergent radiation field at  $\theta = 60^\circ$  for case 1

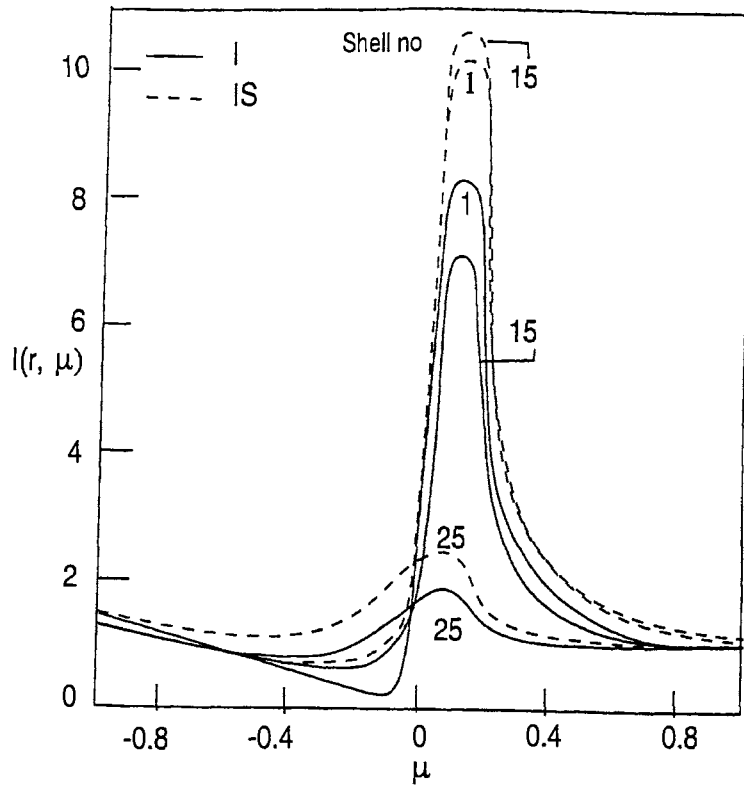


Figure 2.11: Distribution of the emergent radiation field at  $\theta = 60^\circ$  for case 2

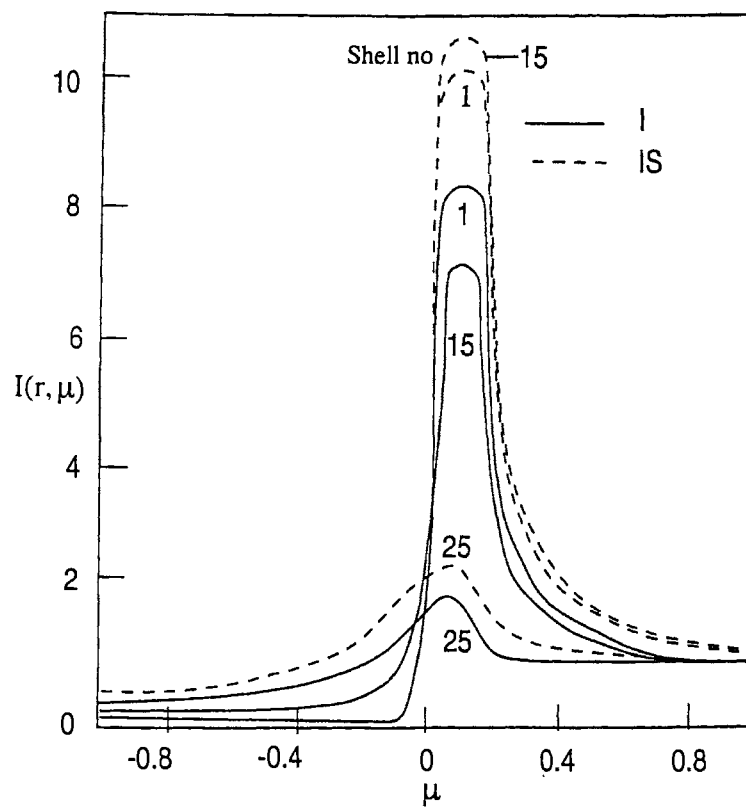


Figure 2.12: Distribution of the emergent radiation field at  $\theta = 60^\circ$  for case 3

## 2.3 Distribution of emergent radiation along the line of sight when incident radiation is from point source

In the previous section we have presented an approach to obtain the reflected radiation from the component of a binary system. We have considered the incident radiation coming from an external point source and estimated how this radiation field has changed the total radiation coming from the irradiated surface. We have noticed several important changes in the radiation field emergent from the irradiated part of the component. The intermediate regions of the irradiated part of the atmosphere become brighter than the extreme regions. This results suggests that the law of limb darkening that is generally used in the light curve analysis( Kopal 1959) should be replaced by the accurate calculations of the distribution of radiation from centre to limb. We shall employ the above procedure to calculate the distribution of radiation from centre to limb as is received at infinity.

### 2.3.1 Method to calculate radiation field from centre to limb

In figure 2.13, we have shown the portion of the star illuminated by radiation from a point source X. The atmosphere is divided into several shells of equal radial thickness. The radiation from this irradiated part of the atmosphere is received by the observer at infinity. We have chosen a set of parallel rays tangential to the shell boundaries at a point on the axis OX where O is the centre of the component. Let one of these rays meet the shell boundaries at  $Q_1, Q_2, Q_3, \dots$  etc. The intensity along the parallel rays is calculated first by obtaining combined source functions (self+irradiated) at points  $Q_1, Q_2, \dots$  etc.

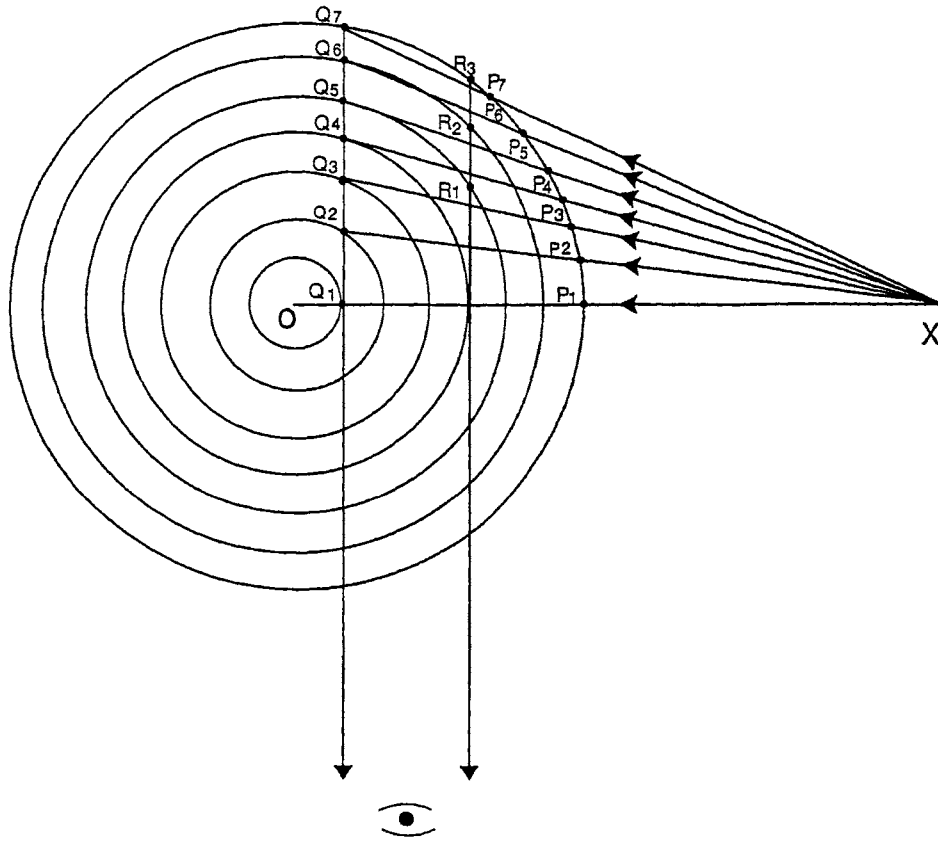


Figure 2.13: Schematic diagram showing the irradiation of the component. X is the point source of radiation. O is the centre of the component. The specific intensities are calculated along the line of sight. ( $Q_7, Q_6$ , etc.,  $R_3, R_2$  etc., )

For this purpose we have (1) the source function at these points due to self-radiation  $S_s$  and (2) source function due to irradiation  $S_I$ . The latter is calculated by using rod model (described in section 2.2). The radiation field is calculated along the lines  $Q_1P_1, Q_2P_2, Q_3P_3 \dots$  etc. We then add the two source functions to obtain the total source function  $S_T$ .

$$S_T = S_s + S_I. \quad (2.21)$$

From figure 2.13 The element QP is given by (see Peraiah 1983a)

$$QP = \{a^2 + b^2 + 2ab \cos(\widehat{OQP} + \widehat{OPQ})\}^{\frac{1}{2}}, \quad (2.22)$$

where

$$a = OP \text{ (} OP_1, OP_2 \text{ etc),}$$

$$b = OQ \text{ (} OQ, OQ_2 \text{ etc),}$$

$$OX = R, \quad OQ_1 = h,$$

(h is measured along  $OX$ ), and

$$\sin O\widehat{Q}P = \frac{R}{b} \left( \frac{b^2 - h^2}{b^2 + R^2 - 2hR} \right)^{\frac{1}{2}},$$

and

$$\sin O\widehat{P}Q = \frac{R}{a} \left( \frac{b^2 - h^2}{b^2 + R^2 - 2hR} \right)^{\frac{1}{2}}.$$

We have obtained the source terms  $S_I$  at  $Q$ 's by calculating the optical depths along  $QP$ 's. This is done by assuming an electron scattering and the electron density  $\rho$  varying as  $\frac{1}{r^2}$  and  $\frac{1}{r^3}$ . The source function due to self radiation  $S_s$  is obtained from the relation

$$S_s(r) = \frac{1}{2} \int_{-1}^{+1} I(r, \mu) d\mu, \quad (2.23)$$

as we are assuming radiative equilibrium. The specific intensity  $I(r, \mu)$  is obtained by solving the equation of radiative transfer in spherical symmetry solved in *Chapter 1* (equations 1.23 and 1.24). The boundary conditions are assumed as follows

$$I_s/I_I = I, \quad (2.24)$$

where  $I_s$  is the intensity of radiation incident at the inner boundary and  $I_I$  is the intensity of radiation incident from the point source. The radiation incident on the surface at points  $P_1, P_2$  etc. is taken to be  $I_I \cos O\widehat{P}Q$  and we have set  $I_s = 1$ . We have considered both plane parallel and spherically symmetric media for the sake of the comparison and set  $\frac{B}{A} = 1$  and 1.5 respectively where  $B$  and  $A$  are the outer and inner radii of the atmosphere. The purpose of this is to see how the spherical term

$$\pm \frac{1}{r} \frac{\partial}{\partial \mu} \left[ (1 - \mu^2) U(r, \pm \mu) \right], \quad (2.25)$$

would change the results.

### 2.3.2 Results and discussion

We have taken the same data as given in the previous section for OX,  $N_0$  etc. In figure 2.14-2.16, we have presented the variation of specific intensities from centre to limb in plane parallel case. The curves labeled I correspond to irradiation and those labeled I+S correspond to irradiation with self-radiation. The quantity  $h$  is the perpendicular distance to the ray from the centre O (see figure 2.13). The contribution from irradiation to the intensities  $I(h)$  is several times smaller than the total contribution from both self and irradiation. Figures 2.14 and 2.15 show that the limb is much darker than the centre. Figure 2.16 shows that an increase in electron density increases the brightness at the limb, but when combined with self-radiation, the limb appears dark. In figures 2.17-2.18 we have shown the specific intensities in the spherically symmetric case. We notice that the limb darken and also the intensities fall sharply compared to those in plane parallel case. When the electron density is increased the character of the intensities change, which is shown in figure 2.20. The intensities due to irradiation always show a brightening tendency towards the limb whereas the total radiation field falls towards limb but at the limb it shows brightening. This is due to the fact that there are more electrons in the region which scatter more light than when  $N_o = 10^{12}$  or  $10^{13} \text{cm}^{-3}$ .

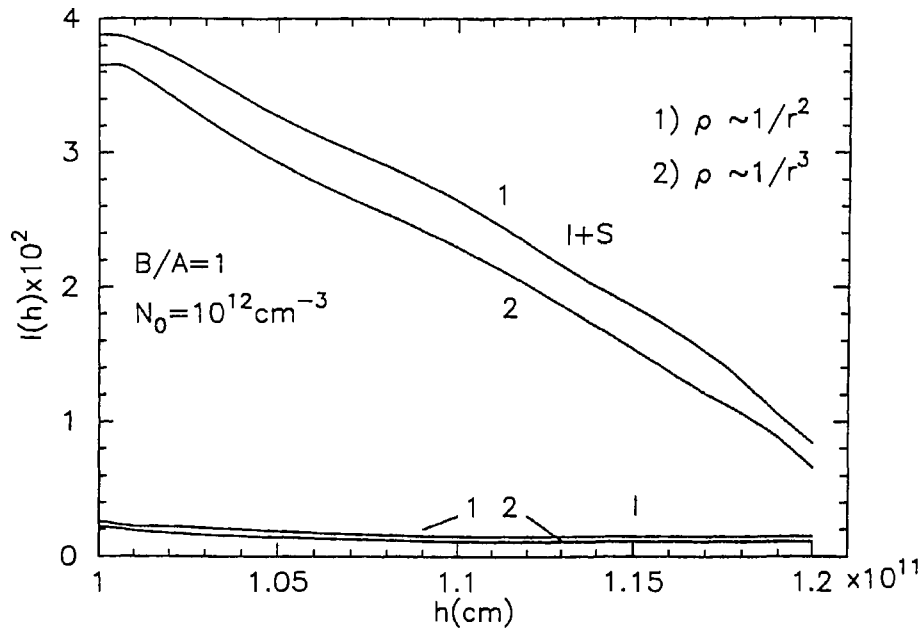


Figure 2.14: The specific intensities  $I(h)(h=OQ)$  are plotted with respect to  $h$ . The curves labeled  $I$  correspond to only irradiation and those  $I+S$  correspond to irradiation plus self radiation.  $N_0$  is the electron density at  $A \frac{B}{A} = 1$ .  $N_0 = 10^{12} \text{cm}^{-3}$  ( $B$  and  $A$  are the outer and inner radii of the atmosphere. Here  $\frac{B}{A} = 1$  means plane parallel atmospheres)

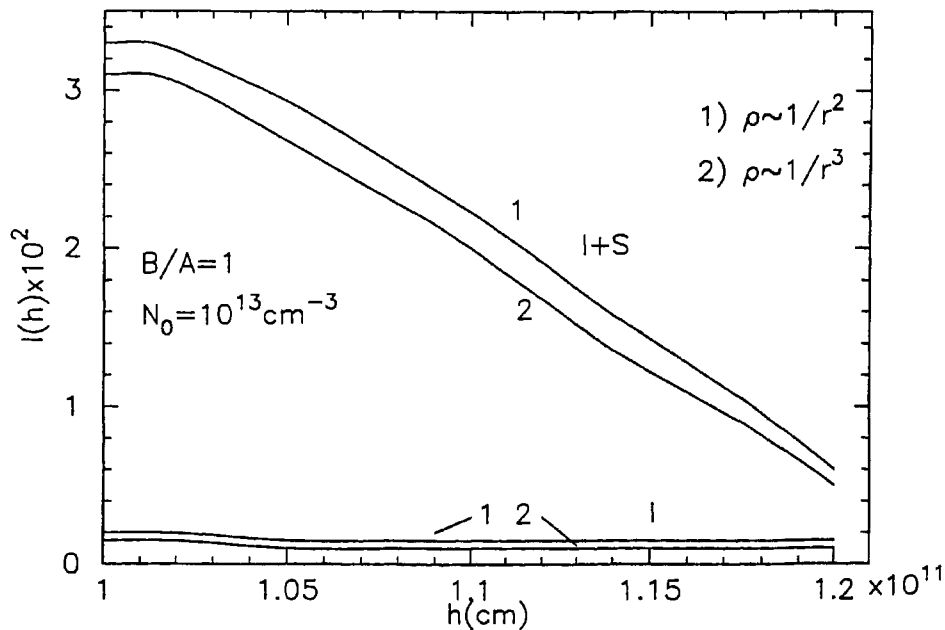


Figure 2.15:  $I(h)$  Versus  $h$  for  $\frac{B}{A} = 1$ ,  $N_0 = 10^{13} \text{cm}^{-3}$

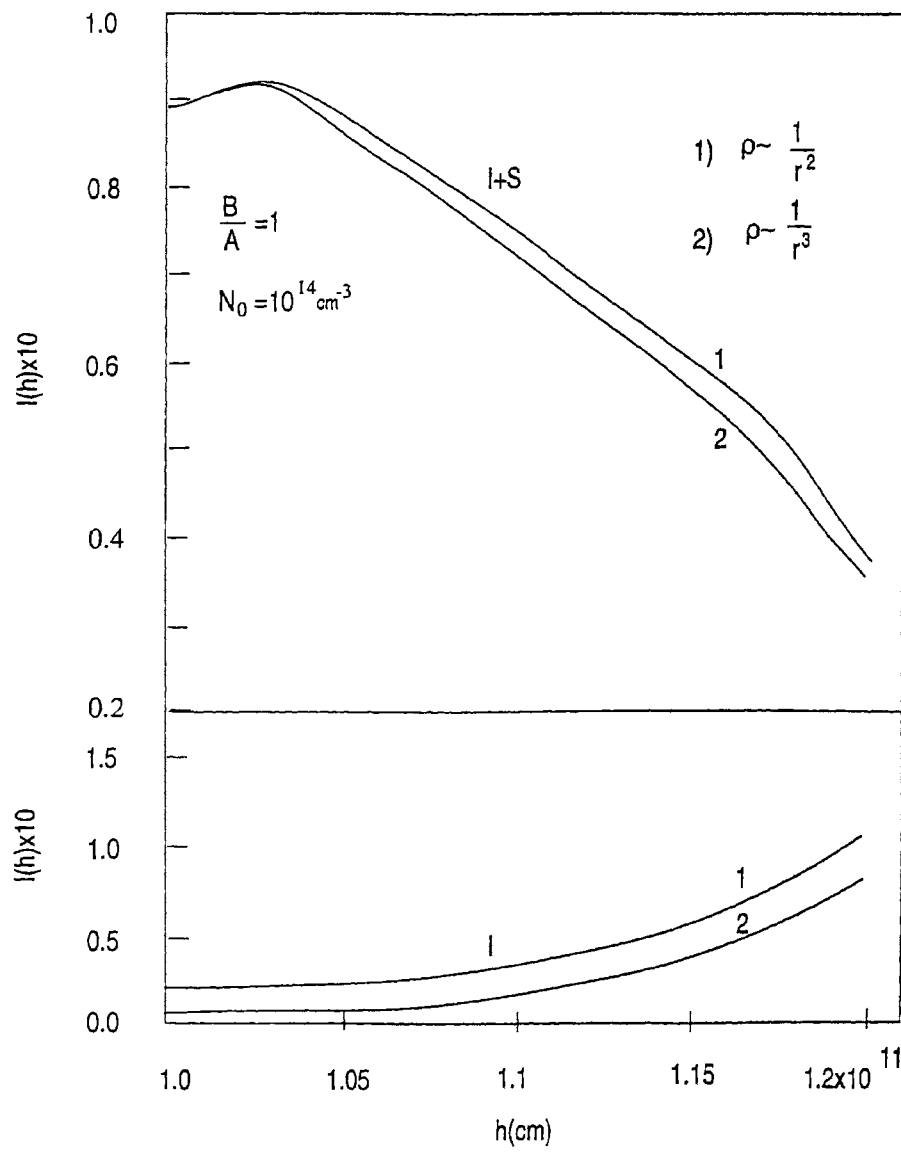


Figure 2.16:  $I(h)$  Versus  $h$  for  $\frac{B}{A} = 1$   $N_0 = 10^{14} \text{ cm}^{-3}$

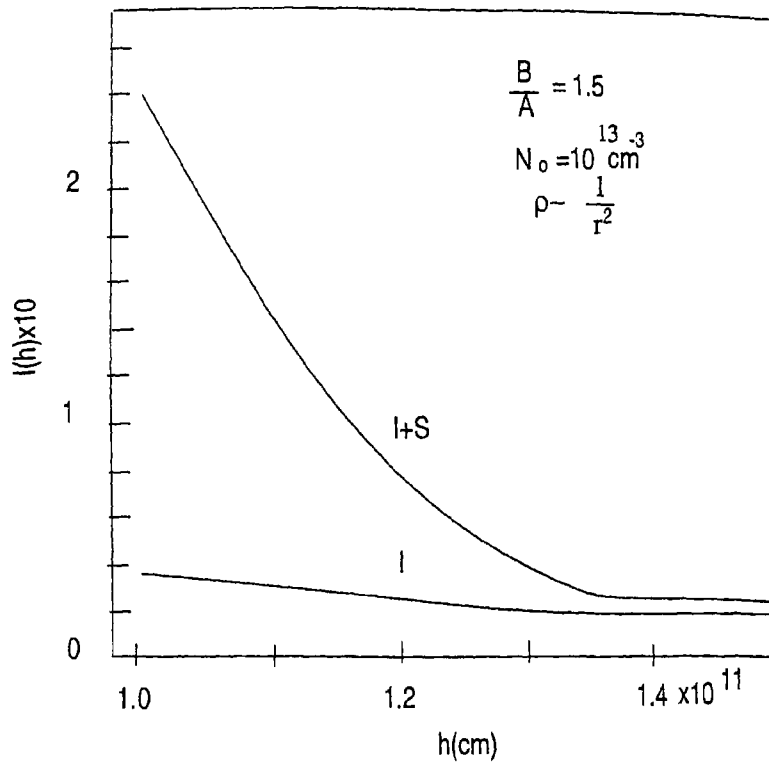


Figure 2.17:  $I(h)$  Versus  $h$  for  $\frac{B}{A} = 1.5$ ,  $N_0 = 10^{13} \text{ cm}^{-3}$ ,  $\rho \approx \frac{1}{r^2}$

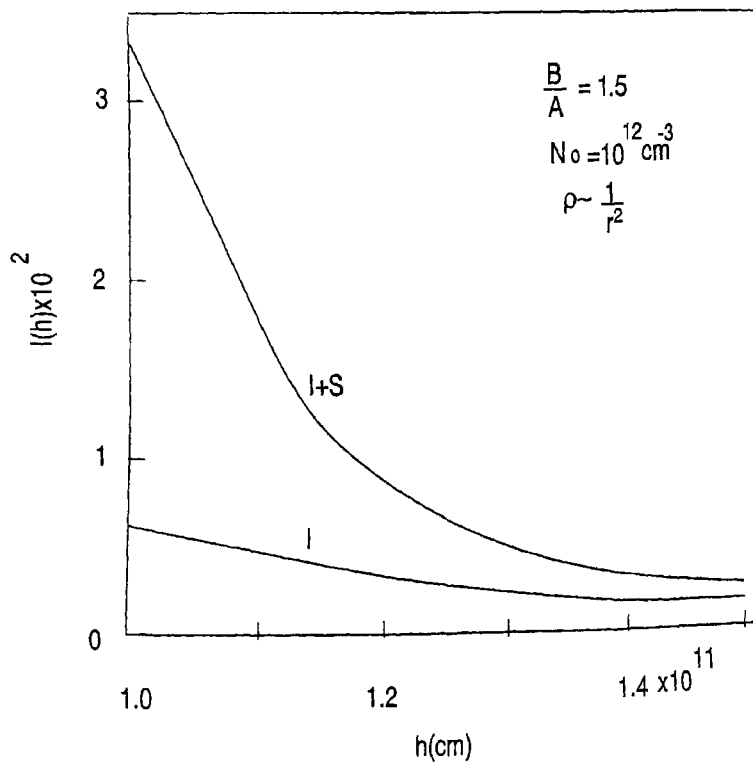


Figure 2.18:  $I(h)$  Versus  $h$  for  $\frac{B}{A} = 1.5$ ,  $N_0 = 10^{12} \text{ cm}^{-3}$ ,  $\rho \approx \frac{1}{r^3}$

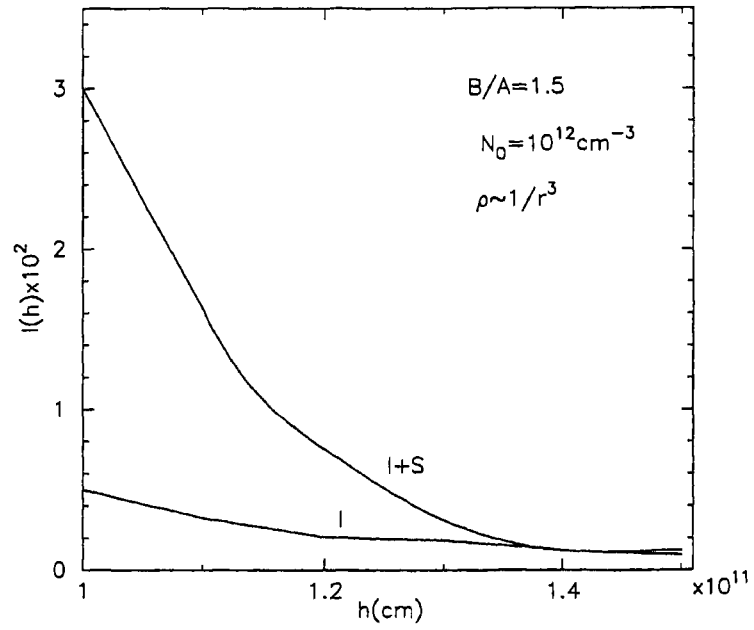


Figure 2.19:  $I(h)$  Versus  $h$  for  $\frac{B}{A} = 1.5$ ,  $N_0 = 10^{12} \text{cm}^{-3}$ ,  $\rho \approx \frac{1}{r^3}$

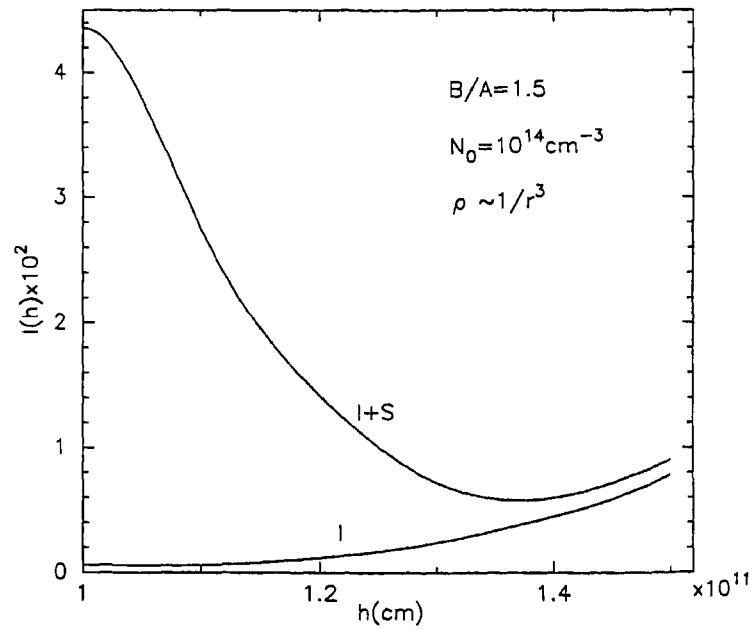


Figure 2.20:  $I(h)$  Versus  $h$  for  $\frac{B}{A} = 1.5$ ,  $N_0 = 10^{14} \text{cm}^{-3}$ ,  $\rho \approx \frac{1}{r^3}$

## 2.4 Temperature changes due to reflection

In this section we investigate how the temperature is redistributed due to incidence of radiation from the point source (figure 2.1). We have assumed radiative equilibrium in scattering medium and therefore, it is easy to calculate the effective temperature, which is proportional to the  $S_T^{\frac{1}{4}}$  where  $S_T$  is the total source function in the scattering medium.

Procedure is described the section (2.1). Here we have considered radius  $R_{out}$  and an atmosphere whose thickness is three times the radius. The point source kept at a distance five times (i.e,  $OS = 5 \times R_{out}$ ) the outer radius in one case, in ten times (i.e,  $OS = 10 \times R_{out}$ ) the outer radius in another case of the component from the centre O. We estimated the changes in temperature along the radii vectors OP corresponding to an angle  $\theta$  made with OX. Here position of the point source S is on OX.

### 2.4.1 Results and discussion

In the regions where  $\theta \geq 90^\circ$  the increase in temperature is in the outer layers where as in the regions for  $\theta \leq 90^\circ$ , the temperature is affected throughout the region. Here figure 2.21 for the density variation for  $\rho \sim \frac{1}{r}$ . Figure 2.22 for the density variation  $\rho \sim \frac{1}{r^2}$ . The results in both the figures show similar characteristics.

In figure 2.21 we have plotted the ratio of  $\frac{T_*}{T_s}$  where  $T_*$  is the new temperature and  $T_s$  is the original temperature along the radius vector OP (see figure 2.1), for various angles. It is very interesting to note that the temperature increases by as much as 40% in the intermediate regions  $\theta = 30^\circ$ . The figures 2.23 and 2.24 are similar as 2.21 and 2.22 respectively except for the parameter OS (see figure 2.1).

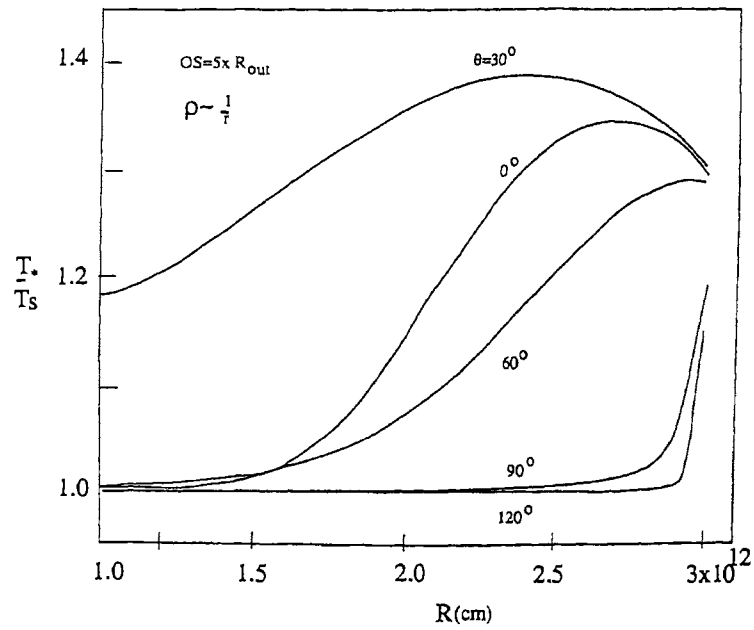


Figure 2.21: Temperature distribution  $\frac{T_*}{T_s}$  along the radius vector for each  $\theta$  density variation is  $\frac{1}{r}$

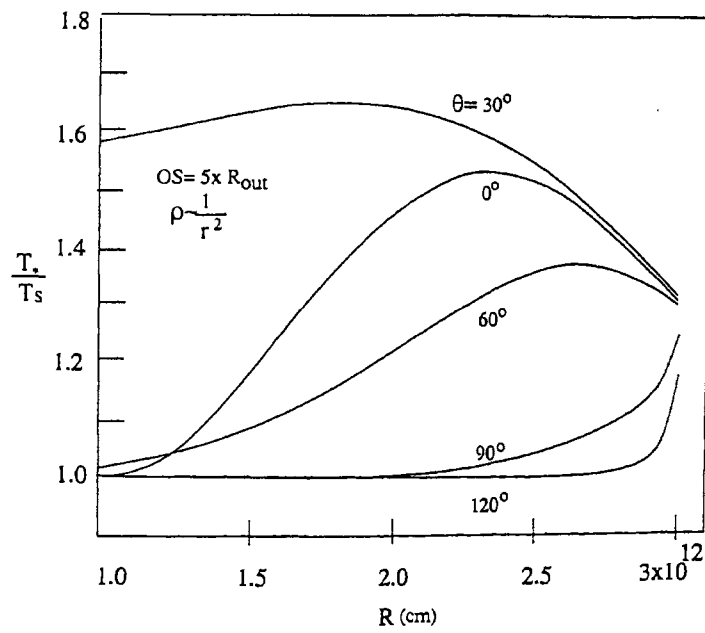


Figure 2.22: Same as figure 2.21, but the density variation is  $\frac{1}{r^2}$

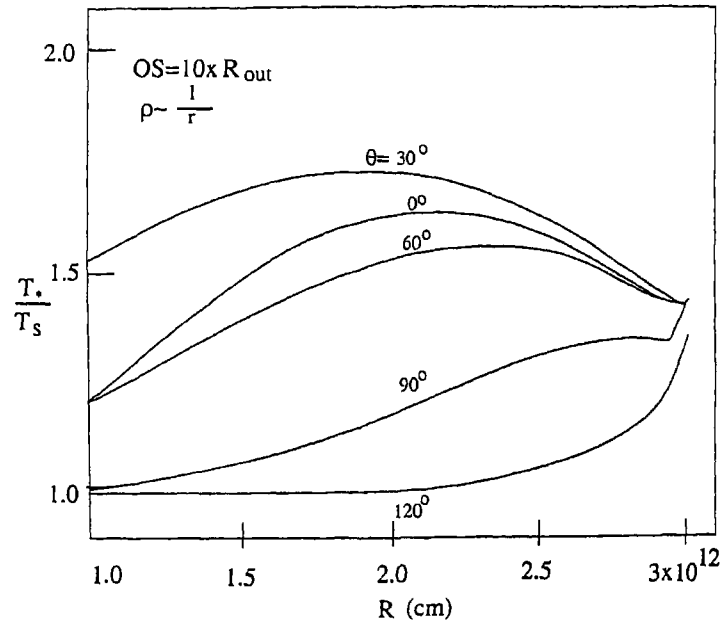


Figure 2.23: Same as figure 2.21, but  $OS = 10 \times R_{out}$

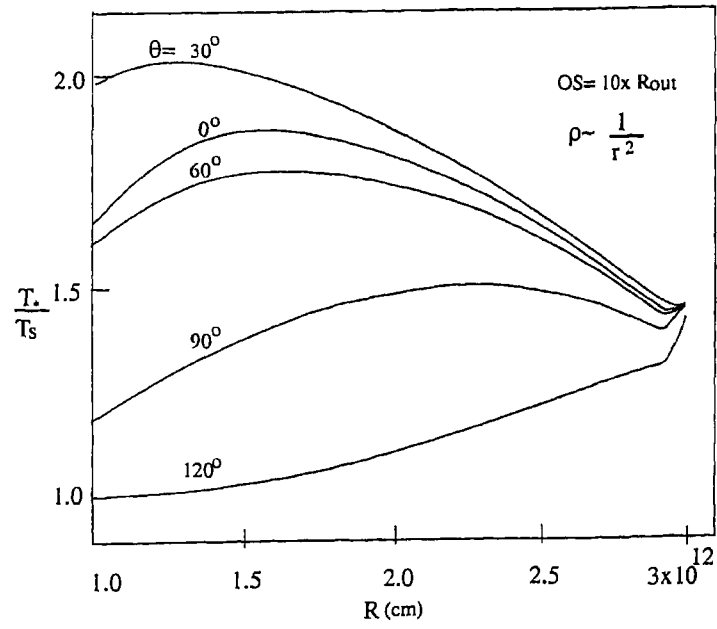


Figure 2.24: Same as figure 2.22, but but  $OS = 10 \times R_{out}$

## *Chapter 3*

### **Incident radiation from an extended source**

#### **3.1 Introduction**

In the previous chapter we have investigated the effect of reflection of radiation emitted by the secondary component on the atmosphere of the primary. We have assumed there that the incident radiation is emitted by a point source. The assumption of emission from a point source makes the calculations easy and is the first step to understand the effects of reflection. We have also seen how the limb darkening changes due to the presence of point source situated outside the primary component.

In treating the reflection effect theoretically, the irradiating component has been frequently assumed to be point source (e.g., Buerger 1969, Wilson and Devinney 1971, Kopal 1954, Kitamura 1954, Napier 1968, Wood 1971) in order to avoid the mathematical difficulty. However it is clear that assumptions of a point source for irradiating component are far from the reality. So one has to consider the finite size of the secondary component while considering the radiation from it. Now we will describe a method for estimating the reflected radiation from a primary component when we consider the secondary component is an extended surface.

### 3.2 Distribution of radiation incident from an extended source

The shapes of the components of the system are assumed to be spherical. The incident radiation is assumed to come from the spherical surface of the secondary. We divide the atmosphere of the primary into several spherical shells. In figure 3.1, we have given the geometrical description of the model. Let A and B are the centres of the two components separated by a distance AB. The atmosphere of the component with centre at A (which received radiation from the component whose centre is at B) is divided into several shells. We draw radii vectors which intersect these shell at points such as P. We wish to calculate the distribution of radiation field at such points of intersection. We see that the point P receives radiation emitted by the surface SW of the component whose centre is at B (the sector between tangents PS and PW from the point P to be circle B). We have to calculate the ray paths  $PT_1, P\tau, PT_2, P\tau, PT_3, \dots$  etc., so that we can calculate the source function at P due to the transfer of radiation along these ray paths. We assume that AP, AB and BS (= BW) are given.  $AT_1 = A\tau = \dots = AT_3$  are the radii of the component which are also assumed to be known. The quantities SE or WE are taken in discrete values to calculate the corresponding ray paths along  $P\tau$  etc., inside the atmosphere. The segment  $P\tau$  corresponding to SB is given by

$$P\tau = A\tau \frac{\nu}{\Delta}, \quad (3.1)$$

where

$$\begin{aligned} \nu &= \mu' + \mu\Delta', & \mu &= \frac{AP}{A\tau} \times \Delta, \\ \mu' &= (1 - \mu^2)^{\frac{1}{2}} & \Delta &= \alpha\beta\gamma + \alpha\beta'\gamma' + \alpha\beta\gamma' - \alpha'\beta'\gamma', \end{aligned}$$

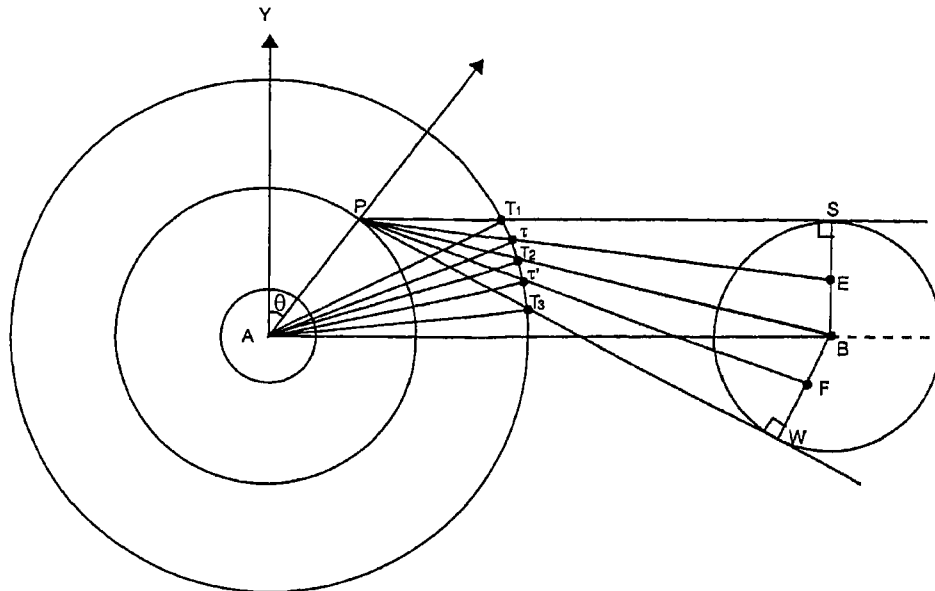


Figure 3.1: Schematic diagram showing the incident of radiation from an extended source.

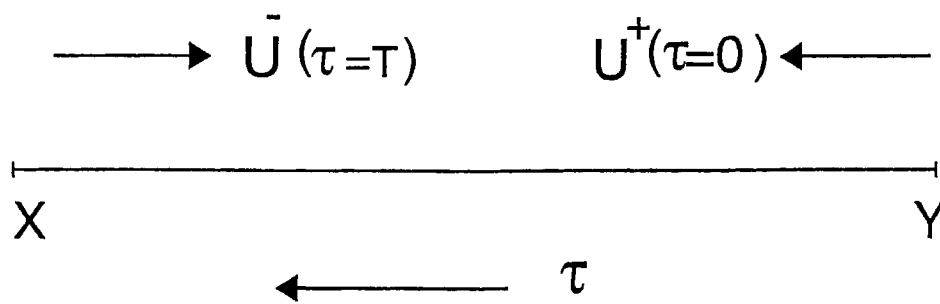


Figure 3.2: Schematic diagram showing the rod model.

$$\begin{aligned}
\Delta' &= (1 - \Delta^2)^{\frac{1}{2}} & \alpha &= \frac{BS}{PB}, & \alpha' &= (1 - \alpha^2)^{\frac{1}{2}}, \\
\beta &= \frac{AB}{PB} \cos \theta, & \beta' &= (1 - \beta^2)^{\frac{1}{2}}, \\
\gamma &= \frac{SE}{PE}, & \gamma' &= (1 - \gamma^2)^{\frac{1}{2}}, \\
PB &= (AP^2 + AB^2 - 2AP \times AB \sin \theta)^{\frac{1}{2}}, \\
PE &= (SE^2 + PS^2)^{\frac{1}{2}}.
\end{aligned} \tag{3.2}$$

Similarly, the segments  $P\tau'$  corresponding to BW is given by

$$P\tau' = A\tau' \frac{e}{c}, \tag{3.3}$$

where

$$\begin{aligned}
e &= cd' + c'd, & d &= \frac{AP}{A\tau'} c, \\
d' &= (1 - d^2)^{\frac{1}{2}}, & c &= \beta b' - \beta' b, \\
c' &= (1 - c^2)^{\frac{1}{2}}, & b &= \alpha a' - \alpha' a, \\
b' &= (1 - b^2)^{\frac{1}{2}}, & a &= \frac{WF}{PF}, \\
a' &= (1 - a^2)^{\frac{1}{2}}.
\end{aligned} \tag{3.4}$$

Now we shall calculate the specific intensities along the ray paths ( $P\tau, P\tau' \dots etc.$ ), and estimate the source functions at points such as P. This is done by using the rod model which has been described in *Chapter 2*. The source function at P in the rod model is given by (see Peraiah 1983b)

$$S_d(\tau) = S(\tau) + \omega(\tau)P(\tau)u_b(\tau), \tag{3.5}$$

where the second term on the right-hand side is due to the incident radiation and the first term is contribution to the source due to diffusely-scattered radiation field. The quantity  $S(\tau)$  is given by

$$S(\tau) = (1 - \omega)B(\tau) + \omega(\tau)P(\tau)u(\tau), \tag{3}$$

where  $\omega$  is the albedo for single scattering. Furthermore

$$P(\tau) = \begin{pmatrix} p & 1-p \\ 1-p & p \end{pmatrix}, B = \begin{pmatrix} B^+ \\ B^- \end{pmatrix} \quad (3.7)$$

$$S = \begin{pmatrix} S^+ \\ S^- \end{pmatrix}, u = \begin{pmatrix} u^+ \\ u^- \end{pmatrix}, \quad (3.8)$$

here  $u^+$  and  $u^-$  are the specific intensities in the two opposite directions along the segments  $P\tau$  etc.,  $B^+$  and  $B^-$  are the Planck functions and  $p$  is the probability that a photon is scattered in each of the two directions (for isotropic scattering, we set  $p = 0.5$ ); and

$$S^+ = [1 - \omega(\tau)]B^+(\tau) + \omega(\tau)[p(\tau)u^+(\tau) + \{1 - p(\tau)\}u^-(\tau)], \quad (3.9)$$

$$S^- = [1 - \omega(\tau)]B^-(\tau) + \omega(\tau)[p(\tau)u^-(\tau) + \{1 - p(\tau)\}u^+(\tau)], \quad (3.10)$$

with boundary conditions at  $\tau = 0$  at  $\tau = T$  (see the figure 3.2) these conditions are written as

$$u^+(0) = u_1,$$

and

$$u^-(T) = u_2.$$

The quantity  $u_b$  in equation (3.5) is given by

$$u_b(\tau) = \begin{pmatrix} u_1 e^{-\tau} \\ u_2 e^{(T-\tau)} \end{pmatrix}, \quad (3.11)$$

we shall specify the quantities  $u_1$  and  $u_2$  in advance. The components of the vector  $u_b(\tau)$  express the fact that the intensity at any point and in a given direction results from all the interior points reduced by  $e^{-\tau}$  of the incident radiation at  $\tau = 0$  and by  $e^{-(T-\tau)}$  of the incident radiation at  $\tau = T$ . In our model we give the incident radiation at the points  $T_1, \tau, T_2 \dots$  etc., and no incident radiation is given at the point P, therefore, we give the boundary conditions

$$u_2 = 0,$$

and

$$u_1 = I \cos \mu', \quad (3.12)$$

where  $I$  is the ratio of intensities corresponding to the two components with centres at B and A respectively (see figure 3.1) and  $\mu'$  is given in equations (3.2). The quantities  $u^+(\tau)$  and  $u^-(\tau)$  given in equation (3.9)&(3.10) are obtained by solving the equations of transfer for the rod given by,

$$\mathbf{M} \frac{d\mathbf{u}}{d\tau} + \mathbf{u} = \mathbf{S}, \quad (3.13)$$

where

$$\mathbf{M} = \begin{pmatrix} 1 & 0 \\ 0 & -1 \end{pmatrix}, \quad (3.14)$$

$$u^+(\tau) = u_1 \frac{1 + (\mathbf{T} - \tau)(1 - p)}{1 + \mathbf{T}(1 - p)}, \quad (3.15)$$

and

$$u^-(\tau) = u_1 \frac{(\mathbf{T} - \tau)(1 - p)}{1 + \mathbf{T}(1 - p)}, \quad (3.16)$$

where

$$\tau(x) = - \int_0^x N_0(X') \sigma dX', \quad (3.17)$$

and  $\mathbf{T}$  is the total optical depth;  $\sigma$  is the electron scattering coefficient and  $N_0(X')$  is the electron density at  $X'$  along the ray path. In our case, equations (3.15), (3.16) are reduced

$$u^+(\tau = \mathbf{T}) = u_1 \frac{1}{1 + \mathbf{T}(1 - p)}, \quad (3.18)$$

$$u^+(\tau = 0) = u_1 \frac{\mathbf{T}(1 - p)}{1 + \mathbf{T}(1 - p)}. \quad (3.19)$$

Using equations (3.9)-(3.19) we can calculate the source function  $S_d$  given in equation (3.5). The source function due to self radiation is calculated by solving the equations of radiative transfer in spherical symmetry which is solved using discrete space theory of radiative transfer described in

*Chapter 1* (the equations are 1.23 & 1.24). In this case the source function due to self radiation  $S_s$  is given by

$$S_s(r) = \frac{1}{2} \int_{+1}^{-1} I(r, \mu) d\mu. \quad (3.20)$$

So finally we obtain the total source function  $S_T$  by adding the source function due to irradiation to the self radiation. From equations (3.5) and (3.20), we have

$$S_T = S_d(r, \tau) + S_s(r), \quad (3.21)$$

with the help of source function  $S_T$  we can estimate the distribution of radiation field at the point P by using the relation (2.19) and (2.20) of *Chapter 2*.

### 3.2.1 Brief description of the method

The inner radius  $R_{in}$  of the component is taken to be equal to  $10^{12}$  cm, the atmosphere is taken to be three times the inner radius ( $R_{out} = 3 R_{in}$ ), and the separation of centres  $AB = 3 R_{out}$ . We have assumed a purely scattering medium with the electron density changing as  $r^{-2}$  in the atmosphere, and taking a value of  $10^{13} \text{cm}^{-3}$  at the inner radius  $R_{in}$ . The radius of the secondary component is taken to be the same as that of the primary (i.e  $R_{out}$ ). We have divided the atmosphere into 25 shells (or 26 shell boundaries).

### 3.2.2 Result and discussion

With the above data, the total radial optical depth will be nearly equal to 4. The optical depths along the segments such as PT etc., change considerably as the rays from the secondary surface are incident at different angles. The optical depth is calculated and is given against the shell numbers in figure 3.3. Figure 3.4 describes the total source functions  $S_T$  in

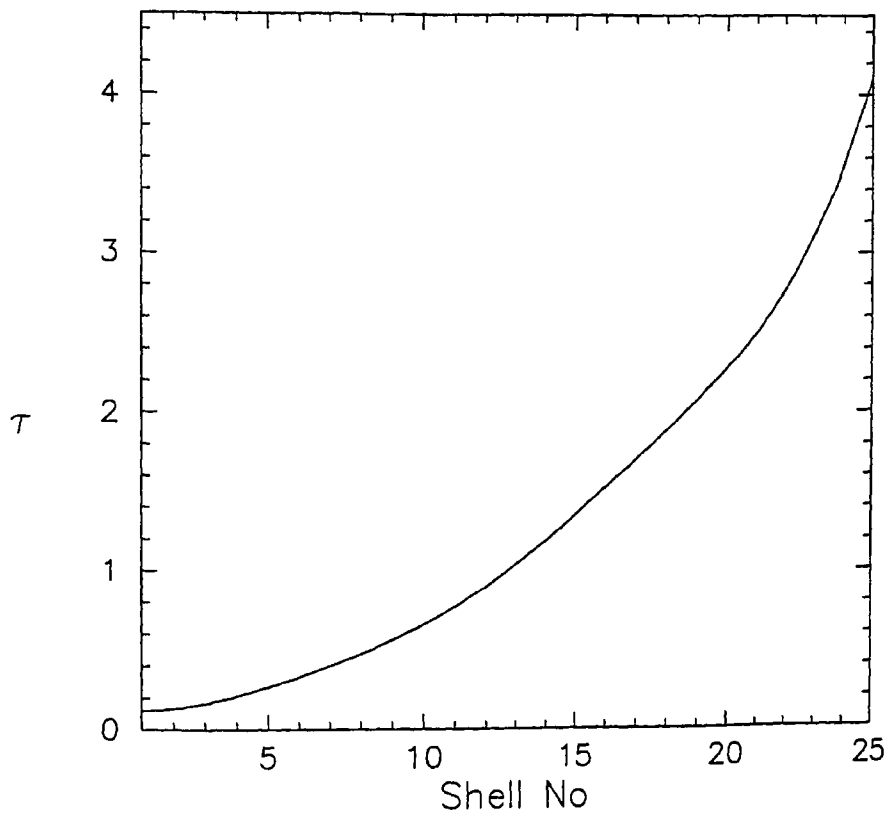


*Figure 3.3:* The run of the optical depth with the shell numbers

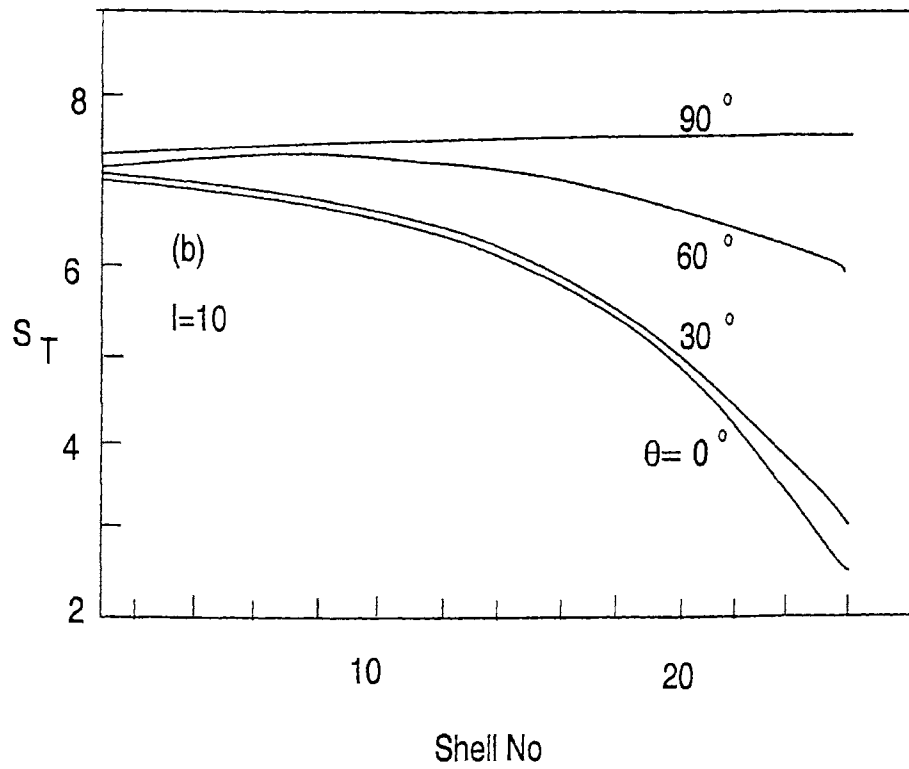
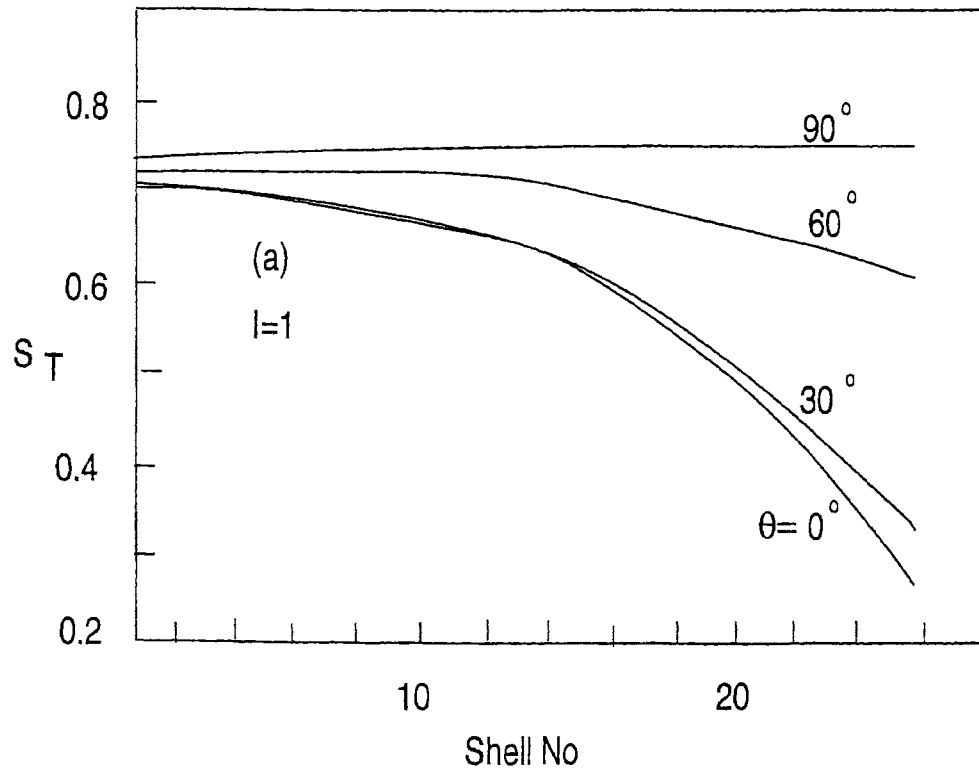


Figure 3.4: Total source function  $S_T$  versus Shell Number for  $\theta = 0^\circ, 30^\circ, 60^\circ$  and  $90^\circ$ , for (a)  $l=1$ , (b)  $l=10$ .

each shell. Shell number 1 starts at  $R_{\text{out}}$  and the boundary of the last shell coincides with the inner radius  $R_{\text{in}}$ . We have set  $\theta$  (colatitude) as a free parameter and calculated the radiation field at  $\theta = 0^\circ, 30^\circ, 60^\circ$  and  $90^\circ$ . In figure 3.4(a), we have shown the total source functions for  $I = 1$  where  $I$  is the ratio of radiations of two components. We notice that the source function is reduced only slightly and it is almost as much as the incident radiation. The reason for this is that the total source function is the sum of the contributions from the irradiation and self-radiation. If we have only self-radiation, then the source function will reduce considerably towards the outer layers of the atmosphere. But the radiation incident from the secondary component enhances the radiation field in the outer layers and raises the value of the source function. At  $\theta = 0^\circ$ , we notice that the source function is decreasing from  $n = 1$  to  $n = 26$ . This is expected as these source functions are along the axis AY (figure 3.1) which is perpendicular to AB. When  $\theta$  is increased gradually, the source functions increase slowly towards larger values of  $n$ . At  $\theta = 90^\circ$ , the source function increases towards higher values of  $n$ . This is because of the direct incidence of the radiation from the secondary component. In figure 3.4(b), we have plotted  $S_T$  with respect to the shell numbers for  $I = 10$ . Except for the fact that the magnitude is enhanced, the nature of variation of  $S_T$  is the same as for  $I=1$  for all angles. Figure 3.5 describe the angular distribution of radiation in  $-1 < \mu < 1$  where  $\mu$  is the cosine of the angle made by the ray with the radius vector at  $(r, \Psi)$  (see figure 2.3). In figure 3.5(a) the angular distribution of radiation at  $n = 1, 12$  and  $26$  are given for  $\theta = 0^\circ$ . The continuous lines represent the radiation due to the irradiation from the secondary while the broken lines represent the composite field due to self-radiation of the primary and ir-

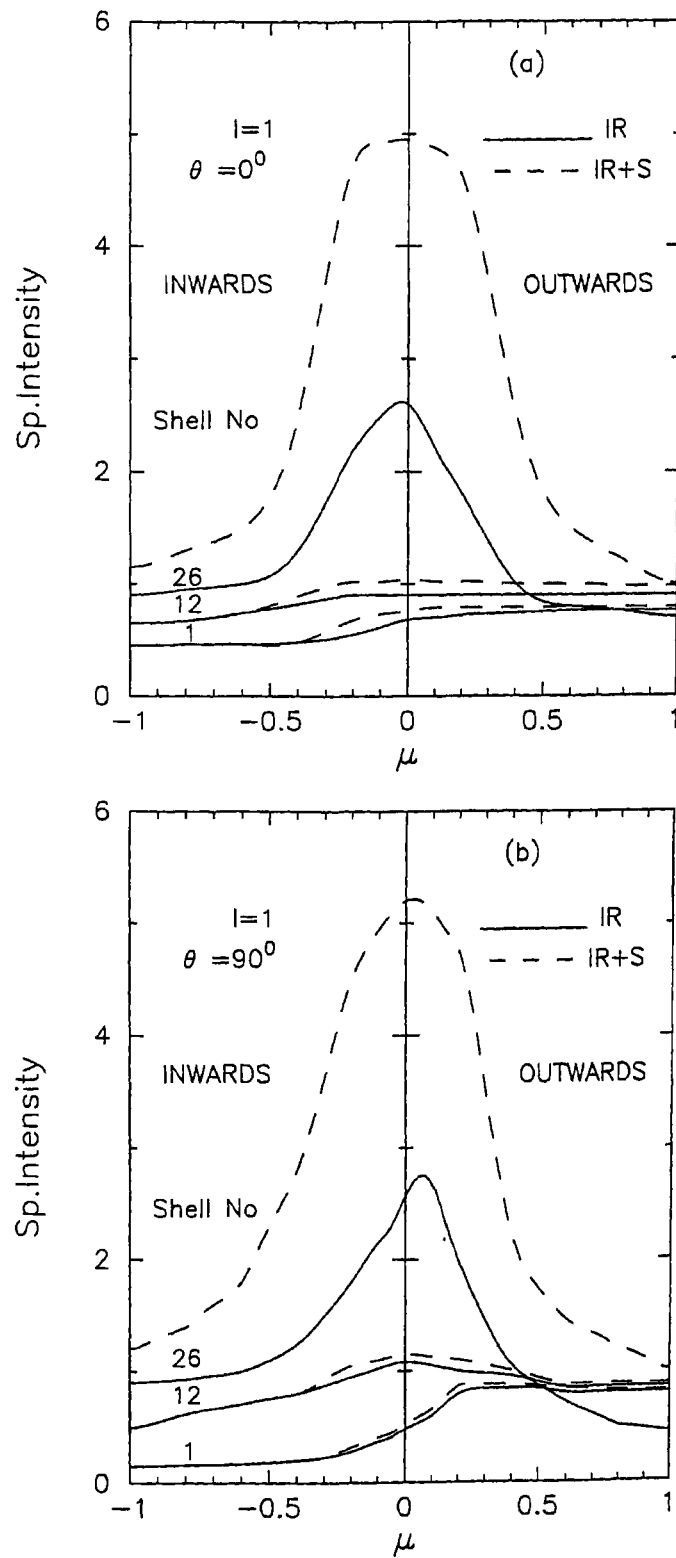


Figure 3.5: Angular distribution of the radiation field at  $I=1$  (a)  $\theta = 0^\circ$ , (b)  $\theta = 90^\circ$ .

radiation due to secondary component. We find that the differences in the fields due to irradiation and total radiation are different at different radial points. At the boundary of the shell number 25, the difference is large and this is due to the fact that the self-radiation is dominant and also that the reflected radiation is scattered much more here (because of higher number of electrons; it can be seen that the optical depth is larger at  $n = 25$ ) than at the boundary of the shell number 1. At  $n = 1$ , we have the intensities reduced considerably because of the fact that the flux in the self-radiation is reduced towards the surface of the atmosphere ( $n = 1$ ) and there are not sufficient number of electrons to scatter the radiation from the secondary component. In figure 3.5(b), we have shown the angular distribution at  $\theta = 90^\circ$ . We notice that the same physical characteristics are shown by the curves at both the angles. From  $n = 1$  to  $n = 25$  we see a gradual increase in the specific intensities of the reflected radiation in both the figures. The optical depth also increases in the same direction. This is because we assumed an increasing density distribution towards the surface of the star. Therefore, one can perhaps interpret the increase of the specific intensities on the basis that there are more electrons scattering the incident radiation as we approach the base of the atmosphere ( $n = 25$ ).

### **3.3 Distribution of emergent radiation along the line of sight when radiation is incident from an extended source**

It is customary to assume a law of limb darkening (Kitamura 1954; Kopal 1959; Peraiah 1970) which is based on blackbody considerations. It is necessary to actually calculate the distribution of radiation field and then



have considered a set of rays along the line of sight and tangential to the shell boundaries at the points where the axis  $OO'$  intersect them. We estimate the radiation field at points such as  $P$  where the parallel rays meet the shell boundaries. The radiation field at  $P$  is calculated by estimating the source function at  $P$  due to the radiation incident at  $P$  from the surface  $SW$  of the secondary facing the primary. We have selected a number of rays from  $SW$  incident on the atmosphere and entering the surface at points as  $T, \tau, \dots$  etc. We intend to calculate the ray paths  $PT, P\tau, \dots$  etc., and optical depths along the rays. The segments such as  $P\tau$  in  $T\widehat{P}T_1$  are given by the segment  $P\tau$  in  $SPO'$  is given as (see figure 3.6)

$$P\tau = OP \left[ A \frac{B'}{B} + A' \right]^{\frac{1}{2}},$$

where

$$\begin{aligned} B &= \frac{OP}{OT} A, & B' &= (1 - B^2)^{\frac{1}{2}}, \\ A &= \xi\eta' - \xi'\eta, & A' &= (1 - A^2)^{\frac{1}{2}}, \\ \eta &= \sin E = \frac{SE}{PE}, & \eta' &= \cos E, \\ \xi &= abc + a'b'c + a'bc' - ab'c', \\ \xi' &= (1 - \xi^2)^{1/2}. \end{aligned}$$

And

$$\begin{aligned} a &= \frac{OQ}{OP}, & a' &= (1 - a^2)^{\frac{1}{2}}, \\ b &= \frac{PS}{O'P}, & b' &= (1 - b^2)^{\frac{1}{2}}, \\ c &= \frac{PQ}{O'P}, & c' &= (1 - c^2)^{\frac{1}{2}}. \end{aligned}$$

Similarly the segments such as  $P\tau'$  in  $O'PW$  are given by,

$$P\tau' = OP \left[ \mu \left( \frac{s'}{s} \right) + \mu' \right],$$

where

$$\begin{aligned}\mu &= \nu' \Delta + \Delta' \nu, & \mu' &= (1 - \mu^2)^{\frac{1}{2}}, \\ s &= \frac{OP}{OT} \mu, & s' &= (1 - s^2)^{\frac{1}{2}}, \\ \nu &= \frac{WE'}{PE'}, & \nu' &= (1 - \nu^2)^{\frac{1}{2}}, \\ PE'^2 &= PW^2 + WE'^2, & \Delta &= \xi(1 - 2\delta^2) - 2\xi'\delta\delta', \\ \Delta' &= (1 - \Delta^2)^{\frac{1}{2}}, & \delta &= \frac{SO'}{PO'}, \delta' = (1 - \delta^2)^{\frac{1}{2}}.\end{aligned}$$

For a given density distribution, we can calculate the optical depth along the segments such as  $P\tau$  and  $P\tau'$ . Using these optical depths, the specific intensities and source functions at the point P due to irradiation from the secondary can be calculated. The boundary conditions and method of calculation as mentioned earlier. Now we solve the equation of radiative transfer in spherical symmetry and obtained the source function  $S_s$  due to self radiation. The optical depths are calculated according to  $\frac{1}{r^2}$  law of variation of electron density and assumed isotropic scattering by electrons. The total source function  $S_T$  is the sum of the source functions due to self radiation  $S_s$  and irradiation  $S_I$  is given by (see Peraiah & Srinivasa Rao 1983a)

$$S_T = S_s + S_I. \quad (3.22)$$

We calculate the radiation field at each shell boundary as shown in figure 3.6. Now we calculate the set of source function at the point of the intersection of the ray parallel to the line of sight and the shell boundary. These source functions are used to calculate the emergent specific intensities at infinity by using the formula

$$I_{n+1}(r) = I_0(n) \exp(-\tau) + \int_0^\tau S_T(t) \exp[-(\tau - t)] dt \quad (3.23)$$

where  $I_{n(r)}$  corresponds to the specific intensity of the ray passing between shell numbers  $n$  and  $n+1$  corresponding to perpendicular radial distance

$r$ , along the axis  $OO'$ .  $I_0(n)$  corresponds to the incident intensity at the boundary of the shell and  $\tau$  is the optical depth in the sector along the ray path. The source function  $S(t)$  is calculated by linear interpolation between  $S_T(n)$  and  $S_T(n+1)$ . The specific intensity at the boundary of each shell is calculated by using equation(3.23)

### 3.3.2 Results and discussion

In figure 3.6, we have given the schematic diagram of the model. We have divided the atmosphere into 25 shells. The line of sight is in the direction of PQ. We have calculated the source functions at the points where PQ meets the shell boundaries.

In figure 3.7 the source functions due to reflection are plotted. Shell number 1 has its inner boundary at the point Q in figure 3.6; the outer boundary of the shell number 25 coincides with that of the outer boundary of the atmosphere. We have assumed a  $\frac{1}{r^2}$  law of density variation, with a density of  $10^{13}\text{cm}^{-3}$  at Q. The total radial optical depth reaches a maximum of 4; along the line of sight it varies between 0 and 5 from outermost layer to the innermost layer at Q, depending upon the perpendicular distance of the ray path from O along the axis  $OO'$ . The source functions S at points of intersection of the axis  $OO'$  and shell boundaries are plotted in figure 3.7(a), the different values of I, the ratio of the radiations of the two components.

We notice that the source functions are almost linear and increase with the shell numbers, i.e., towards the secondary component from whose surface the primary is receiving the incident radiation. This can be understood easily on physical grounds. However, the increase is not as big as one expects because of the fact that the density falls as  $\frac{1}{r^2}$  towards

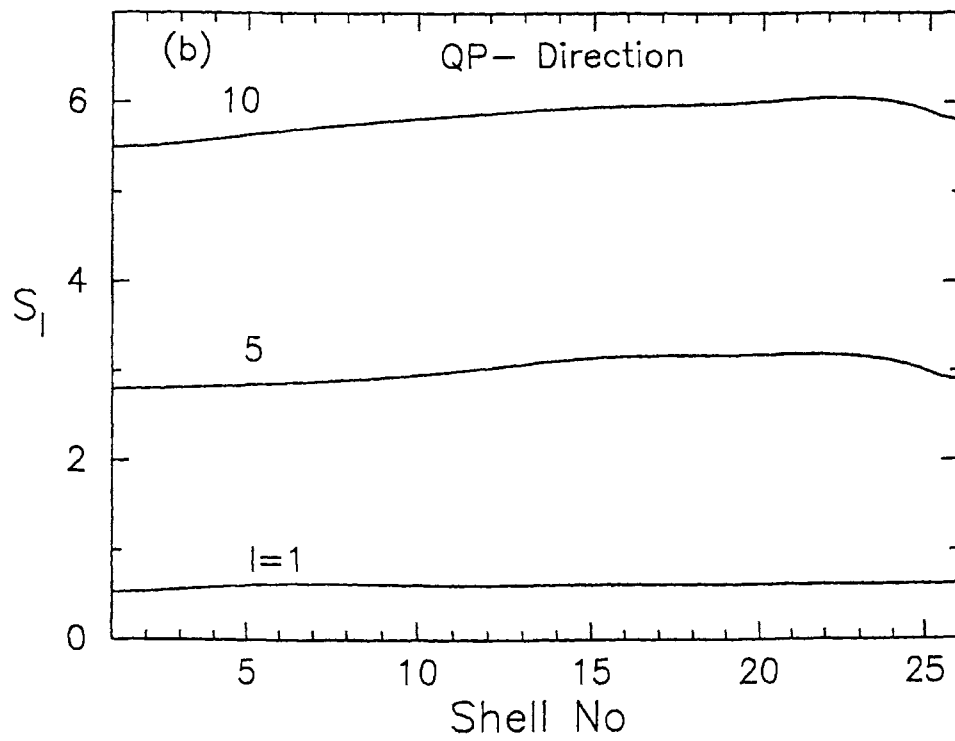
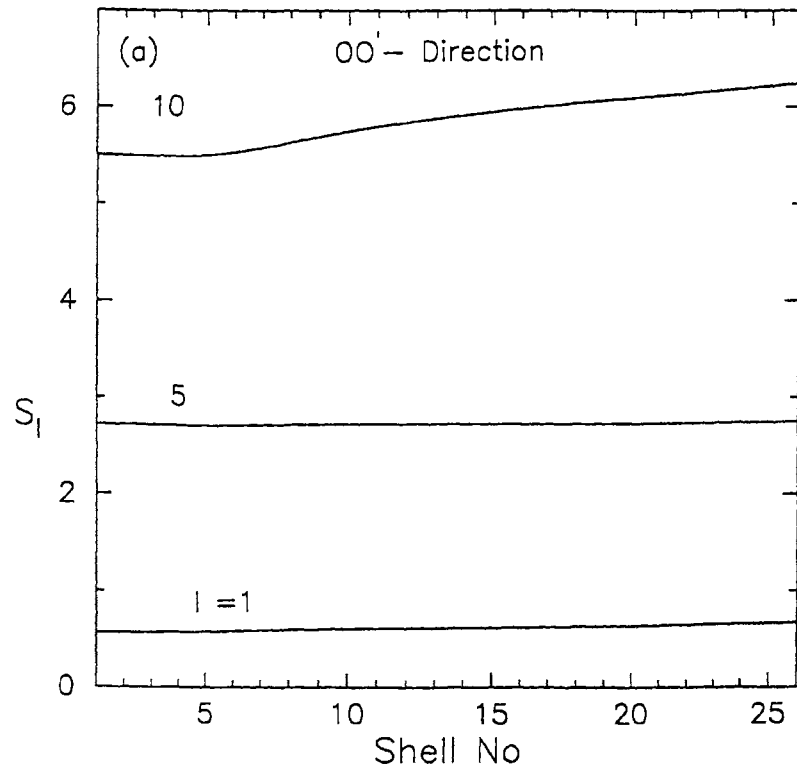


Figure 3.7: The source functions  $S_l$  due to reflection in (a) OO' direction (b)QP direction  $S_l$  is given in arbitrary units.

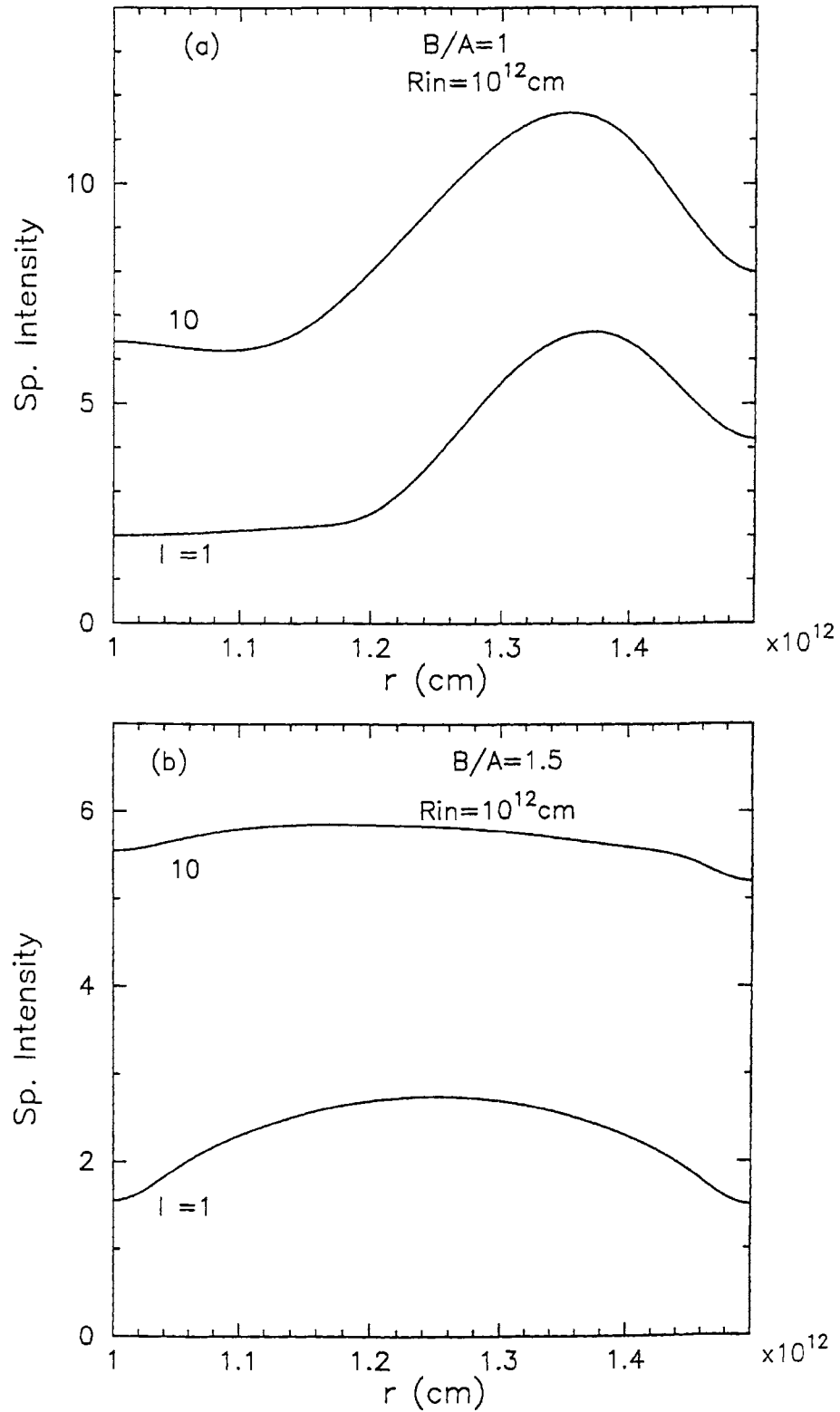


Figure 3.8: Variation of specific intensity from centre to limb is given in arbitrary units with (a) plane parallel geometry ( $\frac{B}{A} = 1$ ) and (b) spherical geometry ( $\frac{B}{A} = 1.5$ ) where  $B$  and  $A$  are outer and inner radii of the atmosphere ( $R_{in} = 10^{12}$  cm).

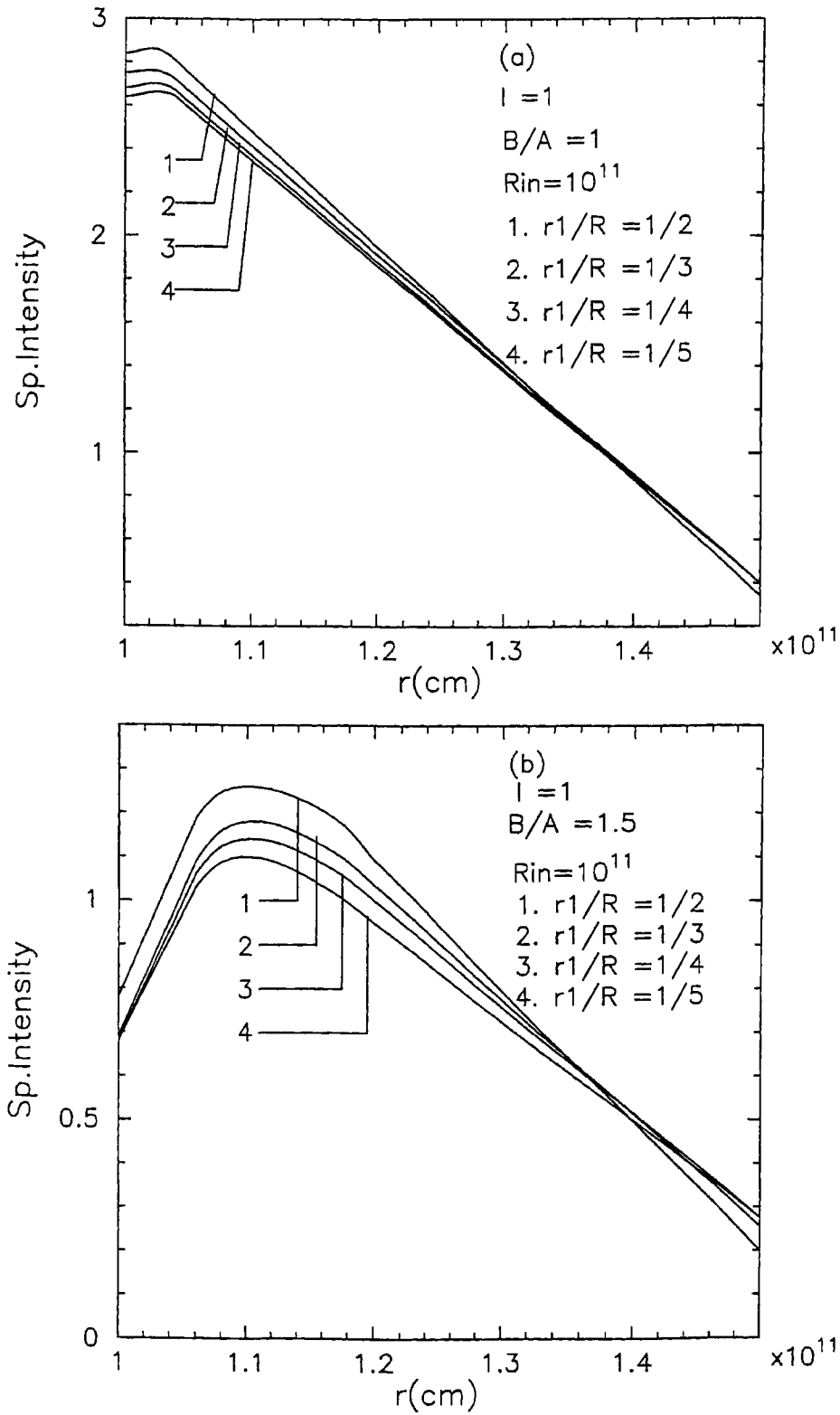


Figure 3.9: Variation of specific intensities from centre to limb in (a) plane parallel geometry and (b) spherical geometry, for  $l=1$  and  $R_{in} = 10^{11}$  cm. The results are given for different values of  $\frac{r_1}{R}$  where  $r_1$  is the outer radius of the star and  $R$  is separation between the centres of the two components.

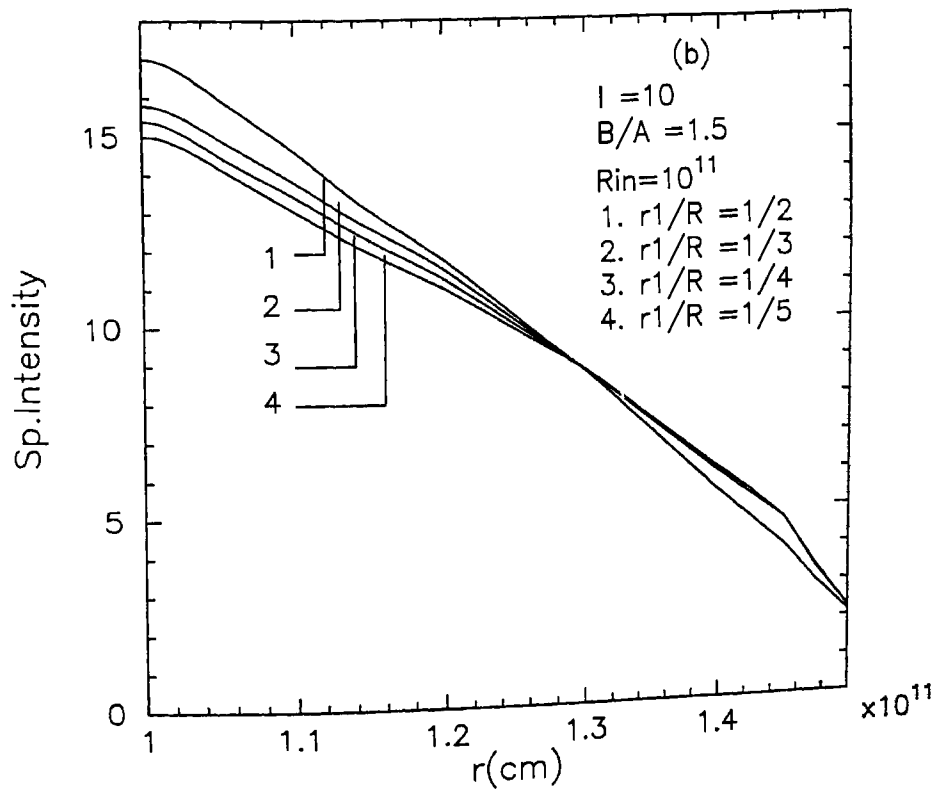
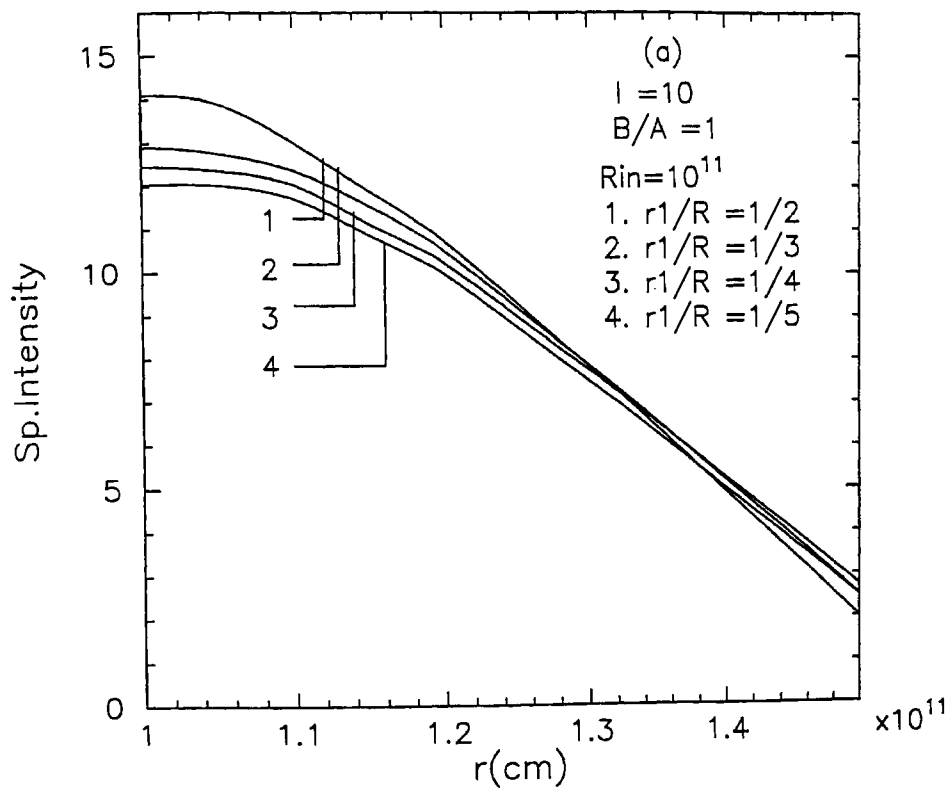


Figure 3.10: variation of specific intensities from centre to limb in (a) plane parallel geometry and (b) spherical geometry, for  $I=10$  and  $R_{in} = 10^{11}$  cm.

the outer layers of the atmospheres. The source functions  $S_I$  (due to incident radiation from the secondary component) along the line of sight QP (tangent to the star's surface) are plotted against the shell numbers in figure 3.7(b). The behavior of  $S_I$  here, is slightly different from that of figure 3.7(a). It increases slowly towards P and then starts falling. This can be understood on the basis that the incident radiation, on reaching points such as P which are away from the centre of the star, is weakened by the cosine factor.

In figure 3.8 we have plotted the source function due to irradiation. The specific intensity along the line of sight is given in figures 3.8-3.10. The results given in figure 3.8 (a) refer to those of plane-parallel and figure 3.8 (b) refer to spherically-symmetric approximations. This means that the source function  $S_s$  due to self radiation is calculated using the above two geometrical stratifications, while the source function  $S_I$  due to incident radiation remains the same in both the cases. The source function in plane-parallel approximation is obtained from the radiative transfer equation without the term,

$$\frac{1}{r} \frac{\partial}{\partial \mu} \left[ (1 - \mu^2) u(r, \mu) \right]. \quad (3.24)$$

We have calculated the optical depth in spherical and plane parallel approximations by assuming the same electron density distribution. We have considered an atmosphere whose thickness is one-half of the stellar radius in calculating the source function due to self radiation. The results given in figure 3.8(a) and figure 3.8(b) show different types of variations in the specific intensities from  $R_{in}$  to  $R_{out}$ . In plane-parallel stratification, the intensities remain constant until some point and then reach a maximum at  $r \sim 1.35 \times 10^{12}$  cm, from here onwards, the intensities decrease as one approaches the outer surface of the atmosphere. In

the case of spherical geometry, the intensities increase slightly and then decrease towards the outer surface. The law of variation of the intensities from centre to limb is different in the two approximations. Although the extension of the atmosphere is only one half of the stellar radius, the differences are quite large. Therefore, one must always use the assumption of spherical symmetry even when the atmosphere is small compared to the stellar radius. In figure 3.9, we have plotted the variation of specific intensities from centre to limb for  $R = 10^{11}$  cm,  $I = 1$ , for various values of  $\frac{r_1}{R}$ , where  $r_1$  is the outer radius of the star and  $R$  is the distance between the centres of the two stars. In plane-parallel approximation, the law of variation of specific intensities is almost linear and falls rapidly towards the surface, whereas in the case of spherical symmetry, the specific intensities reach a maximum and then fall. The results given in figure 3.10 show a trend similar to those given in figure 3.9. The law of limb darkening does not seem to depend much on the ratio  $\frac{r_1}{R}$ .

It is clear now that the law of variation of radiation from centre to limb depends considerably on whether one considers plane-parallel or spherically symmetric geometry and also on the distribution of electron density.

## *Chapter 4*

### **Effects of reflection on spectral lines**

#### **4.1 Introduction**

We have investigated so far how the irradiation from the secondary component changes the radiation field in the atmosphere of the primary. This has been done assuming a purely scattering atmosphere in a monochromatic radiation field. This helps in understanding of the observed total light that is emitted by the system. Napier & Ovenden (1970) tried to explain by means of reflection effect, the correlation between the velocity amplitudes of individual absorption lines and their wavelengths observed in 57Cygni. However they could not succeed in this, because of the fact that they did not use a detailed calculation of the radiation field modified by the incidence of the external radiation. There is another important observational aspect in close binaries that must be understood clearly—the changes in the equivalent widths of the lines between eclipses. The spectral lines in 12 Lacertae undergo a periodic variation in width, the lines become wide and diffuse at periastron and sharper and narrower at apastron (Young 1922). Several ideas are put forward for explaining this phenomenon but no satisfactory explanation was given. The fact that the lines become wide and diffuse at periastron point, indicates that mutually reflected radiation increases the flux in the lines because of the proximity of the two components. One needs to put considerable

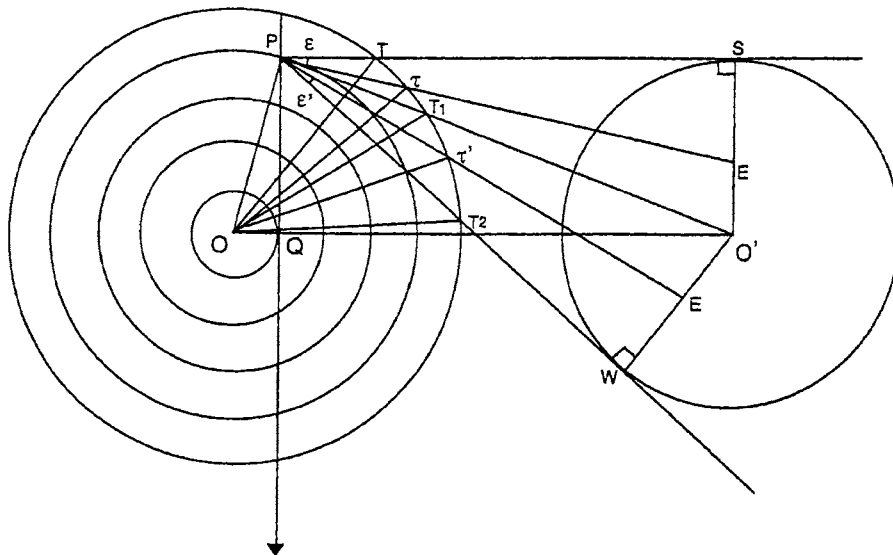


*Figure 4.1:* Schematic diagram of the binary components with incident radiation from the surface of the secondary.  $O$  and  $O'$  are the centres of gravity of the two components.

if one intends to explain the above mentioned complicated phenomena. However, we will begin to study the above phenomena by using simplified assumptions.

#### 4.1.1 Brief description of the method

We have assumed a spherical shape of the reflecting atmosphere to simplify the computational problems of radiative transfer. The geometry of the model is shown in figure 4.1

Let  $O$  and  $O'$  be the centres of the primary and the secondary respectively. The atmosphere of the primary is assumed to be spherical and divided into several discrete shells. We calculate the source functions of the radiation field emerging from the companion whose centre is at  $O'$  (see figure 4.1) and incident on the atmosphere of the component whose centre is at  $O$ . We consider the set of rays such as  $STP$ ,  $ET'P$ ,  $O'T_1P$ ,  $E'T'P$ ,  $WT_2P$  etc, emerging from the surface  $SW$  of the companion and meeting at a point  $P$  in the atmospheres of the component. These rays

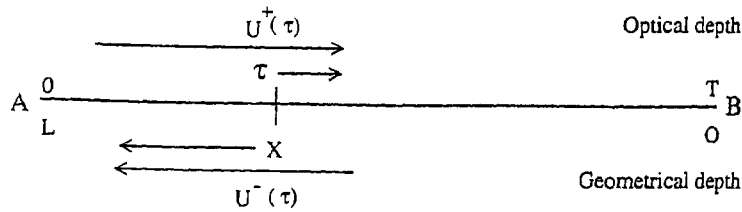


Figure 4.2: Schematic diagram of the rod model

lie within the quadrilateral such as  $PSO'W$  and enter the boundary of the atmosphere of the component at points  $T, \tau, T_1, \tau', T_2$  etc. The surfaces of the companion such as  $SW$  will be different for different points  $P$  in the atmosphere. The radiation field at  $P$  is estimated by calculating the source function whose contribution comes from self radiation of the primary and that due to the incident radiation from the surface  $SW$  of the secondary facing the primary. We need to estimate geometrical length of the ray segments such as  $P\tau, P\tau'$  etc, inside the atmosphere so that the transfer of radiation along these segments is estimated and its contribution to the source function at the point  $P$  due to the incident radiation at  $\tau, \tau'$  etc. The length of the segments such as  $P\tau$  in  $SPO'$  are given in the *Chapter 3* section (3.3.1). For a given density distribution we need to calculate the optical depth along the segments  $P\tau, P\tau', \dots$ , etc. The source function at points such as  $P$  due to the irradiation are calculated using the one-dimensional transfer. We will describe this procedure briefly below. We consider a segment  $AB$  (see figure 4.2) which has two rays oppositely directed to each other. The optical depth  $\tau$  is given by,

$$\tau = \tau(x) = - \int_L^x \sigma(x') dx' ; \quad \tau(0) = T, \quad (4.1)$$

where  $\sigma(x')$  is the extinction coefficient and  $T$  is the total optical depth. The optical depth is measured in the direction opposite to that of the geometrical segment. We assume a steady state, monochromatic condition with local source function  $B^+(\tau)$  in the direction of increasing  $\tau$  and  $B^-(\tau)$  in the reverse direction.  $U^+(\tau)$  and  $U^-(\tau)$  are the specific intensities in the  $\tau$  increasing and decreasing directions respectively. The two equations of transfer for  $U^+(\tau)$  and  $U^-(\tau)$  are

$$\frac{dU^+}{d\tau} + U^+ = S_1^+, \quad (4.2)$$

$$\frac{dU^-}{d\tau} + U^- = S_1^-, \quad (4.3)$$

where

$$S_1^+ = B^+(\tau) + \omega(\tau)[p(\tau)U^+(\tau) + (1 - p(\tau))U^-(\tau)], \quad (4.4)$$

$$S_1^- = B^-(\tau) + \omega(\tau)[(1 - p(\tau))U^+(\tau) + p(\tau)U^-(\tau)], \quad (4.5)$$

are the source functions and  $\omega(\tau)$  is the albedo for single scattering and the phase function  $p = \frac{1}{2}$ . The boundary conditions at  $\tau = 0$  and  $\tau = T$  are given by

$$U^+(\tau = 0) = U_1, \quad (4.6)$$

$$U^-(\tau = T) = U_2, \quad (4.7)$$

where  $U_1$  and  $U_2$  will be specified later. The total source function  $S_d$  at any point  $\tau$  is a combination of the scattered part of the local intensities  $U^\pm(\tau)$  in either directions and the diffuse radiation generated by the incident radiation at the boundaries  $\tau = 0$  and  $\tau = T$  (the quantities  $U_1$  and  $U_2$  in equation (4.6) and (4.7) respectively). This added to the local sources would give the total source function given by,

$$S_d^+(\tau) = S_1^+(\tau) + \omega(\tau)[p(\tau)U_1e^{-\tau} + (1 - p(\tau))U_2e^{-(T-\tau)}], \quad (4.8)$$

$$S_d^-(\tau) = S_1^-(\tau) + \omega(\tau)[(1 - p(\tau))U_1e^{-\tau} + p(\tau)U_2e^{-(T-\tau)}], \quad (4.9)$$

In this case, the boundary conditions are,

$$U^+(0) = U^-(T) = 0. \quad (4.10)$$

We can write the equations (4.2) and (4.3) as

$$\mathbf{M} \frac{d\mathbf{U}}{d\tau} + \mathbf{U} = \mathbf{S}_1, \quad (4.11)$$

where

$$\mathbf{M} = \begin{pmatrix} 1 & 0 \\ 0 & -1 \end{pmatrix}, \mathbf{U} = \begin{pmatrix} U^+ \\ U^- \end{pmatrix}, \mathbf{S}_1 = \begin{pmatrix} S_1^+ \\ S_1^- \end{pmatrix}, \quad (4.12)$$

and equation (4.4) and (4.5) and (4.8) and (4.9) will be written as,

$$S_1(\tau) = B(\tau) + \omega(\tau)P(\tau)U(\tau), \quad (4.13)$$

$$S_d(\tau) = S_1(\tau) + \omega(\tau)P(\tau)U_b(\tau), \quad (4.14)$$

where

$$\mathbf{B} = \begin{pmatrix} B^+ \\ B^- \end{pmatrix}, \mathbf{P} = \begin{pmatrix} p & 1-p \\ 1-p & p \end{pmatrix}. \quad (4.15)$$

$$\mathbf{U}_b(\tau) = \begin{pmatrix} U_1 e^{-\tau} \\ U_2 e^{-(T-\tau)} \end{pmatrix}. \quad (4.16)$$

The mathematical aspects of the solution of the equation (4.2) and (4.3) are discussed in Sobolev (1963) and Grant (1968). We shall merely quote the relevant results. As we are dealing with scattering along the ray and the medium has no sources, we can set  $B = 0$  and  $U_2 = 0$ . Then the intensities  $\tau$  are given by,

$$U^+(\tau) = U_1 e^{-k\tau} \frac{1 - r^2 e^{-2k(T-\tau)}}{1 - r^2 e^{-2k\tau}}, \quad (4.17)$$

$$U^-(\tau) = r U_1 \frac{e^{-k\tau} - e^{-k(2T-\tau)}}{1 - r^2 e^{-2k\tau}}, \quad (4.18)$$

where

$$k^2 = (1 - \omega)[1 + \omega(1 - 2p)], \quad (4.19)$$

and

$$r = \frac{k - 1 + \omega}{k + 1 - \omega}. \quad (4.20)$$

And the emergent intensities are

$$U^+(T) = U_1 \frac{e^{-kT}(1-r^2)}{1-r^2e^{-2kT}}, \quad (4.21)$$

$$U^-(0) = U_1 r \frac{1-e^{-2kT}}{1-r^2e^{-2kT}}. \quad (4.22)$$

If we represent the reflection and transmission coefficients by  $r(T)$  and  $t(T)$  respectively, then and

$$r(T) = r \frac{1-e^{-2kT}}{1-r^2e^{-2kT}}, \quad (4.23)$$

$$t(T) = \frac{(1-r^2)e^{-kT}}{1-r^2e^{-2kT}}. \quad (4.24)$$

We set  $p = \frac{1}{2}$  (for isotropic scattering) then

$$k = (1-\omega)^{\frac{1}{2}}, \quad r = \frac{1-k}{1+k}. \quad (4.25)$$

In the above treatment we assumed that  $\omega < 1$ . If  $\omega = 1$ , the case of pure scattering, the treatment will be different and we obtain, (for  $B = 0$  and  $U_2 = 0$ )

$$U = \frac{U_1}{1+T(1-p)} \left[ \begin{array}{c} 1 + (T-\tau)(1-p) \\ (T-\tau)(1-p) \end{array} \right]. \quad (4.26)$$

The reflection and transmission factors are

$$r(T) = \frac{T(1-p)}{1+T(1-p)} \rightarrow 1 \text{ as } T \rightarrow \infty, \quad (4.27)$$

$$t(T) = \frac{1}{1+T(1-p)} \rightarrow 0 \text{ as } T \rightarrow \infty, \quad (4.28)$$

so that

$$r(T) + t(T) = 1. \quad (4.29)$$

which express conservation of energy.

Using equations (4.17) and (4.18) one can calculate the source function at points such as P, due to the incident radiation from the secondary component.

## 4.2 Calculations of line profiles in a static medium

We assume a scattering medium and solve the transfer equation in the line given for incoming ray,

$$\begin{aligned} \mu \frac{\partial I(x, \mu, r)}{\partial r} + \frac{1 - \mu^2}{r} \frac{\partial I(x, \mu, r)}{\partial \mu} \\ = K_L(r) [\beta + \phi(x)] [S_s(x, r) - I(x, \mu, r)], \end{aligned} \quad (4.30)$$

for outgoing ray

$$\begin{aligned} -\mu \frac{\partial I(x, -\mu, r)}{\partial r} - \frac{1 - \mu^2}{r} \frac{\partial I(x, -\mu, r)}{\partial \mu} \\ = K_L(r) [\beta + \phi(x)] [S_s(x, r) - I(x, -\mu, r)] \end{aligned} \quad (4.31)$$

where  $I(x, \pm\mu, r)$  is the specific intensity of the ray making an angle  $\cos^{-1}\mu$  with the radius vector at the radial point  $r$ . The quantity  $x$  is the standardised frequency given by

$$x = \frac{(\nu - \nu_o)}{\Delta_s}, \quad (4.32)$$

where  $\Delta_s$  is a standard frequency interval.  $S_s(x, r)$  is the source function at  $r$  for the frequency  $x$ . We have considered Doppler profile for  $\phi(x)$ .  $K_L(r)$  is the absorption coefficient at the centre of the line per unit interval of  $\Delta_s$ .  $\beta$  is the ratio of the opacity per unit frequency interval in the continuum to that in the line per unit frequency interval. The procedure of solving the equations (4.30) and (4.31) is described in *Chapter 1* section (1.2.3). We set  $\beta$  equal to zero and the calculations have been done in a purely scattering medium due to electrons and used Thompson scattering coefficient in calculating the optical depth. We have assumed that the continuum radiation is supplied by the star. We specify the quantity  $I(\tau = T, \mu, x)$  where  $T$  is the maximum optical depth (measured from outside towards the centre of the star). The calculation of source function due to irradiation  $S_I$ , is described in section (4.1.1).

This means that we set the orbital plane of the binary system to be perpendicular to the line of sight. We compute the total source functions at points such as P where the rays intersect the boundaries. The total source functions  $S_T$  is given by (see Peraiah & Srinivasa Rao 1983b)

$$S_T = S_I + S_S. \quad (4.33)$$

The radius of primary is taken to be  $R_{\text{out}} = 10^{12}$ cm and the atmosphere is taken to be equal to half of the stellar radius. The primary and the secondary components are assumed to have equal radii. We have assumed an electron density of  $10^{13}$ cm $^{-3}$  at the innermost radius of the atmosphere and let it vary as  $\frac{1}{r^2}$ . The source function due to reflection changes considerably whether we go along OO' direction or QP direction. The quantity  $S_S$  is the same along the boundary of a given shell because of spherical symmetry although this will be different for different shells. We have plotted the total source function with respect to the shell number. We have also studied the effect of proximity of the secondary component to the primary in terms of the parameter  $\frac{r_1}{R}$  where  $r_1$  is the radius of the primary and  $R=OO'$  (see figure 4.1). Another quantity we have used is  $I$ , the ratio of the luminosities of the primary and the secondary.

#### 4.2.1 Result and discussion

The total source function  $S_T$  is plotted in figures 4.3 & 4.4. In figure 4.3(a)  $S_T$  is plotted corresponding to the shell numbers with  $I = 1$  and  $\frac{r_1}{R} = \frac{1}{2}, \frac{1}{3}, \frac{1}{4}, \frac{1}{5}$ . In all these figures, shell number 1 and 26 correspond to the innermost and outermost radii of the atmosphere respectively. The source functions have their maxima at shell number 1 and fall rapidly before they reach shell number 4 where they reach the minimum values and then start to increase slowly towards shell number 25. The increase is not as fast

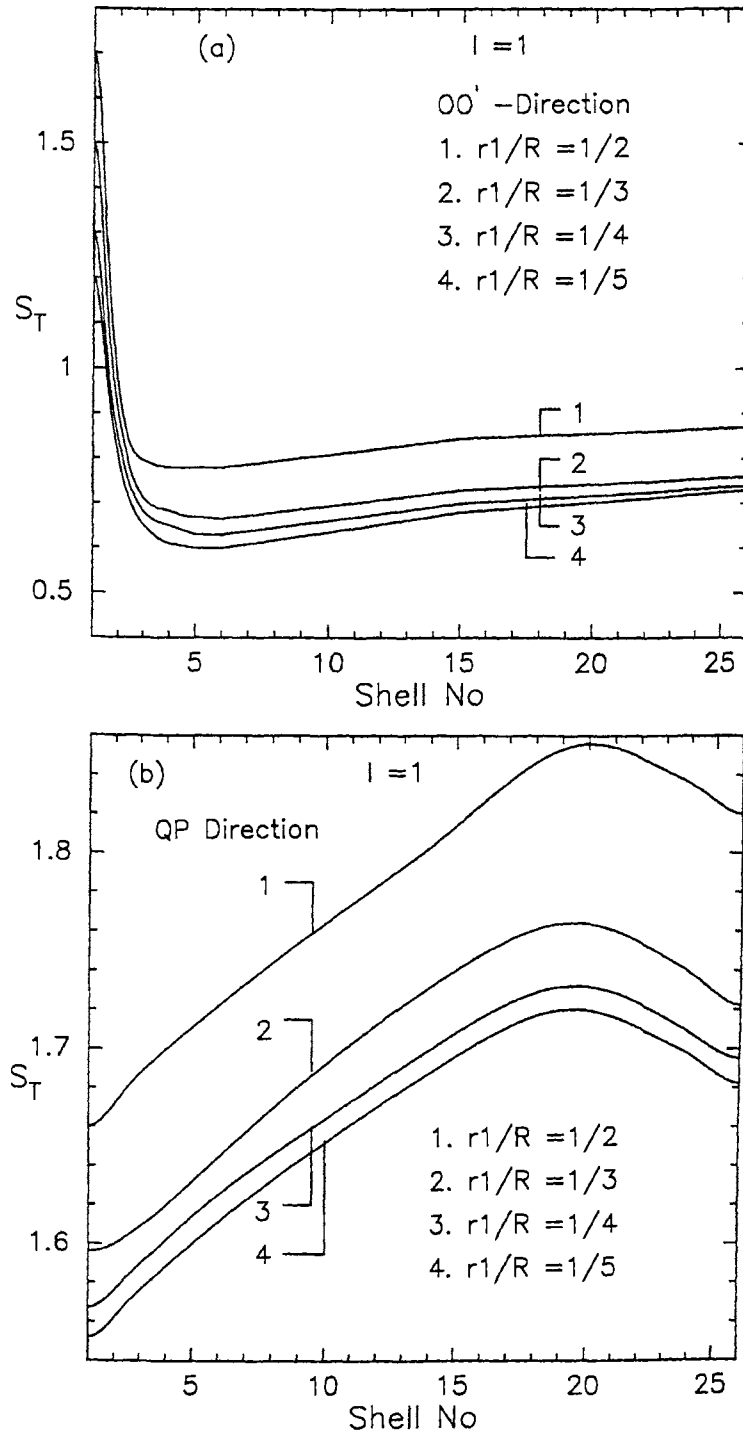


Figure 4.3: The total source function  $S_T$  corresponding to different shell numbers is plotted for  $I = 1$  (a)  $OO'$  direction (b) QP direction.  $S_T$  is given in arbitrary units.

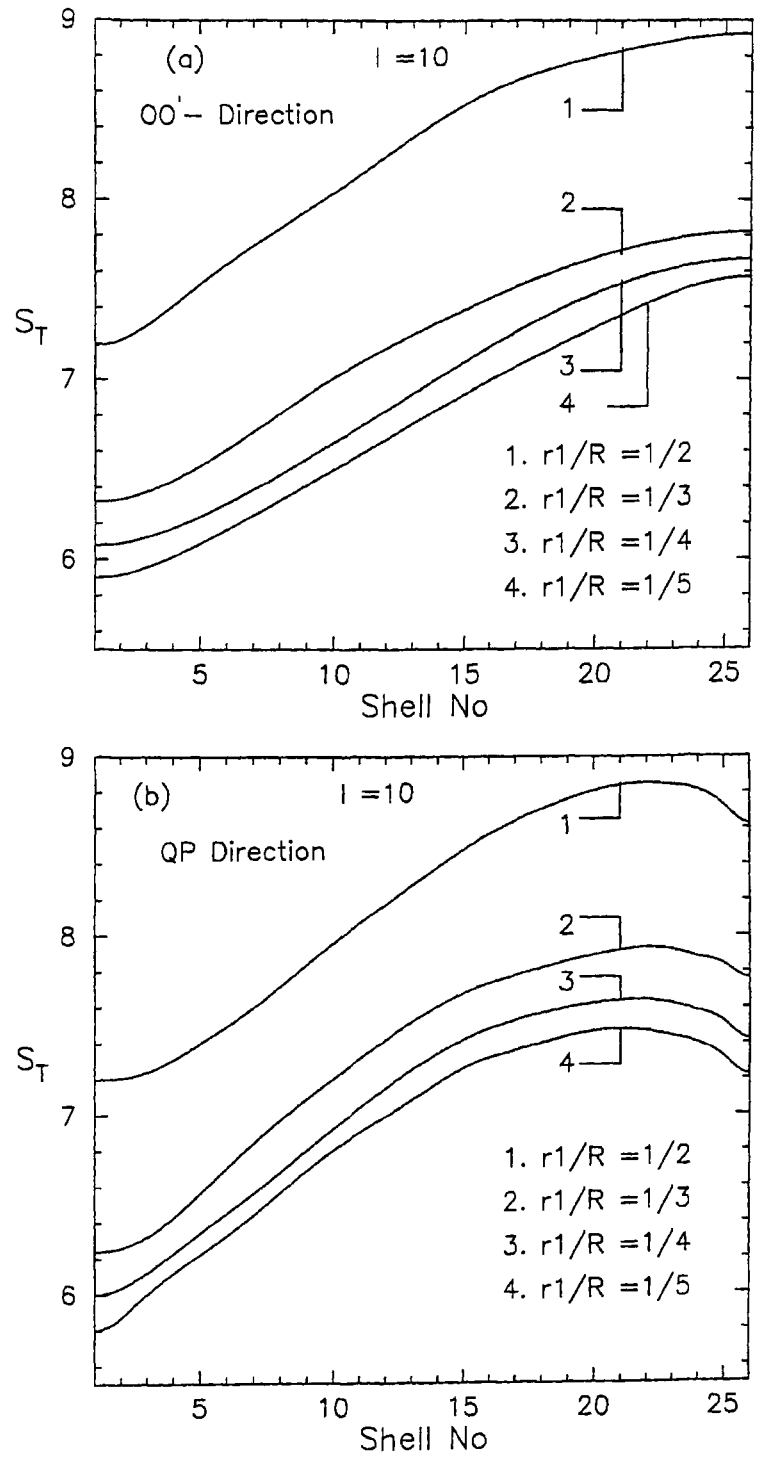


Figure 4.4: The total source function  $S_T$  corresponding to different shell numbers is plotted for  $I = 10$  (a) OO' direction (b) QP direction.  $S_T$  is given in arbitrary units.

as the fall at the innermost shells simply because the electron density falls as  $\frac{1}{r^2}$ ; as soon as the source function reaches a maximum value. the irradiation from the secondary takes over and the source function starts increasing. As the number density of electrons falls towards the outer radius, the amount of scattered radiation also falls. Therefore, the increase in the source function is not steep. The differences introduced into  $S_T$ , by the changes in the parameter  $\frac{r_1}{R}$  are not very large as can be seen from the figure. The curves corresponding to the last cases (i.e)  $\frac{r_1}{R} = \frac{1}{4}$  and  $\frac{1}{5}$  merge together. In figure 4.3(b) we have plotted  $S_T$  with respect to shell number along the line of sight i.e., along QP where OQ is the innermost radius of the atmosphere. The behavior of  $S_T$  along QP direction is completely different from  $S_T$  along OO' direction. The source functions start increasing from the inner shells and the increase is quite high until they reach maxima at about shell number 20 or 21. Then they start falling although quite slowly. This can be understood from the fact that the points such as P are easily reached by the rays as the density of the electrons in these parts falls as  $\frac{1}{r^2}$  and the radiation will not be attenuated as much as it would be along the axis OO'. The slight fall in  $S_T$  in the outermost shells is due to the fact that the incident beam itself is diluted by the  $\cos \theta$  factor where  $\theta$  is angle between the radius vector and the path of the ray.

In figure 4.4(a), we have plotted  $S_T$  along the axis OO' direction corresponding to an increased incident radiation  $I = 10$ . The results are quite different from those given in figure 4.3(a) for  $I = 1$ . The increased irradiation changes the variation of the source function the quantity  $S_T$  along OO' in this case keep on increasing although there is a gradual flattening towards the outer layers of the atmosphere. The source function along

QP direction with the increased irradiation (figure 4.4(b)) behaves very similar to that given in figure 4.3(b), but with the enhanced magnitude.

The flux profiles are plotted in figure 4.5 for  $I = 1, 5$  and  $10$ . We have considered a line with  $x = \pm 5$  Doppler units and employed a Doppler profile. When there is no irradiation, we obtain lines with deep cores. When irradiation is introduced the flux in the lines is increased considerably at all points in the line. But the increase in flux in the cores ( $F_C$ ) is considerably more than in the wings ( $F_W$ ). For example in figure 4.5(a) the ratio  $\frac{F_W}{F_C}$  is about 2.5 when there is no irradiation (the dotted curve). But in the presence of irradiation this ratio reduces to 1.3-1.4 depending on the proximity of the secondary. Because of irradiation, the flux in the whole line is dramatically increased disproportionately, the cores benefiting more than the wings. The same phenomenon occurs when the strength of the incident beam is increased as shown in figure 4.5(b) and 4.5(c).

The equivalent width has been calculated by using the formula

$$W = \int_{+\alpha}^{-\alpha} \left(1 - \frac{F_x}{F}\right) dx, \quad (4.34)$$

where  $F$  and  $F_x$  are the fluxes in the continuum and at frequency  $x$ .  $\alpha$  is the half band width of the line and is taken to be equal to 5 Doppler units. These equivalent widths are given in table 1.

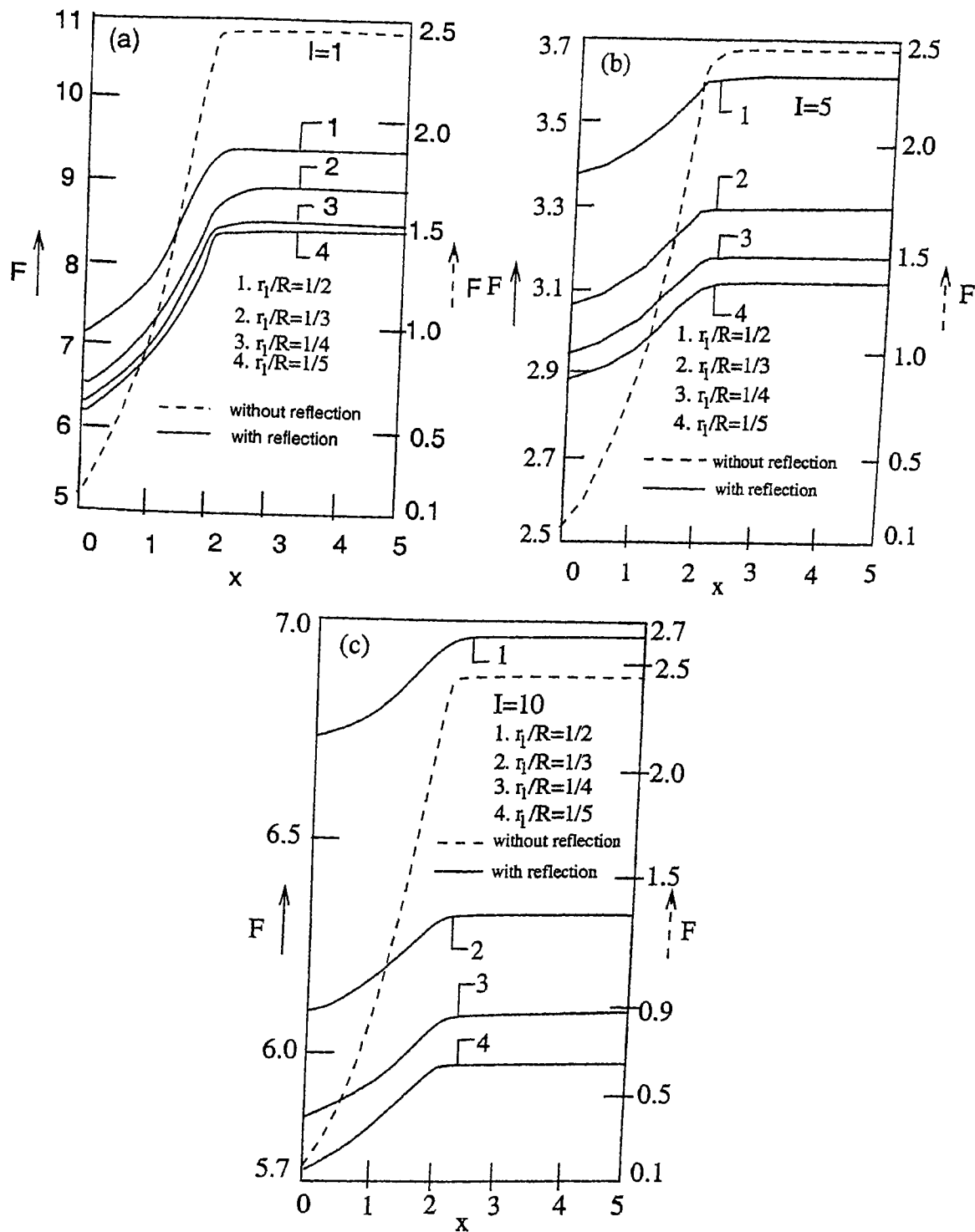


Figure 4.5: The flux profiles of lines are given in arbitrary units for (a)  $I=1$  (b)  $I=5$  (c)  $I=10$ . The dashed line represents the flux profile without irradiation and its ordinate scale is given on the right-hand side. The continuous lines represent the flux profiles with irradiation, whose scale is given on the left-hand side.

Table 1: The equivalent widths ( $W$ ) in Doppler units. Equivalent width without reflection is 2.34. Table shows how the enhanced irradiation reduces the equivalent widths below.

	$\frac{r_1}{R}$	$\frac{1}{2}$	$\frac{1}{3}$	$\frac{1}{4}$	$\frac{1}{5}$
I					
1		0.61	0.65	0.67	0.68
5		0.16	0.17	0.18	0.18
10		0.08	0.09	0.10	0.10

### 4.3 Theoretical line profiles formed in the irradiated expanding atmosphere of close binary components

Theoretical studies about the reflection effect using actual model atmospheres are important. All the three possible combinations (ie. like when primary and the secondary components are hot and hot, cool and cool, and hot and cool) are studied by Buerger (1969, 1972), Nordlund and Vaz (1990), Claret and Gemenz (1992) respectively. Vaz (1985) and Wilson (1990) reviewed several aspects of reflection effect. They found that irradiation from the secondary component will affect lines and as well as equivalent widths. They also found that theoretical bolometric albedos have been found to be in good agreement with observations. In previous section we studied the effects of reflection on formation of spectral lines in a purely scattering atmosphere and studied how the equivalent width change due to irradiation from the secondary. However these calculations were done in static atmospheres.

The purpose of this study is to compute spectral lines formed in the expanding atmospheres with light of the secondary falling on it. These atmospheres are distorted due to the combined effect of self rotation and

tidal effect due to the presence of the secondary component.

Since it is difficult to handle asymmetric atmospheres in the radiative transfer calculations, we restrict our calculations to spherical geometry in this problem. As the gases in the atmospheres of close binaries move with large velocities, the problem can be treated in the comoving frame only. The solution of the radiative transfer equation in the comoving frame is given in (Peraiah, 1980). The radiation in the atmosphere consists of (1) self radiation of the component and (2) the incident radiation from the atmosphere of the companion. We need to treat the combination of these two radiation fields for calculations of the line profiles.

Now we need to estimate the source function due to self radiation of the component. This can be done by solving the line transfer equation for a non-LTE two-level atom in the comoving frame in spherical symmetry. The method of obtaining the solution of radiative transfer equation in comoving frame was described in *Chapter 1* section (1.2.4). Here we have considered the equation of transfer when dust is not present in the atmosphere.

$$\begin{aligned} \mu \frac{\partial I(x, \mu, r)}{\partial r} + \frac{(1 - \mu^2)}{r} \frac{\partial I(x, \mu, r)}{\partial \mu} = & K(x, r)S_L(r) + \\ & K_c(r)S_c(r) - [K(x, r) + K_c(r)]I(x, \mu, r) \\ & + \left[ (1 - \mu^2) \frac{V(r)}{r} + \mu^2 \frac{dV(r)}{dr} \right] \frac{\partial I(x, \mu, r)}{\partial x}, \end{aligned} \quad (4.35)$$

and

$$\begin{aligned} -\mu \frac{\partial I(x, -\mu, r)}{\partial r} - \frac{(1 - \mu^2)}{r} \frac{\partial I(x, -\mu, r)}{\partial \mu} = & \\ & K(x, r)S_L(r) + K_c(r)S_c(r) - [K(x, r) + \\ & K_c(r)]I(x, -\mu, r) + \left[ (1 - \mu^2) \frac{V(r)}{r} \right. \\ & \left. + \mu^2 \frac{dV(r)}{dr} \right] \frac{\partial I(x, -\mu, r)}{\partial x}, \end{aligned} \quad (4.36)$$

where  $I(x, \pm\mu, r)$  is the specific intensity of the ray making an angle  $\cos^{-1} \mu$  [ $\mu \in (0, 1)$ ] with the radius vector at the radial point  $r$  with frequency  $x (= (\nu - \nu_0)/\Delta\nu_D$  where  $\nu_0$  and  $\nu$  are the frequency points at the line centre and at any point in the line and  $\Delta\nu_D$  is the standard frequency interval such as Doppler width),  $V(r)$  is the velocity of the gas at  $r$  in units of mean thermal units (mtu) and  $K(x, r)$  and  $K_c(r)$  are the absorption coefficients per unit frequency interval in the line and the continuum respectively. The quantities  $S_L$  and  $S_c$  are the line and continuum source functions given by,

$$S_L(r) = (1 - \epsilon) \int_{-\infty}^{+\infty} J(x, r) \phi(x) dx + \epsilon B(x, T_e(r)), \quad (4.37)$$

$$S_c(r) = \rho(r) B(x, T_e(r)), \quad (4.38)$$

$$K(x, r) = K_L(r) \phi(x), \quad (4.39)$$

where  $K_L(r)$  is the line-centre absorption coefficient and  $\phi(x)$  is the normalized line profile and  $\rho(r)$  is an arbitrary factor less than one and  $B(x, T_e(r))$  is the Planck function with frequency  $x$ , and temperature  $T_e$  at the radial point  $r$ .  $J(x, r)$  is the mean intensity given by,

$$J(x, r) = \frac{1}{2} \int_{-1}^{+1} I(x, \mu) d\mu. \quad (4.40)$$

The quantity  $\epsilon$  is the probability per scattering that a photon is thermalised by collisional de-excitation of the excited states, and this is given by,

$$\epsilon = C_{21} \left[ C_{21} + A_{21} [1 - \exp(-h\nu_0/kT)] \right]^{-1}, \quad (4.41)$$

where  $C_{21}$  is the collisional transition rate from level 2 to 1 and  $A_{21}$  is the Einstein spontaneous emission probability for transition from level 2 to 1. The quantities  $h$  and  $k$  are the Planck function and Boltzmann constant respectively. From equations (4.35) to (4.40), we obtain the

source function due to self radiation, given by

$$S_s(x, r) = \frac{\phi(x)}{\beta + \phi(x)} S_L(r) + \frac{\beta}{\beta + \phi(x)} S_c(r). \quad (4.42)$$

where  $\beta$  is the ratio of absorption coefficient in the continuum and line centre. Finally we calculate the total source function by adding  $S_d(\tau)$  in equation (4.14) and  $S_s(x, r)$  in equation (4.42) and obtain (see Peraiah & Srinivasa Rao 1998),

$$S = S_s + S_d. \quad (4.43)$$

We calculate the set of source functions at the points of intersection of the ray parallel to the line of sight and the shell boundaries. These source functions are used to calculate the emergent specific intensities at infinity ( or at the observer's point), by using the formula (see Peraiah and Srinivasa Rao, 1983a)

$$I_{n+1}(r) = I_0(n)e^{-\tau} + \int_0^{\tau} S(t)e^{-[\tau-t]} dt, \quad (4.44)$$

where  $I_n(r)$  corresponds to the specific intensity of the ray passing between shell numbers  $n$  and  $n+1$  and corresponding to perpendicular to the axis  $OO'$  at different radii.  $I_0(n)$  corresponds to the incident intensity at the boundary of the shell and  $\tau$  is the optical depth in the sector along the ray path. The source function  $S(t)$  is calculated by linear interpolation between  $S(t_n)$  and  $S(t_{n+1})$ . The specific intensity at the boundary of each shell is calculated by using equation(4.44).

The atmosphere in question is divided into  $n$  shells (see figure 4.1) where  $n = 1$  corresponds  $\tau = T$  and  $n = 100$  corresponding to  $\tau = 0$ , and  $\tau$  is the optical depth at any point and  $T$  is the total optical depth. The total optical depth is set in advance. The incident radiation at  $Q$ , the bottom of the atmosphere, (see figure 4.5) is given as

$$I_s(\tau = T, \mu_j) = 1. \quad (4.45)$$

The incident radiation from the secondary is given in terms of  $I_s$  in the ratio  $I$ , where  $I$  is given by

$$I = \frac{U_1}{I_s}. \quad (4.46)$$

The velocities of expansion of the gas are expressed in terms of mean thermal units  $V_T$  (mtu) given by,

$$V_T = \left[ \frac{2kT}{m_i} \right]^{\frac{1}{2}}, \quad (4.47)$$

where  $k$  is the Boltzmann constant and  $T$  is the temperature and  $m_i$  is the mass of the ion. The velocity at  $n = 1$  or  $\tau = T$  is  $V_A$  and  $V_B$  is the velocity at  $n = 100$  or  $\tau = 0$ . They are given in terms of mtu or  $V_T$  as

$$V_A = \frac{v_A}{V_T}, \quad (4.48)$$

$$V_B = \frac{v_B}{V_T}, \quad (4.49)$$

where  $v_A$  and  $v_B$  are the velocities at the inner radius A, outer radius B at radial point  $r$  respectively in units of mtu of gas. We assume uniform expansion of the gases for the sake of simplicity. The proximity of the component is measured in terms of separation parameter  $\frac{r_1}{R}$ , where  $r_1$  is the radius of the primary and  $R$  is the separation of centres of gravity of the two components. The ratio of the outer to the inner radii  $\frac{B}{A}$  of the atmosphere is always taken to be 2. The actual thickness in the components could be much larger than what we have considered here. As the number of parameters is large, we restricted our calculations to this modest thickness of the atmosphere.

The variation of the source functions are shown against the shell numbers ( $n = 1$  to 100) for different parameters. The line profile fluxes ( $F_Q/F_c$ ) (where  $F_Q$  and  $F_c$  being the integrated fluxes at frequency  $x_Q$  and in the continuum respectively) are plotted against the normalized

frequency  $Q$ , where

$$Q = x_Q/x_{max}, \quad (4.50)$$

$$F_Q = F(x_Q), \quad (4.51)$$

$$F_C = F(x_{max}), \quad (4.52)$$

and

$$x = (\nu - \nu_0)/\Delta\nu_D, \quad (4.53)$$

$$x_{max} = |x| + V_B, \quad (4.54)$$

$$\Delta\nu_D = \nu_0 \frac{v_T}{C}, \quad (4.55)$$

$x$  lies between  $\pm 5$  units. The equivalent widths are calculated by the relation,

$$EQ.W = \int_{x_{min}}^{x_{max}} (1 - F_Q/F_C) dx, \quad (4.56)$$

where

$$x_{min} = -(|x| + V_B). \quad (4.57)$$

### 4.3.1 Results and discussion

The equations of line transfer [equations (4.35) and (4.36)] are solved following the procedure described in *Chapter 1* section (1.2.4). The optical depths along these segments  $P\tau$ ,  $P\tau'$  are calculated using the equation (4.1). We set  $\sigma$  the electron scattering coefficient equal to (Thomson cross section)  $6.6525 \times 10^{-25} \text{cm}^2$ . The lengths of the segments change between 0 and  $2r$  where  $r$  is the radius of the component. We have set an electron density of  $10^{14} \text{cm}^{-3}$ . The maximum optical depth is 97.5 while optical depth of the segment along the x-axis  $OO'$  is 66.525 where the radius of the star is taken to be  $10^{12} \text{cm}$  and the thickness of the atmosphere as  $10^{12} \text{cm}$ . The parameters that are used in the calculations are listed below;

$\frac{B}{A}$  = Ratio of the outer to the inner radii of the atmosphere of the primary component and whose reflection effect is being studied (=2),

$n$  = number of shells into which the atmosphere of the component is divided,

$\frac{r_1}{R}$  = ratio of the radius of the component to that of the line joining the centres of gravity of the two components  $r_1 = 2 \times 10^{12}$  cm,

$V_A$  = initial velocity of expansion in units of mtu at  $n = 1$  (see equation 4.47 and 4.48),

$V_B$  = final velocity in units of mtu at  $n = 100$  (see equation 4.49),

$S$  = total source function (see equation (4.43)),

$S_S$  = source function due to self radiation (see equation (4.42)),

$I$  = ratio of incident radiation to that of self radiation of the star (see equation (4.46)),

$\epsilon$  = probability per scatter that a photon is thermalised by collisional de-excitation (see equation (4.41)),

$\beta$  = ratio of absorption coefficient in continuum to that in the line,

$T$  = total optical depth,

$Q = x/x_{max}$  (see equation (4.50)),

$\frac{F_Q}{F_c}$  = ratio of the line flux at the normalized frequency  $Q$  to that in the continuum or at  $x_{max}$  (see equations (4.51) and (4.52)),

$(R; N.R)$  = with reflection and with no reflection,

$\frac{H_e}{H_a}$  = height of the emission to the depth of absorption in the line,

$T_e$  = temperature in the atmosphere.

Results are presented in figures 4.6, 4.7, and 4.8 for different parameters. The figures are self explanatory as far as the parameters are concerned. The atmosphere of the primary whose centre is at O is divided into 100 shells( see figure 4.1). The separation of the components as  $\frac{r_1}{R}$

where  $r_1$  is the radius of the primary and  $R(= OO')$  is the separation of the centres of gravity of the components. We have considered two cases of separation  $\frac{r_1}{R} = \frac{1}{2}$  and  $\frac{1}{5}$  and the atmospheric extension is set to equal to stellar radius or  $\frac{B}{A} = 2$ . The total radial optical depth  $T$  is taken to be  $10^3$ ,  $10^4$  and  $10^5$ . The velocities of expansion are measured in terms of mean thermal units and uniform expansion velocity law is assumed. If  $V_A$  and  $V_B$  are the velocities at A and B respectively, then the velocity at any shell boundary  $V_n = \left[ V_A + \frac{V_B - V_A}{N} \times n \right]$  where  $N$  is the total number of layers which the atmosphere of the star is divided ( $=100$ ). At A ( $\tau = \tau_{max} = T$ ) the velocity is  $V_A$  and at B ( $\tau = 0$ ) the velocity is  $V_B$ . The parameters  $\epsilon$  which is defined in equation (4.41) is the probability that a photon is destroyed by collisional de-excitation and it is  $< 1$  for non-LTE line formation and this is set equal to 0 and  $10^{-4}$ . The quantity  $\beta$  is set to 0 and  $10^{-4}$  in our calculations.

Figure 4.6(a) gives the source functions  $S_S$  and  $S$  given in equations (4.42) and (4.43) for various parameters shown in the figure, across the atmosphere from  $n = 1$  to  $n = 100$ . These results represent a static and scattering medium with  $V_A = V_B = 0$  and  $\epsilon = \beta = 0$  and the incidence radiation factor  $I = 1$  (see equation (4.46)). The incident radiation at A is given according to equation (4.45). The source function  $S_s$  (which does not contain the reflected radiation) decreases slowly from the point  $\tau = T$  to the point  $\tau = 0$  in the scattering medium with  $T = 10^4$ . When the reflected radiation is included, the source functions for  $\frac{r_1}{R} = \frac{1}{2}$  and  $\frac{1}{5}$  are considerably enhanced as these source functions include the incident radiation from the companion along the axis  $OO'$ . Figure 4.6(b) gives the line profile in the direction of the line of sight, corresponding to the source functions given in figure 4.6(a). The line fluxes are plotted against the

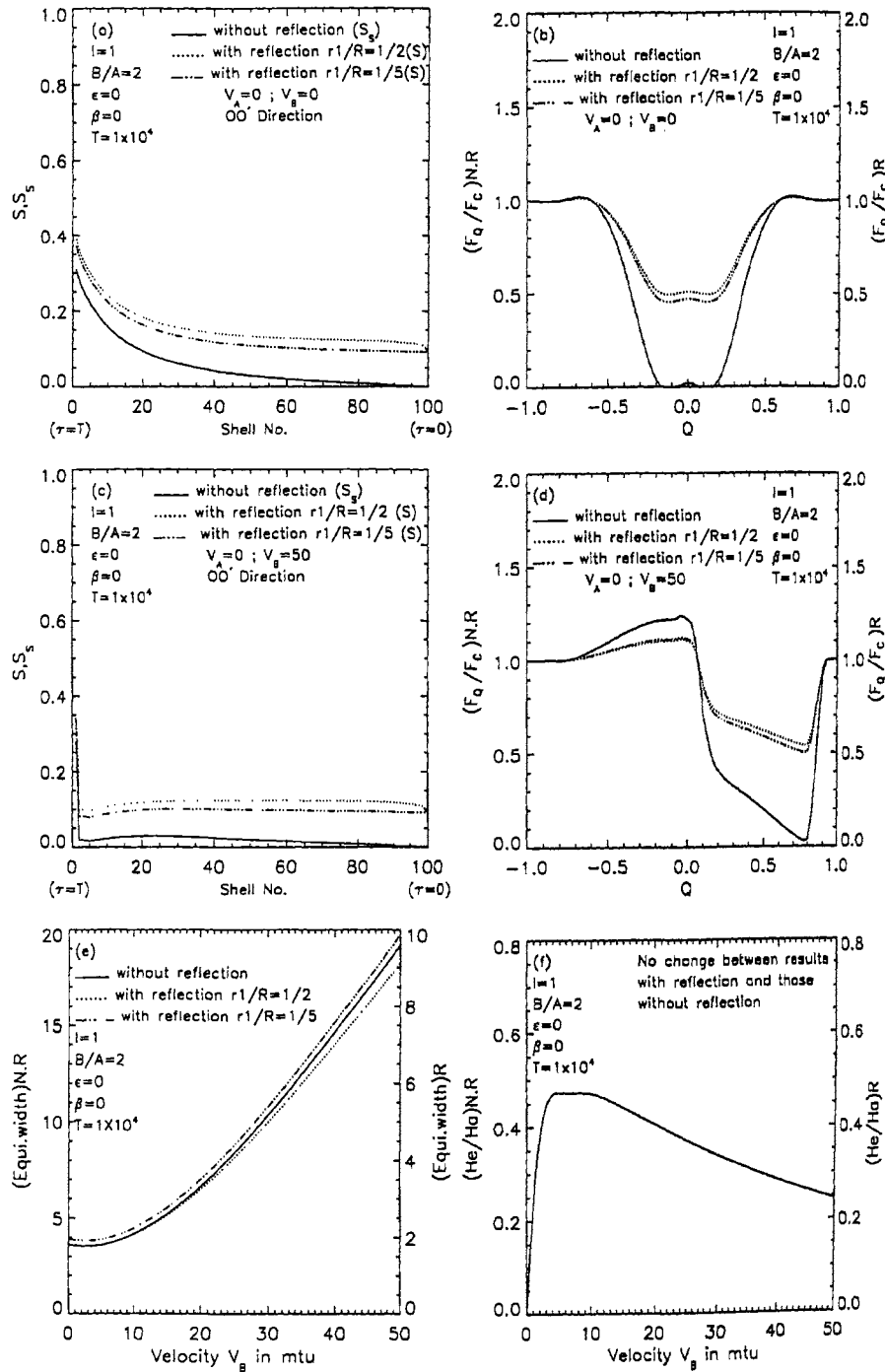


Figure 4.6: In a scattering medium (a) The source functions  $S$  and  $S_s$  are shown with respect to the shell numbers. (b): Line profiles with reflection and without reflection from the secondary components for a static case with total optical depth  $T = 10^4$ . (c) Same as figure (a) but with  $V_B = 50$ . (d) Same as figure (b) but with  $V_B = 50$ . (e) Equivalent widths of the lines are plotted against the expansion velocity  $V_B$ . (f) The ratios of the height of the emission to the depth of the absorption in the lines for both the case of reflected radiation and non reflected radiation are shown against the velocity of expansion  $V_B$ .

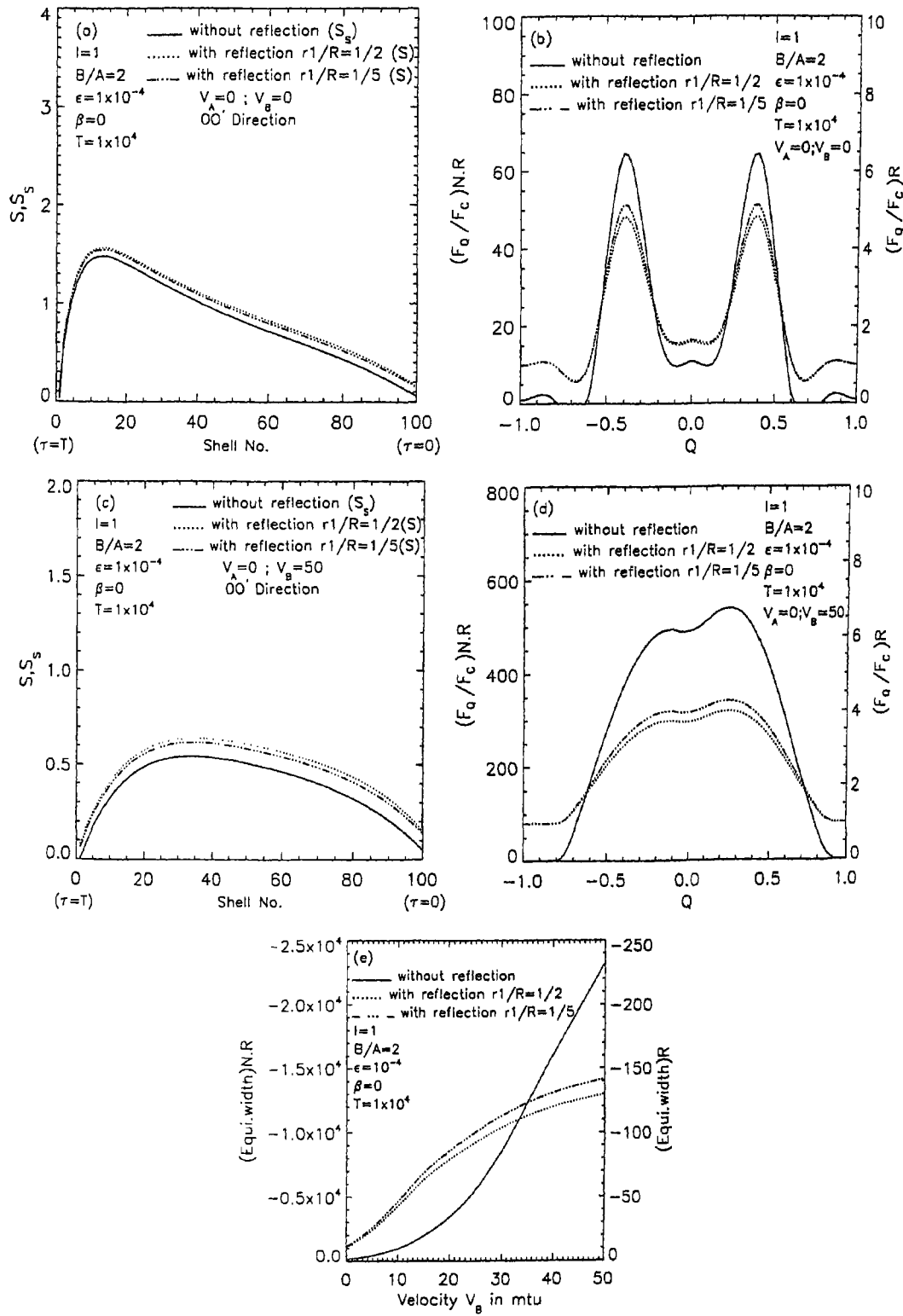


Figure 4.7: (a) Same as those given in figure 4.6(a) but with  $\epsilon = 10^{-4}$  (b) Same as those given in figure 4.6(b) but with  $\epsilon = 10^{-4}$  (c) Same as those given in figure 4.6(c) but with  $\epsilon = 10^{-4}$  (d) Same as those given in figure 4.6(d) but with  $\epsilon = 10^{-4}$  (e) Same as those given in figure 4.6(e) but with  $\epsilon = 10^{-4}$

normalized frequency points  $Q$  (see equation (4.50)). As the medium is static, the profiles are symmetric with central absorption. More photons are removed from the centre as the line central optical depth is  $10^4$ , the centre becomes almost dark. When the incident radiation from the component is added, there is more emission in the central portion of the line. The shapes of the lines in all these cases remain symmetric about the centre of the line. Figure 4.6(c) gives the variation of the same quantities as those given in figure 4.6(a) except that velocity  $V_B=50$  mean thermal units. There is a marked difference in the variation of the source functions in the two cases when  $V_B = 0$  in figure 4.6(a) and  $V_B = 50$  mtu in figure 4.6(c). There is a sudden fall in the source functions near  $\tau = T$  and these remain almost constant throughout the rest of the atmosphere. Figure 4.6 (d) presents the line profiles along the line of sight corresponding to the source functions presented in figure 4.6(c). These are similar to P-Cygni type profiles formed in an expanding media with blue shifted absorption. However the emission although small, confines more or less to the centre of the line formed in static medium. The reason for this is that the absorption core is formed in the portion of the atmosphere which is directly in between the star and the observer. As it is moving towards the observer there will be a Doppler shift of the frequencies of the line photons towards the blue side of the centre of the line. The photons that are emitted in the side lobes of the atmosphere are merely scattered and the Doppler effect due to the velocities in the farther part and nearer part (with respect to the observer's point) will nearly counter each other, maintaining an approximate symmetric emission about the centre. Therefore, the asymmetry caused by the Doppler shifts is minimal in the emission part of the line.

Figure 4.6(e) gives the variation of equivalent widths against the expanding velocities  $V_{\mathbf{B}}$  for the parameters shown in the figure 4.6(e). We can see that when no radiation is incident from the companion the equivalent widths are much larger than when there is incident light falling on the component from the companion. This can be understood from the fact that more photons are emitted through the line when external radiation is falling on the atmosphere from outside, which is also clear from a comparison of profiles given in figures 4.6(b) and 4.6(d). However, in both cases of reflection and no reflection the equivalent widths increase with the increasing velocities of expansion. Figure 4.6(f) gives the variation of the ratio of height of emission ( $H_e$ ) to that of depth absorption ( $H_a$ ). There is no change in the reflection and non reflection cases. However it is noteworthy that this ratio reaches a maximum at about  $V_{\mathbf{B}} = 4$  to 10 mtu and then falls slowly as the expansion velocities increase.

Figure 4.7(a) to 4.7(e) gives the results for the set  $\epsilon = 10^{-4}$  and  $\beta = 0$ . The Planckian  $B(T_e(r))$  is set equal to 1 uniformly throughout the medium. The source functions described in figure 4.7(a) represent the internal emission of photons. Although we have given a uniform emission  $B(T_e(r)) = 1$  throughout the atmosphere more of the radiation is scattered towards the boundary  $\tau = 0$  ( $r = r_{max} = B$ ) this is the effect of sphericity or curvature scattering. The incident radiation increases the source function only marginally. Corresponding line profiles (along the line of sight) are given in figure 4.7(b), these profiles show emission with absorption at line centre and these are symmetric with respect to the centre of the line as the medium treated here is static. Figure 4.7(c) gives the source functions of a medium which is expanding with  $V_{\mathbf{B}} = 50$  mtu. These are different from those given in figure 4.7(a) for a static

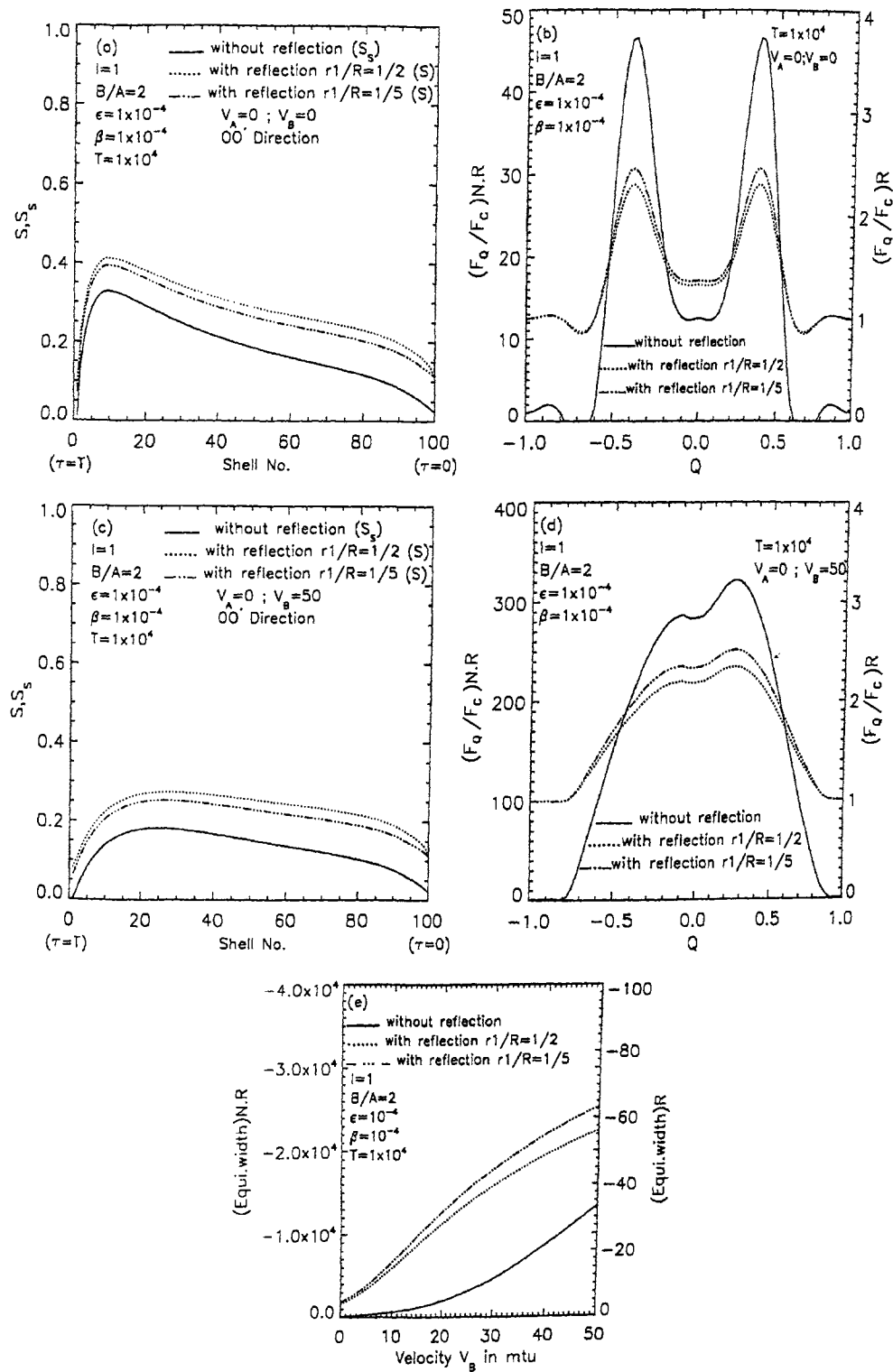


Figure 4.8: (a) Same as those given in figure 4.6(a) but with  $\epsilon = 10^{-4}$  and  $\beta = 10^{-4}$ . (b) Same as those given in figure 4.6(b) but with  $\epsilon = 10^{-4}$  and  $\beta = 10^{-4}$ . (c) Same as those given in figure 4.6(c) but with  $\epsilon = 10^{-4}$  and  $\beta = 10^{-4}$ . (d) Same as those given in figure 4.6(d) but with  $\epsilon = 10^{-4}$  and  $\beta = 10^{-4}$ . (e) Same as those given in figure 4.6(e) but with  $\epsilon = 10^{-4}$  and  $\beta = 10^{-4}$ .

medium. The maximum is spread over a larger spatial extent which is the effect of scattering in an expanding gas. The corresponding line profiles are given in figure 4.7(d). The emission is spread through the line except for a small absorption around the central position of the line. The equivalent widths of those lines are plotted in figure 4.7(e) with respect to expansion velocities  $V_{\text{Bs}}$ . It is interesting to note that when there is no reflection, the equivalent widths of the emission lines increase with velocities of expansion while the incident radiation from outside reduces the emission line equivalent widths considerably.

In figure 4.8(a) to 4.8(e), the results of the cases  $\epsilon = \beta = 10^{-4}$  are plotted. These results show similar characteristics those given in figures 4.7(a) to 4.7(e).

We performed several calculations for different parameters to study the effects of irradiation on line formation in expanding atmosphere of the component of a close binary system. We have studied the variation of source functions, with different velocity gradients and also various values of irradiation from the secondary component. The line profiles computed with reflection are compared with those computed without reflection and for several cases of the proximity of the two components. We obtained P-cygni type profiles.

#### 4.4 Radiative transfer in the dusty, irradiated expanding atmospheres of close binary components

In close binary systems light curves, radial velocity curves and line profiles are the most important sources of information to find the physical parameters of the components. The atmosphere of the component of a close binary system are distorted by the tidal effect due to the presence of

its companion, and self rotation. Nonuniform temperature distribution over its surface (which may arise due to gravity darkening), and the additional heating of the stellar surface by incident radiation from the companion star (particularly important for X-ray binaries), eclipses, stellar wind, and interaction effects associated with circumstellar gas structures (disks, jets, shells etc.) will change the radiation field in the atmosphere. In the previous sections we studied the problem of irradiation on line formation in an expanding atmosphere of the component of a close binary system and P-Cygni type profiles are found to be produced. The study of line formation in the dusty envelopes remains practically unexplored. The presence of dust is revealed in the infrared observations of many stellar objects, like gaseous nebulae, active galactic nuclei, T-Tauri stars and binary stars. Presence of dust, radial expansion, geometrical extension, chemical composition etc., are some of the physical and geometrical properties one should include in any calculation of line formation in such atmospheres. The purpose of this study is to compute the effects of dust on the formation of lines in the expanding atmospheres with light of the secondary falling on the component in a close binary system. We consider that the dust scatters radiation isotropically and neither dust absorption nor emission are taken into account.

#### **4.5 The equation of transfer in comoving frame in a dusty atmosphere**

The equation of line transfer in the comoving frame with absorption and emission due to dust and gas (see Peraiah and Wehrse, 1978; Peraiah

1984, Wehrse and Kalkofen, 1985) is given by,

$$\begin{aligned} \mu \frac{\partial I(x, \mu, r)}{\partial r} + \frac{(1 - \mu^2)}{r} \frac{\partial I(x, \mu, r)}{\partial \mu} &= K(x, r)S_L(r) + \\ K_c(r)S_c(r) - [K(x, r) + K_c(r)]I(x, \mu, r) & \\ + \left[ (1 - \mu^2) \frac{V(r)}{r} + \mu^2 \frac{dV(r)}{dr} \right] \frac{\partial I(x, \mu, r)}{\partial x} & \\ + K_{dust} [S_{dust}(r, \mu, x) - I(r, \mu, x)], & \end{aligned} \quad (4.58)$$

and

$$\begin{aligned} -\mu \frac{\partial I(x, -\mu, r)}{\partial r} - \frac{(1 - \mu^2)}{r} \frac{\partial I(x, -\mu, r)}{\partial \mu} &= K(x, r)S_L(r) + \\ K_c(r)S_c(r) - [K(x, r) + K_c(r)]I(x, -\mu, r) & \\ + \left[ (1 - \mu^2) \frac{V(r)}{r} + \mu^2 \frac{dV(r)}{dr} \right] \frac{\partial I(x, -\mu, r)}{\partial x} & \\ + K_{dust} [S_{dust}(r, \mu, x) - I(r, \mu, x)], & \end{aligned} \quad (4.59)$$

where all the symbols have their respective usual meanings see *Chapter 1* section (1.2.5). Further,  $K_{dust}(r)$  is the absorption coefficient of the dust and the dust source function  $S_{dust}(r, \pm\mu, x)$  is given by,

$$\begin{aligned} S_{dust}(r, \pm\mu, x) &= (1 - \omega)B_{dust} + \\ &\frac{\omega}{2} \int_{-\infty}^{+\infty} P(\mu, \mu', r) I(r, \mu', x) d\mu', \end{aligned} \quad (4.60)$$

where  $B_{dust}$  is the Planck function for the dust emission,  $\omega$  the albedo of the dust and  $P$  the isotropic and coherent scattering phase function. The quantity  $B_{dust}$  is normally neglected because the re-emission will be far away from the line centre and therefore, may not contribute to the line radiation. Although we need not consider the term containing  $B_{dust}$ , we have included it for the sake of completeness.

We have adopted the "CELL" method described by Peraiah (1984) to solve the equation (4.58) and (4.59); This is done by suitable discretisa-

tion in frequency, angle as radius. The details of the method was given in *Chapter 1* section (1.2.5).

#### 4.5.1 Boundary conditions

The atmosphere in question is divided into  $n$  shells where  $n = 1$  corresponds  $\tau = T$  and  $n = 100$  corresponding to  $\tau = 0$ , and  $\tau$  is the optical depth at any point and  $T$  is the total optical depth. The total optical depth is set in advance. We assume that no radiation is incident from outside the spherical shell at  $r = B$  and  $\tau = 0$ , while radiation of unit intensity is incident at  $r = A$ ,  $\tau = \tau_{max} = T$ , in the case of purely scattering medium. Thus we have,

$$\begin{aligned} \mathbf{U}^-(\tau = T, \mu_j) &= 1, \\ \mathbf{U}^+(\tau = 0, \mu_j) &= 0, \quad (\epsilon = 0, \beta = 0) \end{aligned} \quad (4.61)$$

and in the case of the boundary condition of the frequency derivative, we have:

$$\frac{\partial \mathbf{U}}{\partial X} \quad (\text{at } X = |X_{max}|) = 0. \quad (4.62)$$

We have set the velocities at  $r = A$  as  $V_A$ , and at  $r = B$  as  $V_B$  which is set equal to 0 and 50 mtu. If the spherical shell expands with constant velocity, we have;

$$V_A = V_B, \quad (4.63)$$

if there are velocity gradients, then we have;

$$V_A = 0 \quad V_B > 0. \quad (4.64)$$

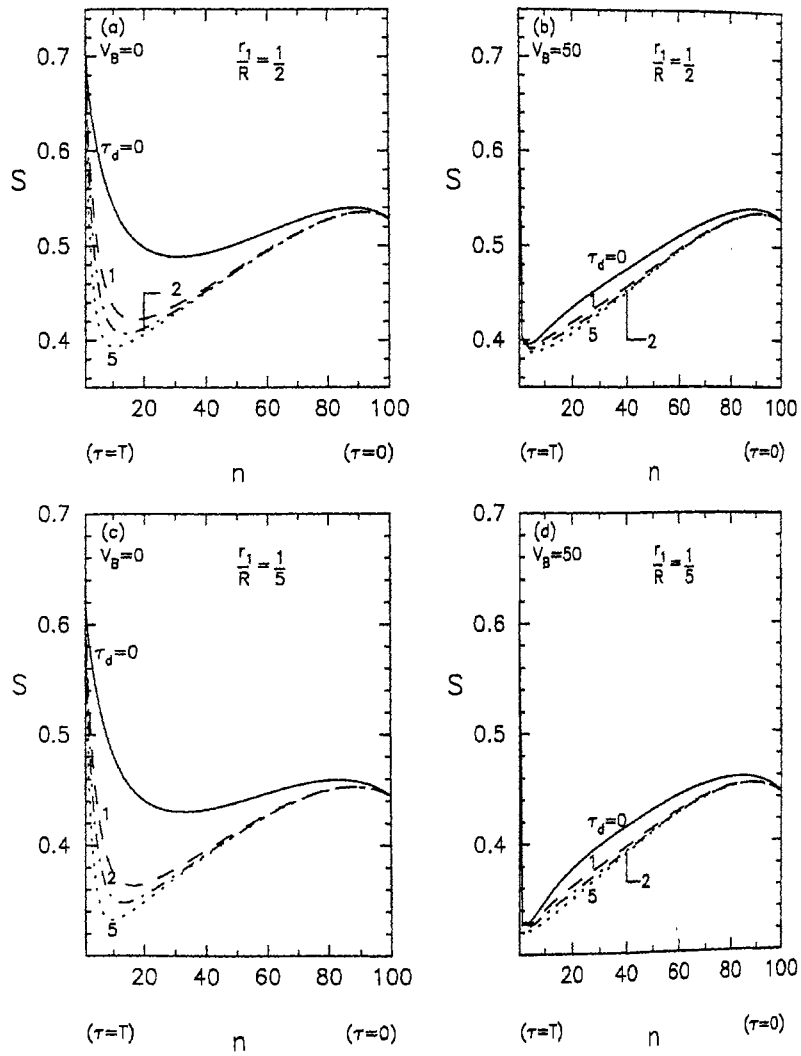


Figure 4.9: The source functions  $S$  are shown with respect to the shell numbers in a scattering medium for different dust optical depths, velocities, with  $\frac{r_1}{R} = \frac{1}{2}, \frac{1}{5}$  and  $I = 5$ .

Finally we calculate total source function  $S$  by adding  $S_d(\tau)$  in equation (4.14) and  $S_s(x, r)$  in equation (4.60) and obtain (see Srinivasa Rao & Peraiah 2000)

$$S = S_s + S_d. \quad (4.65)$$

#### 4.5.2 Result and discussion

Results are presented in figures 4.9 to 4.15 for different parameters. The figures are self explanatory regarding the parameters used. The atmosphere of the primary is divided into 100 shells. The separation of the components  $\frac{r_1}{R}$  where  $r_1$  is the radius of the primary component and  $R$  is the separation of the centers of gravity of the components. We have considered two cases of separation  $\frac{r_1}{R} = \frac{1}{2}$  and  $\frac{1}{5}$ , and the atmosphere extension  $\frac{B}{A} = 2$ . The total radial optical depth  $T$  is taken to be  $10^4$ . The velocities of expansion are measured in terms of mean thermal units and uniform expansion velocity law is assumed. If  $V_A$  and  $V_B$  are the velocities at A and B respectively, then the velocity at any shell boundary  $V_n = V_A + \left[ \frac{V_B - V_A}{N} \times n \right]$  where  $N$  is the total number of layers which the atmosphere of the star is divided ( $=100$ ). At A ( $\tau = \tau_{max} = T$ ) the velocity is  $V_A$  and at B ( $\tau = 0$ ) the velocity is  $V_B$ . The parameter  $\epsilon < 1$  for non-LTE line formation and this is set to equal to 0. The quantity  $\beta$  is set equal to 0 in our calculations. The dust optical depth is taken to be  $\tau_d = 0, 1, 2, 5$ . The expansion velocities are taken to be  $V_B = 0, 5, 25, 50$ . But the results are presented for static medium with  $V_A = 0, V_B = 0$  and expanding medium with  $V_A = 0, V_B = 50$ . The irradiation from the secondary component is taken to be  $I = 1, 5, 10$  times the self radiation of the star. However, the results are presented for  $I = 5$  only.

In figure 4.9(a), the source function  $S$  are plotted for a static dusty

medium, with  $\frac{r_1}{R} = \frac{1}{2}$  and  $I = 5$  when  $\tau_d = 0$  (dust free medium), the source function falls rapidly in magnitude from the boundary  $\tau = T$  towards the boundary  $\tau = 0$ . It reaches a minimum at around  $n=20$  at which point it starts to raise because of the diffuse radiation incident from the secondary. It reaches a maximum at about  $n=80$ . This is due to the diffuse reflection of the incident light from the secondary by the gaseous medium immediately inside the atmosphere at the boundary at  $\tau = 0$ . When dust is introduced the source functions have been reduced proportionately to the amount of dust present in it but nature of variation of the source function remain the same. The reduction in the source functions in dusty medium is due to the physical effect that dust removes photons from the radiation field and that these are not replaced by emission. In figure 4.9(b) we introduced expansion with  $V_B = 50$  mtu. The source functions fall more rapidly near the boundary  $\tau = T$  ( $n=1$ ) but otherwise the variation is similar to those shown in the case of static medium (figure 4.9(a)). Figures 4.9(c) and 4.9(d) are the same as those given in figures 4.9(a) and 4.9(b) respectively but with  $\frac{r_1}{R} = \frac{1}{2}$  replaced by  $\frac{1}{5}$ . In both the situations there is no change in variation of the source functions but the values of the source functions are much smaller because of the fact that the distance between the components is increased and therefore, the incident radiation is reduced by an approximate factor of  $\frac{1}{(R - r_1)^2}$

Figure 4.10(a, b) gives the source function  $S_s$  and  $S$  given in equation (4.65) for various parameters shown in the figure, across the atmosphere for  $n = 1$  to  $n = 100$ . Figure 4.10(a) represents a static and scattering medium with  $V_A = V_B = 0$  and  $\epsilon = \beta = 0$  and the incidence radiation factor  $I = 5$  (see equation 4.45). The source function  $S_s$  decreases slowly from the point  $\tau = T$  to the point  $\tau = 0$  in the scattering medium, with

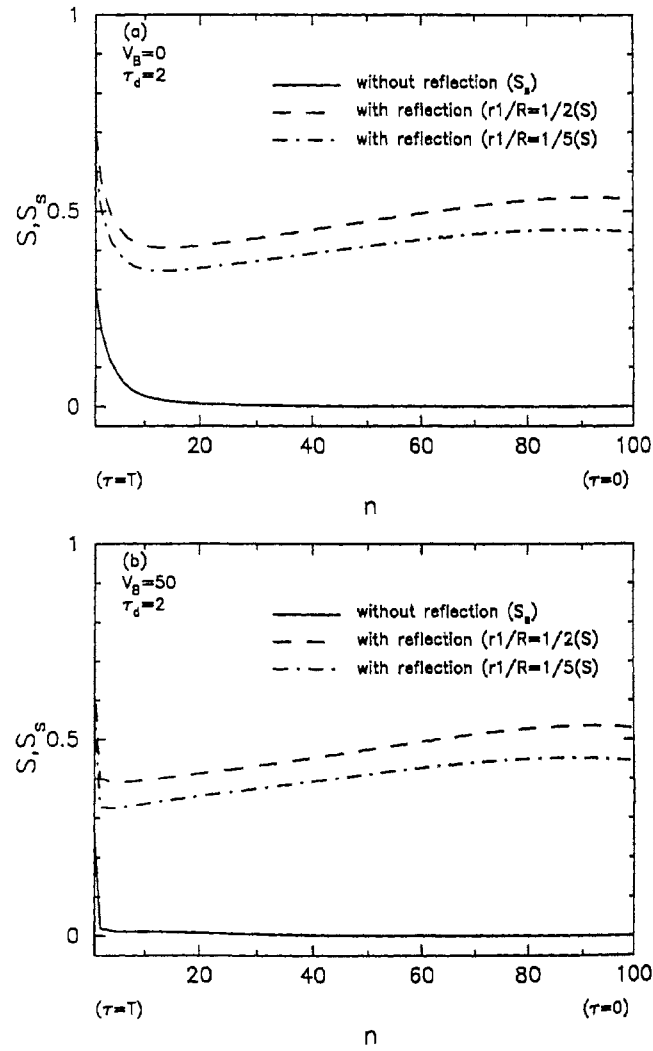


Figure 4.10: A comparison of the source function  $S$  and  $S_s$  are shown with respect to the shell numbers in a scattering medium for a static medium and for a expanding medium when the dust optical depth  $\tau_d = 2$  and  $\frac{r_1}{R} = \frac{1}{2}$  and  $\frac{1}{5}$ .

$T = 10^4$ . When the reflected radiation is included, the source function for  $\frac{r_1}{R} = \frac{1}{2}$  and  $\frac{1}{5}$  are considerably enhanced as these source functions include the incident radiation from the companion. Similar trend is observed in figure 4.10(b) when the expansion velocity is  $V_B = 50$ .

In figure 4.11(a, b, c, d) the line fluxes are plotted against the normalized frequency points  $Q$  (see equation 4.50) along the line of sight. Each one of the graphs in figure (4.11 a, b, c, d) gives the line profiles for different  $\tau_{ds}$ . Figures (4.11 (a)) and (4.11(b)) represent the static atmosphere but with  $\frac{r_1}{R} = \frac{1}{2}$  and  $\frac{1}{5}$  respectively. As the fluxes are normalized, there do not seem to be any change in the symmetric profiles. However, the effect of dust is significant as dust scatters more photons into line core thereby increasing the emission in the core of the line, and more emission in the cores of the lines formed in the former case (ie)  $\frac{r_1}{R} = \frac{1}{2}$  appears and this is because more light falls on the component in the former case than in the latter case. Figures 4.11(c) and 4.11(d) give the flux profiles for the same parameters as those in figures 4.11(a) and 4.11(b) respectively except that a velocity of expansion  $V_B = 50$  mtu is introduced into the medium. The profiles show asymmetry with red emission and blue absorption and a blue shift of the centre of the line - a P Cygni type profile. The part played by the dust is similar to that shown in figures 4.11(a) and 4.11(b). It scatters more photons into the line centre and at high dust optical depth, the line may even disappear altogether.

In figure 4.12(a-f) line profiles without reflection are compared with those formed with the incident radiation from the secondary component i.e,  $I = 1, 5, 10$ . The line profiles are plotted with normalized frequency points  $Q$ , and the ratios of the flux  $\frac{F_Q}{F_C}$ . The solid curves (scale given

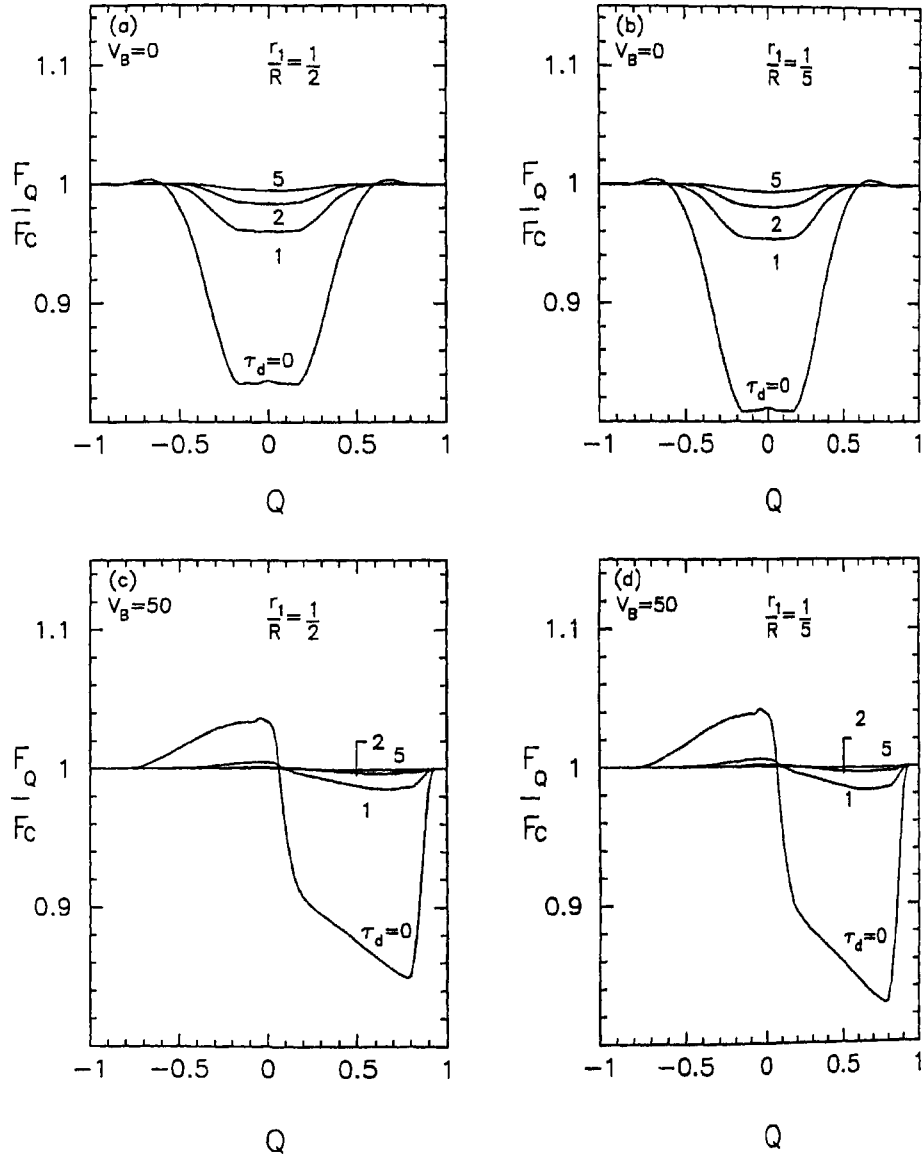


Figure 4.11: Comparison of line profiles for different dust optical depths when  $\frac{r_1}{R} = \frac{1}{2}$  and  $\frac{1}{5}$  and for  $V_B=50$

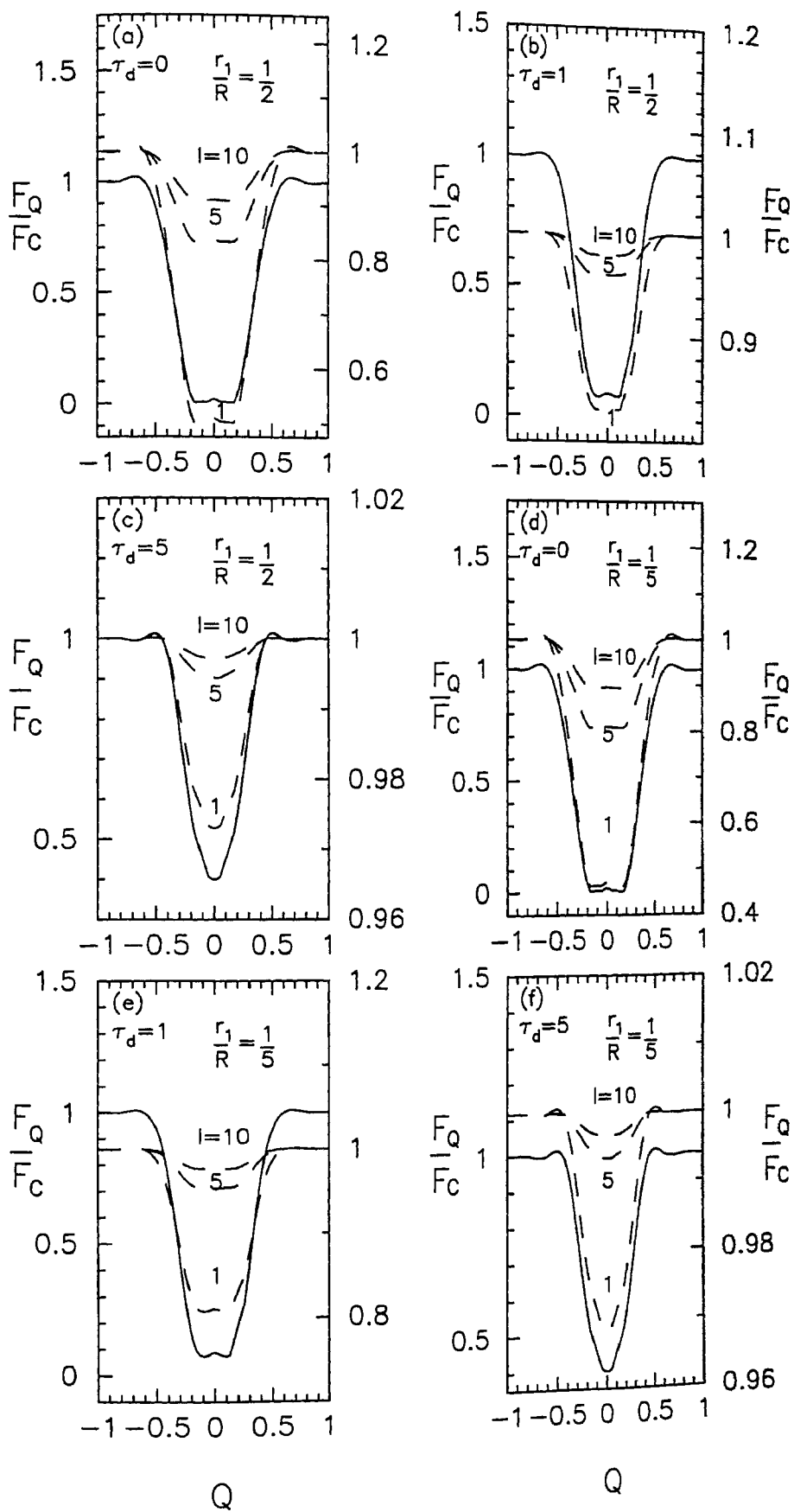


Figure 4.12: Comparison of line profiles for different irradiation ( $I = 1, 5, 10$ ) when  $\frac{r_1}{R} = \frac{1}{2}$  and  $\frac{1}{5}$  for different dust optical depths.

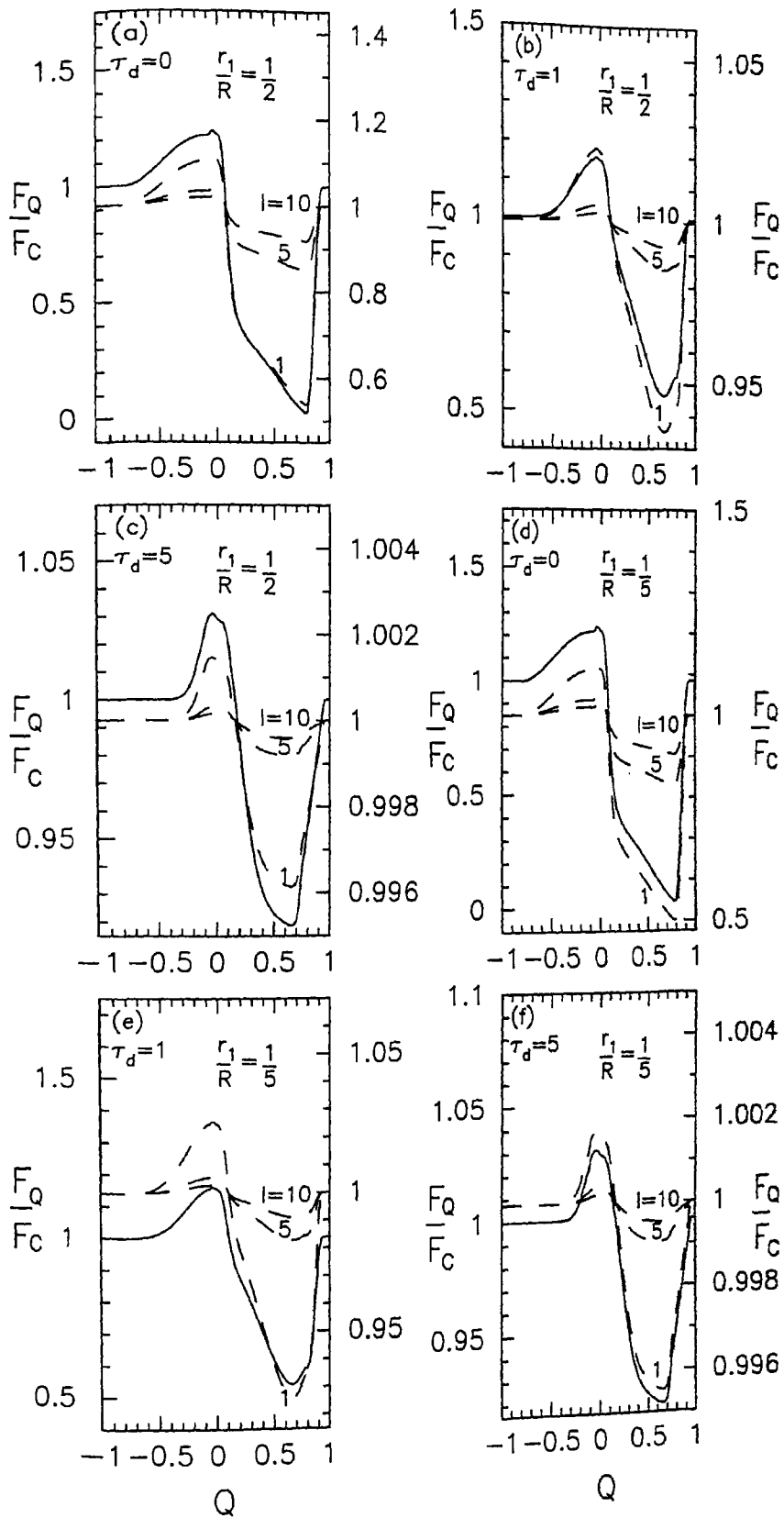


Figure 4.13: Same as figure 4.12 but  $V_B=50$

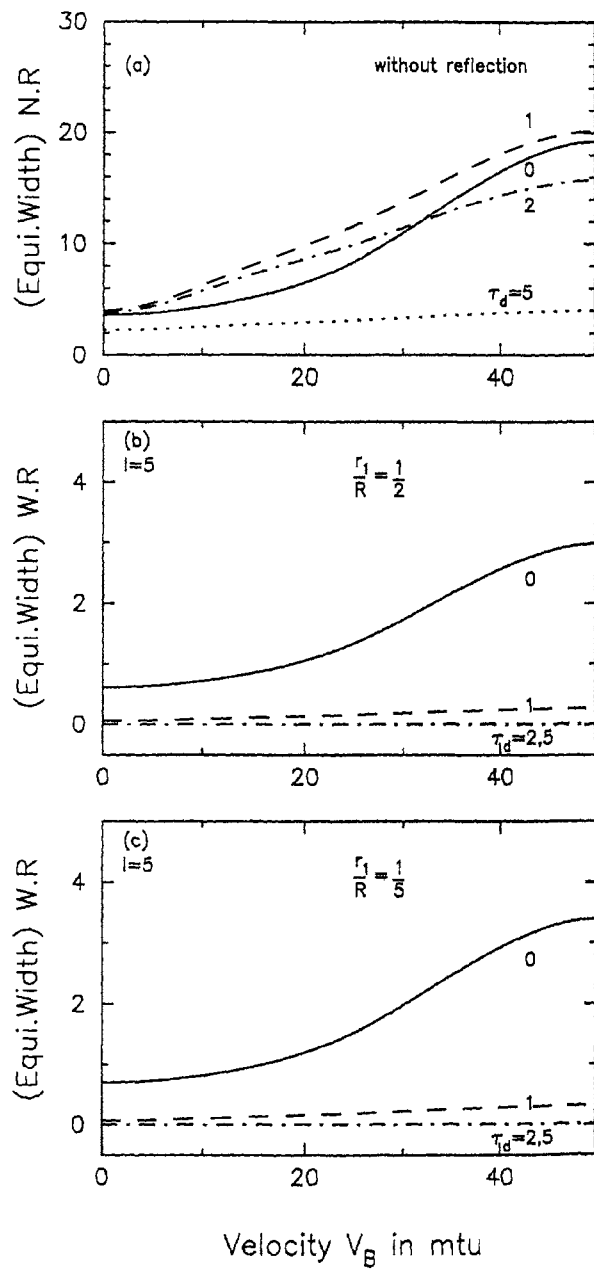


Figure 4.14: Equivalent widths are plotted against the expansion velocity with reflection and without reflection.

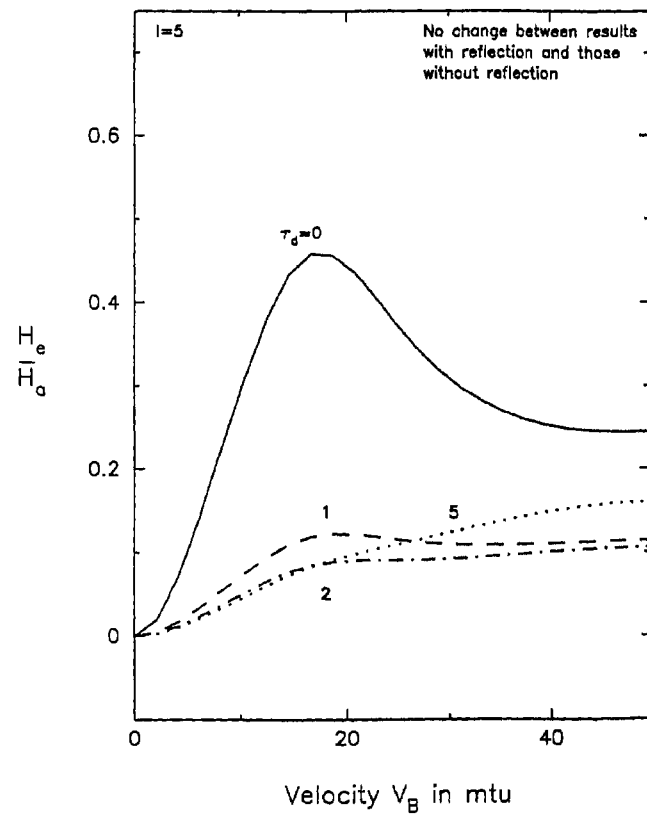


Figure 4.15: The ratios of the heights of the emission to the depth of the absorption in the lines for both the case of reflected radiation and non reflected radiation are shown against the velocity expansion  $V_B$ .

on the right side of the figure) are for the case without irradiation while the dashed are the ones formed with irradiation from the secondary. As the medium is static, the profiles are symmetric with central absorption. Figures 4.12(a-f) give a comparison of profiles formed in the condition of no irradiation and those with irradiation from the secondary component, and each of the six figures drawn for different  $\tau_d$ 's are shown in the respective figures. Each figure contains profiles for  $I = 0, 1, 5$  and  $10$  where  $0$  means no incident radiation. It appears that the higher values of  $I$  give higher line fluxes and in particular, more emission is seen in cores of the lines.

Figures 4.13(a-f) contain the flux profiles for the same parameters as those in figures 4.12(a-f) but with  $V_B = 50$  mtu. The P Cygni type profiles are obtained similar to those shown in figure 4.11.

Figures 4.14(a, b, c) give the variation of equivalent widths against the expansion velocity  $V_B$  for the parameters shown in the figure. We can see that when there is no radiation incident from the companion, the equivalent widths are much larger as the absorption core is deeper. In the presence of dust  $\tau_d = 1, 2, 5$  the equivalent widths reduce considerably for the reason given above that more photons are scattered into the core, thus reducing absorption and increasing core emission.

Figure 4.15 gives the variation of the ratio of height of emission ( $H_e$ ) to that of depth absorption ( $H_a$ ). There is no change between the reflection case and the non-reflection case. However, it is noteworthy that this ratio reaches a maximum at about  $V_B = 4$  to  $10$  mtu and then falls slowly as the expansion velocity increases. Similar kind of trend is observed in the presence of dust. It is different in the case of  $\tau_d = 5$ , here the ratio increases slowly as the expansion velocity increases. This can

be understood again from the argument that more dust scatters more photons into the line core enhancing emission of the core of the line.

Now we would like to study effects of reflection on distorted surface due to self rotation and tidal effect in a binary system in the next chapter.

## Chapter 5

### Distortion due to rotation and tidal forces

#### 5.1 Introduction

Many of the well-known stars such as Sirius, Procyon, Antares are double stars, with faint companions orbiting the bright primary stars. Since the two components are so close, they invariably appear as a single object even with the largest telescopes. Astronomers identify them by measuring the minute blue shifts and red shifts in the spectrum produced by the system as the stars alternatively approach and recede from us are variable stars. Those systems whose orbital planes lie close to the line of sight of an observer on Earth undergo periodic eclipse. The changes in brightness may lie within a few tenths of a magnitude to a little more than one magnitude. Variation in light output also occur out of eclipse, however, and this suggests an exchange of material between two extremely close components.

**Roche lobe :** The Roche lobe is a mathematically defined surface that exists around each star in any binary system. When a binary star is extremely close to its partner, it interacts through its Roche lobe, or realm of gravitational influence. Massive stars have larger Roche lobes than small stars.

In general stars tend to rotate rapidly, and this can have a strong influence on star's atmosphere. Rotation tends to flatten a star, and this

oblateness in turn causes a redistribution of both its effective gravitational potential and its emergent radiative flux, an effect called "gravity darkening".

It is well known fact that some of the close binary systems with both components on the main sequence and with periods less than about 5 days (Olsen 1968, Plaut 1959, Huang 1966) rotate around their axes of rotation perpendicular to the orbital plane in synchronism with their Keplerian orbits. This is very interesting case because of its simplicity: the four independent parameters  $x$  the ratio of angular velocities at the equator and pole,  $f$  the ratio of centrifugal to gravity forces at the equator (equal to the value of the function  $f_r(\theta)$  defined in equation (5.7) at  $r = r_e$ ,  $\theta = \frac{\pi}{2}$ ),  $\frac{m_2}{m_1}$  the mass ratio of the components and  $\frac{r_e}{R}$ , the ratio of equatorial radius to the distance between the centers of gravity of the two components, reduce to only three.

We adopted a spherical polar coordinate system in which any point is represented by  $(r, \theta, \phi)$ . The polar angles are related according to the usual convention with rectangular frame of reference in which the x-axis coincides with the line joining the centers of gravity of the components and the z-axis ( which is identical with the axis of rotation of the primary is perpendicular to the orbital plane. The origin coincides with the center of gravity of the primary. The polar angle  $\theta$  is measured from the axis of rotation (z-axis) towards the x-y plane and  $\phi$  is measured in the x-y plane between x-axis and the projected radius vector.

## 5.2 Formulation of equations for the distorted surface of the component due to rotation and tidal force

We shall describe a method for obtaining temperature of the distorted component, and luminosities etc.,. The total potential ( rotational and gravitational) for the components in the close binaries as a function of  $r, \theta, \phi$  is given (se Peraiah 1969, 1970),

$$\psi = \frac{Gm_1}{r_p^2} \left[ \frac{1}{\rho} + Q\rho^2 (3 \sin^2 \theta \cos^2 \phi - 1) + \gamma\rho^2 \sin^2 \theta + 3\rho^4 \sin^4 \theta + \alpha\rho^6 \sin^6 \theta \right], \quad (5.1)$$

where  $\rho = \frac{r}{r_p}$ , and the coefficients

$$\alpha = \frac{f(x-1)^2}{6x^2} \left( \frac{r_p}{r_e} \right)^7 ; \quad \beta = \frac{f(x-1)^2}{2x^2} \left( \frac{r_p}{r_e} \right)^5 ;$$

$$\gamma = \frac{f}{2x^2} \left( \frac{r_p}{r_e} \right)^3 ; \quad Q = \frac{1}{2} \mu \left( \frac{r_p}{r_e} \right)^3 ; \quad \mu = \frac{m_2}{m_1} \left( \frac{r_e}{R} \right)^3.$$

where  $\left( \frac{r_e}{r_p} \right)$  is given by

$$\left( \frac{r_e}{r_p} \right)^3 - u \left( \frac{r_e}{r_p} \right)^2 - \frac{1}{2} \mu = 0, \quad (5.2)$$

where

$$u = 1 + \frac{f(x^2 + x + 1)}{6x^2} + \mu. \quad (5.3)$$

At the pole we have

$$\begin{aligned} \psi &= \text{Constant} \\ &= \frac{Gm_1}{r_p^2} (1 - Q) = \epsilon, \end{aligned} \quad (5.4)$$

where  $\epsilon$  is a constant. From equations (5.1) and (5.4) the equation of the surface  $\psi = C$  is therefore, given by

$$\alpha\rho^7 \sin^6 \theta + \beta\rho^5 \sin^4 \theta + (\gamma \sin^2 \theta + J)\rho^3 - (1 - Q)\rho + 1 = 0. \quad (5.5)$$

where  $J = Q(3 \sin^2 \theta \cos^2 \phi - 1)$ . The surface gravity  $\mathbf{g}$  is given by

$$\begin{aligned}\mathbf{g} &= -\text{grad } \psi \\ &\equiv (g_r, g_\theta, g_\phi),\end{aligned}\tag{5.6}$$

where  $(g_r, g_\theta, g_\phi)$  are the components of  $\mathbf{g}$  in the three orthogonal directions defined by the curvilinear coordinates  $(r, \theta, \phi)$  given by

$$\begin{aligned}g_r &= -\frac{\partial \psi}{\partial r} \\ &= -\frac{1}{r_p} \frac{\partial \psi}{\partial \rho} \\ &= \frac{Gm_1}{r_p^2} \frac{1}{\rho^2} (1 - f_r(\theta) \sin^2 \theta - 2J\rho^3), \\ g_\theta &= -\frac{\cos \theta}{r_p} \frac{1}{\rho} \frac{\partial \psi}{\partial(\sin \theta)} \\ &= \frac{Gm_1}{r_p^2} \frac{1}{\rho^2} [-f_r(\theta) \sin \theta \cos \theta - 6Q\rho^3 \sin \theta \cos \theta \cos^2 \phi], \\ g_\phi &= -\frac{1}{r_p} \frac{1}{\rho \sin \theta} \frac{\partial \psi}{\partial \phi} \\ &= \frac{Gm_1}{r_p^2} \frac{1}{\rho^2} [6Q\rho^3 \sin \theta \sin \phi \cos \phi],\end{aligned}$$

and

$$\begin{aligned}f_r(\theta) &= \frac{\Omega^2 r^3}{gm_1} \\ &= 2\gamma\rho^3 + 4\beta\rho^5 \sin^2 \theta + 6\alpha\rho^7 \sin^4 \theta,\end{aligned}\tag{5.7}$$

$f_r(\theta)$  being the ratio of centrifugal to gravity forces at the point  $(r, \theta)$  on the surface of the component, and  $\Omega$  is the angular velocity. Therefore, the total gravity  $g$  is given by,

$$\begin{aligned}g &= \frac{Gm_1}{r^2} \left[ (1 - f_r(\theta) \sin^2 \theta - 2J\rho^3)^2 \right. \\ &\quad + \left. (f_r \theta \sin \theta \cos \theta + 6Q\rho^3 \sin \theta \cos \theta \cos^2 \phi)^2 \right. \\ &\quad \left. + 36Q^2 \rho^6 \sin^2 \theta \sin^2 \phi \cos^2 \phi \right]^{\frac{1}{2}}.\end{aligned}\tag{5.8}$$

The mean temperature  $T_*$  on the surface of the distorted component can be calculated from the equations (Ireland, 1966)

$$T_* = T_0 g^{\frac{1}{4}}, \quad (5.9)$$

and

$$\bar{T} = \frac{\int T_0 g^{\frac{1}{4}} ds}{\int ds}, \quad (5.10)$$

where the integrals are taken over the whole surface of the distorted component and  $T_0$  is a constant.

If  $\mathbf{n}$  is a unit normal in a point P on the surface and  $\mathbf{e}_r$  a unit vector in the direction of  $r$  in the same point P, we see that the real element at P in terms of the parameters  $\theta, \phi$  is

$$\begin{aligned} ds &= \frac{r^2 \sin \theta d\theta d\phi}{\mathbf{n} \cdot \mathbf{e}_r}, \\ &= \frac{g r^2 \sin \theta d\theta d\phi}{g_r}, \end{aligned} \quad (5.11)$$

since  $\mathbf{g} = g\mathbf{n}$ , where  $g$  and  $g_r$  are given by equation (5.8) and (5.7) respectively. From the equations (5.9), (5.10) and (5.11) we have,

$$T_* = \bar{T} \frac{g^{\frac{1}{4}} \int \int \frac{g r^2 \sin \theta d\theta d\phi}{g_r}}{\int \int \frac{g^{\frac{5}{4}} r^2 \sin \theta d\theta d\phi}{g_r}}. \quad (5.12)$$

Similarly, we can compute the ratio of luminosity in the line of sight to the total luminosity using Von Zeipel's theorem (Ireland, 1966, ; Von Zeipel, 1924). The later is given by

$$L = k \int g ds, \quad (5.13)$$

and the former by

$$L(l) = k \int \mathbf{g}(\mathbf{n} \cdot \mathbf{l}) ds, \quad (5.14)$$

where the integrations are taken over the surface of the visible disc,  $\mathbf{l}$  is a unit vector in the line of sight, and  $\mathbf{k}$  is a Von Zeipel's constant. Now

$$\begin{aligned} g\mathbf{n}\cdot\mathbf{l} &= g\cdot\mathbf{l}, \\ &= (g_r\mathbf{e}_r + g_\theta\mathbf{e}_\theta + g_\phi\mathbf{e}_\phi)\cdot\mathbf{l}, \end{aligned} \quad (5.15)$$

where

$$\begin{aligned} \mathbf{e}_r &= \sin\theta\cos\phi\mathbf{i} + \sin\theta\sin\phi\mathbf{j} + \cos\theta\mathbf{k}, \\ \mathbf{e}_\theta &= \cos\theta\cos\phi\mathbf{i} + \cos\theta\sin\phi\mathbf{j} - \sin\theta\mathbf{k}, \\ \mathbf{e}_\phi &= -\sin\phi\mathbf{i} + \cos\phi\mathbf{j}, \\ \mathbf{l} &= \cos\psi'\sin i\mathbf{i} + \sin\psi'\sin ij + \cos ik, \end{aligned} \quad (5.16)$$

and we can immediately calculate  $\mathbf{e}_r\cdot\mathbf{l}$  etc., in the equation (5.15) by using equation (5.16). Here  $\mathbf{i}, \mathbf{j}, \mathbf{k}$  are the unit vectors along x-, y-, z-axes and  $\psi'$  and  $i$  are the true anomaly of the secondary component and the inclination of the orbital plane respectively.

From the equations (5.13)-(5.14) we write  $l_1$  the ratio of luminosity in the line of sight without limb darkening to the luminosity as,

$$l_1 = \frac{\int g(\mathbf{n}\cdot\mathbf{l}) ds}{\int g ds}. \quad (5.17)$$

The effect of limb darkening can be estimated by using a quadratic law (p 156, Kopal, 1959)

$$\begin{aligned} I &= \frac{I(0, \mu)}{I(0, 1)} \\ &= 1 - u_1 - u_2 + u_1(\mathbf{n}\cdot\mathbf{l}) + u_2(\mathbf{n}\cdot\mathbf{l})^2, \end{aligned} \quad (5.18)$$

where  $u_1=0.65$  and  $u_2=-0.0226$  (p, 182, Kopal, 1959) and  $l_2$ , the ratio of luminosity with the limb darkening, to the total luminosity becomes (p. 177, 172, Kopal, 1959)

$$l_2 = \frac{\int (g_0(1 - \tau_0) + \tau_0 g) + I(\mathbf{n}\cdot\mathbf{l}) ds}{\int g ds}, \quad (5.19)$$

and  $l_3$ , the ratio of luminosity in the line of sight with limb darkening to the luminosity in the line of sight without limb darkening is given by,

$$l_3 = \frac{\int (g_0(1 - \tau_0) + \tau_0 g) + I(\mathbf{n.l}) ds}{\int g(\mathbf{n.l}) ds}, \quad (5.20)$$

where

$$g_0 = \frac{\int g ds}{\int g ds}, \quad (5.21)$$

and  $\tau_0$  is taken corresponding to temperature of  $T_e=20000^\circ$  K and  $\lambda=5240$  Å. In equation (5.18), one only computes the right hand side in order to obtain the limb darkening. These values of luminosities can be converted to stellar magnitude by using the relation

$$\Delta_m = -2.5 \log_{10} l, \quad (5.22)$$

where  $l$  can take the values of  $l_1, l_2$ , and  $l_3$ . We have already noted that some binaries rotate synchronously. In this case we have to set  $\Omega_e = \frac{2\pi}{P}$  where  $P$  is the orbital period of the system in seconds. Applying Kepler's third law, we find that,

$$\begin{aligned} \Omega_e^2 &= \left(\frac{2\pi}{P}\right)^2, \\ &= \frac{G(m_1 + m_2)}{R^3}, \end{aligned} \quad (5.23)$$

or using this value of  $\Omega_e$  in  $f_{re}\left(\frac{\pi}{2}\right)$ ,  $\left(= \frac{\Omega_e^2 r_e^3}{Gm_1}\right)$  we obtain

$$f_{re}\left(\frac{\pi}{2}\right) \Big|_{\text{forsynchronism}} = \left(1 + \frac{m_2}{m_1}\right) \left(\frac{r_e}{R}\right)^3, \quad (5.24)$$

where  $f_{re}(\theta)$  and  $\Omega$  corresponds to  $f_r(\theta)$  and  $\Omega$  at the equator. The above equation can be used for both uniform ( $x = 1$ ) and non-uniform ( $x > 1$ ) rotation.

### 5.3 Results and discussion

Here the calculations are straightforward although some care has to be taken in solving equation (5.5) and equation (5.2) for  $\rho = \frac{r}{r_p}$  and  $\frac{r_e}{r_p}$  respectively. It was found that Newton-Raphson method, starting from an initial estimate of 1.0 to 1.01 for  $\rho$  and  $\frac{r_e}{r_p}$  gave good convergence. The values are used in the subsequent calculations. The double integration in equation (5.12) are calculated by Simpson's rule. We have selected few representative values for each of the parameters. The cases of  $x \left( = \frac{\Omega_e}{\Omega_p} \right)$  treated here mainly are for,  $x=1$  corresponding to uniform rotation and  $x=10$  corresponding to highly non-uniform rotation. We have also taken  $f=0.5$  in most of the calculations so that we can select a good number of pairs of  $\frac{m_2}{m_1}$  and  $\frac{r_e}{R}$ .

Figure 5.1 shows that the equatorial temperatures fall rapidly for increasing values of  $f$  and also we plotted the polar and equatorial temperatures are plotted against  $f$ . It appears that the fall in the equatorial temperature is more rapid than the increase in the polar temperature.

#### 5.3.1 Effects on luminosity

The results of equation (5.17) which gives the ratio of un-limb darkened luminosity in the line of sight to the total luminosity ( $l_1$ ) are given in figure 5.2. In figure 5.2 values of  $l_1$  are plotted against the mass ratios for various parameter choices. The values of  $l_1$  for polar view are larger than those in intermediate direction and much larger than those of equatorial values. It is very interesting to note that the values of  $l_1$  in both polar and intermediate views for uniform rotation are larger than their counterparts in non-uniform rotation. Exactly the opposite happens in the equatorial view. These values seem to be consistently smaller than those

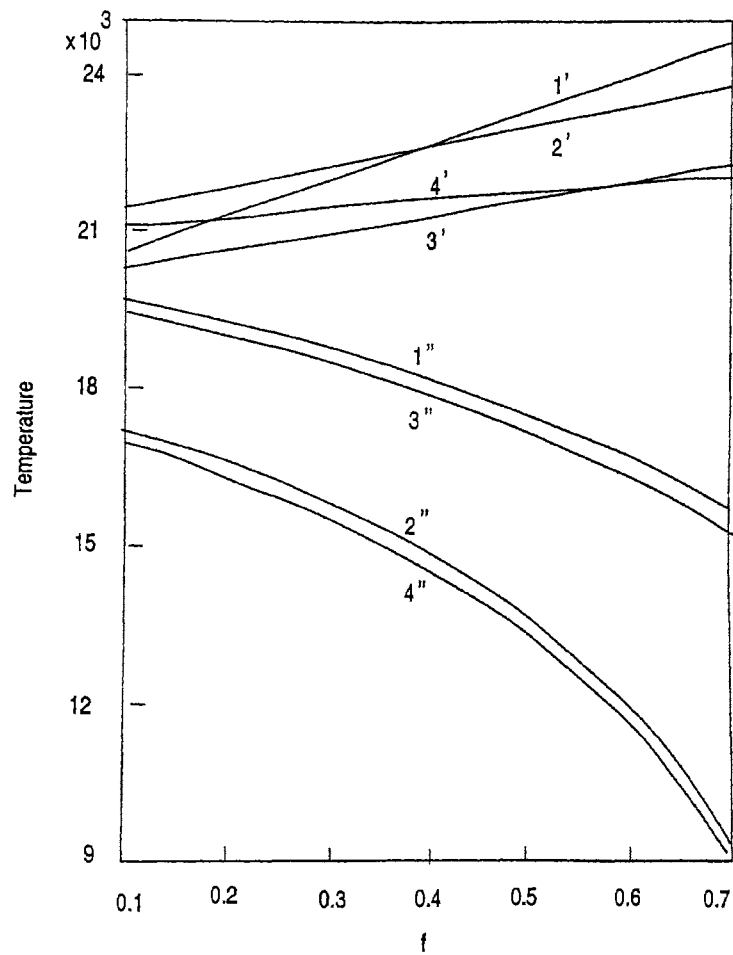


Figure 5.1: The polar and equatorial temperatures (in thousands of degrees of Kelvin) are plotted against  $f$ . Single primed curves are for polar and double primed curves for equatorial temperatures. (1') and 1'' are for  $\frac{m_2}{m_1} = 0$ ,  $x = 1$ ; (2') and (2'') are for  $\frac{m_2}{m_1} = 1$  and  $x = 1$ ; (3') and (3'') are for  $\frac{m_2}{m_1} = 0$ ,  $x = 10$ , and (4'') are  $\frac{m_2}{m_1} = 1$ ,  $x = 10$ ;  $\frac{r_e}{R} = 0.5$  and  $\bar{T} = 20000^\circ \text{K}$

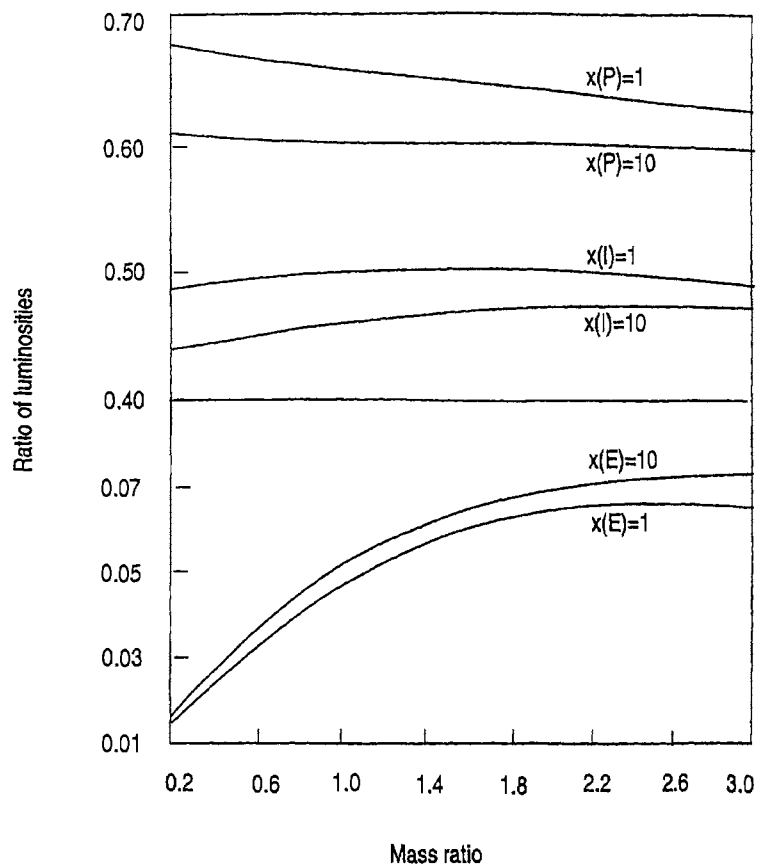


Figure 5.2: Ratios of luminosities ( $l_1$ ) in the line of sight without limb darkening to the total luminosity of equation (5.17) are plotted against  $\frac{m_2}{m_1}$ . P, I and E are for Polar, Intermediate, and Equatorial views respectively.  $f = 0.5$ ,  $\frac{r_e}{R} = 0.5$ .

corresponding to non synchronism (see figure 5.2) for all three views. As we have mentioned earlier, all values of  $f$  determined by the equation (5.24) in the case of synchronism are less than the value  $f=0.5$  we have used to present the non synchronism case. From this, we can conclude that  $f$  would give smaller values of  $l_1$  and vice versa.

### 5.3.2 Limb darkening

We will now discuss the effect of the quadratic law of darkening incorporated in equation (5.18). In figure 5.3 the law of darkening at  $\theta=50^\circ$  on the surface is plotted against the mass ratios for the three lines of sight

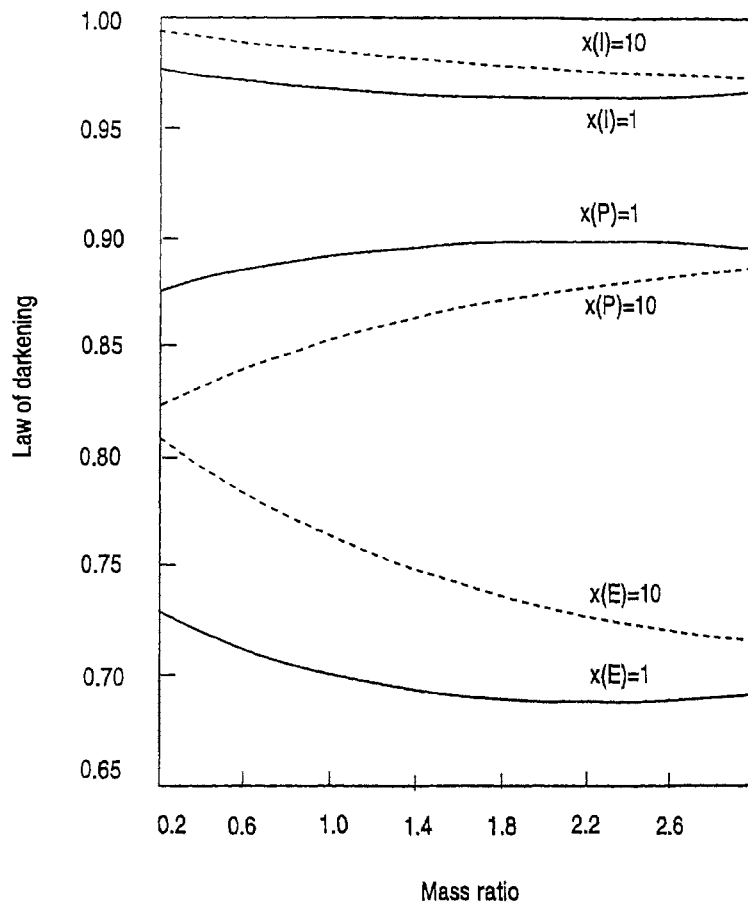


Figure 5.3: The law of darkening is plotted against  $\frac{m_2}{m_1}$ . P, I and E are for Polar, Intermediate, and Equatorial views respectively. The values are calculated for  $\theta = 50^\circ$ . Continuous line and dashed line represents the uniform and nonuniform rotation respectively

for uniform and non-uniform rotation. In the intermediate and equatorial view, the luminosity for non-uniform rotation is larger than that for uniform rotation; for the polar view the opposite is true. Figure 5.3 demonstrates the important result that laws of darkening for uniform and non-uniform rotation tend to converge as the mass ratio increases irrespective of the line of sight.

### 5.3.3 Luminosities with limb darkening

In this section we compare the luminosity ratios  $l_2$  and  $l_3$  computed from equations (5.19) and (5.20) respectively. The results are displayed in figure 5.4. In figure 5.4 (a) the ratios of luminosity are plotted against the mass ratios. All subsequent results are only for non synchronous cases. In synchronous rotation the only effective parameter is  $f$ , and we have seen that the distribution of luminosity is insensitive to changes in this quantity.

In figure 5.4 (b) the luminosity ratios are plotted against the mass ratio in the intermediate view for uniform and non-uniform rotation. The luminosity ratio  $l_2$  for uniform rotation starts to decrease when  $\frac{m_2}{m_1} \geq 0.6$  and for increase non-uniform rotation, but with the reduced rate of growth. The curves of  $l_3$  for both uniform and non-uniform rotation are quite similar. In both the cases the ratios fall from  $\frac{m_2}{m_1}=0.1$  to  $\frac{m_2}{m_1} \simeq 2.0$  after which there is a steep rise.

So far, we have only been able to discuss a few of the effects to be expected. It is clear that the effects we have considered tend to make the light changes extremely complicated in close binary systems between eclipses and make their interpretation more difficult. There is another important effect- reflection effect- which enhances the complications but is one of the more important factors especially in very close pairs that has still to be considered.

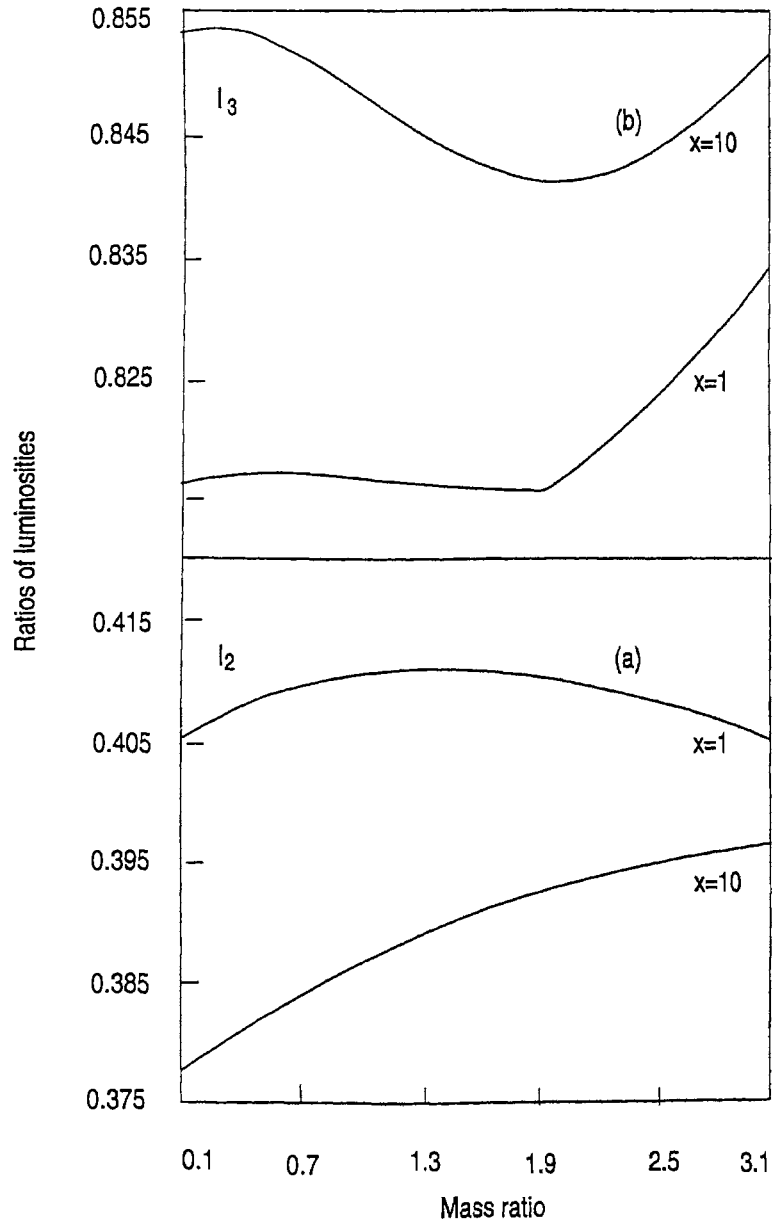


Figure 5.4 (a): The ratios ( $l_2$ ) of luminosities with limb darkening to the total luminosity of equation (5.19) versus  $\frac{m_2}{m_1}$  for intermediate view.  $f=0.5$ ,  $\frac{r_e}{R}=0.5$  (b) the ratios ( $l_3$ ) luminosities in the line of sight without limb darkening of equation (5.20) versus  $\frac{m_2}{m_1}$  for intermediate view.

## 5.4 Rotational effects on line source function

Now we intend to study how the source functions change when the rotational velocities change. We have made use of Von Zeipel's law (1924) which states that the emergent flux of total radiation over the surface of a rotationally (and/or tidally) distorted star in radiative equilibrium varies proportionately to the local gravity. This law has been used for obtaining the incident radiation at  $\tau = \tau_{max}$  and for calculating the source functions the medium by using the comoving frame solution of radiative transfer in *Chapter 4* equation (4.35-4.36).

### 5.4.1 Brief description of the method and Computational procedure

Now we shall consider only the rotation of a single star. According to the Von Zeipel's law, the flux of radiation at a given point is proportional to the local gravity. Von Zeipel's law is given by

$$F_n = -\frac{C}{\kappa\rho} \frac{dp}{dn}, \quad (5.25)$$

where  $F_n$  is the flux of radiant energy across a level surface of constant potential,  $C$  is the velocity of light,  $K$  is the absorption coefficient,  $\rho$  is the density,  $p$  is the pressure and  $dn$  is the normal distance between adjacent level surface. If  $\psi$  is the total potential (i.e., sum of potentials due to self gravitation, rotation and tidal interaction) then the radiant flux is given by

$$F_n \sim \frac{d\psi}{dn}. \quad (5.26)$$

$$\frac{d\psi}{dn} = -g, \quad (5.27)$$

where  $g$  is the local gravity. For rotationally distorted star without tidal forces from external sources (see Peraiah 1970)

At the bottom of the atmosphere, we have introduced the incident radiation proportional to  $g$  given by equations (5.26) and (5.27) and this is written as

$$\mathbf{U}_{n+1}^-(\tau = T, \mu_j) = \frac{g}{N\mu_j C_j}, \quad (5.28)$$

so that

$$\begin{aligned} \int \mathbf{U}_{n+1}^-(\tau = T, \mu) \mu d\mu &= \sum \mathbf{U}(\tau = T, \mu_j) \mu_j C_j, \\ &= \sum \frac{g}{N\mu_j C_j} \mu_j C_j = g, \end{aligned} \quad (5.29)$$

where  $\mu_j$  and  $C_j$  are roots and weights of the Gauss-Legendre quadrature,  $N$  is the total number of angles and  $T = \tau_{max}$ . This has been on the grounds that radiation is incident on the atmosphere in spherically symmetric approximation. Here  $\mathbf{U}$  is the specific intensity multiplied by  $4\pi r^2$ . By assuming a velocity law and optical depth ( $T=1200$ ), we have solved the line transfer equation equation in comoving frame with the boundary condition given in (5.29). While calculating the gravity  $g$  we have assumed  $x = 1$  (uniform rotation) and the ratio of centrifugal to gravity forces at the equator is set to equal to 0.1, 0.4, and 0.8. The geometrical extension of the medium is taken to be  $\frac{B}{A}=3$  and 10 where  $B$  and  $A$  are the outer and inner radii of the atmosphere with constant velocity gradient. the frequency independent source function is calculated by the formula,

$$S(r) = \int_{-\infty}^{\infty} S(x, r) dx, \quad (5.30)$$

where

$$S_s(x, r) = \frac{\phi(x)}{\beta + \phi(x)} S_L(r) + \frac{\beta}{\beta + \phi(x)} S_c(r), \quad (5.31)$$

$S_c$  is the continuous source function and  $S_L$  is the source function given by

$$S_L(r) = (1 - \epsilon) \int J_x \phi(x) dx + \epsilon B(r), \quad (5.32)$$

$$S_c(r) = B(r), \quad (5.33)$$

where  $B(r)$  is the Planck function,  $J_x$  is the mean intensity,  $\phi(x)$  is the profile function (Doppler) and  $\epsilon$  is the probability per scatter a photon is lost by collisional de-excitation. We have set  $\epsilon = \beta = 0$  in all cases. We have taken  $V_{\text{rot}}$  equal to 1, 4, 8 mean thermal units corresponding to  $f=0.1, 0.4, \text{ and } 0.8$ . The total source functions plotted with respect to the optical depths are given in figures 5.5(a) and 5.5(b) for  $\frac{B}{A}=3$  and 10. respectively. We have considered the maximum expansion velocities  $V_B=0, 3, \text{ and } 6$  as these are sufficient to show the differences due to the velocity gradients. The effects of rotation are to reduce the source function considerably and it is interesting to note that the variation  $S$  runs almost parallel to various velocity gradients. The source functions are reduced considerably when rotational velocities are introduced. The reduction is almost an order of magnitude from  $V_{\text{rot}}=1$  to  $V_{\text{rot}}=8$ . The main reason for dilution is that when rotation increases the equatorial parts tend to extend and the density of radiation field decreases. As we are considering uniform rotation, constant velocity gradients would reduce the radiation field uniformly which explains the reason why the source functions are almost parallel to each other for  $V_{\text{rot}}=1, 4, \text{ and } 8$ . The source functions are very similar for  $\frac{B}{A} = 3$  and 10. When the geometrical extension is increased the fall in the source functions corresponding to  $V_{\text{rot}}$  is large in the case of an atmosphere  $\frac{B}{A} = 10$  than that of  $\frac{B}{A} = 3$ . This is so because we have chosen the same optical depth

in both cases and therefore, the density in the atmosphere with  $\frac{B}{A}=10$  is less than that in the atmosphere with  $\frac{B}{A}=3$ . This effect is enhanced when the rotational velocities are increased.

In figures 5.6 (a) (b) (c) we plotted  $\frac{F_q}{F_c}$  (where  $F_q$  and  $F_c$  being the integrated fluxes at frequency  $X_q$  and in the continuum respectively see *Chapter 4* section(4.3) equations (4.50-4.55)) for  $\frac{B}{A}=3$  the line profiles observed at infinity for  $V_B=0, 3, 6$  mean thermal units respectively. We define the following quantity which is similar (see *Chapter 4*, section (4.3), equation (4.50)),

$$Q = \frac{X_q}{X_{max}} \quad -1 \leq Q \leq 1. \quad (5.34)$$

The purpose of this kind of representation is to accommodate all profiles corresponding to different velocities in a single figure. In each of these figures we have also presented profiles for  $V_{rot}=1, 4, 8$  mean thermal units. In figure 5.6(a) we note that all profiles are symmetric. For  $V_{rot}=1$ , we obtain a profile with a slight emission in the wings. However when  $V_{rot}$  is increased to 4 mean thermal units the wings become boarder whereas the core of the line becomes narrower. When  $V_{rot}$  is increased to 8 mtu the lines becomes broader uniformly and emission in the wings disappear. When the expansion velocity increases we find P-Cygni type profile becoming more prominent when  $V_B = 6$  (see figure 5.6(c)). In figure 5.7 (a), (b), (c) the flux profiles have been plotted for  $\frac{B}{A}=10$ . These are similar to those given in figure 5.6 (a)(b)(c).

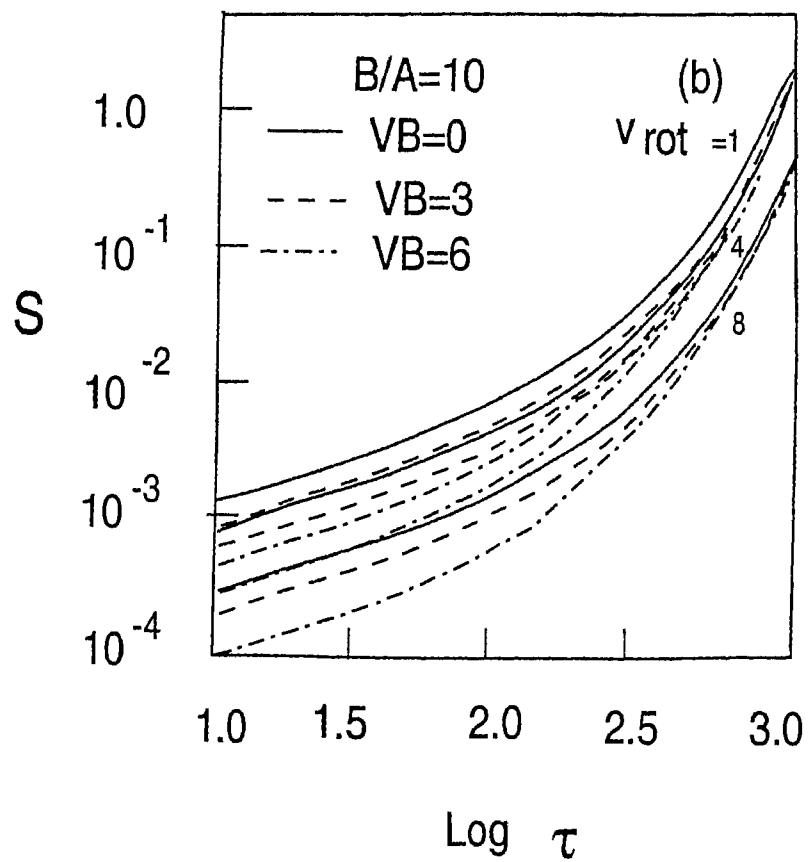
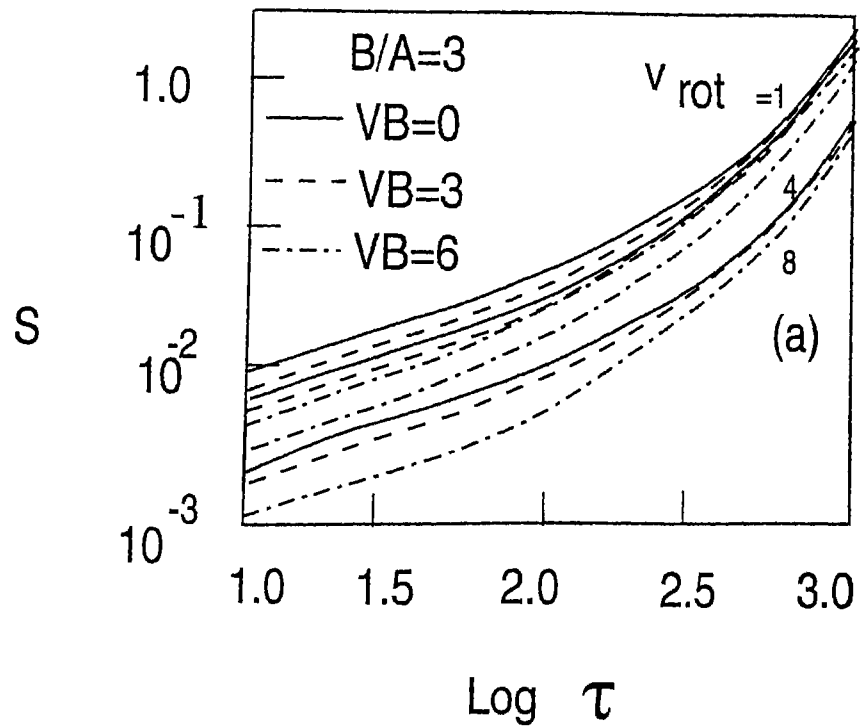


Figure 5.5 : Frequency independent source functions for  $\epsilon = \beta = 0$  for  $\frac{B}{A}=3$  and  $10$

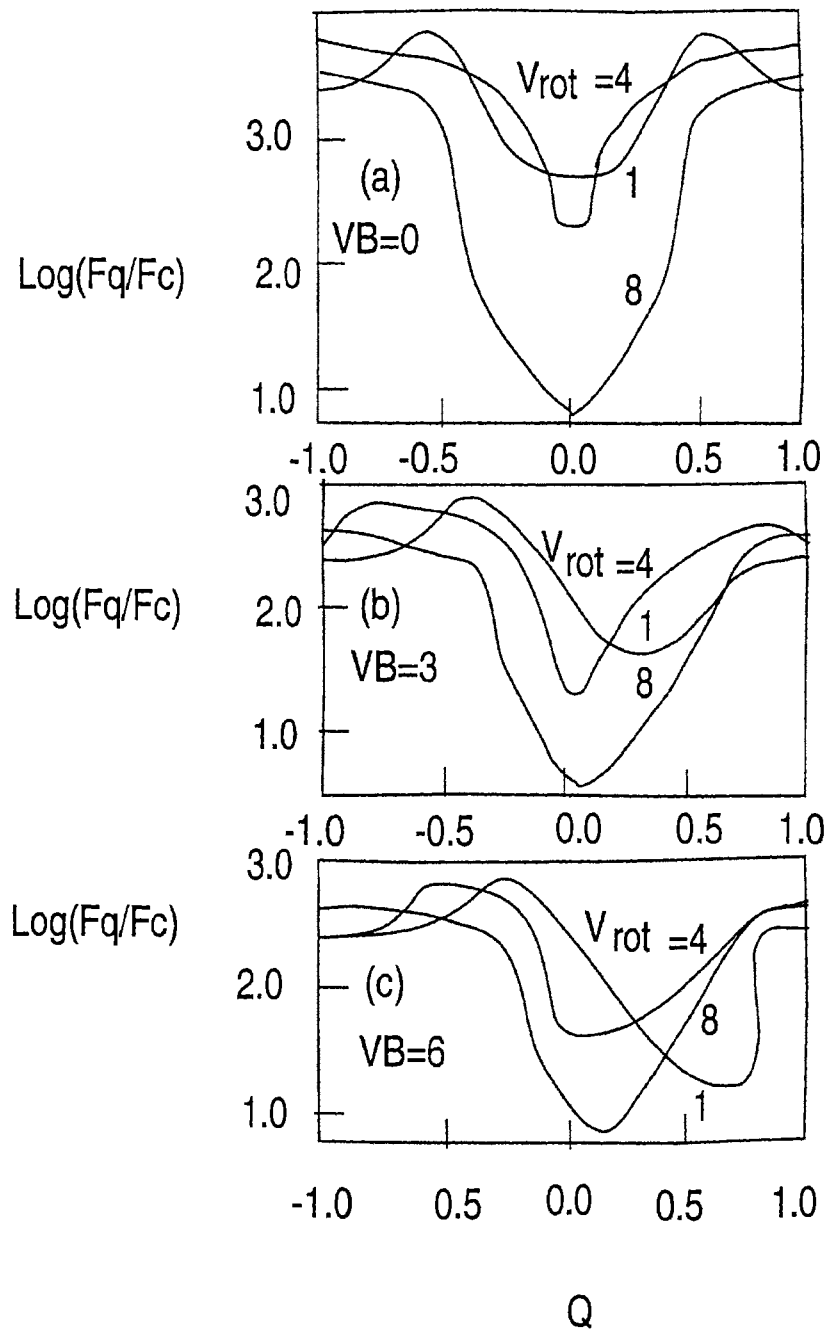


Figure 5.6: Corresponding flux profiles for  $\frac{B}{A}=3$  for figure 5.5(a)

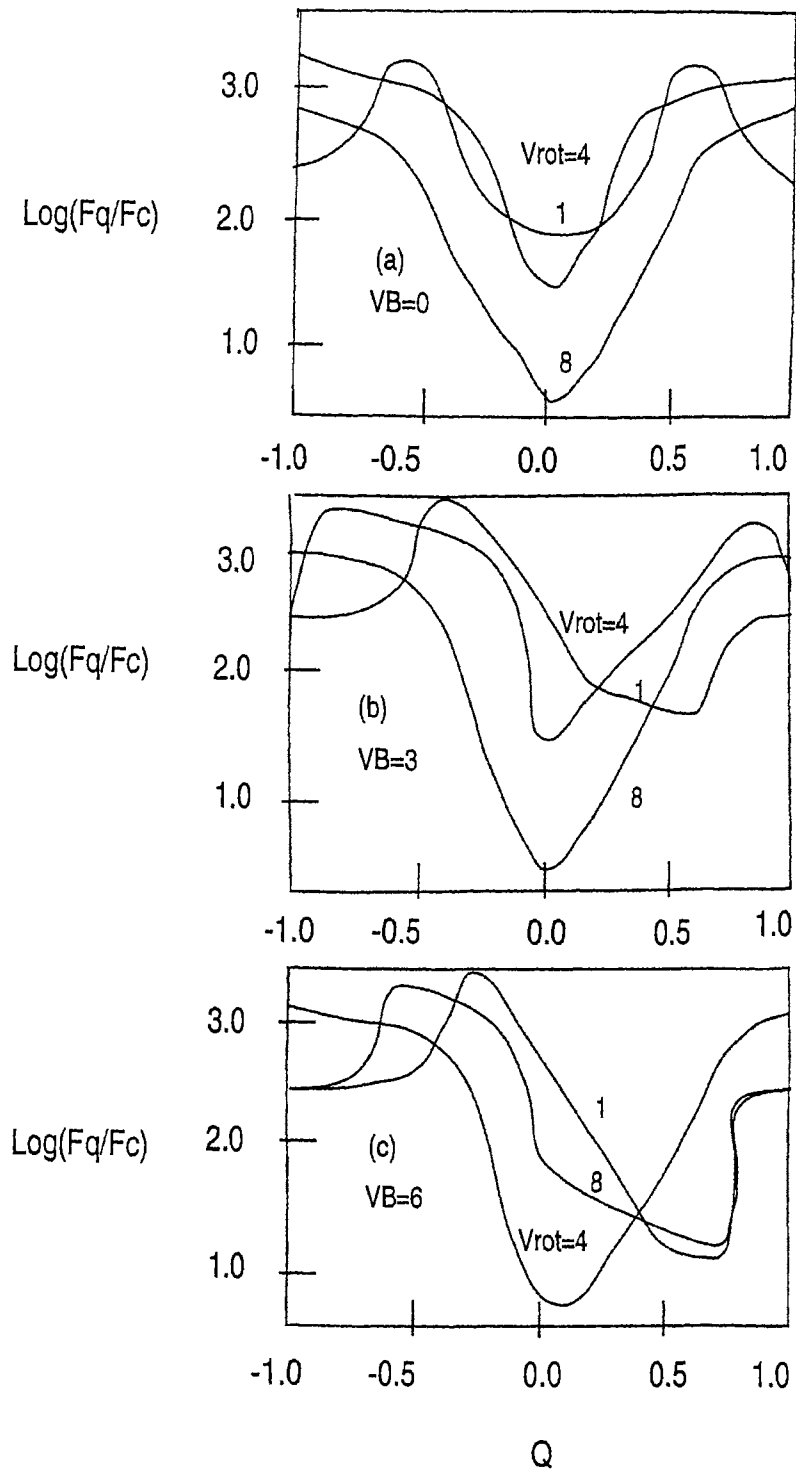


Figure 5.7: Corresponding flux profiles for  $\frac{B}{A}=10$  for figure 5.5(b)

## Chapter 6

# Effects of gravity darkening on spectral lines

### 6.1 Introduction

It is well known that when two components of binary system are sufficiently close to each other, their mutual irradiation is very important. The study of close binary stars is of great importance in stellar astrophysics. The atmospheres of the components of a close binary system are distorted mainly by two physical effects : (1) rotation of the component and (2) the tidal effect due to the presence of its companion. These effects make the atmospheres of these stars non-spherical. de Jager (1992) summarized the problem of non-spherical atmospheres and flows in outer layers of young stars and other objects. Non-sphericity changes the density distribution of the matter through which the radiation passes and as a consequence, the lines formed in such medium are modified. In addition to this, the presence of the secondary component's light falling on such distorted components atmosphere will affect the line profiles formed in these atmospheres. One also encounters the systematic mass motions in the atmospheres of these stars.

In this chapter we compute theoretical line profiles from the extended atmospheres of the components of close binary systems whose surfaces are distorted due to rotation and tidal effects interms of mass ratio of the two component  $\frac{m_2}{m_1}$ , ratio of equatorial radius of the primary to the

distance between the centres of gravity of two components  $\frac{r_e}{R}$ , ratio of centrifugal to gravity forces at equator  $f$  and the ratios of angular velocities at the equator and the pole  $x$ . The line profiles are calculated for different velocity laws and compared their fluxes.

In *Chapter 4* we studied the line transfer in expanding and extended spherically symmetric atmospheres with dust free and dusty medium respectively with radiation incident from the secondary component on the atmosphere of the primary.

Now we shall study the line transfer in the distorted atmospheres. We have to calculate the source function in such media which arises out of the incidence of the radiation from the atmosphere of the secondary component. We describe below the method of calculation.

## 6.2 Calculation of the source functions in the distorted atmosphere

We compute the distorted surface by solving the following 7<sup>th</sup> degree equation described in *Chapter 5*. Although better description of the surfaces are available, they do not change our scheme of computation of the source functions in the distorted atmospheres. This is a simple equation to solve and fast solutions can be obtained easily. The equation for the equipotential surface is given by,

$$\alpha\rho^7 \sin^6 \theta + \beta\rho^5 \sin^4 \theta + (\gamma \sin^2 \theta + J)\rho^3 - (1 - Q)\rho + 1 = 0, \quad (6.1)$$

where

$$J = Q(3 \sin^2 \theta \cos \phi - 1),$$

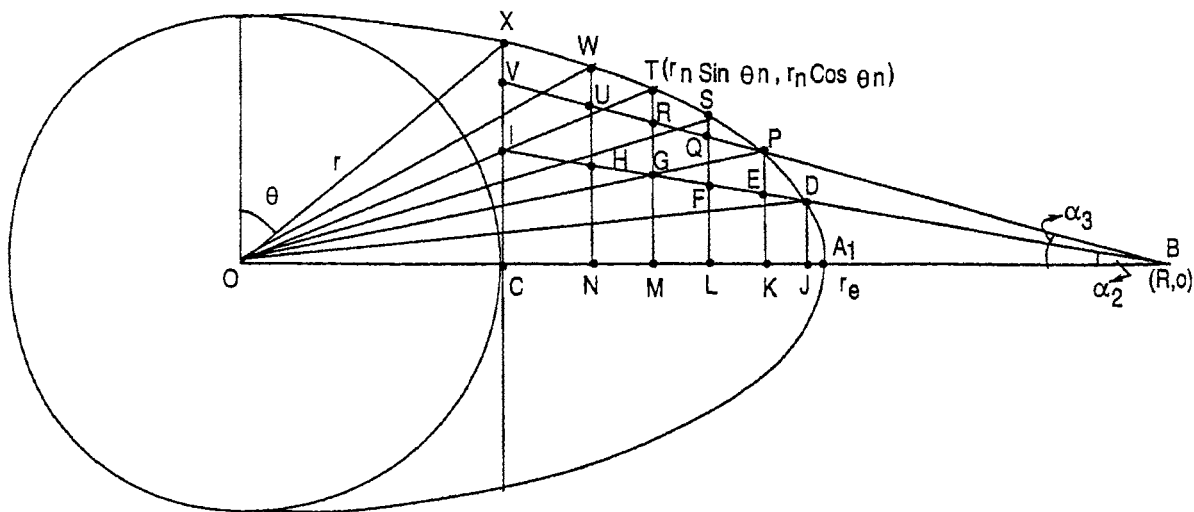


Figure 6.1: Schematic diagram of the distorted atmosphere of the component

and  $\theta$  and  $\phi$  are the colatitude and the azimuthal angles respectively.

Further,  $\rho = \frac{r}{r_p}$ ,  $r$  and  $r_p$  are the radii and the radius at the pole and

$$\alpha = \frac{f(x-1)^2}{6x^2} \left(\frac{r_p}{r_e}\right)^7 ; \quad \beta = \frac{f(x-1)^2}{2x^2} \left(\frac{r_p}{r_e}\right)^5 ;$$

$$\gamma = \frac{f}{2x^2} \left(\frac{r_p}{r_e}\right)^3 ; \quad Q = \frac{1}{2}\mu \left(\frac{r_p}{r_e}\right)^3 ; \quad \mu = \frac{m_2}{m_1} \left(\frac{r_e}{R}\right)^3 ,$$

The ratios  $\frac{r_p}{r_e}$  can be obtained from a third degree equation given by,

$$\left(\frac{r_e}{r_p}\right)^3 - u \left(\frac{r_e}{r_p}\right)^2 - \frac{1}{2} \mu = 0, \quad (6.2)$$

where

$$u = 1 + \frac{f(x^2 + x + 1)}{6x^2} + \mu.$$

Equation (6.1) is solved for various values of  $\theta$  and  $\phi$  for obtaining the surface for given parameters of  $\frac{m_2}{m_1}$ ,  $f$ ,  $x$  and  $\frac{r_e}{R}$ . The solution is obtained by using numerical methods with a starting value of  $\frac{r}{r_p} = 1$ . Equation (6.2) is solved by Newton-Rophson method are described in *Chapter 5*.

We have drawn a schematic diagram in figure 6.1 below for the purpose of computing the source functions. The points O and B are respectively the centers of the primary and secondary which are supposed to be point sources. The rays such as BA<sub>1</sub>, BD, BP ..., etc., from the secondary (B) are incident on the atmosphere at points such as A<sub>1</sub>, D, P, ... etc. These points A<sub>1</sub>, D, P, ..., etc., are joined to the centre of the primary O. Further we draw perpendiculars from these points to the axis OB. These perpendiculars meet the rays at the points as shown in the figure 6.1. We need to find the source functions (1) along the rays A<sub>1</sub>D, BD, BP, ..., etc., to compute the radiation field in the medium generated by the incidence of the light from the secondary. We also need to find the source functions along the perpendiculars such as DJ, PK, SL, ..., etc., to calculate the radiation field along the line of sight and at the observers point. For this we have to calculate their geometrical lengths.

We find the point (or radius of the atmosphere) where the outermost tangent from the point B touches the star. Assume at that, in the case of an unperturbed star OC=r<sub>p</sub>. Specifying the parameters  $x$ ,  $f$ ,  $\frac{r_e}{R}$  and  $\frac{m_2}{m_1}$  and using the equations (6.1) and (6.2) we can find the  $\theta=\theta_c$  where  $r_1 \sin \theta_c=r_p$ . This is done by repeatedly solving equations (6.1) and (6.2) with small values of  $\theta$  ( by steps of 1°). Now we can divide  $(90 - \theta_c)$  into N intervals and compute the radii  $r_n$  to the surface of the distorted reflecting atmosphere. Each radius  $r_n$  to the surface can be computed by using  $\theta_n = 90 - (n - 1)\Delta\theta$ , where  $\Delta\theta=\frac{(90 - \theta_c)}{N}$ . Let x- axis coincide with OB and y- axis be perpendicular to it. Then the x- coordinates of the point C, N, M, L, K, ..., etc., will be  $r_1 \sin \theta_1, \dots, r_{N-1} \sin \theta_{N-1}(=r_e)$  and the y- coordinates all zeros OB. The general coordinates of any ray which meets the surface are  $(r_n \sin \theta_n, r_n \cos \theta_n)$ . The x- coordinate

of  $A_1$  is  $r_{N-1} \sin \theta_{N-1}$ . Therefore,  $BA_1 = R - r_{N-1} \sin \theta_{N-1}$ .

Let the angle made by the ray with CB is  $\alpha$ , then

$$\tan \alpha_{N-1} = \frac{r_{N-1} \cos \theta_{N-1}}{(R - r_{N-1} \sin \theta_{N-1})}$$

Similarly

$$\tan \alpha_n = \frac{r_n \cos \theta_n}{(R - r_n \sin \theta_n)}$$

If we start with

$$\theta = 90^\circ = \theta_1, \text{ then } x = r_e = r_1 \sin 90 = r_1,$$

$$y = 0 \text{ (this is the point } A_1 \text{)}.$$

$$\theta_2: \quad x_2 = r_2 \sin \theta_2, \quad y = r_2 \cos \theta_2, \quad DJ = r_2 \sin \theta_2,$$

$$\tan \theta_2 = \frac{DJ}{JB} = \frac{r_2 \cos \theta_2}{(R - r_2 \sin \theta_2)} = T_2 \text{ (say).}$$

From figure 6.1, we have,

$$OA_1 = r_e = r_1,$$

$$OJ = r_2 \sin \theta_2,$$

$$OK = r_3 \sin \theta_3,$$

$$OL = r_4 \sin \theta_4 \dots, \text{ etc.}$$

$$DB^2 = DJ^2 + JB^2 = r_2^2 \cos^2 \theta_2 + (R - r_2 \sin \theta_2)^2,$$

$$EB^2 = EK^2 + KB^2 = (1 + T_2^2)(R - r_3 \sin \theta_3)^2,$$

$$FB^2 = FL^2 + LB^2 = (1 + T_2^2)(R - r_4 \sin \theta_4)^2, \dots, \text{ etc.}$$

$$DJ = r_2 \cos \theta_2$$

$$EK = T_2 \cdot KB = T_2(R - OK) = T_2(R - r_3 \sin \theta_3)$$

$$FL = T_2 \cdot LB = T_2(R - OL) = T_2(R - r_4 \sin \theta_4)$$

$$GM = T_2 \cdot MB = T_2(R - OM) = T_2(R - r_5 \sin \theta_5), \dots, \text{ etc.}$$

$$\begin{aligned}
A_1B &= R - r_e (= r_1), \\
JB &= R - r_2 \sin \theta_2, \\
KB &= R - r_3 \sin \theta_3, \\
LB &= R - r_4 \sin \theta_4, \dots, \text{etc.} \\
\tan \alpha_3 &= T_3 = \frac{PK}{KB} = \frac{r_3 \cos \theta_3}{(R - r_3 \sin \theta_3)}. \\
PK &= r_3 \cos \theta_3, \\
QL &= T_3.LB = T_3(R - r_4 \sin \theta_4), \\
RM &= T_3.MB = T_3(R - r_5 \sin \theta_5), \\
UN &= T_3.NB = T_3(R - r_6 \sin \theta_6), \dots, \text{etc.}, \\
PB^2 &= PK^2 + KB^2 = r_3^2 \cos^2 \theta_3 + (R - r_3 \sin \theta_3)^2, \\
QB^2 &= QL^2 + LB^2 = (1 + T_3^2)(R - r_4 \sin \theta_4)^2, \\
RB^2 &= RM^2 + MB^2 = (1 + T_3^2)(R - r_5 \sin \theta_5)^2, \dots, \text{etc.} \\
\tan \alpha_n &= \frac{r_n \cos \theta_n}{(R - r_n \sin \theta_n)}. \tag{6.3}
\end{aligned}$$

We need to know the geometrical length of all the above segments for the computation of the optical depths and source functions along these segments.

We consider an atmosphere of the primary whose radius is twice as large as that of the star(primary). The velocity of expansion varies linearly with the radius. Thus, the variation of density is according to the law  $\rho \sim \frac{1}{r^3}$  which obeys the law of conservation of mass that is  $4\pi r^2 \rho v = \text{constant} (\dot{M})$  where  $r$  is the radius,  $\rho$  is the density,  $v$  is the velocity of expansion and  $\dot{M}$  is rate of mass loss. We set the inner radius equal to  $5 \times 10^{11}$  cm and outer radius is  $10^{12}$  cm. The distortion is considered from the outer radius  $10^{12}$  cm of the atmosphere. We have used a value of electron density equal to  $10^{14}$  cm $^{-3}$ . We compute the source

functions along the rays BA<sub>1</sub>JK ..., BDEFG ..., BPQR ..., etc., using the above data and using the rod model (which is described in detail in *Chapter 4* section (4.1.1)) with the incident radiation given at points A<sub>1</sub>, D, P, S, ..., etc., for the rays passing through these points. We have given the incident radiation at the points A<sub>1</sub>, D, P, S, ..., etc., equal to  $\left(\frac{\sigma T_e}{r_\alpha^2}\right) \cos \alpha$ , where  $\sigma$  is the Stefan Boltzmann constant,  $T_e$  is the effective temperature of the component centered at B and  $\alpha$ s are the angles made by the ray with the axis OB and  $r_\alpha$  correspond to the ray lengths such as BA<sub>1</sub>, BD, BP, ..., etc.

### 6.3 Result and discussion

The source functions for the self radiation ( $S_s$ ) are calculated using the procedure described in *Chapter 4*. These are represented by the (—) line in figure 6.2 (a-f) with the scale given on the left side of the graph. The source functions along the rays ( $S_r$ ) are represented by the (- - - -) lines whose scale is given on the right side of the graph. The combined source function ( $S = S_s + S_r$ ) are represented by the (- · - · - · - ·) lines. The parameters are given in the captions corresponding to the rays A<sub>1</sub>C, DI, PV, ..., etc., are plotted against the distances  $R_{imp}=A_1O$ , JO, KO, ..., etc. The ray corresponding to A<sub>1</sub>C is labelled as 1 and that corresponding to DI will be ray number 2 and so on. We plotted the source functions for 24 rays. In practice we can compute sufficient number of rays to suit the desired accuracy. We labelled rays 1, 10, 15, 20, 24. In figure 6.2 (d-f). The curves for  $S$  the total source function (- · - · - · - ·) are not seen because source functions are much larger than those of self radiation by a factor of 10<sup>4</sup>. Addition of the values of  $S_r$  and  $S_s$  do not differ from those of  $S_r$  (see the scales on the right and

left of the graph). However, the results in figure 6.2(a-c) show all the three source functions  $S_s$ ,  $S_r$  and  $S$  through solid (—), dashed (- - - -), and dash and dot (- · - · - · - ·) curves respectively. The source function labelled corresponding to the ray along  $A_1O$  and that labelled 2 correspond to the ray DEF, ..., etc. As the incident radiation at the point  $A_1$  is maximum ( $\cos \alpha = 1$ ), the source function along the ray  $A_1O$  is maximum at  $A_1$  and slowly reduced in the interior points in the direction of  $O$  along the axis. The behaviour of all the rays from (1 to 24) show the same behaviour.

Figures 6.3 (a-f) give the source functions along the rays  $A_1O$ , DI, PV, ..., etc., labelled as 1, 2, 3, ..., etc, versus the optical depths along the rays 1, 2, 3, ..., etc., respectively for the corresponding parameters figures 6.2 (a-f). The curve labelled 1 correspond to the ray  $A_1O$  which is the longest as it is along the axis  $A_1O$ , ( $\cos \alpha = 1$ ) and the source function labelled 24 correspond to the ray with  $\alpha = \alpha_{max}$  or  $\cos \alpha$  is minimum ( $0 < \alpha < \frac{\pi}{2}$ ). We measured the optical depths from from the points of incidence of the rays at such as  $A_1$ , D, P, ..., etc... At these points, the source function is maximum for each ray and slowly falls as the optical depth increases along the ray towards the interior of the distorted medium of the atmosphere and maximum for each ray.

Figures 6-4 (a-f) give the line profiles at the observers point. these profiles correspond to the parameters for which figures 6.2 (a-f) and the figures 6.3 (a-f) are drawn. The profile with (—) line is due to the self radiation while the profiles with (- - - -) is due to the incident radiation and the (- · - · - · - ·) curve represent the profile due to the combined source function  $S = S_s + S_r$  represented by the right side scale of the these figures. It is interesting that while the profile due to the self

radiation is an absorption profile, those due to incident radiation and combination of self and incident radiation are emission profiles.

Figure 6.5 - 6.9 contain these panels each. The first panel (a) contains the ray source functions against the total optical depths for rays 1, 6, 12, and 18. The graphs are given for  $\frac{r_e}{R} = 0.1, 0.3, \text{ and } 0.5$ . The graphs in the panel(b) contain the corresponding source functions  $S(= S_r + S_s)$  with respect to the  $R_{imp}$ . The third panel (c) contain the corresponding profiles along the line of sight. The line fluxes  $\frac{F_Q}{F_C}$  are plotted against normalized frequency  $Q$  defined in *Chapter 4* section 4.3 equation (4.50-4.52). Figure 6.5 (c) contain the profiles in a stationary atmosphere and one obtains symmetric lines. The self radiation produces absorption profiles while the incident radiation produces emission profiles and the combination of the self and incident radiation produces emission profiles. Figure 6.6 gives the results for an expanding atmosphere with  $V_A=0$  and  $V_B=10$  mtu. The profiles due to the self radiation is almost non-existent and while those due to incident radiation and combination of self and incident radiation are prominent emission line with P Cygni characteristics. There is a perceptible change in the profiles when the parameter  $\frac{r_e}{R}$  is changed from 0.1 to 0.3 and 0.5. Figures 6.7 , 6.8. and 6.9 show same features as those shown in figure 6.6.

$$S = S_r + S_s, \quad (6.4)$$

along the line of sight are given in figure 6.4 (a-f).

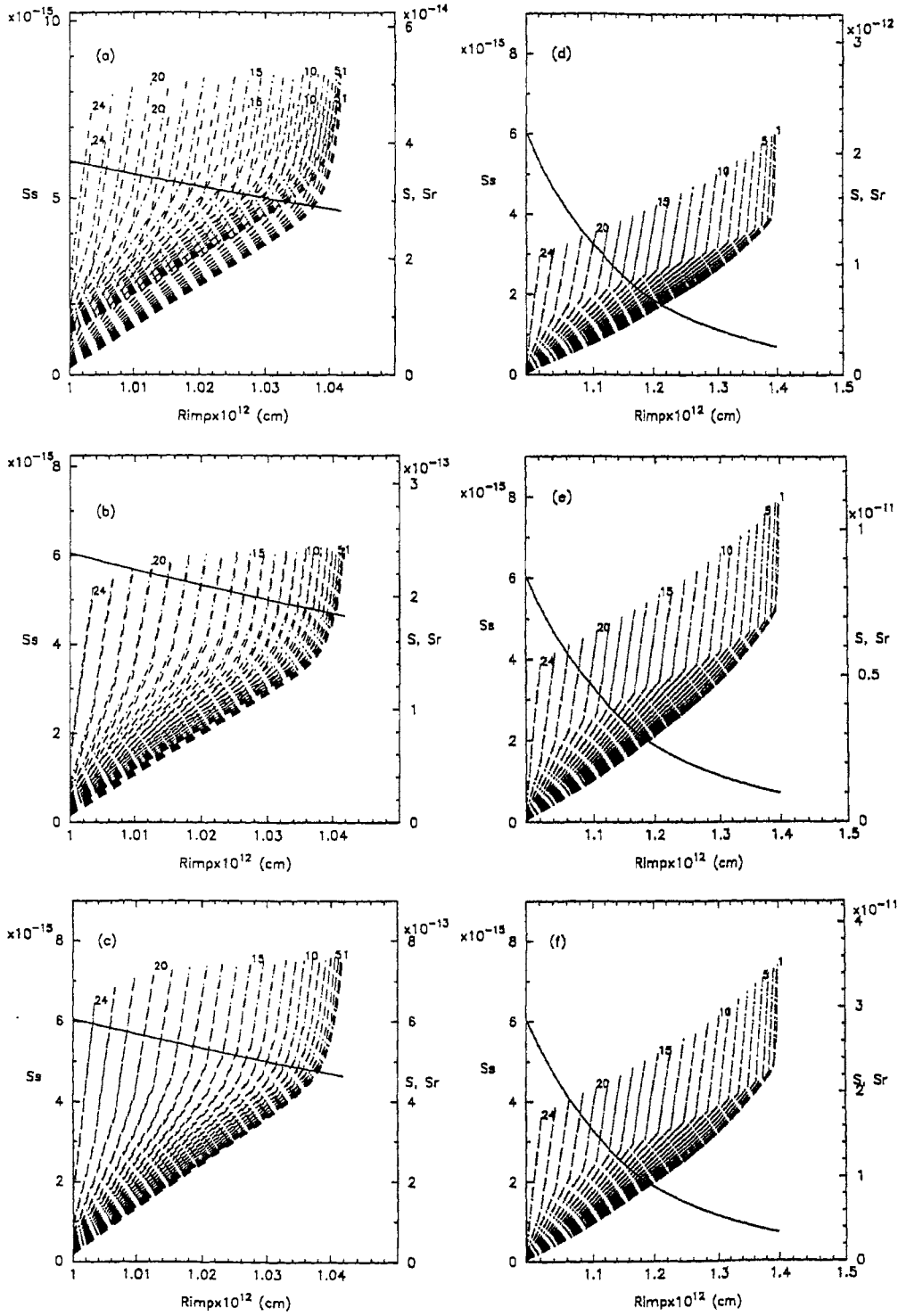


Figure 6.2(a)-(f): Source functions along the rays inside the distorted respect to the distances along the axes  $OA_1$  (see figure 6.1) (a)  $T_* = 20000K$ ,  $T_c = 20000K$ ,  $\frac{r_s}{R} = 0.1$ ,  $f = 0.1$ ,  $\frac{m_2}{m_1} = 1$  ( where  $T_*$  is the temperature of the primary,  $T_c$  is the temperature of the secondary component) (b)  $T_* = 20000K$ ,  $T_c = 30000K$ ,  $\frac{r_s}{R} = 0.1$ ,  $f = 0.1$ ,  $\frac{m_2}{m_1} = 1$  (c)  $T_* = 20000K$ ,  $T_c = 40000K$ ,  $\frac{r_s}{R} = 0.1$ ,  $f = 0.1$ ,  $\frac{m_2}{m_1} = 1$  (d)  $T_* = 20000K$ ,  $T_c = 20000K$ ,  $\frac{r_s}{R} = 0.5$ ,  $f = 0.5$ ,  $\frac{m_2}{m_1} = 0.1$  (e)  $T_* = 20000K$ ,  $T_c = 30000K$ ,  $\frac{r_s}{R} = 0.5$ ,  $f = 0.5$ ,  $\frac{m_2}{m_1} = 0.1$  (f)  $T_* = 20000K$ ,  $T_c = 40000K$ ,  $\frac{r_s}{R} = 0.5$ ,  $f = 0.5$ ,  $\frac{m_2}{m_1} = 0.1$

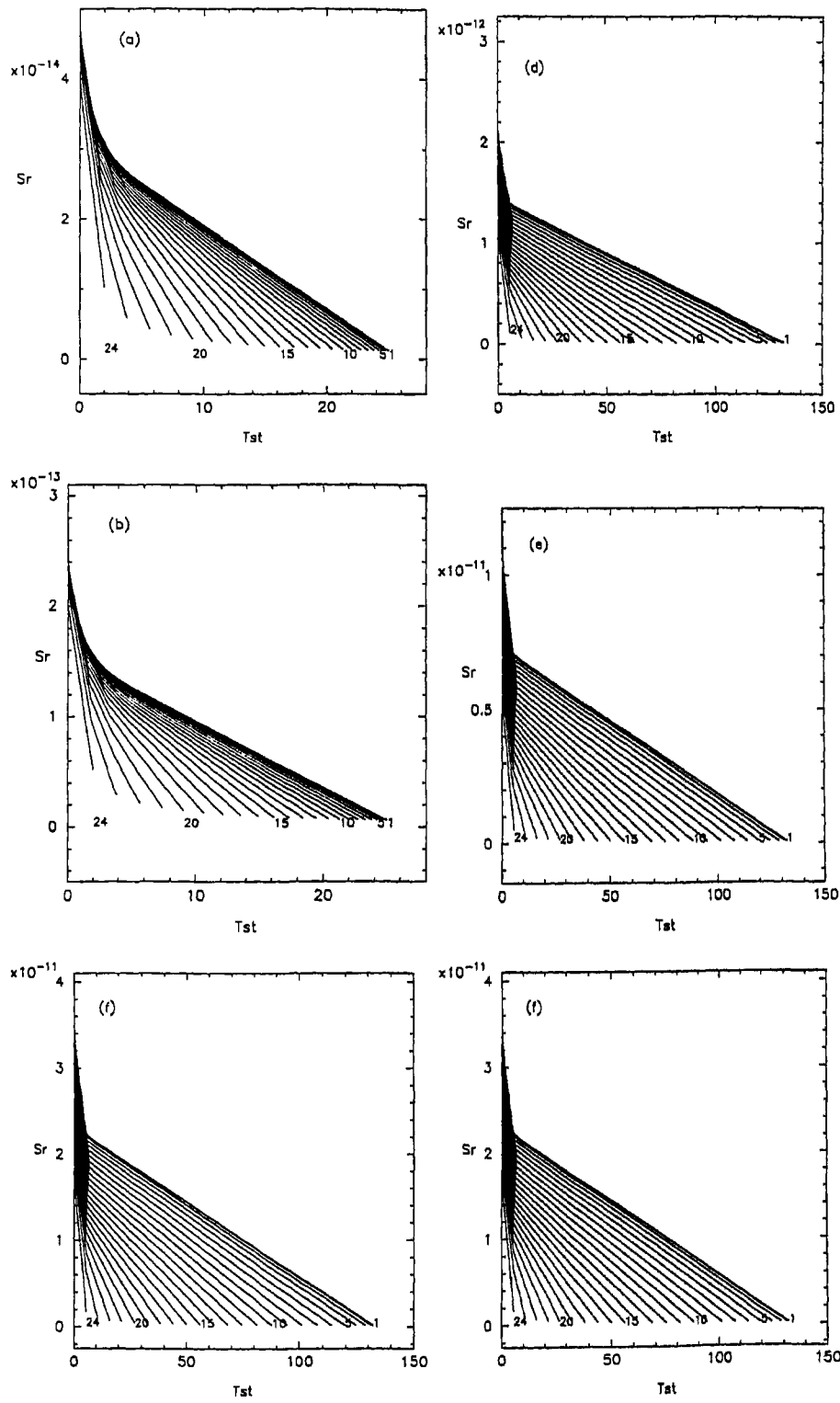


Figure 6.3(a)-(f): The source functions are plotted against the optical depths measured along the rays such as  $A_1JKL, \dots, DEFG, \text{etc.}$ , (a)  $T_* = 20000K, T_c = 20000K, \frac{r_c^e}{R} = 0.1, f = 0.1, \frac{m_2}{m_1} = 1$  (b)  $T_* = 20000K, T_c = 30000K, \frac{r_c^e}{R} = 0.1, f = 0.1, \frac{m_2}{m_1} = 1$  (c)  $T_* = 20000K, T_c = 40000K, \frac{r_c^e}{R} = 0.1, f = 0.1, \frac{m_2}{m_1} = 1$  (d)  $T_* = 20000K, T_c = 20000K, \frac{r_c^e}{R} = 0.5, f = 0.5, \frac{m_2}{m_1} = 1$  (e)  $T_* = 20000K, T_c = 30000K, \frac{r_c^e}{R} = 0.5, f = 0.5, \frac{m_2}{m_1} = 1$  (f)  $T_* = 20000K, T_c = 40000K, \frac{r_c^e}{R} = 0.5, f = 0.5, \frac{m_2}{m_1} = 1$

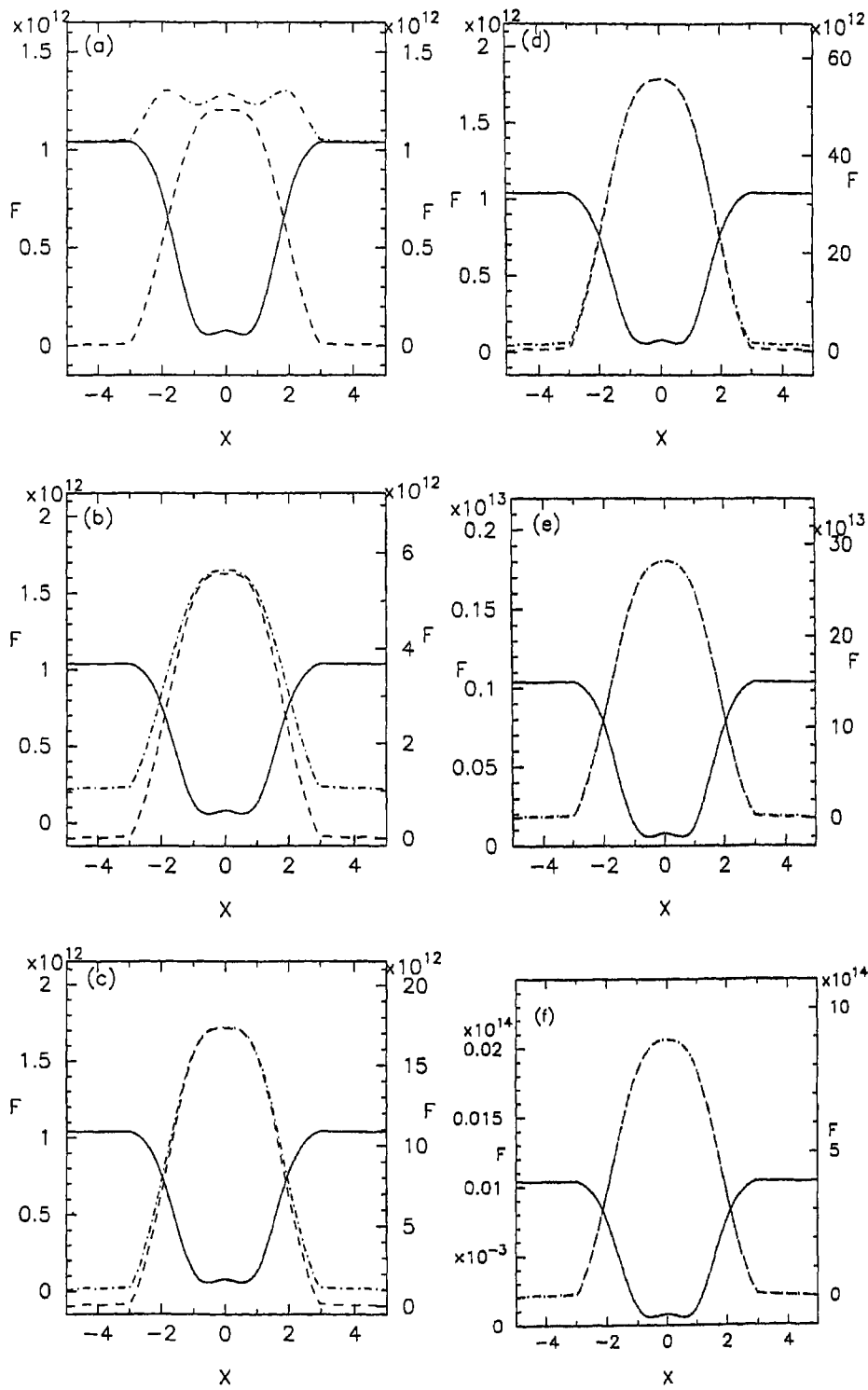


Figure 6.4(a)-(f): The fluxes are plotted against the frequency (a)  $T_* = 20000K$ ,  $T_c = 20000K$ ,  $\frac{r_e^e}{R} = 0.1$ ,  $f = 0.1$ ,  $\frac{m_2}{m_1} = 1$  (b)  $T_* = 20000K$ ,  $T_c = 30000K$ ,  $\frac{r_e^e}{R} = 0.1$ ,  $f = 0.1$ ,  $\frac{m_2}{m_1} = 1$  (c)  $T_* = 20000K$ ,  $T_c = 40000K$ ,  $\frac{r_e^e}{R} = 0.1$ ,  $f = 0.1$ ,  $\frac{m_2}{m_1} = 1$  (d)  $T_* = 20000K$ ,  $T_c = 20000K$ ,  $\frac{r_e^e}{R} = 0.5$ ,  $f = 0.5$ ,  $\frac{m_2}{m_1} = 1$  (e)  $T_* = 20000K$ ,  $T_c = 30000K$ ,  $\frac{r_e^e}{R} = 0.5$ ,  $f = 0.5$ ,  $\frac{m_2}{m_1} = 1$  (f)  $T_* = 20000K$ ,  $T_c = 40000K$ ,  $\frac{r_e^e}{R} = 0.5$ ,  $f = 0.5$ ,  $\frac{m_2}{m_1} = 1$

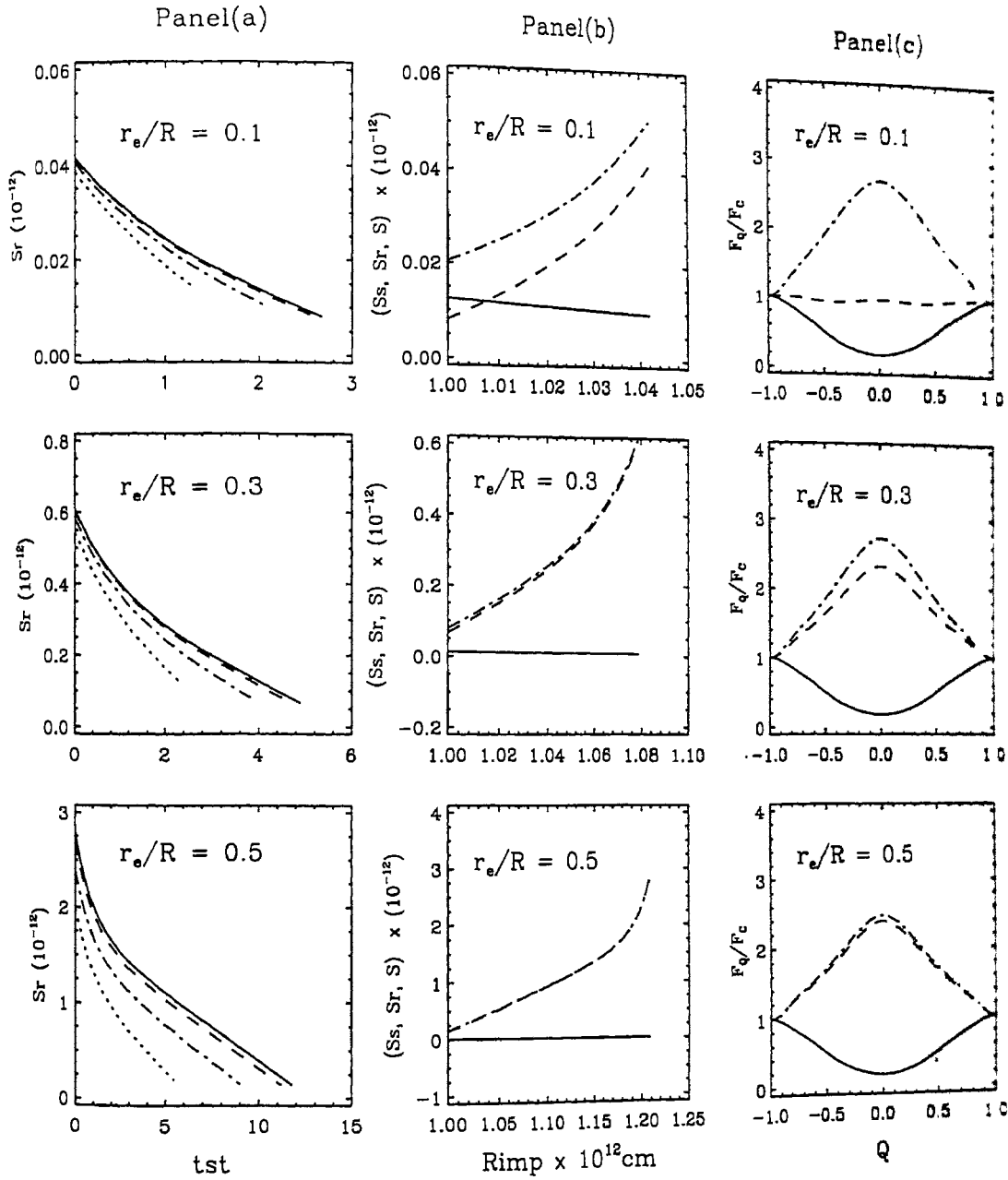


Figure 6.5: Panel (a) shows the results for  $\rho \sim \frac{1}{r}$ ;  $v \sim \frac{1}{r}$   $T_* = 20000K$ ,  $T_c = 20000K$ .  $V_A = 0$ ,  $V_B = 0$ ,  $f=0.1$ ,  $\frac{m_2}{m_1}=1$ ,  $x = 1$ . The ray source functions versus the optical depths along the ray for  $\frac{r_e}{R} = 0.1, 0.3, 0.5$ . (—) line for ray 1, (- - -) ray 6, (- . . . .) ray 12 and (. . . .) ray 18. Panel (b) shows the source functions versus  $R_{imp}$  for ray 12 and (. . . .) ray 18. Panel (b) shows the source functions versus  $R_{imp}$  for ray 12 and (. . . .) ray 18. Source functions for self radiation (—) ( $S_s$ ), distorted source function (- - -) ( $S_r$ ), Total source function (S) (- . . . .) are plotted for  $\frac{r_e}{R} = 0.1, 0.3, 0.5$ . Panel (c) shows flux profiles corresponding to the source function given in panel (b). Fluxes due to self radiation (—), fluxes due to distorted source function (- - -), fluxes due to total source function (- . . . .)

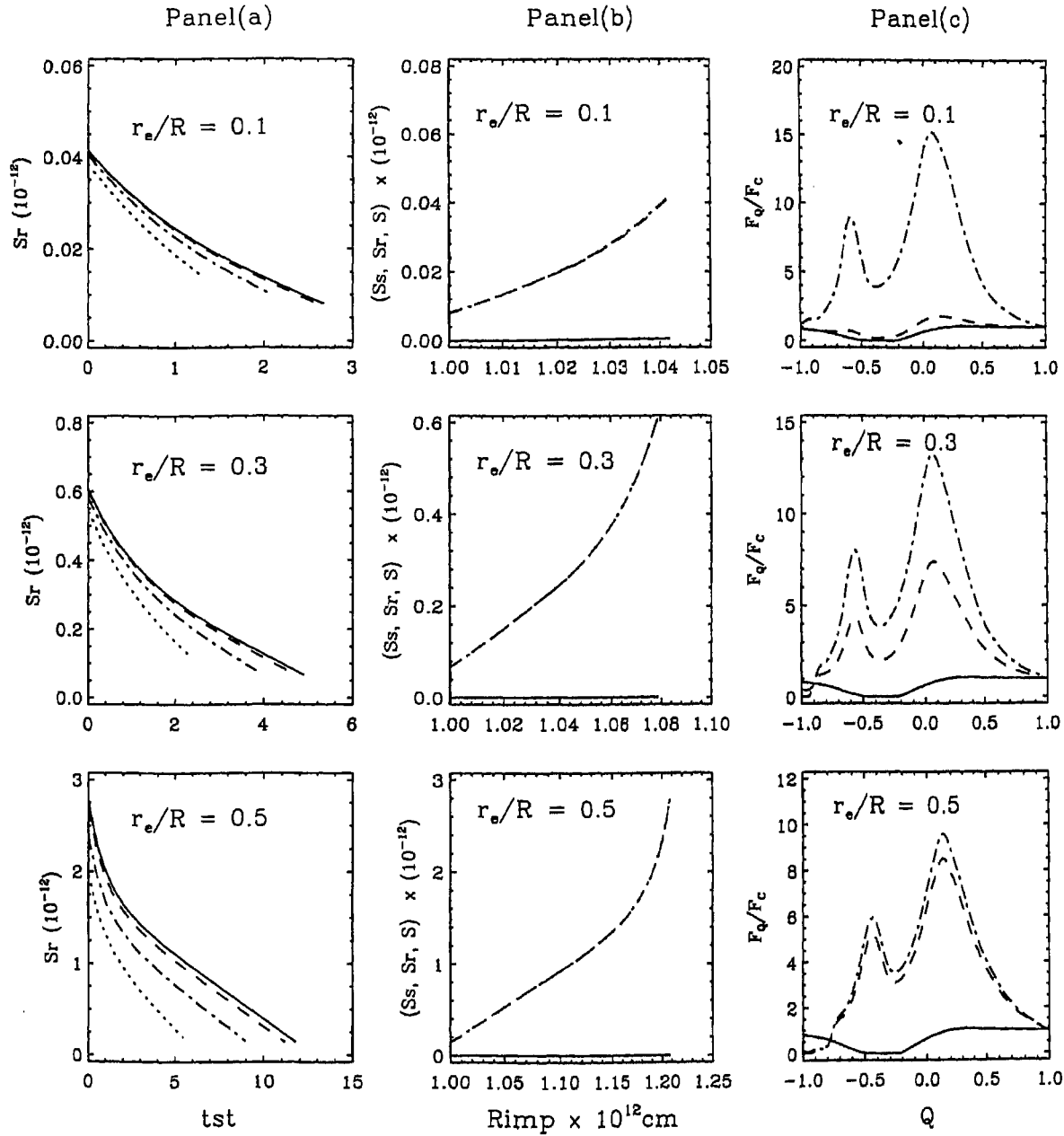


Figure 6.6: Panel (a) is same as those in figure 6.5 Panel (a) with  $V_A=0$ ; and  $V_B=10$  mtu (mean thermal units): Panel (b) is same as those in figure 6.5 Panel (b) with  $V_A=0$ ; and  $V_B=10$  mtu (mean thermal units): Panel (c) is same as those in figure 6.5 Panel (c) with  $V_A=0$ ; and  $V_B=10$  mtu (mean thermal units)

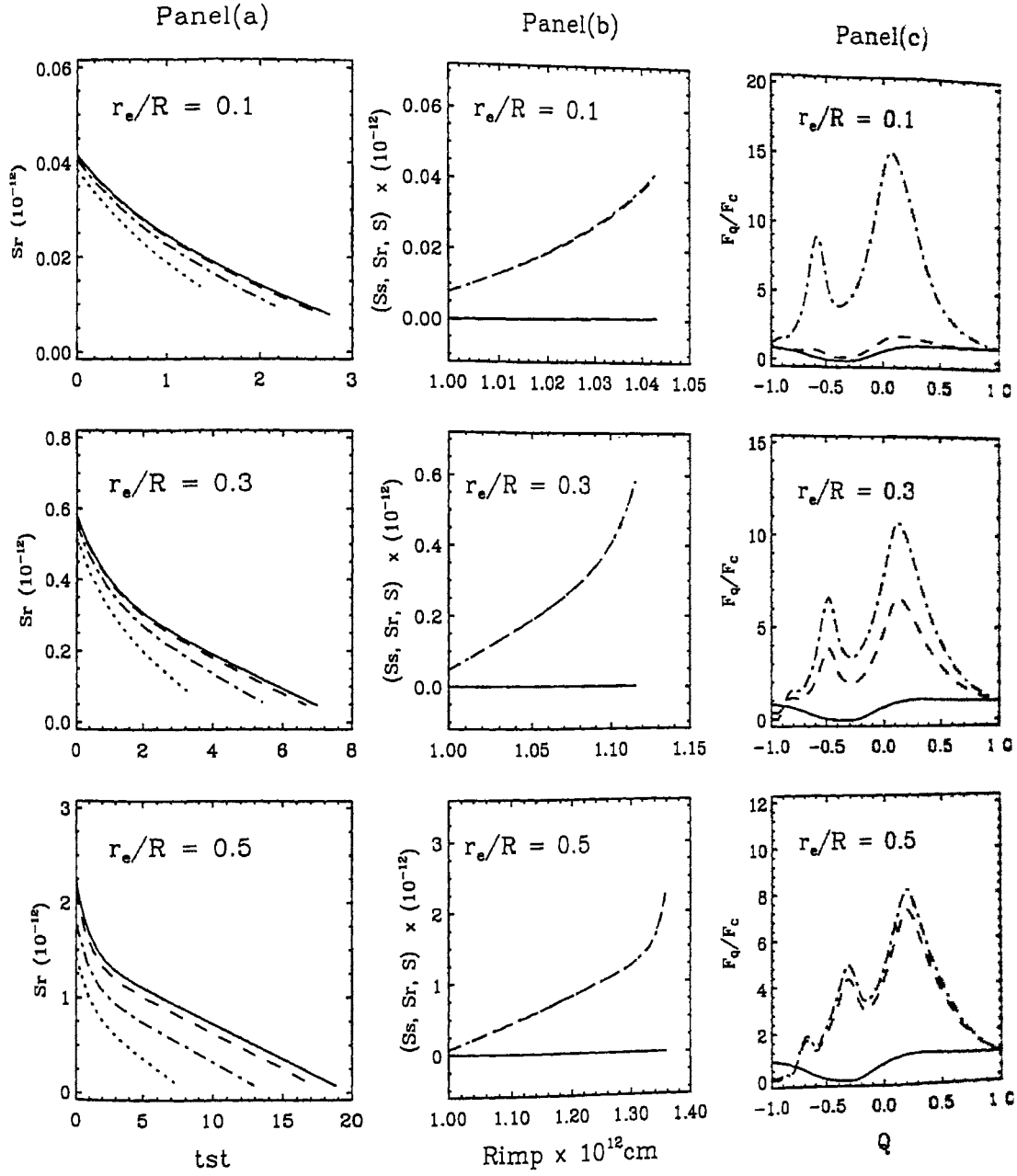


Figure 6.7: Panel (a) is Same as those in figure 6.6 Panel (a) but  $\frac{m_2}{m_1}=2$ : Panel (b) is same as those in figure 6.6 Panel (b) but with  $\frac{m_2}{m_1}=2$ : Panel (c) is same as those in figure 6.6 Panel (c) but with  $\frac{m_2}{m_1}=2$

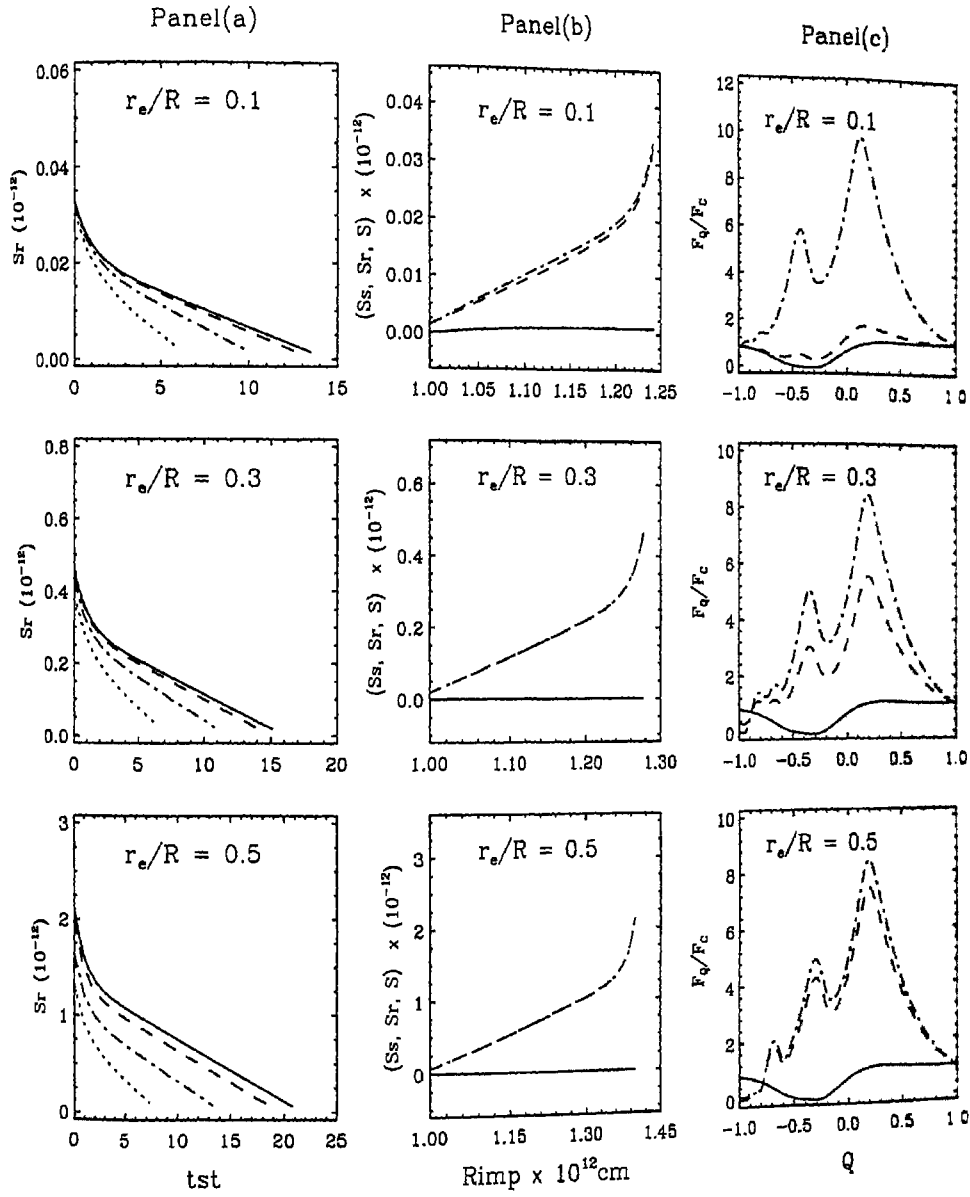


Figure 6.8: Panel (a) is same as those in figure 6.6 Panel (a) but  $f=0.5$ : Panel (b) is same as those in figure 6.6 Panel (b) but with  $f=0.5$ : Panel (c) is same as those in figure 6.6 Panel (c) but with  $f=0.5$

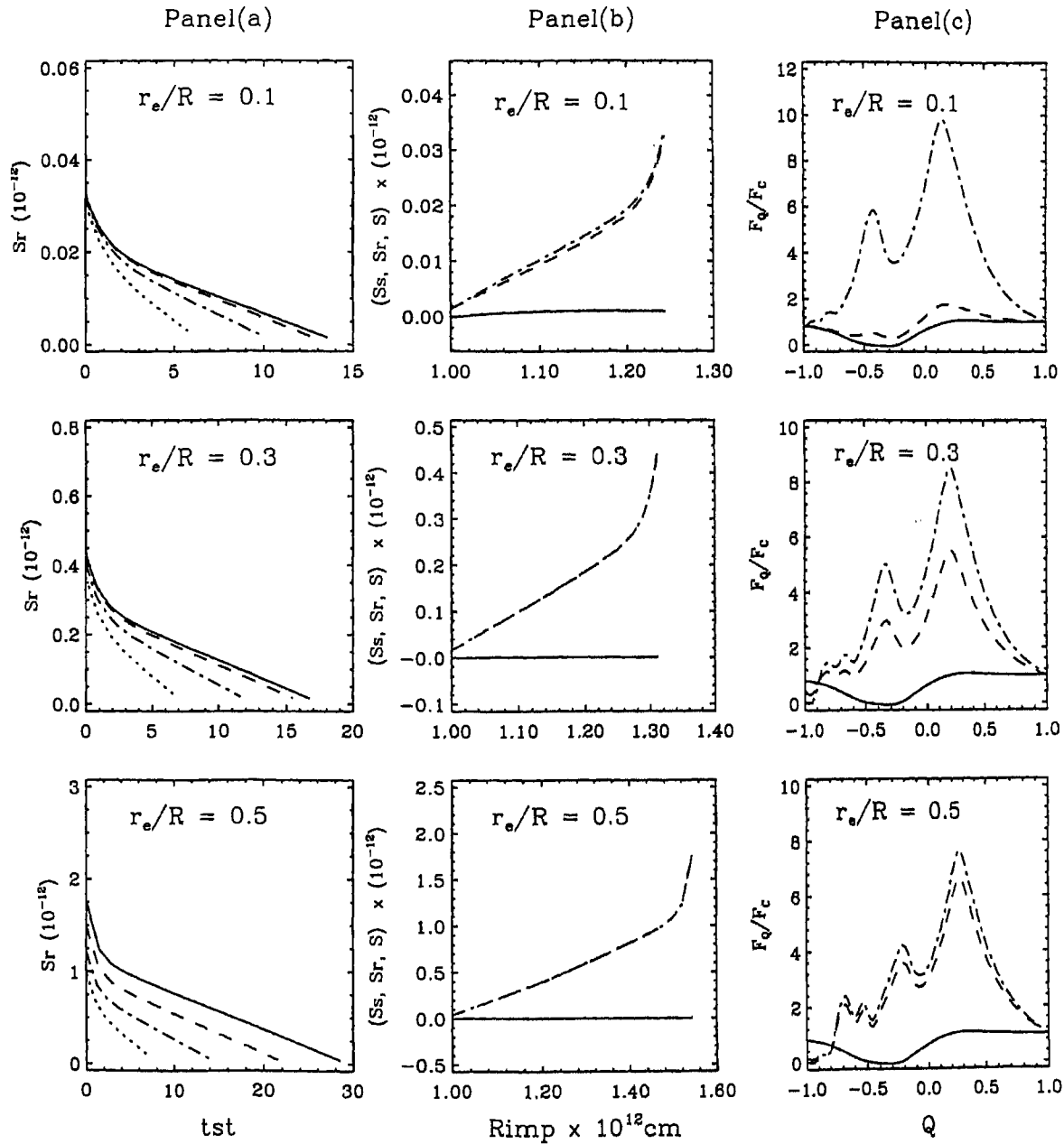


Figure 6.9: Panel (a) is same as those in figure 6.7 Panel (a) but  $f=0.5$ : Panel (b) is same as those in figure 6.7 Panel (b) but with  $f=0.5$ : Panel (c) is same as those in figure 6.7 Panel (c) but with  $f=0.5$

## Chapter 7

### Conclusions

#### 7.1 Discrete space theory of radiative transfer

- We have given a concise description of the method of obtaining the solution of monochromatic radiative transfer equation in spherical symmetry, equation of transfer in comoving frame in the presence of dust and the calculation of line profiles for an observer at infinity. These solutions are used to calculate self radiation of the primary star in a binary system.

#### 7.2 Incident radiation from a point source

- We found that maximum radiation comes from intermediate points of the atmosphere, the reason being that we have combined radiation from the star together with the incident radiation from a point source outside the star.
- We also calculated the effects of irradiation from a point source observed at infinity. The radiation is calculated and compared with two approximations i.e., plane parallel and the spherical symmetry. In plane parallel case the limb is darker than the centre. When the electron density is increased the irradiance brightens the limb but when combined with self radiation the same variation is noticed.

- In spherical case (i.e.,  $\frac{B}{A} = 1.5$ , where B and A are the outer and inner radius of the star), the limb darkening is noticed. Intensities fall sharply when compared to those in plane parallel approximation. When electron density is increased, the irradiation definitely shows limb brightening and intensities fall gradually but at the limb, they start increasing.

### 7.3 Incident radiation from an extended source

In reality extended source can not be considered as a point source. We extended the method for calculating the radiation field on the primary component when secondary component is an extended source.

- We found that the reflection gradually decreases from the component towards the surface of the outermost layers of the atmosphere, since the medium is illuminated uniformly, the intensities decreasing from inner radius to the outer radius of the star.
- The specific intensities calculated at infinity show marked changes when the plane parallel approximation is replaced by the assumption of spherical symmetry. The surface along the axis facing illumination reflect maximum radiation while the innermost and outermost layers show lesser amount of reflected radiation.
- In plane parallel approximation the law of specific intensities is almost linear and falls rapidly towards the surface, whereas in spherical symmetric case the specific intensities reach maximum and then fall.
- It appears that the law of limb darkening does not depend much on the ratio  $\frac{r_1}{R}$  where  $r_1$  is the outer radius of the star, and R is distance between centers of two components.

- The law of variation of radiation from center to limb depends on whether one considers plane parallel or spherical symmetry geometry and also on the distribution of electron density.
- We also noticed that the limb is darker than the center, when we increased the electron density the irradiance brightens the limb but when combined with self radiation, the same variation is noticed.

#### 7.4 Effects of reflection on spectral lines

- In the next step we studied the effects of reflection on formation of spectral lines in a purely scattering atmosphere, absorbing medium, and partially scattering medium and studied how the line profiles change and how the equivalent widths change when irradiation from the secondary is taken into account. These calculations were done in a static and moving atmospheres. We also computed line profiles when dust is present in the atmosphere. We obtained P-cygni type profiles.

#### 7.5 Distortion due to rotation and tidal forces

We studied the transfer of line radiation in the atmospheres of close binary components whose atmospheres are distorted by the self radiation and tidal forces due to the presence of the secondary component. The distortion is measured in terms of the ratio of angular velocities at the equator and pole, mass ratio of the two components, the ratio of centrifugal force to that of gravity at the equator and the ratio of the equatorial radius to the distance between the centers of gravity. We obtain the equation of the distorted surface by solving a seventh degree equation which contains the above parameters.

- We found that equatorial temperatures fall rapidly for increasing value of  $f$ . In the case of luminosity  $f$  would give smaller values of  $l_1$  ( ratio of luminosity along the line of sight) and vice versa.
- We found that rotation will dilute the radiation field which is similar to the effect of expansion.

## 7.6 Effects of gravity darkening on spectral lines

Transfer of line radiation is studied in such asymmetric atmosphere assuming complete redistribution and a two-level atom approximation. The atmosphere is assumed to be expanding radially. Various black body temperatures are being used to describe the total luminosity of the components for the purpose of irradiation. The line profiles in a stationary atmosphere are symmetry. The self radiation produces absorption profiles while the incident radiation produces emission profiles and the combination of the self and incident radiation produces emission profiles.

- In an expanding atmosphere with  $V_A=0$  and  $V_B=10$  mtu the profiles due to the self radiation is almost non-existent and while those due to self and incident radiation are prominent emission lines with P Cygni characteristics. There is a perceptible change in the profiles when the parameter  $\frac{r_e}{R}$  is changed from 0.1 to 0.3 and 0.5.
- The same variation is seen in other velocity laws.
- We have developed a method of obtaining radiation field along the spherical surface irradiated by an external point source, extended source of radiation as first step to understand the reflection effect in close binary systems. And also the method has been extended to the

case of atmospheres distorted due to self rotation of the component and tidal effects due to the presence of its companion. We notice that the expansion of the medium produces P Cygni type profiles and the irradiation enhances the emission in the lines although the equivalent widths reduce considerably. Finally we suggest that while modeling the binary system one has to consider the effects of reflection.

- ⊕ In future we would like consider reflection model for light curves of close binary systems considering multiple reflections and Roche geometry ( primary component heats the secondary component and secondary component heats the primary component).
- ⊕ We also would like to consider the reflection effect in 3-D geometry which will help us to achive accuracy, to approach exactness in the fine computation limit.

## References

- [1] Abramowitz, M., and Stegun, I, 1970, Handbook of Mathematical Functions (New York: Dover)
- [2] Ambarzumian, V. A., 1943, C. R Doklady Sci, U. R. S. S, **38**, 229
- [3] Buerger, P., 1969, ApJ, **158**, 1151
- [4] Buerger, P. F., 1972, ApJ, **177**, 657
- [5] Chandrasekhar, S., 1945, Rev. Mod. Phys. **17**, 138
- [6] Chandrasekhar, S., 1947, ApJ, **106**, 143
- [7] Chandrasekhar, S., 1950, Radiative Transfer, London, Oxford University Press
- [8] Chandrasekhar, S., 1958, Proc. Nat. Acd. Sci. Am **44**, 933
- [9] Chandrasekhar, S., 1960, Radiative Transfer, Dover, New York
- [10] Claret, A., and Gem 'e nez, A., 1992, A & A, **256**, 572
- [11] de Jager, C., 1992, Workshop on Non-isotropic and variable outflows from stars. Baltimore, Maryland, MD (USA). L. Drissen, C. Leitherer, A. Nota (Eds); Astron. Soc. Pac. Conf. Ser. Vol.22 Page 400 Astronomical Society of Pacific. San Francisco CA (USA).
- [12] Dugan, R. S., 1908, PAASA, **1**, 311.
- [13] Eddington, A. S., 1926, MNRAS, **86**, 320.
- [14] Ferguson, D. H., & James, T.A., 1994, ApJS., **94**, 723
- [15] Grant, I. P., 1968, Unpublished Lecture Notes on New Methods in Radiative Transfer

- [16] Grant, I. P., Hunt, G. E., 1968, MNRAS., **141**, 27
- [17] Grant, I. P., Hunt, G. E., 1969a, Proc. Roy. Soc. Lond A., **313**, 183
- [18] Grant, I. P., Hunt, G. E., 1969b, Proc. Roy. Soc. Lond A., **313**, 199
- [19] Grant, I. P., Peraiah, A., 1972, MNRAS, **160**, 239
- [20] Huang, S. S., 1966, Annual Rev. Astron. and Astrophys. **4**, 35
- [21] Ireland, J. G., 1966, Publ. Roy. Obs. Edinburgh **5**, 63
- [22] Kopal, Z., 1954, MNRAS, **114**, 101
- [23] Kopal, Z., 1959, Colse Binary Systems, Chapman and Hall, London
- [24] Kitamura, M., 1954, Publ. Astr. Soc, Japan, bf 5, 114
- [25] Lathrop, K. D., Carlson, B. G., 1967, J. Comp. Physics, **2**, 173
- [26] Lathrop, K. D., Carlson, B. G., 1971, JQSRT **11**, 921
- [27] Matukuma, T., 1950, Sendai Astronomiaj Raportj, **2**, 10
- [28] Mihalas, D., Kunasz., P. B., Hummer, D. G., 1975, ApJ., **202**, 465
- [29] Mihalas, D., 1978, Stellar Atmospheres, 2<sup>nd</sup> edn (San Francisco: W. H. Freeman)
- [30] Milne, E. A., 1927, MNRAS, **87**, 43.
- [31] Napier, W. McD., 1968, Ap & SS., **2**, 61
- [32] Napier, W. McD., Ovenden, M. W., 1970, A & A., **4**, 129
- [33] Nordlund, Å., Vaz, L. P. R., 1990, A & A **228**, 231
- [34] Olsen, E. C., 1968, P. A. S. P., **80**, 185
- [35] Parthasarathy, M., Hack, M., Tektunali, G., 1990, A & A, **230**, 136

- [36] Peraiah, A., 1969, A & A., **3**, 163
- [37] Peraiah, A., 1970, A & A., **7**, 473
- [38] Peraiah, A., 1980, Acta Astron., Vol **30**, No 4, 525
- [39] Peraiah, A., 1982, J. Astrophys. Astron, **3**, 485
- [40] Peraiah, A., 1983a, J. Astrophys. Astron, **4**, 11
- [41] Peraiah, A., 1983b, J. Astrophys. Astron, **4**, 151
- [42] Peraiah, A., 1984, from ' Methods in Radiative Transfer ' ed., W. Kalkofen, Cambridge University Press
- [43] Peraiah, A., Grant, I. P., 1973, J. Inst. Math. Appl., **12**, 75
- [44] Peraiah, A., Wehrse, R., 1978, A & A, **70**, 213
- [45] Peraiah, A., Srinivasa Rao, M., 1983a, J. Astrophys. Astr, **4**, 175
- [46] Peraiah, A., Srinivasa Rao, M., 1983b, J. Astrophys. Astr, **4**, 183
- [47] Peraiah, A., Srinivasa Rao, M., 1998, A & AS, **132**, 45
- [48] Peraiah, A., Varghese, B. A., Rao. M. S., 1987, A & AS., **69**, 345
- [49] Plaut, L., 1959, P. A. S. P., **71**, 167
- [50] Preisendorfer, R. W., 1965, Radiative Transfer on Discrete Spaces, Pergamon Press, Oxford
- [51] Redheffer, R. M., 1962, J. Math. phys, **41**, 1
- [52] Russel, H. N., 1949, Harv. Obs. Circ **452**
- [53] Sobolev, V. V., 1963, A Treatise on Radiative Transfer Van Nostrand, New York
- [54] Srinivasa Rao, M., Peraiah, A., 2000, A & AS, **145**, 525

- [55] Stebbins, J., 1911, ApJ **33**, 395.
- [56] Van de Hulst, H.C., 1965, A New Look at Multiple Scattering, NASA Institute for Space Studies, New York
- [57] Vaz, L. P. R., 1985, Ap & SS., **113**, 349
- [58] Vaz, L. P. R., and Nordlund, Å., 1985, A & A, **147**, 281
- [59] Von Zeipel., 1924, MNRAS., **84**, 702
- [60] Wilson, R. E., 1990, ApJ **356**, 613
- [61] Wilson, R. E., and Devinney E. J., 1971, ApJ, **166**, 605
- [62] Wing, G. M., 1962, An introduction to Transfer Theory John Wiley, New York
- [63] Wehrse, R., Kalkofen, W., 1985, A & A, **147**, 71
- [64] Wood, D. B., 1971, AJ, **76**, 701
- [65] Young, R. K., 1922, Pub. Dominion Astrophys. Obs., **1**, 105
- [66] Yu. Skul'skij, M., 1993, Soviet Astron. Lett. **19**, No 1, (Translated from Pis'ma Astron. Zh., Tom 19, No 1, p45)